

7-5-2019

Evaluating Fluid Fluxes From Deep-Sea Seepage Habitats

Leigha E. Peterson
Coastal Carolina University

Follow this and additional works at: <https://digitalcommons.coastal.edu/etd>



Part of the [Geochemistry Commons](#), and the [Oceanography Commons](#)

Recommended Citation

Peterson, Leigha E., "Evaluating Fluid Fluxes From Deep-Sea Seepage Habitats" (2019). *Electronic Theses and Dissertations*. 115.

<https://digitalcommons.coastal.edu/etd/115>

This Dissertation is brought to you for free and open access by the College of Graduate Studies and Research at CCU Digital Commons. It has been accepted for inclusion in Electronic Theses and Dissertations by an authorized administrator of CCU Digital Commons. For more information, please contact commons@coastal.edu.

Evaluating Fluid Fluxes From Deep-Sea Seepage Habitats

by
Leigha E. Peterson

Ph.D. Dissertation

Submitted to the faculty at Coastal Carolina University in partial fulfillment of the requirements
for the degree of Doctor of Philosophy in Marine Science.

Department of Coastal and Marine Systems Science
School of the Coastal Environment
Coastal Carolina University

2019

Ph.D. Advisor
Paul T. Gayes, Ph.D.

Committee:

Erin E. Hackett, Ph.D.
Coastal Carolina University

Samantha B. Joye, Ph.D.
University of Georgia

Christof D. Meile, Ph.D.
University of Georgia

Willard S. Moore, Ph.D.
University of South Carolina

Richard F. Viso, Ph.D.
Coastal Carolina University

ACKNOWLEDGEMENTS

This work represented a collection of ideas inspired by individuals with whom I have had the privilege of knowing both professionally and personally as a developing scientist. Paul Gayes, thank you for being more than a science advisor. I can remember accompanying your undergraduate class to the Outer Banks many years before our working together. You tolerated my relentless questioning about working on ships and some of the experiences that may accompany such a venture. Those discussions are partly to blame for my interest in oceanography.

Over the years, I had the privilege of working with many talented individuals associated with the Groundwater Discharge Measurement Facility. Thank you Patrick Hutchins, I read more papers because of you. I am grateful for my time working with Chris McHugh and Kelly Nifong, you guys were the best science friends a girl could hope for! Sarah Chappel, your commitment and vision were exactly what I needed as an example of how to work toward what you want. Sam Corley, you were an excellent office-mate and a genuinely great person; thank you for your optimism. Brad Craig, you stepped in more than once to help out in the field and even got me some stylish field gear, thank you! Matt Carter, thank you for letting me work with you in Sapelo so many years ago, I learned a lot from you. Austin Waldorf, I am grateful for our game nights and camp outs to help stay sane through the journey. Elana Ames, I am forever indebted to you; thank you for introducing me to running during my time in grad school and for brining balloons! Matt Kurpiel, thank you for your help in the lab and for tolerating my insistence to label EVERYTHING. Charlie Kollman, thank you for catching my math errors and being nice about it, I think you are perfect for science.

I am grateful for the opportunities provided to me through Coastal Carolina University and the School of the Coastal Environment. Thank you to the Center for Marine and Wetland Studies and to the Department of Coastal and Marine Systems Science for supporting incredible faculty who promote a place for thought and discussion. Thank you to my research committee for improving the work and to Rich Viso for allowing a younger me to volunteer in your lab. Thank you to collaborators from East Carolina University, the Georgia Institute of Technology, the University of Georgia, and Florida State University as well as the captain and crew of the *R/V Atlantis*, the *R/V Acadiana*, the *R/V Lawrence M. Gould*, the *R/V Endeavor*, and also the pilots and operators of the AUV *Sentry*, the HOV *Alvin*, and the ROV *Odysseus*. You all make life better.

Thank you to my mother, Dianne, who used to drive me to businesses, one after another and refuse to leave until I went in and talked to a manager. As far as I can remember, this started my life of employment! You have always refused to passively accept anything unpleasant and have shown me that life is what we are currently living, not something we aspire to create.

Rick Peterson, there aren't even words that feel significant enough to describe how grateful I am for you. Thank you for our incredible family and for lifting me higher through these experiences. Mostly, thank you for simply trying. Thank you for showing up and for caring.

This work was partially supported by funds contributed by the National Science Foundation, The Gulf of Mexico Research Initiative, and by the Center for Marine and Wetland Studies and the Department of Coastal and Marine Systems Science at Coastal Carolina University.

DEDICATION

This work is dedicated to Jake, Lyra, and Bryan Peterson. Allow yourself to find the thing that you cannot stand the thought of being without. You have my forever support to do the things you can't not do! Trust yourself to try, especially after failing a time or two. And occasionally, take time to live in awe of the simple and unsuspecting components of the world.

TABLE OF CONTENTS

LIST OF FIGURES.....	viii
LIST OF TABLES.....	xiv
ABSTRACT.....	xvi
 CHAPTER 1	
INTRODUCTION AND MOTIVATION.....	1
1.1.General Overview.....	1
1.2.References.....	7
 CHAPTER 2	
THE VERTICAL EXCHANGE MODEL.....	9
2.1.Introduction.....	9
2.2.Theory.....	13
2.3.Analytical Methods.....	16
2.4.Radium Model Component Evaluation.....	19
2.4.1.Exchange with Sedimentary Surfaces.....	20
2.4.1.1.Temporal Changes in Distribution.....	22
2.4.1.2.Spatial Changes in Distribution.....	26
2.4.2.Particulate Radium.....	30
2.4.2.1.Incorporation into Barite.....	30
2.4.2.2.Oxidation-Reduction and Sorption.....	36
2.4.3. ²²⁴ Ra Production (P) and Decay (D).....	42
2.5.Synthesis.....	46
2.5.1.Vertical Exchange Model.....	46
2.5.2. Radiotracer Corrections.....	50
2.5.3.Model Assumptions.....	53
2.5.3.1.Adsorption and Desorption.....	53
2.5.3.2.Barite Incorporation.....	55
2.5.3.3.Sorption onto Metal Hydr(oxides).....	56
2.5.3.4.Isotopic Production and Decay.....	58
2.6.References.....	60
 CHAPTER 3	
ESTIMATING SUBSURFACE POREFLUID RESIDENCE TIME AND FLUID FLUX AT COLD SEEPS IN THE GULF OF MEXICO.....	66
3.1.Introduction.....	66
3.2.Methods.....	69
3.2.1.Gulf of Mexico Study Site.....	69

3.2.2. Core Collection and Sample Processing.....	72
3.2.2.1. Core Descriptions.....	73
3.2.3. Advective Fluid Flux Calculations.....	77
3.3. Results and Discussion.....	78
3.3.1. Porefluid Residence Time and Advective Transport.....	78
3.3.1.1. Mat Core.....	79
3.3.1.2. Seep Core.....	83
3.3.1.3. Control Core.....	88
3.3.2. Effective Fluid Fluxes.....	92
3.4. Conclusions.....	97
3.5. References.....	99

CHAPTER 4

SPATIAL ASSOCIATIONS BETWEEN FLUID FLUX, TEMPERATURE, AND MICROBIAL MAT IN GUAYMAS BASIN.....	104
4.1. Introduction.....	104
4.2. Methods.....	108
4.2.1. Site and Core Descriptions.....	108
4.2.2. Geochemical Methods.....	111
4.2.2.1. Calibrations.....	112
4.2.2.2. Radiotracer Corrections.....	114
4.2.2.3. Radium Partitioning.....	114
4.3. Results and Discussion.....	115
4.3.1. Radium Distribution.....	116
4.3.2. General Overview.....	120
4.3.3. Temperature and Fluid Transport.....	125
4.3.4. Fluid Flux and Microbial Colonies.....	129
4.3.5. Potential for Fluid Recharge.....	134
4.4. Summary and Conclusions.....	138
4.5. References.....	142

CHAPTER 5

GULF OF MEXICO AND GUAYMAS BASIN FLUID FLUXES.....	146
5.1. Gulf of Mexico and Guaymas Basin Revisited.....	146
5.2. Gulf of Mexico Fluid Flux Observations.....	150
5.3. Gulf of Mexico and Guaymas Basin Comparison.....	157
5.4. References.....	163

CHAPTER 6

CLOSING REMARKS.....	167
----------------------	-----

6.1.Synthesis and Significance.....	167
6.2.References.....	170
APPENDICIES.....	171
Appendix I.....	173
Appendix II.....	214
Appendix III.....	220

LIST OF FIGURES

Figure 1.1. Schematic depicting common cold seep features associated with passive margin systems associated with large (A) and small spatial scales (B). Panel A is modified from Suess (2014) and panel B is inspired by Santos et al. (2012). Fluid migration pathways over large scales are associated with fracturing and often associated with subsurface salt, thermal, or gas reservoirs. Although hydrate is shown in the figure, for hydrothermal sites similar features could affect potential flowpaths as minerals precipitate. The red line indicates the relative vertical scale of the regions studied through this work. Panel B includes suspected mechanisms potentially contributing to the radium budget depicted in Figure 2.1. Note: the vertical and horizontal scale is not necessarily the same and that figures not drawn to scale. Vertical scales correspond to spatial scales each mechanism is likely to act over..... **5**

Figure 2.1. Conceptual mass balance diagram where the activity of ^{224}Ra dissolved in a defined volume of deep-sea porefluid (R_{T} ; dpm L^{-1}) is related to the fluid residence time in interstitial sediment spaces and several potential sources (+) and sinks (-). At radioactive equilibrium (where interstitial fluid residence time is ≥ 21 days), R_{I} equals R_{T} and the difference between production from ^{228}Th decay (R_{P}) and decay of ^{224}Ra (R_{Decay}) is zero. When the porefluid residence time is < 21 days, dissolved ^{224}Ra is advected into the box initially (R_{I}). Adsorption onto sediments (R_{A}) could remove ^{224}Ra from solution while desorption (R_{D}) could be a source. Radium precipitation into barite (R_{B}) could remove radium from solution as could the formation of metal-hydroxides and subsequent scavenging (R_{M}). The impact of each source on R_{T} is explored throughout Chapter 2. It is assumed porewater leaving the box would contain a ^{224}Ra activity equal to R_{T} **16**

Figure 2.2. (A) Aqueous ^{226}Ra activities measured at sea (filled circles) and at ^{224}Ra equilibrium via laboratory analysis (open circles). **(B)** Aqueous ^{224}Ra activities at equilibrium for replicate (a and b) temperature storage treatments. Error bars represent $\pm 1\sigma$ analytical uncertainty determined by standard error propagation of counting statistics..... **24**

Figure 2.3. (A) Results of the serial extraction experiments using vertically adjoining sediment sections. Linear regression lines are shown for each experiment. Depth intervals are presented in cmbsf. **(B)** In-situ porosity (gray symbols and solid line) and ^{224}Ra distribution coefficients (K_{d} ; green symbols) derived from the slope of each experimental regression line. Units of K_{d} are simplified from dpm kg^{-1} divided by dpm L^{-1} . Error bars represent **(A)** $\pm 1\sigma$ analytical uncertainty determined by standard error propagation of counting statistics and **(B)** the standard error of the slope for each linear model..... **28**

Figure 2.4. Aqueous porefluid ^{226}Ra activities recovered from 18 GOM cores ($n=96$) plotted against porosity. Error bars represent $\pm 1\sigma$ analytical uncertainty determined by standard error propagation of counting statistics. Results of the linear

regression model are depicted as a solid line. Symbol color denotes distinct samples as many symbols overlap..... 30

Figure 2.5. ^{222}Rn activity in air (purple symbols) estimated using the initial activity measured at sea ($^{222}\text{Rn}_t^*$; orange symbols) and at equilibrium (black symbols). (A) Shaded region corresponds to time depicted in B where ^{222}Rn activities measured in air at sea ($^{222}\text{Rn}_t$) are compared to those predicted as a function of time. Thin black line depicts regression line for observed activities. Error bars represent $\pm 1\sigma$ analytical uncertainty determined by standard error propagation of counting statistics..... 34

Figure 2.6. (A) Dissolved ^{224}Ra activities at equilibrium versus those observed at sea, recovered from vertically adjoining sediment sections (0 to 16 cmbsf). Linear regression lines are shown (A, B) for air (circle) and He (square) treatments. (B) Aqueous ^{226}Ra activities measured at sea for each treatment. Error bars represent $\pm 1\sigma$ analytical uncertainty determined by standard error propagation of counting statistics. Sediments recovered from the Gulf of Mexico..... 39

Figure 2.7. Dissolved ^{224}Ra activities at equilibrium versus those observed at sea, recovered from vertically adjoining sediment sections (0 to 12 cmbsf). Error bars represent $\pm 1\sigma$ analytical uncertainty determined by standard error propagation of counting statistics. Sediments recovered from the Gulf of Mexico. Linear regression lines are shown for air (circle) and Ar (triangle) treatments. Sediment cores recovered from Guaymas Basin..... 41

Figure 2.8. (A) Aqueous ^{224}Ra activities measured across several contact times (open symbols) compared to predicted activities (pink symbols) estimated from an initial (dark pink symbol) and an equilibrium (black symbols) activity. Error bars represent standard error propagation using counting statistics. (B). Effective residence time estimated for each treatment using a standard ingrowth equation compared to known incubation durations. Error bars represent $\pm 1\sigma$ standard deviation of all estimates determined using standard propagation of error related to counting statistics for each Ra term (Equation 2.5)..... 45

Figure 2.9. Theoretical dissolved ^{224}Ra (A) ingrowth and (B) decay as a function of time. Predicted change in aqueous ^{224}Ra activity (thick dashed line) from an initial condition (square) and a known equilibrium activity (thick gray line). Theoretically, the precise ingrowth/decay time may be determined for any activity measured at time t (circle). Error bars represent $\pm 1\sigma$ standard deviation of all estimates determined using standard propagation of error related to counting statistics of ^{224}Ra analysis..... 48

Figure 3.1. Gulf of Mexico field sampling stations integrated with BOEM’s deepwater bathymetry grid (<https://www.boem.gov/Gulf-of-Mexico-Deepwater-Bathymetry>). Filled symbols indicate sampling locations for Mat (red) and Seep (yellow) cores within the GC600 domain. Control core (green symbol) recovered

from GC699. Location of Deepwater Horizon spill site (DWH) shown for reference. Figure best viewed in color. 71

Figure 3.2. Sampling site of Mat core recovered from GC600. (A) Mat situated within a depression surrounded by olive-green sediments and shell hash. Arrows indicate (B) Mat core recovery site and (C) dark, reducing sediment exposed after sampling. Scale bars correspond to (A, B) 10 cm and (C) 5 cm. 75

Figure 3.3. Sonar generated image depicting 1 km² of GC600 seafloor including the region where Seep core was collected. Anomalous water column sounding (red feature) suggests active fluid expulsion from the sediments during the time of sampling. Anomalous water column feature estimated to extend ~50 m into overlying ocean. Image courtesy of Rich Viso. 76

Figure 3.4. (A) Aqueous ²²⁴Ra depth profiles measured at sea (R_{a_i} and R_{a_t} ; triangles) and at equilibrium ($R_{a_{eq}}$; circles) for Mat core. Error bars represent $\pm 1\sigma$ standard deviation of all estimates determined using standard propagation of error related to counting statistics of ²²⁴Ra analysis. (B) Porefluid residence time where solutions were only possible imposing a +z transport direction. The solid line represent the depth-averaged mean and dashed lines illustrate the mean $\pm 1\sigma$ standard deviation. X-axis scales set to match those in Figures 3.6 and 3.7 to facilitate direct comparison. 81

Figure 3.5. Mean advective velocities required to support aqueous interstitial porefluid ²²⁴Ra distributions. Velocities are estimated using the 1-D advective transport equation (Equation 3.1; shaded bars) and by dividing our sampling interval by the porefluid residence time determined using the vertical exchange model (Equation 2.5; hatched bars). Effective fluid flux (open squares; right-hand Y-axis) is plotted for each core using contact times generated using the vertical exchange model, sampled area, and porosity (see section 3.2). Error bars represent $\pm 1\sigma$ standard deviation of estimates determined via standard propagation of error related to counting statistics for each ²²⁴Ra term. Positive values indicate transport in the +z direction and negative values indicate possible transport in the -z direction. 84

Figure 3.6. (A) Aqueous ²²⁴Ra depth profiles measured at sea (R_{a_i} and R_{a_t} ; triangles) and at equilibrium ($R_{a_{eq}}$; circles) for Seep core. Error bars represent $\pm 1\sigma$ standard deviation of all estimates determined using standard propagation of error related to counting statistics of ²²⁴Ra analysis. (B) Porefluid residence time where solutions were only possible imposing a +z transport direction. The solid line represent the depth-averaged mean and dashed lines illustrate the mean $\pm 1\sigma$ standard deviation. Scales set to match those in Figures 3.4 and 3.7 to facilitate direct comparison. 87

Figure 3.7. (A) Aqueous ²²⁴Ra depth profiles measured at sea (R_{a_i} and R_{a_t} ; triangles) and at equilibrium ($R_{a_{eq}}$; circles) for Control core. Error bars represent $\pm 1\sigma$ standard deviation of all estimates determined using standard propagation of

error related to counting statistics of ^{224}Ra analysis. **(B)** Porefluid residence time assuming $-z$ transport direction where residence time estimated for 2 cmbsf equals 21 days assuming a $+z$ transport direction. Solid lines represent the depth-averaged mean while dashed lines illustrate the mean $\pm 1\sigma$ standard deviation. Scales set to match those in Figures 3.4 and 3.6 to facilitate direct comparison..... **91**

Figure 4.1. (A, B) Northern and Southern troughs within Guaymas Basin, Gulf of California. Collection sites integrated with bathymetric and DEM models provided by NOAA’s NCEI (<https://maps.ngdc.noaa.gov>). Symbol color indicates sediment cover characteristic (brown: inconspicuous; white: white mat; orange: orange mat) **(C)** Core recovery sites within the Southern trough indicated by dive radius integrated with multibeam data obtained using the ROV *Sentry*. Numbers shown in **C** indicate HOV *Alvin* dive number..... **109**

Figure 4.2. (A) Results from serial volume extraction experiments used to determine ^{224}Ra distribution coefficient (K_d) for samples collected during AT37-06 (green) and AT45-02 (blue). Standard error propagation using $\pm 1\sigma$ analytical uncertainties was used to determine uncertainties associated with each estimated term **(B)** Subsurface temperature profiles measured in-situ for each sample..... **118**

Figure 4.3. Depth-averaged aqueous porefluid ^{224}Ra activities (circles) estimated using sediment-coated filters (open symbols; AT37-06 cruise, this study; n=19) and Mn-fibers (filled symbols; AT45-02 cruise; n=16). Shown are mean dissolved ^{224}Ra activity in overlying water (squares) determined using Mn-fibers for AT37-06 cores (open) and AT45-06 cores (filled). Error bars represent $\pm 1\sigma$ standard deviation of activities determined using standard error propagation of counting statistics..... **120**

Figure 4.4. Depth profiles of aqueous ^{224}Ra activities in porefluid **(A)** observed at sea and **(B)** at equilibrium for all sediment cores. **(C)** Depth-dependent interstitial porefluid residence time for all sediment cores and corresponding **(D)** effective fluid fluxes. **(C, D)** Estimates separated by assumed $-z$ (open symbols; n=45) and $+z$ (filled symbols; n=100) transport direction. Median values are indicated by a horizontal line and 25th and 75th percentiles are indicated by box edges. The remaining 50% of the data are indicated by error bars and circles denote outliers. Note that median residence times for most $-z$ transport directions are ≥ 21 days. **(E)** In-situ subsurface temperatures of all sampled sites..... **124**

Figure 4.5. (A) Average aqueous porefluid ^{224}Ra activity depth profile measured at sea and **(B)** at equilibrium grouped by maximum subsurface temperature category. Error bars depict the average analytical uncertainty. **(C)** Interstitial porefluid residence time and **(D)** effective fluid flux for $-z$ (open symbols) and $+z$ (filled symbols) transport directions grouped by maximum observed temperature. Error bars represent $\pm 1\sigma$ standard deviation..... **127**

Figure 4.6. (A) Mean effective fluid flux grouped by sediment cover. Mean effective net fluid flux versus in-situ subsurface temperature at (B) 10 cmbsf and (C) 50 cmbsf. Color indicates sediment cover variable as established in A.....	131
Figure 4.7. Effective fluid flux versus temperature range ($^{\circ}\text{C}$ at 50 cmbsf – $^{\circ}\text{C}$ at 10 cmbsf) for (A) all cores excluding orange mat sediment cover, (B) white mat, (C) inconspicuous sediment cover, and (D) orange mat. Linear correlation function and square of the correlation coefficient are plotted for each relationship. Where possible, symbols match those in Figure 4.6 and indicate data are from the same sediment core.....	133
Figure 4.8. (A) Seafloor topography near Aceto balsamico (star). Spatial data obtained via sonar surveys during cruise AT37-06 using <i>ROV Sentry</i> . (B) In-situ subsurface temperature measured through Aceto balsamico. (C) Framegrabber image of the mineral crust at Aceto balsamico. Scale bar corresponds to 10 cm. Location details available in Table 4.3.....	136
Figure 5.1. (A) Core recovery region within the Gulf of Mexico. (B) Suspected oil-rich (black), non-oil-rich (gray) seepage, and control (white) sampling sites integrated with BOEM bathymetry data. Samples were recovered during cruises AT26-13 (square), EN559 (triangle), and EN586 (circle).....	152
Figure 5.2. Effective fluid flux for all sediment cores recovered from prolific natural oil seep site (GC600) within the GOM. Core numbers are arbitrary, but consistent with Figures 5.3 and 5.4, Table A.1, and Table A.2.....	154
Figure 5.3. Effective fluid flux for suspected seepage sites distinguished by (A) oil-rich and (B) non-oil-rich porefluid characteristics for sediment cores recovered from the Gulf of Mexico. (A) Hatched bars designate data associated with Taylor Energy (MC20), a shallow water site situated in water depths of ~120m. All other sampling sites are located at depths >200 m.....	156
Figure 5.4. Effective fluid flux for sediment cores recovered from (A) Guaymas Basin and (B) Gulf of Mexico. Negative fluxes indicate a net –z transport direction while positive fluxes indicate a +z direction. Non-mat and non-seep cores (denoted by color bars) indicate sites where seepage was not expected.....	161
Figure A.1. Conceptual diagram illustrating the process of correcting ^{224}Ra activities to estimate porefluid residence time using the vertical exchange model. Here, ‘equilibrium and ‘at-sea ^{224}Ra boxes indicate data in need of correcting. Equations used to correct data have been placed in large horizontal arrows with the corrected data indicated by gray boxes. Note the corrected equilibrium activity is used to correct the ‘at-sea activity. Corrected data (gray boxes) serve as inputs to the vertical exchange model (Equation 2.5) to estimate porefluid residence time (red box). See Chapter 2 for a description of data corrections.....	173

Figure A.2. Calibration curves and counting efficiency (slope) for RaDeCC analysis of sediment-coated filters. Standards were prepared using the method of standard addition for systems (A) 1, (B) 2, (C) 3, (D) 4. Note that calibrations were applied only for sediment-coated filter analysis relevant to analysis discussed in Chapter 4 and Chapter 5. Separate calibrations were performed for analysis of Mn-fibers..... **197**

Figure A.3. Calibration curves and counting efficiency (slope) for RaDeCC analysis of sediment-coated filters. Standards were prepared using the method of standard addition for systems (A) 5, (B) 6, (C) 7, (D) 8. Note that calibrations were applied only for sediment-coated filter analysis relevant to analysis discussed in Chapter 4 and Chapter 5. Separate calibrations were performed for analysis of Mn-fibers..... **198**

LIST OF TABLES

Table 2.1. Metadata for sediment samples used in vertical exchange model experiments. Experimental significance is related to sources and sinks identified in Figure 2.1.....	18
Table 2.2. Excess particulate ²²⁴ Ra activities associated with redox experiments from Gulf of Mexico sediment cores.....	38
Table 2.3. Results from laboratory-based contact time experiments.....	44
Table 3.1. Metadata for sediment cores analyzed in for Chapter 3.....	73
Table 4.1. Compilation of metadata concerning material used in the ²²⁴ Ra solid:aqueous phase partitioning (K _d) experiments.....	116
Table 4.2. Site metadata for sediment cores collected during the AT37-06 cruise from which fluid flow rate and direction are evaluated.....	121
Table 4.3. Core metadata for the Aceto balsamico core. Collection date/time is in EST, ²²⁴ Ra activities are given in dpm L ⁻¹ and residence time is presented in days.....	137
Table A.1. Metadata for sediment cores recovered from the Gulf of Mexico. Site name refers to that designated by the Bureau of Ocean Energy Management (BOEM) and core number refers to the fluid flux rank variable used in Chapter 5 (Fig. 5.2, Fig. 5.3, and 5.4). Collection date and time are given in Eastern Standard Time (EST) and seep condition indicates characteristics of the sampling region.....	174
Table A.2. Aqueous porefluid ²²⁴ Ra activities recovered from cores collected within the Gulf of Mexico. Site name refers to that designated by BOEM and core number refers to the fluid flux rank variable used in Chapter 5 (Fig. 5.2, Fig. 5.3, and 5.4) and Table A.1. Initial activities are those measured at-sea and equilibrium activities are those measured in solution following a 21 day incubation.....	176
Table A.3. Porefluid residence time and porosity for sediment samples associated with sediment cores recovered from the Gulf of Mexico. Residence time is estimated by assuming transport toward the overlying ocean (+z) and also into the sediments (-z).Site name refers to that designated by BOEM and core number refers to the fluid flux rank variable used in Chapter 5 (Fig. 5.2, Fig. 5.3, and 5.4) and Table A.1 and Table A.2 and Table A.4.....	183
Table A.4. Vertical volumetric porefluid flux determined for sediment samples associated with sediment cores recovered from the Gulf of Mexico. Fluid flux is estimated by assuming transport toward the overlying ocean (+z) and also into the sediments (-z).Site name refers to that designated by BOEM and core number refers	

to the fluid flux rank variable used in Chapter 5 (Fig. 5.2, Fig. 5.3, and 5.4) and Table A.1 and Table A.2 and Table A.3.....	190
Table A.5. Surface-sorbed ²²⁴ Ra and aqueous activities measured at sea and at equilibrium for samples recovered from Guaymas Basin. Dive number refers to the HOV <i>Alvin</i> dive number during cruise AT37-06 and core number refers to the fluid flux rank variable used in Chapter 5 (Figure 5.4).....	199
Table A.6. Porefluid residence time and porosity for sediment samples associated with sediment cores recovered from Guaymas Basin. Residence time is estimated by assuming transport toward the overlying ocean (+z) and also into the sediments (-z). Dive number refers to the HOV <i>Alvin</i> dive number during cruise AT37-06 and core number refers to the fluid flux rank variable used in Chapter 5 (Figure 5.4).....	204
Table A.7. Vertical volumetric porefluid flux determined for sediment samples associated with sediment cores recovered from the Gulf of Mexico. Fluid flux is estimated by assuming transport toward the overlying ocean (+z) and also into the sediments (-z). Dive number refers to the HOV <i>Alvin</i> dive number during cruise AT37-06 and core number refers to the fluid flux rank variable used in Chapter 5 (Figure 5.4).....	209

ABSTRACT

The permanently dark deep-sea, located at oceanic water depths greater than 200 m, represents the largest potential habitat space on Earth. The physicochemical conditions of the planet's largest biome are tightly coupled to the exchange of matter and energy from terrestrial and sea-floor end-members. In fact, global ocean and climate systems are significantly impacted by deep-sea processes. Seafloor vents and seeps appear to act as geologic exchange conduits, returning recycled materials to the hydrosphere to sustain another generation of life. Despite submarine seepage having control on global elemental cycling, it is estimated that less than 1% of the deep-sea has been mapped in detail sufficient to truly understand the spatial extent of regions of especially active material and energy exchange at regions of seafloor venting and seepage. Slow-flow discharge occurring at elevated temperatures (hydrothermal seepage) is suspected to exchange ~ 90% of the water required to balance heat budgets as compared to energetic vents. Deep-sea seepage occurring at ambient ocean temperatures (cold seeps), first discovered in the Gulf of Mexico, represents a second seepage environment where chemosynthetic primary production supports some of the most diverse biomes in the bathypelagic zones. However, methods and research directly applicable for understanding the rate of fluid discharge at low-flow submarine seepage sites are lacking, resulting in poorly constrained global chemical cycling estimates.

This Dissertation provides a vertical exchange model designed to determine an effective fluid flux of porefluid from deep-sea environments. The vertical exchange model utilizes vertical distributions of aqueous ^{224}Ra in porefluid recovered from regions impacted by hydrothermal and cold seepage and determines porefluid residence time related to radiogenic changes attributable to production and decay. The vertical exchange model is qualitatively tested whereby isotope proxy

estimates confirm seepage in areas where seepage is indicated by ancillary evidence and suggest porefluid transport into the sediments best explains vertical isotope distributions observed for Control core. The vertical exchange model is applied to a hydrothermal site in Guaymas Basin to test whether spatial associations between microbial mats and seepage rates exist. We identify spatial relationships between subsurface temperature range and fluid flux where white colored microbial colonies exist; however, fluid flux appears unrelated to subsurface temperature range where orange filaments are found. Fluid flux estimates for sampled regions within both sites were observed to be similar despite the unique thermal source present only at Guaymas Basin. This work offers a novel approach to quantify fluid flow both into and out of the sediments across a variety of deep-sea habitats where seepage moderates the success of unique benthic ecosystems.

CHAPTER 1

INTRODUCTION AND MOTIVATION

1.1. General Overview

Deep-sea regions, defined here as marine water depths greater than 200 m, are our planet's largest potential living space (Orcutt et al., 2011). This habitat, including the seabed regularly exchange mass and energy with terrestrial and atmospheric systems. Chemical processes that occur in the deep-sea are known to moderate biogeochemical cycles upon which many terrestrial species, including humans, depend (Armstrong et al., 2012). In other words, material and energy exchange between the deep-sea and the seafloor are relevant for life as we know it (Danovaro et al., 2016; Levin et al., 2016). In fact, these environments may have served as a critical refuge for marine life that was nearly annihilated in euphotic zones during historic global mass extinction events (Van Dover et al., 2002).

Several exchange mechanisms have been recognized to support unique deep-sea habitats (e.g., Corliss et al., 1979; Paull et al., 1984) where entire ecosystems are sustained by bacterial communities which add new organic carbon to the otherwise carbon-poor environments. These microbes accomplish this metabolic process via chemosynthesis using hydrogen sulfide, methane, or heavy metals (e.g., iron) as energy sources to convert inorganic carbon into biomass (Little and

Vrijenhoek, 2003). Thus, compounds relevant to global climate (e.g., methane and carbon dioxide,) are moderated by these chemosynthetic communities (Judd et al., 2002). Similar genetic lineages and evolutionary histories have been found between invertebrate taxa associated with deep-sea seeps and appear across a variety of porefluid discharge habitats across a range of temperatures and fluid fluxes (Van Dover et al., 2002).

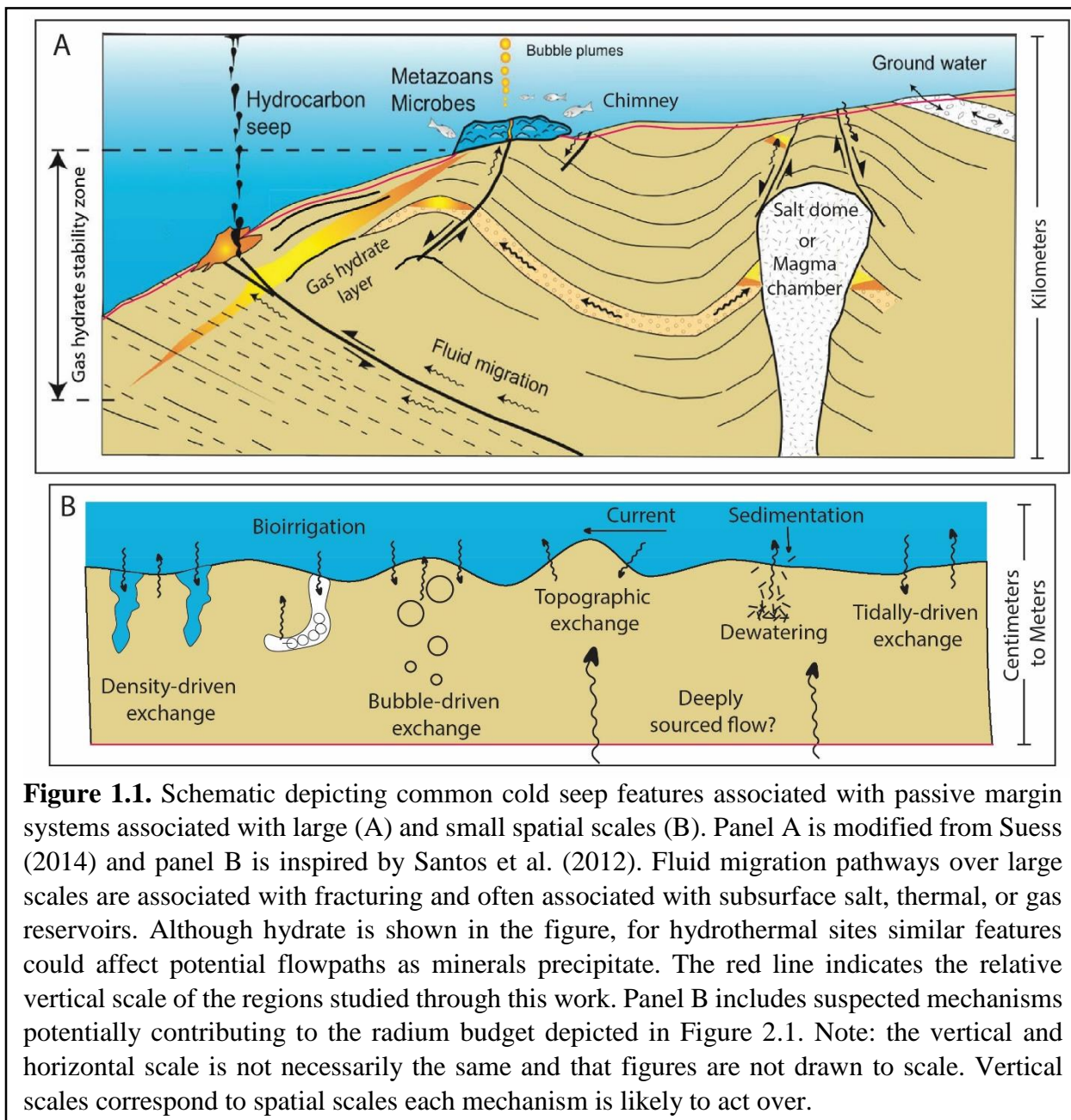
In general, subsurface fluid will be transported from regions of high hydrodynamic and chemical potential to low potential as described by Bjørlykke (1993). A few common mechanisms are credited with instigating pressure and chemical gradients related to transport. At hydrothermal sites, porefluid transport may be driven by thermal convection whereby the thermal expansion of water establishes an inverse subsurface density gradient potentially causing layers of porewater to overturn (Bjørlykke, 1993). Fluid flow may also be driven by sediment compaction and subsequent dewatering (Bjørlykke and Høeg, 1997) or be related to the release of pressurized porefluids associated with rapid sedimentary loading or tectonic compression (Foucher et al., 2009). Additional mechanisms of fluid transport may include subsurface phase change and subsequent overpressurization (Sun et al., 2012). Such phase changes can be linked to hydrate stability, carbonate formation, and methanogenesis which may influence both permeability and porefluid composition. However, site specific factors including depth of fluid origination, rate of fluid flow, temperature of rock-water interaction, and tectonic framework may influence the geochemistry of the seeping fluids more so than the physical mechanisms acting to transport fluid. It is also recognized that in some cases, mechanisms of fluid flow (e.g., halite dissolution) could most greatly moderate the composition of discharged fluid. Such complex associations between geochemistry, fluid flux, and driving mechanism could be related to the many different marine environments associated with active seafloor seepage (Ramirez-Llodra et al., 2010).

It is estimated that less than 1% of the deep seafloor has been studied in detail toward a comprehensive understanding of the significance of deep-sea seepage (Ramirez-Llodra et al., 2010), yet sites where such discharge has been identified are known to support some of the highest levels of biodiversity on Earth with significant mineral and biological resources including seafloor massive sulfides and manganese nodules (Lusty and Murton, 2018). Although it is difficult to know exactly how many deep-sea seepage environments exist globally (Bris et al., 2016), researchers suspected ~2% of global cold seeps have been sampled directly (Ramirez-Llodra et al., 2010). The term ‘cold seep’ describes an environment associated with/dependent upon the discharge of subsurface porefluid at or near ambient ocean temperatures. Similarly, only 10% of the hydrothermal vents globally have been directly sampled (Ramirez-Llodra et al., 2010). Here, ‘hydrothermal site’ refers to the locations of communities dependent upon/directly influenced by the discharge of porefluid at temperatures greater than that of the ambient ocean. Likely because energetic venting of subsurface fluids has been easier to identify, much less is known about slow-flow seepage sites where species richness is often higher and discharge rates are lower (Portail et al., 2016). Still, the relationship between seep-associated organisms and the rate of fluid flow is largely unknown, especially for slow flow, seepage sites (Sibuet and Olu, 1998). Although there have been several studies to address fluid seepage rates, water circulation, and porefluid transport rates, our understanding of these processes still remains limited (Suess, 2014), and presents challenges towards our ability to evaluate the ecosystem goods and services provided by these environments (Armstrong et al., 2012). While the discrepancy between understanding and effort is likely best explained by the vastness of the deep-sea, the need nonetheless exists to determine water and material transfer occurring at deep-sea cold and hydrothermal seeps (Suess, 2014; Levin et al., 2016).

The overarching objective of this dissertation is to develop a model for evaluation of deep-sea fluid fluxes and apply it across a variety of sedimented seepage sites. Throughout we use the term fluid flux to represent a volumetric vertical porefluid flux, hereafter referred to as fluid flux for simplicity). Broadly, this work concerns the utility of geochemical profiles to evaluate fluid fluxes through cold seep and hydrothermal sites. This objective is satisfied through work detailed in a series of chapters, each organized around a set of secondary objectives. This dissertation details the development of a model used to quantify volumetric vertical fluid flux through shallow (decimeter scale) sediment sections recovered from seepage sites where both relatively large and small scale fluid transport mechanisms may influence transport quantities (Figure 1.1).

Chapter 2 describes conditions and assumptions previously applied in coastal settings for using chemical proxies to estimate fluid flow rates. A series of parameters unique to deep-sea sediments are discussed as they may differ from coastal materials for which much of the referenced work was developed. Specifically, this chapter examines the assumptions applied by Krest and Harvey (2003), where the origins of the proposed deep-sea model were developed. Results are used toward the development of a vertical exchange model appropriate for determining porefluid flux in deep-sea seepage habitats.

In Chapter 3, model performance is qualitatively evaluated by determining the effective fluid fluxes at suspected cold seep and control sites. Model-based fluid fluxes are considered in the context of observational evidence as an indication of active seepage. Vertical exchange model results are also compared to those derived from a 1-dimensional advection-diffusion equation. This chapter serves as a proof of concept of the model using deep-sea sediments recovered from the Gulf of Mexico.



In Chapter 4, the vertical exchange model is employed to identify the range in fluid flux through hydrothermal sediments in Guaymas Basin, Gulf of California. An effective fluid flux is determined for a series of sediment cores associated with microbial indicators of seepage and results are compared to fluid fluxes determined for areas of inconspicuous sediment cover. We

sample across sediment cover type (i.e., different color microbial mats) and across various subsurface thermal regimes to ultimately discuss spatial associations between fluid flux, temperature, and sediment cover.

Chapter 5 concludes this work with a brief comparison between fluid fluxes determined for a series of cores recovered from cold seeps in the Gulf of Mexico and hydrothermal environments in Guaymas Basin. This chapter offers a discussion of fluid flux magnitude determined using the vertical exchange model between the cold seep and hydrothermal sites studied.

Ultimately, through development and application of a vertical exchange model, this dissertation offers a novel approach to evaluate fluid flow through deep-sea sediments that has been applied at two distinct seepage habitats.

1.2. References

- Armstrong, C.W., Foley, N.S., Tinch, R., van den Hove, S., 2012. Services from the deep: Steps towards valuation of deep sea goods and services. *Ecosystem Services* 2, 2–13. <https://doi.org/10.1016/j.ecoser.2012.07.001>
- Bjørlykke, K., 1993. Fluid flow in sedimentary basins. *Sedimentary geology, basin analysis and dynamics of sedimentary basin evolution* 86, 137–158. [https://doi.org/10.1016/0037-0738\(93\)90137-T](https://doi.org/10.1016/0037-0738(93)90137-T)
- Bjørlykke, K., Høeg, K., 1997. Effects of burial diagenesis on stresses, compaction and fluid flow in sedimentary basins. *Marine and Petroleum Geology* 14, 267–276. [https://doi.org/10.1016/S0264-8172\(96\)00051-7](https://doi.org/10.1016/S0264-8172(96)00051-7)
- Bris, N.L., Arnaud-Haond, S., Beaulieu, S., Cordes, E., Hilario, A., Rogers, A., van de Gaever, S., Watanabe, H., 2016. Chapter 46 – Hydrothermal vents and cold seeps 18.
- Corliss, J.B., Dymond, J., Gordon, L.I., Edmond, J.M., Herzen, R.P. von, Ballard, R.D., Green, K., Williams, D., Bainbridge, A., Crane, K., Andel, T.H. van, 1979. Submarine Thermal Springs on the Galápagos Rift. *Science* 203, 1073–1083. <https://doi.org/10.1126/science.203.4385.1073>
- Danovaro, R., Molari, M., Corinaldesi, C., Dell’Anno, A., 2016. Macroecological drivers of archaea and bacteria in benthic deep-sea ecosystems. *Science Advances* 2, e1500961. <https://doi.org/10.1126/sciadv.1500961>
- Foucher, J.P., Westbrook, G., Boetius, A., Ceramicola, S., Dupré, S., Mascle, J., Mienert, J., Pfannkuche, O., Pierre, C., Praeg, D., 2009. Structure and drivers of cold seep ecosystems. *Oceanography* 22, 92–109. <https://doi.org/10.5670/oceanog.2009.11>
- Judd, A.G., Hovland, M., Dimitrov, L.I., Gil, S.G., Jukes, V., 2002. The geological methane budget at Continental Margins and its influence on climate change. *Geofluids* 2, 109–126. <https://doi.org/10.1046/j.1468-8123.2002.00027.x>
- Krest, J.M., Harvey, J.W., 2003. Using natural distributions of short-lived radium isotopes to quantify groundwater discharge and recharge. *Limnology and Oceanography* 48, 290–298. <https://doi.org/10.4319/lo.2003.48.1.0290>
- Levin, L.A., Baco, A.R., Bowden, D.A., Colaco, A., Cordes, E.E., Cunha, M.R., Demopoulos, A.W.J., Gobin, J., Grupe, B.M., Le, J., Metaxas, A., Netburn, A.N., Rouse, G.W., Thurber, A.R., Tunnicliffe, V., Van Dover, C.L., Vanreusel, A., Watling, L., 2016. Hydrothermal vents and methane seeps: Rethinking the sphere of influence. *Frontiers in Marine Science* 3. <https://doi.org/10.3389/fmars.2016.00072>
- Little, C.T.S., Vrijenhoek, R.C., 2003. Are hydrothermal vent animals living fossils? *Trends in Ecology & Evolution* 18, 582–588. <https://doi.org/10.1016/j.tree.2003.08.009>

- Lusty, P.A.J., Murton, B.J., 2018. Deep-Ocean mineral deposits: metal resources and windows into Earth processes. *Elements* 14, 301–306. <https://doi.org/10.2138/gselements.14.5.301>
- Orcutt, B.N., Sylvan, J.B., Knab, N.J., Edwards, K.J., 2011. Microbial ecology of the dark ocean above, at, and below the seafloor. *Microbiology and Molecular Biology Reviews* 75, 361–422. <https://doi.org/10.1128/MMBR.00039-10>
- Paull, C.K., Hecker, B., Commeau, R., Freeman-Lynde, R.P., Neumann, C., Corso, W.P., Golubic, S., Hook, J.E., Sikes, E., Curray, J., 1984. Biological communities at the Florida Escarpment resemble hydrothermal vent taxa. *Science* 226, 965–967. <https://doi.org/10.1126/science.226.4677.965>
- Portail, M., Olu, K., Dubois, S.F., Escobar-Briones, E., Gelinas, Y., Menot, L., Sarrazin, J., 2016. Food-web complexity in Guaymas Basin hydrothermal vents and cold seeps. *PLOS ONE* 11, e0162263. <https://doi.org/10.1371/journal.pone.0162263>
- Ramirez-Llodra, E., Brandt, A., Danovaro, R., Escobar, E., German, C.R., Levin, L.A., Arbizu, P.M., Menot, L., Buhl-Mortensen, P., Narayanaswamy, B.E., Smith, C.R., Tittensor, D.P., Tyler, P.A., Vanreusel, A., Vecchione, M., 2010. Deep, diverse and definitely different: unique attributes of the world's largest ecosystem. *Biogeosciences Discussions* 7, 2361–2485. <https://doi.org/10.5194/bgd-7-2361-2010>
- Santos, I.R., Eyre, B.D., Huettel, M., 2012. The driving forces of porewater and groundwater flow in permeable coastal sediments: A review. *Estuarine, Coastal and Shelf Science* 98, 1–15. <https://doi.org/10.1016/j.ecss.2011.10.024>
- Sibuet, M., Olu, K., 1998. Biogeography, biodiversity and fluid dependence of deep-sea cold-seep communities at active and passive margins. *Deep-Sea Research II* 45, 517-567.
- Suess, E., 2014. Marine cold seeps and their manifestations: geological control, biogeochemical criteria and environmental conditions. *International Journal of Earth Sciences : Geologische Rundschau; Berlin* 103, 1889–1916. <http://dx.doi.org/10.1007/s00531-014-1010-0>
- Sun, Y., Wu, S., Dong, D., Lüdmann, T., Gong, Y., 2012. Gas hydrates associated with gas chimneys in fine-grained sediments of the northern South China Sea. *Marine Geology* 311–314, 32–40. <https://doi.org/10.1016/j.margeo.2012.04.003>
- Van Dover, C.L., German, C.R., Speer, K.G., Parson, L.M., Vrijenhoek, R.C., 2002. Evolution and biogeography of deep-sea vent and seep invertebrates. *Science* 295, 1253–1257. <https://doi.org/10.1126/science.1067361>

CHAPTER 2

THE VERTICAL EXCHANGE MODEL

2.1. Introduction

A volume equivalent to the entire global ocean is thought to circulate through the oceanic crust every 10^5 to 10^6 years (Orcutt et al., 2011). Water enters the crust via lithospheric subduction, infiltration through basement outcrops (Fisher et al., 2001), and burial of oceanic sediments (Suess, 2014) after which it may undergo chemical alterations due to high-temperature water/rock interactions, dissolution of geologic strata, and oxidation/reduction reactions. Subsequent discharge of this altered water occurs at highly localized zones of energetic advective flow (venting) and also over much larger regions of slower flow (seepage). High-temperature water/rock interactions and subsequent venting at hydrothermal regions are estimated to contribute significantly to global ocean Mg and Ca budgets (Seyfried and Bischoff, 1981) and also supply a significant fraction of iron and other trace metals to oceanic environments (Fitzsimmons et al., 2014).

Even at settings where such discharging water has not experienced high-temperature water/rock interactions (i.e., cold seeps), the vertical flow of subsurface water through geologic strata often mobilizes biogeochemical constituents (forms of C, N, P, and S) that support chemosynthetic ecosystems at the seafloor (Dekas et al., 2009; Suess, 2014). Endemic

communities of mussels/clams, worms, fishes, and other high-level benthic organisms associated with discharging subsurface water are generally supported by vast microbial populations and endosymbionts (Kennicutt II et al., 1985; Brooks et al., 1987). Seep products have even been spatially linked to elevated biomass in photic zones (D'souza et al., 2016) suggesting the impact of such discharge on the marine environment is far-reaching. Community structure and ecosystem complexity at these sites is thought to be inversely related to fluid discharge rates as sites of rapid venting are generally associated with lower species diversity and simpler food-web structures as compared to seepage sites characterized by slower flow (Portail et al., 2016). While energetic venting may be ecologically significant over global scales, localized seepage appears to exert greater control on an individual community.

Diffuse seepage is often inferred from the presence of an oasis type community emerging from regions of otherwise inconspicuous sediment cover. Especially in deep-sea aphotic zones, seeping fluids sustain communities supported almost entirely by the relative enrichment of reduced compounds, an otherwise uncommon characteristic among nearby abyssal regions (Paull et al., 1984; Fisher and Becker, 1991; Orcutt et al., 2011). Although it is not an objective of this work to identify specific mechanisms or even the relative importance of any one mechanism over another, many factors driving porefluid transport through deep-sea sediments have been proposed. For example, Fluid seepage through passive margin systems can occur at near-ambient ocean temperatures (cold seeps) as a result of increased pore-pressure related to the movement of buried evaporite deposits, subsurface oil/gas production, and/or sediment slumping (Orcutt et al., 2011). Exchange through surficial sediments may also be related to tidal, and topography-induced flow as well as several other potential mechanisms identified in Figure 1.1). Diffuse seepage can also occur at slightly elevated temperatures associated with exothermic chemical reactions (Kelley et

al., 2005) or remnant lithospheric heat (Wheat et al., 2004). Even considering hydrothermal systems where intense venting represents a visually extraordinary form of subsurface discharge, diffuse seepage is thought to discharge 90% of the water mass circulated through oceanic crust (Orcutt et al., 2011). Such estimates are suggestive of the expansive magnitude of diffuse seepage, yet are also subject to a high degree of uncertainty as localized seepage rate estimates across a variety of geobiologic environments remain one of the least understood components of marine element cycling (Suess, 2014).

Seepage rates may be evaluated via both direct and indirect measurement approaches. Direct approaches involve the placement of observational instrumentation on the seabed, which may limit feasibility due to logistical challenges of operating in the deep-sea. Indirect methods utilize distributions of conservative thermal and chemical proxies whereby spatial trends are often assessed as profiles through geologic strata and may be related to an advective velocity. However, indirect methods to evaluate seepage rates in deep-sea environments are largely only applicable under certain conditions (e.g., a sufficiently strong thermal gradient through sediments at hydrothermal settings and a strong ion gradient for brine seeps). Efforts to date suggest fluid transport rates range from 30 to 470 cm yr⁻¹ for low-temperature hydrothermal sites (Fisher and Becker, 1991) and from 7 to 65 cm yr⁻¹ for brine seeps (Lapham et al., 2008). Such velocities suggest that subsurface residence time in a 1 cm sediment depth-interval could then range from 0.8 to 12 days near hydrothermal ridges and from 5 to 52 days near cold seeps.

For any indirect means of evaluating subsurface fluid flow and discharge dynamics, the utilized proxy should be influenced by seepage-related mechanisms more strongly than other sources and sinks to minimize uncertainty. It should also be that an effective proxy is enriched/depleted in the seeping fluids relative to ocean waters and responds on time frames

appropriate to those of the process(es) being evaluated. The paucity of diffuse, seepage rate estimates across deep-sea sedimentary settings is due to the lack of robust tools that meet these criteria across the wide range of seepage environments. The development of additional tools to constrain seepage rates in deep-sea settings thus remains a strong area of research need.

In this work, we explore whether ^{224}Ra could serve as such a proxy for indirect assessment of porefluid flow through deep ocean sediments. With a half-life of 3.6 days, the effective dating range of this chemical proxy ranges from 1 to 21 days. Many authors have shown the utility of ^{224}Ra to provide fluid flux estimates (and assess geochemical controls) from coastal and shallow water systems (Krest and Harvey, 2003; Colbert and Hammond, 2008; Gonnee et al., 2008; Cai et al., 2012; Beck and Cochran, 2013). However, the use of ^{224}Ra to quantify 1-dimensional fluid fluxes through deep-sea sediments by evaluating porefluid tracer distributions in a vertical exchange model is novel.

Krest and Harvey (2003) first described a vertical exchange model that utilizes ^{224}Ra disequilibria to estimate porefluid flow rates in a freshwater marsh. Here, we use components of that model and the various assumptions behind it to determine effective flow rates through deep-sea sediments where diffuse seepage rates are poorly constrained. In this chapter, we characterize various ^{224}Ra sources and sinks to/from sedimentary porefluid and assess how measurements, and in some cases simplifications, of those sources/sinks may be used toward development of a model that would ultimately estimate porefluid residence times and resulting fluid flux. As is common with indirect approaches toward understanding a process, our estimates may include large error. We attempt to identify sources of potential error and consider the likely way(s) in which our fluid flux estimates may be affected by such uncertainties.

The goal of this work is to develop a vertical exchange model adequate to estimate porefluid residence time in deep-sea sediments based on that originally presented by Krest and Harvey (2003). From residence time, a rate of replacement (i.e., fluid flux) may be estimated for cold seep (Chapter 3) and hydrothermal (Chapter 4) environments. To meet that goal, we address the following objectives throughout this chapter: (1) identify potential sources and sinks of ^{224}Ra within deep-sea porefluid; (2) experimentally characterize the relationship between aqueous ^{224}Ra and associated sources and sinks; and (3) discuss the potential consequence(s) for residence time and subsequent fluid flux estimates if these source/sink terms are insufficiently constrained.

2.2. Theory

Radium-224 is a naturally-occurring radioisotope ($T_{1/2} = 3.6$ days) and a common proxy to study water mass mixing and porefluid exchange (Moore, 2000; Weber et al., 2016; Corbett et al., 2017; Hong et al., 2017; Sadat-Noori et al., 2017). Soluble ^{224}Ra in porefluid is generally sourced from decay of parent ^{228}Th isotopes adsorbed to particle surfaces. Although a significant portion of ^{224}Ra remains adsorbed to the grain surface when surrounded by sea water (Gonneea et al., 2008), a considerable amount may also be dissolved in solution. The sum of ^{224}Ra adsorbed to sediment surfaces that is available for desorption combined with that which is dissolved in porewater is termed ‘exchangeable’ ^{224}Ra .

Being a dissolved ion, radium may be transported via porefluids migration. Changes in porefluid radium activity with time thus represent a balance between dispersion, advection, production, decay, and exchange with sedimentary surfaces (from Krest and Harvey, 2003):

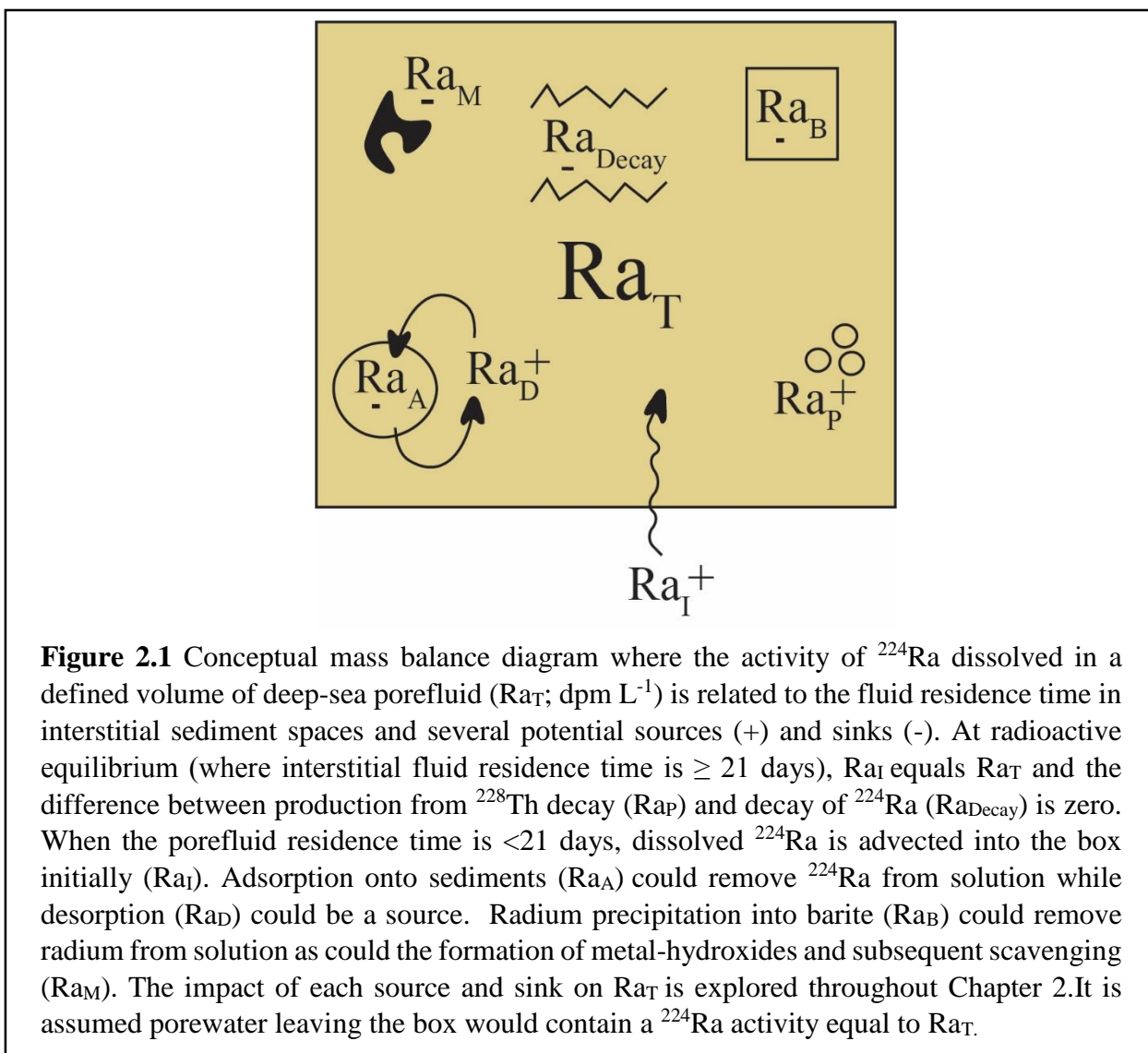
$$\frac{dC}{dt} = D \frac{\partial^2 C}{\partial Z^2} - \omega \frac{\partial C}{\partial Z} + \frac{\hat{P}\rho}{fK_d + (1-f)} - \lambda C + \frac{\partial C^*}{\partial t} \frac{\rho}{K_d} \quad (2.1)$$

Equation. 2.1 is an adaptation of the standard advection-diffusion equation (Berner, 1980) and directly from Krest and Harvey (2003). Here, C is the number of dissolved atoms per volume of water, D is the hydrodynamic dispersion coefficient (with units of length² per time), Z is depth below the sediment-water interface, ω is the porefluid advective vertical velocity (with units of length per time), \hat{P} is the production rate of exchangeable radium via parent isotope decay (with units of number of atoms per time per mass of bulk sediment), ρ is the porefluid density (with units of mass per volume), f is the mass of dry sediment per mass of bulk sediment, K_d is the radium distribution coefficient equal to the ratio of ²²⁴Ra atoms adsorbed to particle surfaces relative to those in solution, λ is the decay constant of ²²⁴Ra (0.189 day⁻¹), and C^* is the number of ²²⁴Ra atoms adsorbed to particles per mass of dry sediment.

According to Krest and Harvey (2003), the following conditions must be met before estimating ω using Equation 2.1: (1) production and decay affecting dissolved ²²⁴Ra are unequal (i.e., a state of radioactive disequilibrium must exist); (2) ²²⁴Ra production rates are estimated and constant in space and time over the considered sediment column; and (3) the partition coefficient of ²²⁴Ra (K_d) is constant and uniform throughout the sediment column. The authors plainly state that layered systems or otherwise geochemically heterogeneous environments must account for changes in the rate of ²²⁴Ra production and subsequent distribution. This is likely because variables related to sediments (f) and ²²⁴Ra geochemistry (\hat{P} , K_d) are represented by a single term over the considered domain. Several papers have identified common factors influencing environmental levels of radium in solution and several researchers have posited many environmental controls on porefluid ²²⁴Ra activities, concluding that the influence of any one parameter on radium partitioning may be highly variable and so warrant evaluation in new environments before using

radium as a proxy for fluid transport (Rama and Moore, 1996; Gonnee et al., 2008; Beck and Cochran, 2013). Additionally, vertical advective velocities are assumed to be significantly larger than horizontal advective velocities so that this equation may be simplified to one spatial dimension.

Prior to adapting the conceptual framework developed by Krest and Harvey (2003), we therefore need to explore the assumptions and potential controls on ^{224}Ra in deep-sea porefluid as the original model was developed for a freshwater marsh system. We maintain the assumption that advective vertical velocities are significantly larger than horizontal velocities and simplify our approach as done by Krest and Harvey (2003) to 1-dimension. We also evaluate the need to include additional terms that may be required for the deep-sea that were not needed in the marsh studied by Krest and Harvey (2003). For example, in-situ reactions involving chemical precipitation (e.g., barite formation) and oxidation/reduction alterations (e.g., iron and manganese (hydr)oxide formation) may scavenge ^{224}Ra and thus represent another radium sink from the porefluids. In the following sections, we describe several laboratory experiments intended to characterize the various relationships between aqueous ^{224}Ra and each identified source/sink term as they may change ^{224}Ra distribution. We also explore how the logistical issues related to sample collection, preservation, and subsequent laboratory analysis may influence the suitability of applying these assumptions. Perhaps most importantly, we intend to eliminate the assumption of a constant production rate applied by Krest and Harvey (2003) in our vertical exchange model. Potential sources and sinks of ^{224}Ra to porewater are presented in Figure 2.1 and serve to accommodate the coming sections as we test for effects of the potentially important mechanisms unique to the deep-sea.



2.3. Analytical Methods

We describe several laboratory experiments used in the construction of our vertical exchange model. In this section, we describe methods common across all experiments to determine ^{224}Ra activities regardless of where or how the sample was collected. Details unique to specific experiments are described in Section 2.4 as appropriate.

Sediments were recovered from the deep-sea and coastal marine environments where materials were continuously bathed in seawater. In some instances, we use sediment cores collected from the Gulf of Mexico (GOM) and the Gulf of California (Guaymas Basin) obtained during research cruises spanning from June 2015 to November 2018 as well as grab samples recovered from South Carolina salt marshes (Table 2.1). Sediment cores were recovered from water depths >500 m using a shipboard multiple core deployment and recovery system, the human-occupied vehicle (HOV) *Alvin*, or the remotely-operated vehicle (ROV) *Odysseus*. Sample porosity was determined by water mass loss upon drying at 60 °C and grain density was determined by volume displacement (Lambe, 1951).

For analysis of dissolved ^{224}Ra , porefluid/experimental seawater was recovered from sediment samples via centrifugation at 5,000 RPM for 15 min and subsequently filtered through a 0.45 μm millipore filter to remove any suspended particles. ‘Porefluid’ is distinguished from ‘experimental water’ in that it is environmental water recovered from recently obtained sediments, whereas experimental water refers to Ra-free seawater used to rehydrate sediments that is later recovered for analysis. All water recovered from sediments was diluted with 1L Ra-free seawater to facilitate processing and passed twice slowly ($< 1 \text{ L min}^{-1}$) over a 25 g aliquot of dry MnO_2 -impregnated acrylic fiber to quantitatively adsorb dissolved Ra (Moore, 1976; Moore, 2008; $97.8 \pm 1.3 \%$ ^{224}Ra sorption efficiency). Mn-fiber was then rinsed with Ra-free tap water to remove residual salt and dried using a compressed air stream until an optimal mass for analysis was achieved (Sun and Torgersen, 1998). Fibers were immediately analyzed on a Radium Delayed Coincidence Counter (RaDeCC; Moore and Arnold, 1996) and reanalyzed three weeks later to correct initial measurements for any contribution from dissolved ^{228}Th (Porcelli and Swarzenski, 2003). To determine the equilibrium activity of ^{224}Ra in the dissolved phase associated with any

sediment source ($R_{a_{eq}}$), sediments were dried at 60 °C and rehydrated to in-situ porosity using Ra-free seawater. Slurries were incubated for a >3 weeks and then experimental waters were separated via centrifugation and analyzed as discussed above.

Table 2.1. Metadata for sediment samples used in vertical exchange model experiments. Experimental significance is related to sources and sinks identified in Figure 2.1.

Experimental significance	Text section	Collection site [§]	Collection date & time (EST)	Cruise ID; collection method	Latitude and longitude	Sample description
R_{aA} and R_{aD} lab/at-sea	2.4.1.1	GOM-GC767	6/16/2015 17:20	EN559; multiple core	27° 12.59' N, 91° 00.59' W	1 sediment core
Temperature & R_{aA} and R_{aD}	2.4.1.1	MYR-WPS	March, 2016	Sediment grab	33° 45.845' N, 78° 46.930' W	Surficial sediment
Depth & R_{aA} and R_{aD}	2.4.1.2	GOM-GC600	9/4/2018 13:49	PS 1905; ROV <i>Odyseus</i> pushcore	27°22.1906'N, 90°34.2668'W	1 sediment core
Porosity & R_{aA} and R_{aD}	2.4.1.2	GOM- [#] EcoGIG targets	July- August, 2016	EN586; multiple core	27° 29.966' N, 91° 58.721' W	18 sediment cores
R_{aB}	2.4.2.1	GOM-GC600	9/4/2018 13:41	PS 1905; ROV <i>Odyseus</i> pushcore	27°22.1906'N, 90°34.2668'W	1 sediment core
$R_{a_{Ads}}$	2.4.2.2	GOM-OC26	8/6/2016 8:31	EN586; multiple core	28°41.503'N, 88°22.770'W	2 sediment cores
$R_{a_{Ads}}$	2.4.2.2	GY-CH	11/20/2018 15:07 & 14:20	AT45-02; HOV <i>Alvin</i> pushcore	27°00.6726'N, 111°24.2613'W	2 sediment cores
Change in activity, R_{aP} , and R_{aD}	2.4.3	MYR-WPS	March, 2016	Sediment grab	33° 45.845' N, 78° 46.930' W	Surficial sediment

[§] Site acronyms: GOM- Gulf of Mexico; GC- Green Canyon; GY Guaymas Basin; MYR- Myrtle Beach, SC; WPS-White Point Swash; CH-Cathedral Hill

* Location presented as a range of coordinates encompassing collection sites for all considered samples.

[#]EcoGIG targets refers to a series of previously identified seepage sites determined using a variety of direct observational evidence and also indirect means including acoustic imaging.

Ra-226 was measured on each Mn-fiber to serve as a stable (i.e., non-decaying) isotope proxy for ^{224}Ra . For ^{226}Ra analysis, fibers were stored in air-tight cartridges to allow the radiogenic daughter, ^{222}Rn , to grow in toward equilibrium. After at least 1 week (~75 % ingrown), the activity of ^{222}Rn was analyzed on a radon emanation line (following Peterson et al., 2009). When dissolved ^{228}Ra activities are reported, they were measured by analyzing the Mn-fibers on the RaDeCC again after ~ 1 year as per Moore (2008). Activities of grain-adsorbed ^{224}Ra were determined following methods outlined by Cai et al. (2012). In short, a slurry was prepared using 150 mL of Ra-free tap water and recently collected sediments. The slurry was pH adjusted by adding 5-10 drops of $\text{NH}_3\text{-OH}$ followed by 1 mL of 19 mM KMnO_4 and 1 mL of 40 mM MnCl_2 solutions to precipitate any ^{224}Ra that may have entered the dissolved phase following the addition of Ra-free tap water (Cai et al., 2012). Solids were vacuum filtered onto preweighed 47 mm GFF filters and the filtration was terminated when water drops no longer passed into the filtrate reservoir. Sediment-covered filters were then dried completely and analyzed on the RaDeCC twice, where any difference between the first and second measurement indicates a deviation from equilibrium and suggests an additional supply/removal of ^{224}Ra that would affect the ^{224}Ra in solution.

2.4. Radium Model Component Evaluation

Here, we consider the potential control several common sources/sinks of ^{224}Ra in coastal and shallow water and deep-sea systems (Figure 2.1). We have organized the text into distinct sections to address each source and sink term potentially affecting interstitial porefluid ^{224}Ra activities. Our intention is, through experimentation, to identify which parameters may be relevant

to incorporate into a model to determine porefluid flux using ^{224}Ra profiles recovered from deep-sea seepage systems.

2.4.1. Exchange with Sedimentary Surfaces

The activity of ^{224}Ra adsorbed to particle surfaces (Ra_A) is related to that present in solution (Ra_D) by the distribution coefficient (K_d ; Figure 2.1). The relationship between adsorption and desorption can then be evaluated by experimentation by a series of methods (e.g., Rama and Moore, 1996; Colbert and Hammond, 2008; Gonnee et al., 2008; Beck and Cochran, 2013). Although it is unclear which factors in deep-sea environments predominantly control ^{224}Ra distribution (e.g., Gonnee et al., 2008; Beck and Cochran, 2013), the effect of changing salinity on solid-aqueous distribution is known to exert consistent control across many environment types (Kraemer and Reid, 1984; Webster et al., 1995). Because we focus on shallow sections (< 50 cm below the seafloor; cmbsf) of deep-sea sediment where salinity change is minimal, localized parameters such as grain size and charge, sediment geochemistry (e.g., metals and organics), temperature, porosity, and redox potential may be important considerations. We evaluate the net effect many of these parameters (e.g., grain size and charge) may have on ^{224}Ra partitioning by measuring aqueous ^{224}Ra activities produced under contrasting treatment conditions associated with homogenous subsamples of larger marine sediments.

Two distinct instances exist in which a change in radium partitioning occurring over time and space may influence our ability to use ^{224}Ra to determine deep-sea fluid transport rates. The first is through our measurement of the dissolved equilibrium ^{224}Ra activity (Ra_{eq}) in contact with specific sediments, principally the effect of drying and rehydrating samples for later analysis in

the laboratory at room temperature. We consider this a change in time, potentially related to sample handling procedures. The second opportunity for ^{224}Ra partitioning to influence radium in solution includes a change in distribution over space. Specifically, a change in K_d vertically, between adjoining sediment layers could appear indistinguishable from a change in ^{224}Ra activity related to fluid transport. To evaluate radium distribution, we performed serial extraction experiments to examine K_d associated with different handling protocols, and vertically adjoining sediment sections.

To determine how the exchangeable pool of ^{224}Ra is distributed between the surface-sorbed and dissolved fractions (K_d), we completed a series of consecutive fluid replacement experiments similar to those described by Colbert and Hammond (2008). Briefly, a known mass of aged sediment (M_s) was combined with a volume of Ra-free seawater (V_T). The slurry was briefly agitated and held for 10 minutes to achieve sorption equilibrium before the dissolved ^{224}Ra activity (C_i) was measured by removing an aliquot of water (ΔV). Following removal, an equivalent volume of Ra-free seawater was added to maintain V_T and held again for 10 minutes before additional removals and replacements occurred. Radium partitioning may then be estimated by the following relationship (from Colbert and Hammond, 2008):

$$\frac{1}{M_s} (\Delta V \sum \lambda C_{i-1} + V_T \lambda C_i) = -K_d \lambda C_i + E \quad (2.2)$$

where E represents the ^{224}Ra emanation rate and $\sum \lambda C_{i-1}$ is equal to the sum of the dissolved ^{224}Ra activity removed prior to removal step i . Here, the ^{224}Ra partition coefficient is the slope of a line characterizing the relationship between the adsorbed ^{224}Ra activity (calculated) and the dissolved ^{224}Ra sorbed to Mn-fiber as determined via RaDeCC analysis. Although the ^{224}Ra distribution coefficient and emanation rate were central to the work which originally developed Equation 2.2

(Colbert and Hammond, 2008), we apply this model for the sole purpose of identifying the partition coefficient and so focus discussion exclusively on K_d .

2.4.1.1. Temporal Changes in Distribution

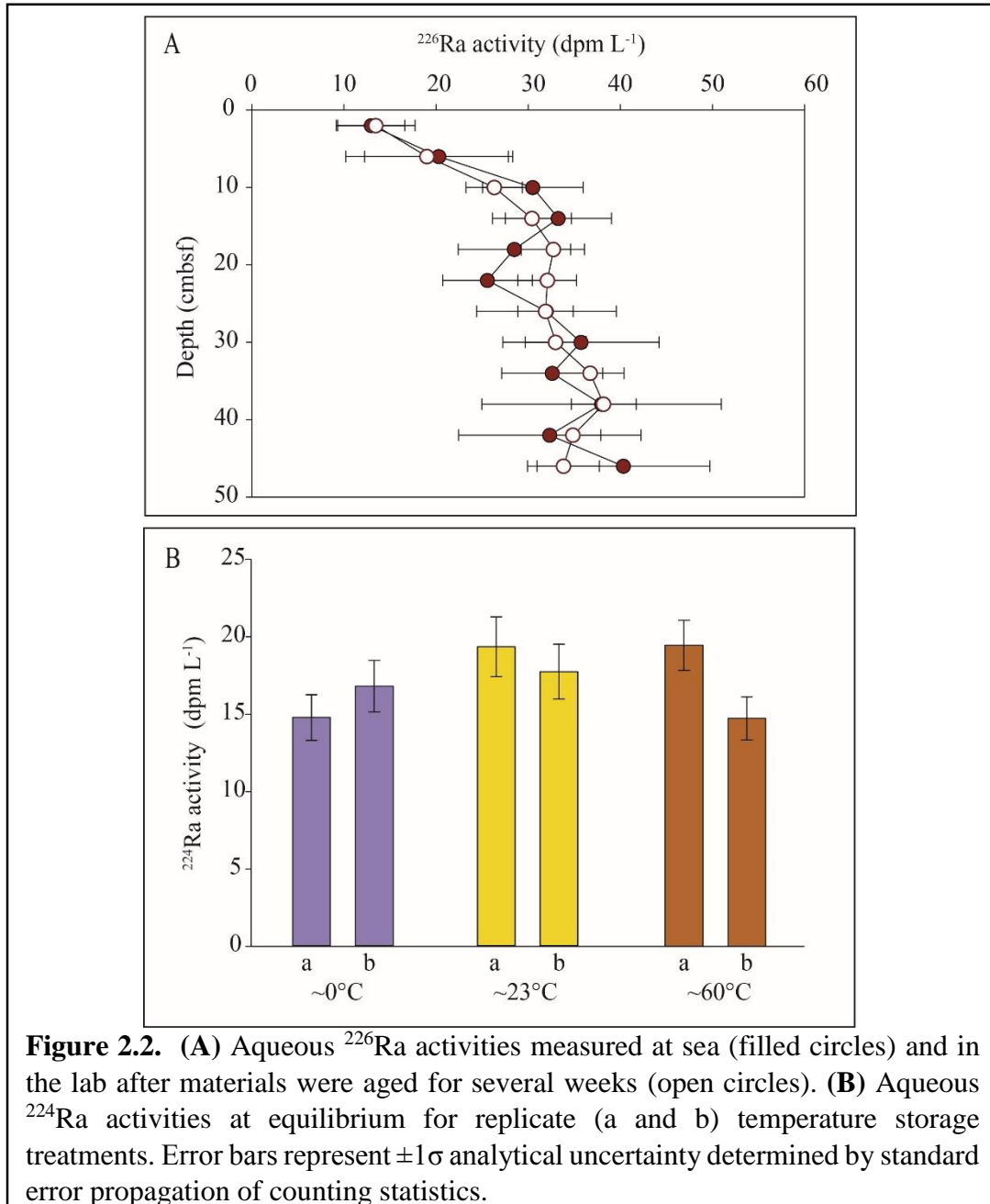
We determine the dissolved equilibrium ^{224}Ra activity (Ra_{eq}) by incubating sediment with seawater at ambient porosity. Throughout, we use the term equilibrium, to indicate secular equilibrium, where the rate of ^{224}Ra production is equal to the rate of ^{224}Ra decay and the activity of ^{224}Ra (both in solution and adsorbed to particulate surfaces) therefore remains unchanged. This procedure is done in the laboratory following the cruise during which sediment cores were collected, sectioned, centrifuged, and preserved. To determine Ra_{eq} , we dry and then rehydrate marine sediments to perform the incubations. As demonstrated by Beck and Cochran (2013), no significant effect on radium partitioning is expected from such sample handling protocols provided that drying is achieved at temperatures at or below 60 °C. However, it is worth noting that drying the sediments could have altered organic materials associated with the sediment matrix, which may have a considerable effect on partitioning (Rama and Moore, 1996). Here, we evaluate whether the application of laboratory based methods to determine Ra_{eq} alters ^{224}Ra distribution between particulate and aqueous phases.

We tested for the potential effect of sample handling on ^{224}Ra distribution in two ways. The first experiment compared porefluid radium activities measured at sea to those measured at equilibrium following ~ 1 year of storage, drying, and subsequent rehydration to examine the potential effects on radium distribution. For this experiment, we use ^{226}Ra as an indicator of potential ^{224}Ra sensitivity to our sample handling protocols. Because the half-life of ^{226}Ra is

sufficiently long ($T_{1/2} = 1602$ years), we expect distributions of the isotope to be a consequence of sorption equilibrium (K_d) and geochemistry rather than ingrowth or decay as ^{226}Ra activities are not expected to vary between the two measurement periods. Although we do not need to assume the distribution coefficient for ^{224}Ra and ^{226}Ra is equal, we do assume that a change in dissolved activity between our at-sea and laboratory evaluations of ^{226}Ra is indicative of a change in the distribution coefficient of ^{226}Ra . We then assume that a change in solid:aqueous distribution for ^{226}Ra is indicative of a change in ^{224}Ra solid:aqueous distribution. Similarly, if no discernable change in ^{226}Ra partitioning is observed between at-sea and laboratory measurements, then changes to ^{224}Ra partitioning related to sample handling protocols are assumed negligible.

To experimentally evaluate if changes in radium sorption could be identified between measurements made at sea and in the lab, we collected a sediment core from the Gulf of Mexico (Table 2.1). Sediments were sectioned 4 cm thick slabs from which porefluid was recovered and analyzed for dissolved radium according to methods previously described. Each 4 cm thick sediment slab was archived for later rehydration and incubation with Ra-free seawater at ambient porosity. Comparing dissolved ^{226}Ra activities recovered after core collection with those measured in the lab during the equilibrium experiments among 12 samples through a sediment core (Figure 2.2A), no difference beyond error was observed between ^{226}Ra recovered from porefluid and experimental fluid (t-test; $p = 0.49$). Because the two measurements yield similar patterns and magnitudes in activity, it is likely that the ^{226}Ra initially recovered from the sediment core had a residence time significantly less than 1602 years and so porefluid ^{226}Ra activities are related to sediment geochemistry and radium partitioning. While it is possible that the change in radium distribution as a consequence of storage and handling could explain equal activities for all layers

measured at each interval, it is much more reasonable that this result indicates that no change in radium partitioning was observed beyond error and can therefore be considered negligible.



Our second experiment tested for an effect of storage temperature on radium distribution. To address this, we held sediments at ambient porosity at three different storage temperatures for two weeks and subsequently measured the dissolved ^{224}Ra activity associated with each temperature treatment group. Sediments were tested with a porosity of 0.52 in duplicate with temperature treatments including frozen, room temperature, and 60 °C. We did not observe an apparent effect between dissolved equilibrium ^{224}Ra activities with storage temperature (Figure 2.2B) as equilibrium activities were not observed to be different beyond error across temperature treatments. Although isotope activities have been observed to correlate with temperature related to seasonal trends (e.g., Bollinger and Moore, 1993; Rama and Moore, 1996; Hughes et al., 2015), there is also evidence to suggest radium distribution may be unaffected by temperatures ranging from 2°C to 60°C for a variety of sediment sizes and compositions as per laboratory manipulations (Beck and Cochran, 2013). It is likely that external forcings such as changes in groundwater flow rate and precipitation could explain the connection between seasonal temperature fluctuations and groundwater ^{224}Ra activities observed in the environment. Although organic content may have been altered during processing (Rama and Moore, 1996), the effects on ^{224}Ra of such change are not evident by these experiments. Although sediments used for this experiment were not recovered from the deep-sea, the organic content of these sediments was likely greater than that of deep-sea sediments and so the effects of storage temperature on samples with less organic material is expected to be less effected by such change (Rama and Moore, 1996; Hughes et al., 2015).

2.4.1.2. Spatial Changes in Distribution

Potential vertical changes in K_d were evaluated using material recovered at sea (Table 2.1), archived in 4 cm thick samples, and aged for >3 weeks such that aqueous ^{224}Ra reached equilibrium with those sediments. Solid-aqueous partitioning for each sediment section was determined via serial extraction experiments (Equation 2.2; Colbert and Hammond, 2008). By evaluating the partition coefficient vertically through a sediment core, we can estimate how any potential redistribution would affect the dissolved ^{224}Ra activity through porefluids

We did not observe a depth-dependent trend on ^{224}Ra solid-aqueous partitioning for the material tested (Pearson correlation; $p = 0.16$). Although the ^{224}Ra distribution coefficient was observed to be fairly consistent from 4 to 20 cmbsf (ranging from 53.0 ± 32.7 to $64.3 \pm 13.0 \text{ L kg}^{-1}$) distribution coefficients for 0-4 cmbsf and 20-24 cmbsf sediment sections were quite different (160.7 ± 117.4 and $205.6 \pm 51.2 \text{ L kg}^{-1}$, respectively). However, with the exception of the 20-24 cmbsf section, no difference in K_d beyond error is resolvable (Figure 2.3A). It was expected that radium partitioning associated with 0-4 cmbsf could be most distinct as organic content/grain size may exert significant control over ^{224}Ra distribution (Beck and Cochran, 2013). Factors most greatly controlling ^{224}Ra distributions including distinct geochemical properties are most likely present in the shallow sediments especially as redox boundaries are expected to exist here creating conditions unique to the shallow-most sediment section relative to sediments deeper in the column. Due to such large error associated with K_d estimated for sediments recovered from 0-4 cmbsf, it is unknown if significant deviations with depth occur between surficial sediments and those recovered from 5-20 cmbsf. Despite the large uncertainties, our results indicate that if K_d changes with depth, the difference appears to be less than the error associated with the experimental

approach. As we did not identify evidence to the contrary we assume vertical changes in solid-aqueous ^{224}Ra distribution from 0 to 20 cmbsf is negligible.

It is important to note that we used a constant porosity for the serial extraction experiments used to determine K_d for each sediment section although in-situ porosities did decrease somewhat with increased depth into the sediments. While we did maintain the sediment:water ratio suggested by Colbert and Hammond (2008; ~0.80 to 0.95, depending on grain density), this porosity is higher than that normally found >4 cmbsf in deep-sea sediments. This potential problem is discussed by Beck and Cochran (2013) with the conclusion that much of the literature presents distribution experiments with similar proportions although it is recognized that experimental porosities are greater than those expected in-situ, quick processing with such small recovery volumes is not reasonably possible. While changes in porosity may influence partitioning, high experimental porosities are required to recover sufficient water volumes from the slurries while still maintaining experimental times below ~ 40 min so that influences from production/decay are limited. Yet, the lack of a depth-dependent trend in K_d (at a constant porosity) suggests no systematic grain size or geochemical control on ^{224}Ra distribution with depth.

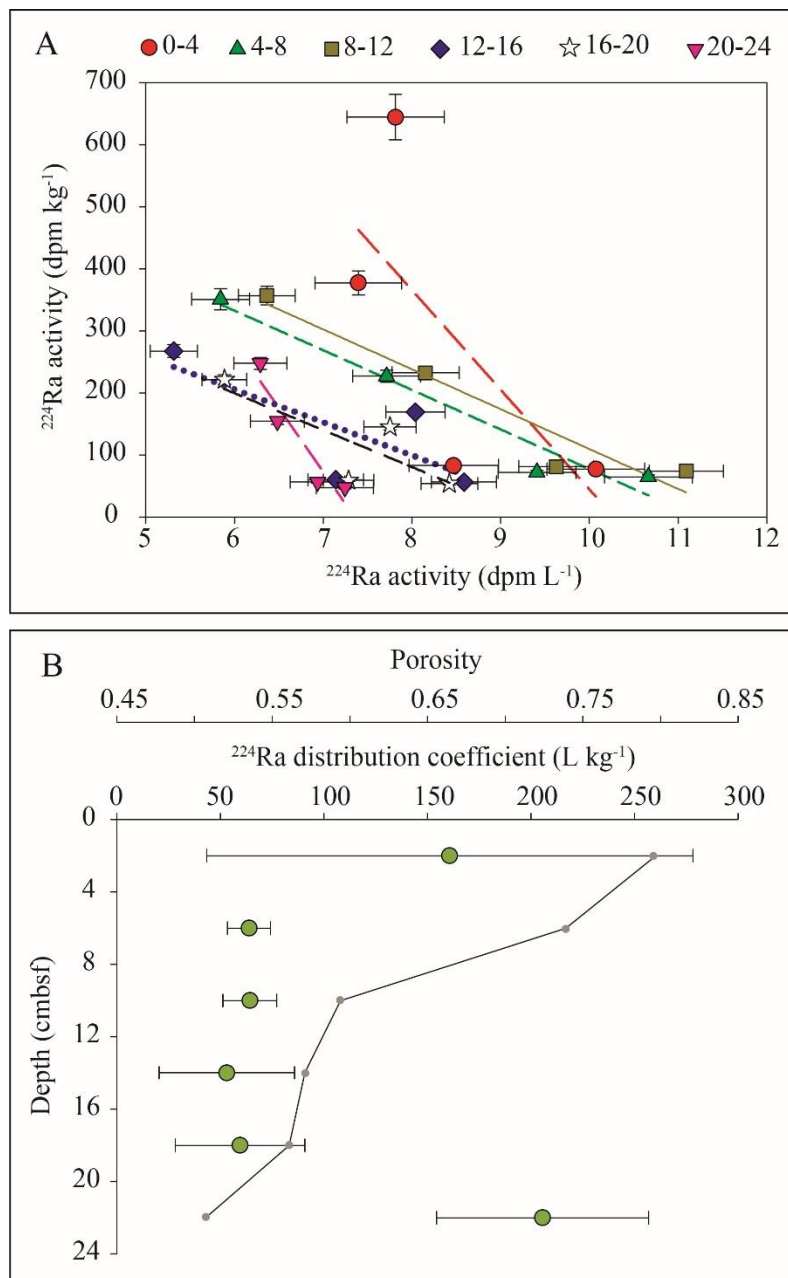
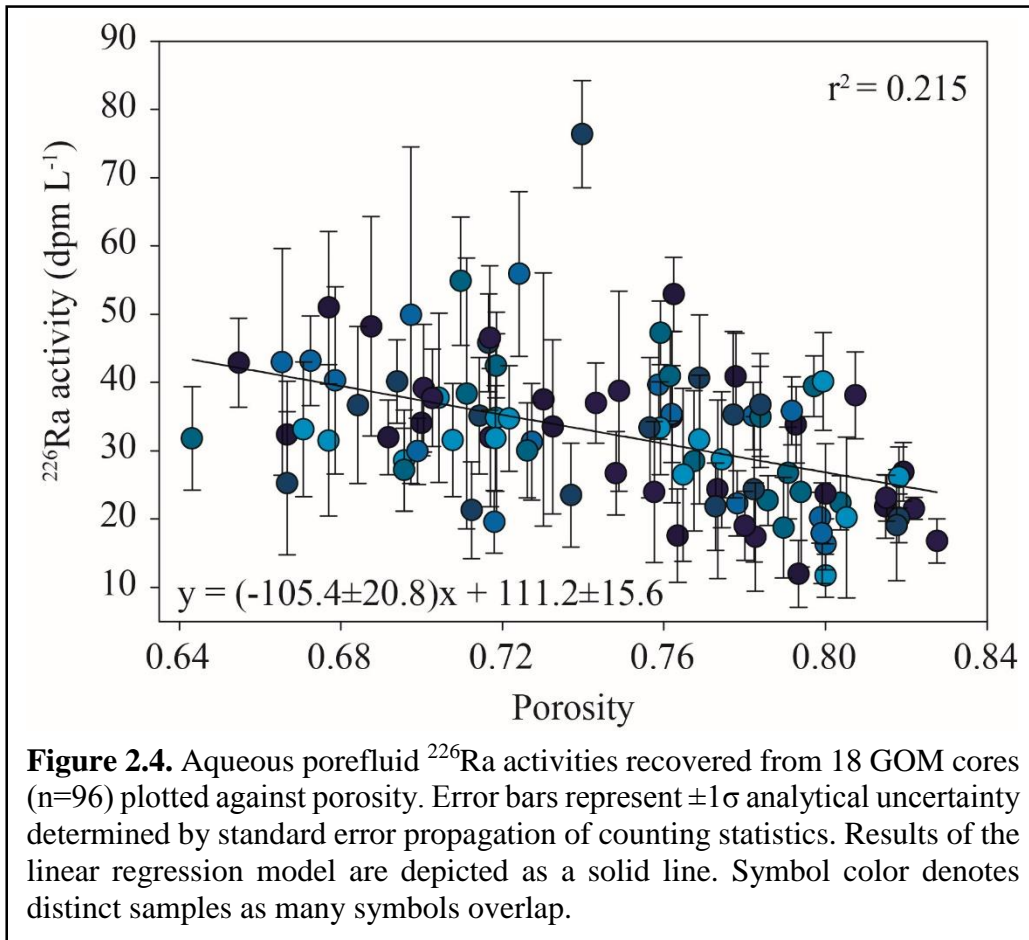


Figure 2.3. (A) Results of the serial extraction experiments using vertically adjoining sediment sections. Linear regression lines are shown for each experiment. Depth intervals are presented in cmbsf. (B) In-situ porosity (gray symbols and solid line) and ^{224}Ra distribution coefficients (K_d ; green symbols) derived from the slope of each experimental regression line. Units of K_d are simplified from dpm kg^{-1} divided by dpm L^{-1} . Error bars represent (A) $\pm 1\sigma$ analytical uncertainty determined by standard error propagation of counting statistics and (B) the standard error of the slope for each linear model.

To examine the control of porosity on K_d , we measured dissolved activities of ^{226}Ra in porefluid recovered from 18 deep-sea sediment cores (Table 2.1). Because ^{226}Ra has such a long half-life, changes in activity related to production or decay are minimal, and a relationship between deep-sea porefluid ^{226}Ra activities and in-situ porosities could indicate a spatial association between K_d and porosity down core.

^{226}Ra will usually diffuse into overlying ocean waters as seawater activities are typically lower than those contained within interstitial porefluid. For this reason, we only include data ≥ 8 cmbsf (Figure 2.4) where the effects of diffusion are assumed to be minimal and a substantial range in porosity is still observed down core. Although we observed a significant relationship between porosity and radium partitioning in deep-sea sediments based on regressing the absolute activities against porosity, ($r=-0.46$, $p < 0.05$), the relatively low correlation coefficient suggests a weak relationship and the effect of porosity on partitioning is therefore considered negligible. Because of the relative enrichment of organic material in seep sediments relative to non-seep affected sites, the range of possible distribution coefficients could be reduced and the variability in K_d is therefore expected to be small. This relationship between organic-rich sediments and radium partitioning was described by Hughes et al (2015). Although organic content is not expected to be as high in deep-sea sediments as that for the coastal marsh studied by Hughes et al. (2015), organic matter is often present at elevated levels at diffuse deep-sea seepage sites (MacDonald et al., 1989; Paull et al., 1992; Joye et al., 2004; Pohlman et al., 2011), so the natural range in K_d values as a function of variable porosity in these sediments could be relatively narrow.



2.4.2. Particulate Radium

2.4.2.1. Incorporation into Barite

Co-precipitation of radium into a barite matrix in marine sediments can act a sink of radium from the exchangeable pool under certain conditions (Doerner and Hoskins, 1925; Figure 2.1). Fluids emanating from energetic hydrothermal vents as well as mud volcanoes at cold seep are commonly enriched in barium, radium, and sulfate, and as such, may favor this mineral precipitation (Feng and Roberts, 2011; Núñez-Useche et al., 2018). Enrichments in dissolved

barium can precipitate as barite with a Ra/Ba co-precipitation to Ba(Ra)SO₄ (Aharon et al., 2001). Although barite formation is most commonly associated with highly saline water (Cl⁻ concentrations > 2000 mM), significant halite deposits beneath the GOM (Land et al., 1988) and Guaymas Basin (Miller and Lizarralde, 2013) suggest past evaporative conditions may have acted as a radium sink (Rosenberg et al., 2018). This potential sink, if occurring during sampling and unaccounted for in the model, may render Ra ineffective as a proxy for porefluid flow at brine seeps. For this reason, we test for radium removal via radium-barium co-precipitation (Ra_B) via experiments detailed in here.

This radium removal mechanism was evaluated experimentally by monitoring gaseous daughter products of radium isotopes following methods presented by Chanoytha et al. (2016). The general premise behind this experiment is that monitoring of gaseous ²²²Rn using a closed-loop continuous measurement system (Chanoytha et al., 2016) may be used to identify any radium removal occurring in freshly collected material. If radium becomes incorporated into a barite lattice, gaseous radon would not easily escape the solid matrix so concentrations in water (and therefore air) would decrease over time. For this experiment, a sediment core was recovered from GC600 in the GOM, a site of prolific natural hydrocarbon seepage (Table 2.1). Roughly 200 g of sediment was placed in a 500 mL glass reaction flask and Ra/Rn-free seawater was added to achieve a slurry volume of 400 mL. Sediments from 2 to 8 cmbsf were used, as continued contact with overlying seawater may have encouraged barite formation under favorable conditions prior to analysis. A bubbler was used to degas radon from the overlying water in the reaction flask and circulate this headspace to a commercial radon detector. Measurements were integrated continuously over 10 minute intervals for 45 hours to observe ²²²Rn activity in air through time. Before the sample was placed in the analysis loop, the ²²²Rn background was reduced by flushing

the ambient air in the analysis loop through a closed system including desiccant and activated charcoal for at least 1 hour. A valve system was used to bypass the charcoal loop and incorporate the reaction flask containing the sample once measurements began (Chanoytha et al., 2016).

We compare measured ^{222}Rn activities over time to those that would result from production (via decay of parent isotope ^{226}Ra) and radioactive decay. Isotope activities are estimated using a standard radioactive ingrowth equation (Bateman, 1910 reported by Faure and Mensing, 2005):

$$A_d = \frac{\lambda_p \lambda_d}{(\lambda_d - \lambda_p)} \frac{A_p^0}{\lambda_p} (e^{-\lambda_p t} - e^{-\lambda_d t}) + A_d^0 e^{-\lambda_d t} \quad (2.3)$$

where the activity of a daughter isotope (A_d) is estimated as a function of ingrowth time (t), initial daughter activity present at t=0, parent activity present at t=0, and daughter (λ_d) and parent (λ_p) decay constants (see Appendix for more details). This equation can be modified specifically to predict how ^{222}Rn activity in air would change (difference between $^{222}\text{Rn}_t$ and $^{222}\text{Rn}_0$) from 0 to 45 hours (t) toward equilibrium with the supporting parent activity ($^{222}\text{Rn}_{eq}$) using the decay constants of ^{222}Rn ($\lambda_{\text{Rn-222}}$: $1.81 \times 10^{-1} \text{ day}^{-1}$) and ^{226}Ra ($\lambda_{\text{Ra-226}}$: $1.17 \times 10^{-6} \text{ day}^{-1}$).

$$^{222}\text{Rn}_t = \frac{\lambda_{\text{Ra-226}} \lambda_{\text{Rn-222}}}{\lambda_{\text{Rn-222}} - \lambda_{\text{Ra-226}}} \frac{^{222}\text{Rn}_{eq}}{\lambda_{\text{Ra-226}}} (e^{-\lambda_{\text{Ra-226}} t} - e^{-\lambda_{\text{Rn-222}} t}) + ^{222}\text{Rn}_0 e^{-\lambda_{\text{Rn-222}} t} \quad (2.4)$$

Equilibrium ^{222}Rn activities ($^{222}\text{Rn}_{eq}$) were measured by incubating the same sediments with Ra/Rn-free seawater at the same sediment:water ratio described above in an air-tight reaction flask for ~4 weeks. Analysis procedures were identical to those utilized during the initial measurement. Measurements of ^{222}Rn in air were made from 0 to 23 hours and this time we noticed a significantly different time dependent relationship as the ^{222}Rn activity reached a sustained maximum after ~7 hours of measurement as secular equilibrium between ^{222}Rn and ^{226}Ra was

achieved. This equilibrium activity of 85.4 Bq m^{-3} ($^{222}\text{Rn}_{eq}$) is then used to estimate $^{222}\text{Rn}_t$ where t varies from 0 to 45 hours using Equation 2.4 (Figure 2.5A).

We assume an initial activity of ^{222}Rn in air equal to the average recorded during our first hour of measurements at sea (so $^{222}\text{Rn}_0 = 3.76 \text{ Bq m}^{-3}$). If no incorporation of radium into barite is occurring, we would expect our measured ^{222}Rn activities during the initial experiment ($^{222}\text{Rn}_t^*$) to overlie those predicted ($^{222}\text{Rn}_t$) based on ingrowth toward $^{222}\text{Rn}_{eq}$ (Figure 2.5). Thus, a difference between measured and predicted values could indicate a change in the desorbable radium inventory. Such a change would best be explained by a removal of Ra only after sediments containing significant quantities of Ra and Ba have been exposed to seawater sulfate. This process would affect our equilibrium activities by removing ^{226}Ra capable of supporting ^{222}Rn , thus lowering our equilibrium activity to that affecting our initial measurement. Subsequently, we would then predict lower activities ($t = 0$ to 23 hours) compared to those measured.

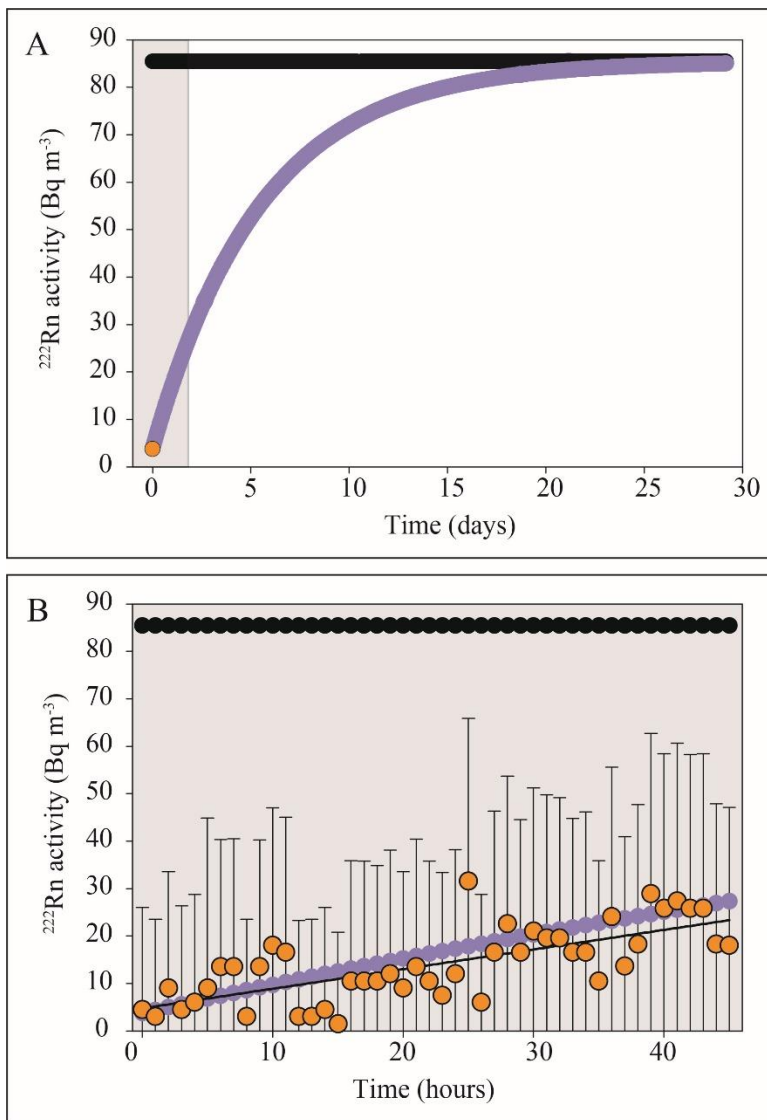


Figure 2.5. ^{222}Rn activity in air (purple symbols) estimated using the initial activity measured at sea ($^{222}\text{Rn}_t^*$; orange symbols) and at equilibrium (black symbols). **(A)** Shaded region corresponds to time depicted in **B** where ^{222}Rn activities measured in air at sea ($^{222}\text{Rn}_t$) are compared to those predicted as a function of time. Thin black line depicts regression line for observed activities. Error bars represent $\pm 1\sigma$ analytical uncertainty determined by standard error propagation of counting statistics.

For this experiment, a few important assumptions were considered. (1) We assume temperature was constant between the first and second measurement. Temperature affects gas

solubility and therefore presents an additional experimental variable. Because the detector can only monitor radon-in-air levels, aqueous ^{222}Rn is derived empirically using a calculated solubility based on the water temperature. At sea, the sediments warmed to room temperature over the course of the 45 hour experiment, given such long analysis times at room temperature, we believe that this is an appropriate assumption. (2) We also assume the air-water distribution of ^{222}Rn remained constant. By maintaining constant laboratory conditions (e.g., sediment surface area, diffusion loop volume, and detector efficiency) we minimized change in ^{222}Rn distribution.

We did not observe a discernable deviation of predicted ^{222}Rn activities compared to those measured (Figure 2.5), although we cannot completely discredit the potential effect of Ra-removal via incorporation into barite minerals due to significant error associated with the ^{222}Rn measurements. However, these results suggest that if Ra_B is a sink for radium in solution, the subsequent reduction in radium activities were not resolvable beyond our analytical error associated with the analysis procedure. While error associated with individual ^{222}Rn measurements was often $>30\%$, a slightly lower slope through time characterizes measured ^{222}Rn compared to predicted activities (Figure 2.5B). This effect is most evident at $t > 10$ hours. This difference is opposite what we would expect for barite formation to remove Ra. Barite formation and resulting Ra removal is a slow process with maximum removal occurring after 200 to 350 days without the additions of heat or strong acid (Brandt et al., 2015). Mechanisms of barite formation and subsequent radium removal vary widely depending on barite structure, Ra concentration, and RaSO_4 solubility (Brandt et al., 2015; Weber et al., 2017; Heberling et al., 2018). Although there is no evidence to indicate that surfacing the sediments and diluting with Ra-free seawater for processing immediately removes exchangeable radium, it is possible that in-situ barite formation and sufficiently long porefluid residence times could act as a significant radium sink. Therefore, it

is advised that additional tracers of fluid transport be used to verify model results for sediments collected with particularly high ionic strength porefluid.

2.4.2.2. Oxidation-Reduction and Sorption

In general, molecular oxygen (O_2) concentrations are greatly reduced a few mm below the sediment-water interface in seep sediments, leaving a reducing environment in the interstitial sediment spaces. This is evidenced by recovered porefluid often enriched in reduced carbon, nitrogen, and sulfur species relative to non-seep porefluid (Joye et al., 2010). Local enrichments of dissolved (reduced) iron and manganese associated with seepage (Lemaitre et al., 2014) can also moderate activities of dissolved ^{224}Ra (Mott et al., 1993; Gonnee et al., 2008). In the absence of molecular O_2 , these metals would not affect the dissolved pool of Ra as they remain soluble in their reduced oxidation states. However, once sediment cores are surfaced and exposed to ambient atmospheric conditions, iron and manganese could oxidize and form metal (hydr)oxide precipitates which effectively scavenge ^{224}Ra from the dissolved pool (Beck and Cochran, 2013; Ra_M). Unlike barite co-precipitation, this mechanism would remove ^{224}Ra from solution by adsorbing onto newly formed particulate surfaces, temporarily affecting solid-aqueous partitioning until the unsupported ^{224}Ra decayed away. Unlike radium co-precipitation into barite, metal scavenging cannot be detected by gaseous daughter monitoring as daughter products are not trapped within a mineral matrix. Instead, radiogenic gases remain free to exchange into surrounding fluid medium.

To test for a potential effect of porefluid exposure to atmospheric conditions during sample collection, recovery, and handling on aqueous ^{224}Ra , we collected duplicate sediment cores from deep-sea locations (Table 2.1) and exposed them to contrasting environments during sediment

extrusion. Cores recovered from the GOM were sectioned into 4 cm thick slabs from 0 to 14 cmbsf under oxidizing (air) and reducing (He) conditions. All materials used for processing under non-oxidizing conditions were purged with He and the core was sectioned under a He-filled gas bag to minimize potential oxidation until solids were separated from the recovered porefluid. Following centrifugation and filtration, porefluid was processed with ^{224}Ra and ^{226}Ra activities measured according to methods previously described (Section 2.3). Particle filters were also analyzed for excess ^{224}Ra as metal scavenged ^{224}Ra would not be supported by ^{228}Th and so would initially appear in excess on the filters.

We compare aqueous ^{224}Ra activities recovered from each of these cores to those measured at equilibrium (Figure 2.6A). By evaluating initial dissolved activities associated with air and He treatments in the context of the equilibrium activity, we remove the potential for differences due to geochemical heterogeneities in the sediment cores. We compare the slope characterizing the relationship between observed aqueous ^{224}Ra and that observed at equilibrium. We find ~40% of the maximum desorbable ^{224}Ra activity present in solution for the He treatment ($r^2= 0.9985$) compared to ~50% in solution for the atmospheric treatment ($r^2= 0.9976$) when excluding the sample having an equilibrium activity >40 dpm L^{-1} (Figure 2.6A). Although we observed a difference in the slope between treatments, this trend is opposite than one we would expect if Mn and Fe oxides had removed Ra from solution. The higher dissolved ^{224}Ra for the air treatment could be indicative of a longer porefluid residence compared to that of the He treatment, but this cannot be determined independently. We also cannot explain the deviation from a linear relationship observed for the He treatment (sample depth 12 to 16 cmbsf) as no difference beyond error in ^{226}Ra activities for both the He and air treatments were observed (Figure 2.6B). Although our small sample size limited statistical evaluation, ^{226}Ra activities do not appear to be substantially

influenced by processing environment. Further, excess particulate ^{224}Ra activities measured on porefluid filters did not exhibit behavior consistent with effects of scavenging onto metal (hydr)oxide precipitates and therefore the He treatment sample (12 to 16 cmbsf) was excluded from the regression analysis (Table 2.2; Figure 2.6A).

Table 2.2 Excess particulate ^{224}Ra activities associated with redox experiments from Gulf of Mexico sediment cores.

Core ; treatment	Depth (cmbsf)	Excess ^{224}Ra (dpm g ⁻¹)	Uncertainty (dpm g ⁻¹)
He			
	2	1.4	0.2
	6	-0.2	0.1
	10	-1.6	0.4
	14	-0.6	0.1
Air			
	2	-0.5	0.1
	6	-1.9	0.8
	10	3.3	0.7
	14	-1.4	0.8

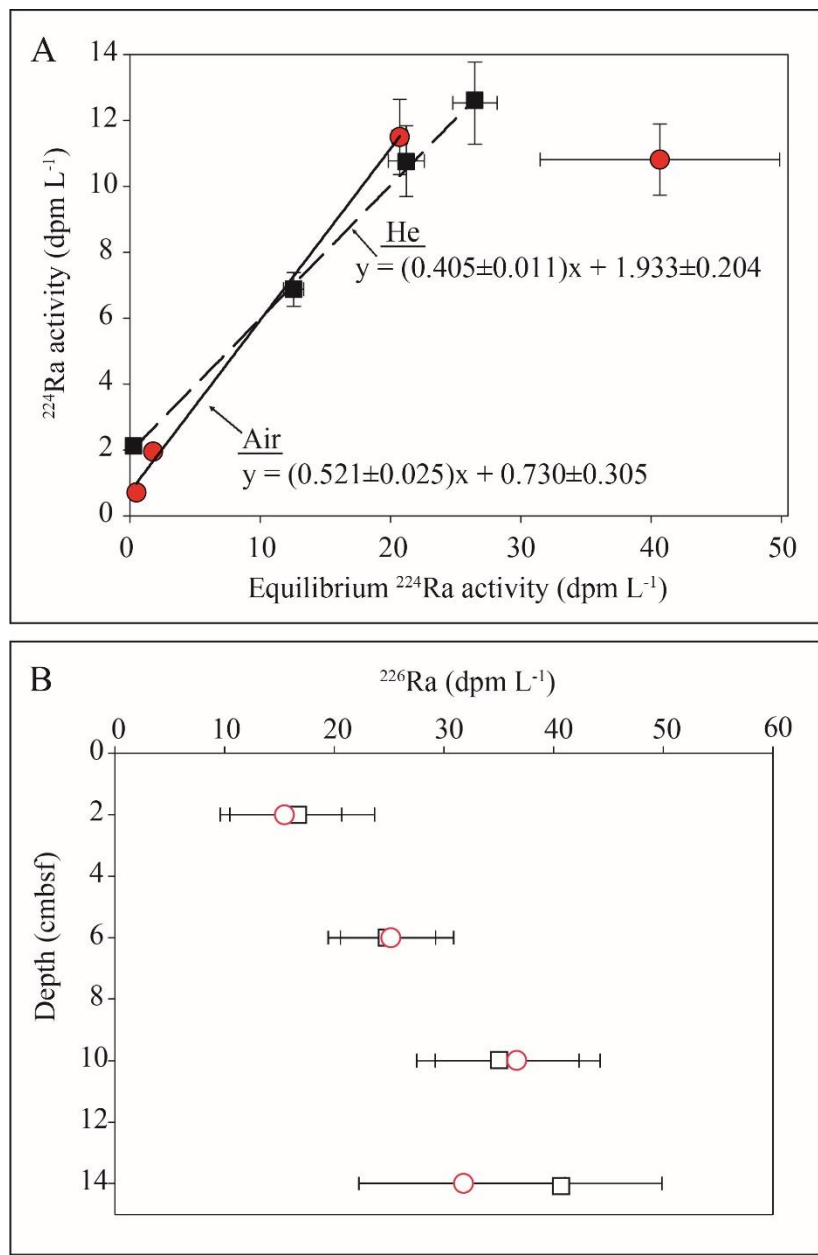
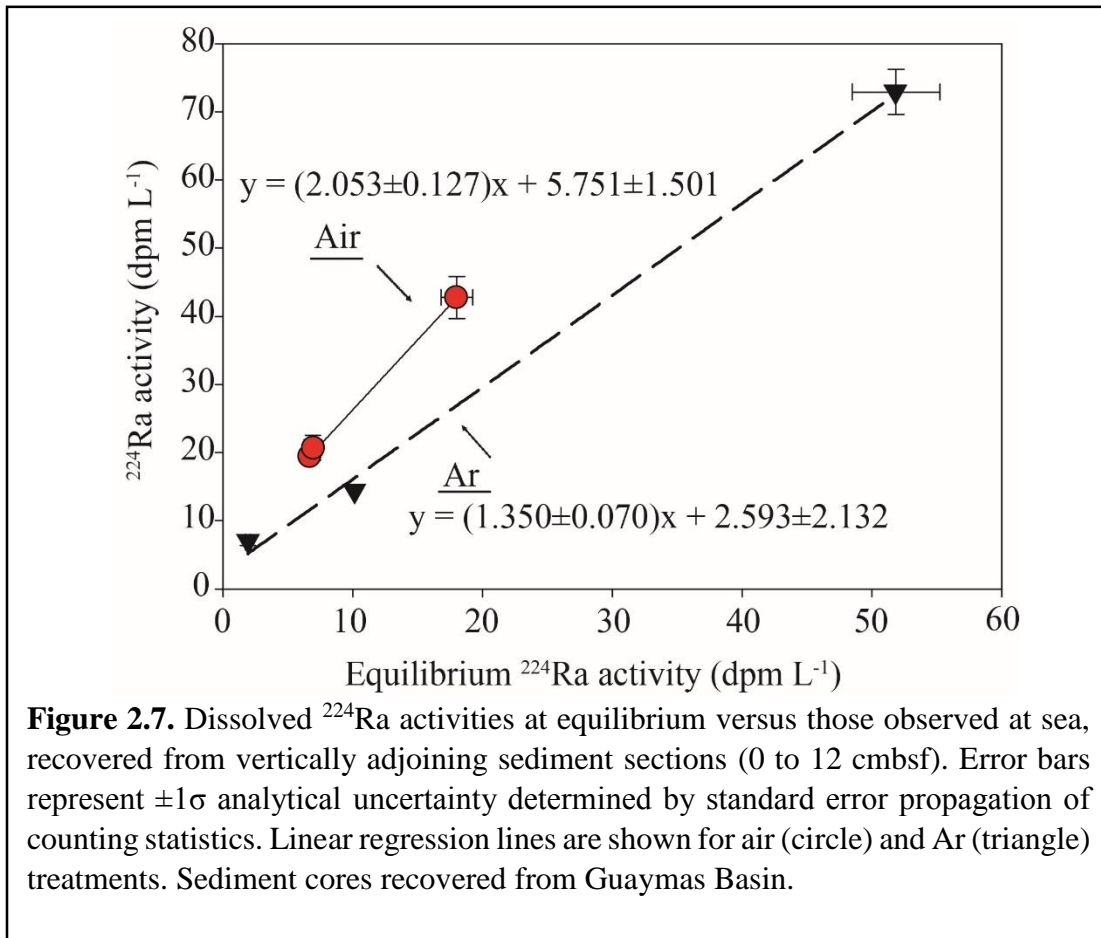


Figure 2.6. (A) Dissolved ^{224}Ra activities at equilibrium versus those observed at sea, recovered from vertically adjoining sediment sections (0 to 16 cmbsf). Linear regression lines are shown for air (circle) and He (square) treatments. (B) Aqueous ^{226}Ra activities measured at sea for each treatment. Error bars represent $\pm 1\sigma$ analytical uncertainty determined by standard error propagation of counting statistics. Sediments recovered from the Gulf of Mexico.

We similarly tested for the effect of redox condition on aqueous ^{224}Ra activities using sediment cores recovered from Guaymas Basin (Table 2.1). Here, ambient air interactions were prevented using Ar, a dense inert gas (as compared to He). A steady stream of Ar was used to fill an extraction well during sediment processing. For the Ar treatment, porefluid was separated from sediments according to procedures described above while extreme care was taken to minimize atmospheric exposure including Ar purged laboratory equipment. Dissolved ^{224}Ra activities were compared to a ‘duplicate’ core processed under ambient atmospheric conditions (air treatment). No particulate filters were collected for analysis via this procedure from Guaymas Basin.

We again observed a linear relationship between ^{224}Ra activity in porefluids relative to dissolved equilibrium activities for both treatments (Ar: $r^2=0.997$; air: $r^2=0.996$; Figure 2.7). However, unlike interstitial ^{224}Ra recovered from Gulf of Mexico cores, initial measurements were in excess of aqueous equilibrium ^{224}Ra activities supported by recovered sediments. If exposure to ambient air during processing was affecting radium distribution by scavenging onto precipitated metal (hydr)oxides, we would expect a lower slope for the air core as compared to the argon core in Figure 2.7. However, more ^{224}Ra was present in solution for the air treatment as compared to the Ar treatment suggesting the differences between aqueous ^{224}Ra activities cannot be explained by redox related radium scavenging by iron and manganese (hydr)oxides alone at Guaymas Basin.



The excess in dissolved ^{224}Ra activities observed initially relative to what could be supported at equilibrium for all treatments can be explained in two ways. It could be that although iron and manganese scavenging did not appear to affect our initial measurements, oxidation of these metals occurred later during our laboratory incubations used to determine equilibrium activities effectively reducing maximum aqueous activities. However, because the ratio of dissolved ^{224}Ra measured at sea relative to that observed at equilibrium was greater for the Air treatment, oxidation of such metals likely did not occur so as to influence ^{224}Ra . This result suggests that if present, reduced metals would have remained in solution and would have therefore been removed following initial porefluid extraction. There is no existing mechanism to

support the occurrence of such variable scavenging behavior and so it is more likely that an additional source of dissolved ^{224}Ra such that $A_d^0 > A_d$ (Equation 2.3) affected our observations. These enrichments indicate fluid (and ^{224}Ra) transport from a source region characterized by significantly larger production rates could have been occurring during core recovery since observed activities cannot be sustained by in-situ production rates associated with sediments from which the porefluid was extracted. Because the symbols shown in Figure 2.7 represent discrete sampling depths within the sediment column (0 to 12 cmbsf), the strong linear trends suggest ^{224}Ra mass is conserved with depth across the sampled areas for both Guaymas Basin sediments tested.

2.4.3. ^{224}Ra Production (P) and Decay (D)

A change in dissolved ^{224}Ra activity observed over time or space may be related to the production and/or decay of the radiogenic nuclide. Such isotopic change can be used to estimate the contact time (t) required to change an initial isotope activity (A_d^0) into that observed in solution (A_d) based on the equilibrium activity (Ra_{eq}) specific to a particular sediment sample. We illustrate this concept to estimate contact time between sediment and experimental fluid by manipulating the incubation period and evaluating the resulting effect on dissolved ^{224}Ra activities. ‘Contact time’ is defined here as the isotopically-derived time required to change an initial activity into that observed in solution, whereas ‘incubation time’ is defined here as the manipulated time elapsed since sediment hydration. If contact time and incubation time are equal, then the net effect of production and decay can be shown to exert significant control on the dissolved activity of ^{224}Ra where $t > 0$.

Contact time is determined using a modified form of the standard ingrowth equation (from Equation 2.3) as:

$$Ra_t = \frac{\lambda_{Th-228}\lambda_{Ra-224}}{\lambda_{Ra-224} - \lambda_{Th-228}} \frac{Ra_{eq}}{\lambda_{Th-228}} \left(e^{-\lambda_{Th-228}t} - e^{-\lambda_{Ra-224}t} \right) + Ra_i e^{-\lambda_{Ra-224}t} \quad (2.5)$$

where λ_{Th-228} is the ^{228}Th decay constant ($9.99 \times 10^{-4} \text{ day}^{-1}$) and λ_{Ra-224} is the ^{224}Ra decay constant (0.189 day^{-1}).

To ensure dissolved ^{224}Ra isotope enrichments are predictable through time, dried and homogenized sediments (see Table 2.1) were incubated with Ra-free seawater over ten different time points ranging from 1 to 46 days (13% to 99% ingrown toward equilibrium- Ra_{eq} ; Equation 2.5). Homogenized, dry sediment (3 kg) was bathed in 10 L of Ra-free seawater and subsequently centrifuged to remove a significant fraction of the desorbable ^{224}Ra . This step ensured that porefluid and sediments were not already equilibrated with respect to exchangeable ^{224}Ra so that time dependent change of dissolved ^{224}Ra could be evaluated as a function of production and decay (Equation 2.3).

We take the dissolved equilibrium ^{224}Ra activity as the mean of the incubation periods ≥ 19.8 days ($7.7 \pm 0.6 \text{ dpm L}^{-1}$). However, the sediment bath and subsequent porefluid removal appears to have also removed some ^{228}Ra , the parent of ^{228}Th , resulting in a temporary excess of unsupported ^{228}Th (Table 2.3). This occurrence is evidenced by dissolved ^{224}Ra activities being more enriched than ^{228}Ra throughout the experiment as ^{224}Ra activities would return to equilibrium much faster than ^{228}Ra activities. It is still likely that our dissolved ^{224}Ra equilibrium activity is at secular equilibrium with the exchangeable portion of ^{224}Ra produced by decay of surface-sorbed ^{228}Th , however, this activity would be decreasing over time. For this reason, we adjust our equilibrium activity for decay occurring during the 6 week incubation period (~6% correction) to

represent the $^{224}\text{Ra}_{\text{eq}}$ activity present at the experimental onset ($t=0$). Contact time (t) is then estimated for all measured $^{224}\text{Ra}_t$ activities (Equation 2.5) where $^{224}\text{Ra}_i$ is a constant (taken as incubation period = 0 days; 3.7 ± 0.2 dpm L^{-1}). A significant linear relationship was identified between isotopically-derived contact time estimates and manipulated incubation period indicating estimated times changed predictably and consistently relative to incubation period (Pearson correlation; $r=0.926$, $p \leq 0.1$; Figure 2.8), confirming isotopic ingrowth/decay theory that time required to generate observed change in dissolved ^{224}Ra activities can be accurately estimated.

Table 2.3. Results from laboratory-based contact time experiments.

Incubation period (days)	*Contact time (days)	^{224}Ra activity (dpm L^{-1})	$^{\$}$ Variable type (Eq. 2.5)	^{228}Ra activity (dpm L^{-1})
0	-	3.7 ± 0.2	$^{224}\text{Ra}_i$	0.6 ± 0.0
0.8	0.6 ± 0.3	4.1 ± 0.2	$^{224}\text{Ra}_t$	0.9 ± 0.1
1.7	2.1 ± 0.4	5.1 ± 0.2	$^{224}\text{Ra}_t$	0.7 ± 0.1
2	2.7 ± 0.4	5.3 ± 0.2	$^{224}\text{Ra}_t$	0.7 ± 0.0
5.7	3.0 ± 0.5	5.5 ± 0.3	$^{224}\text{Ra}_t$	0.9 ± 0.1
11.8	8.5 ± 3.3	7.0 ± 0.3	$^{224}\text{Ra}_t$	0.7 ± 0.1
13.7	16.4 ± 3.9	7.6 ± 0.6	$^{224}\text{Ra}_t$	0.8 ± 0.1
19.8	-	7.4 ± 0.7	$^{\!}^{224}\text{Ra}_{\text{eq}}$	1.0 ± 0.1
34.8	-	7.1 ± 0.5	$^{\!}^{224}\text{Ra}_{\text{eq}}$	1.1 ± 0.1
45.7	-	8.0 ± 0.5	$^{\!}^{224}\text{Ra}_{\text{eq}}$	0.7 ± 0.0

*Contact time is determined using measured isotope activities and error is determined by standard error propagation of uncertainties associated with ^{224}Ra terms ($^{224}\text{Ra}_i$, $^{224}\text{Ra}_t$, and $^{224}\text{Ra}_{\text{eq}}$; Equation 2.5)

$^{\$}$ To estimate contact time associated with several incubation periods, Ra_i and Ra_{eq} are taken as constants while Ra_t is substituted over incubation periods ranging from 0.8 to 13.7 days to solve for contact time (t) using Equation 2.5.

$^{\!}$ Ra_{eq} is taken as the average activity measured at incubation periods ranging from 19.8 to 45.7 days (~97 to 99 % ingrown toward equilibrium)

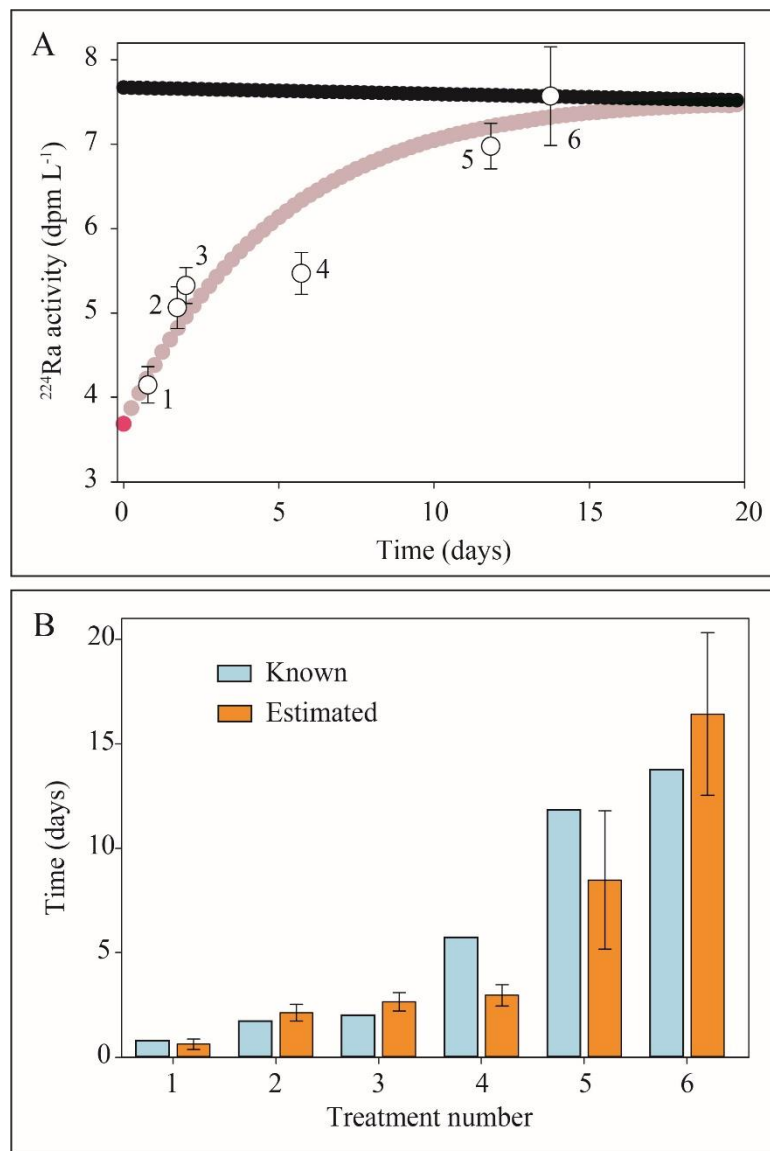


Figure 2.8. (A) Aqueous ^{224}Ra activities measured across several contact times (open symbols) compared to predicted activities (pink symbols) estimated from an initial (dark pink symbol) and an equilibrium (black symbols) activity. Error bars represent standard error propagation using counting statistics. (B). Effective residence time estimated for each treatment using a standard ingrowth equation compared to known incubation durations compared to known incubation durations. Error bars represent $\pm 1\sigma$ standard deviation of all estimates determined using standard propagation of error related to counting statistics for each Ra term (Equation 2.5).

2.5. Synthesis

2.5.1. Vertical Exchange Model

As a dissolved substance, ^{224}Ra in interstitial porefluid would be distributed as a consequence of vertical fluid transport. Upon core collection, any ongoing flow would be disrupted and ^{224}Ra distributions subsequently archived for analysis. We utilize this behavior by applying a modified version of an existing model (Krest and Harvey, 2003) to estimate ^{224}Ra vertical transport through sediments via diffusive and advective transport mechanisms for the deep-sea. While this work has focused efforts for model development on deep-sea applications, the concepts are generally applicable provided all ^{224}Ra sources and sinks are accounted for. Whereas Krest and Harvey (2003) solved the advection-dispersion equation for an advective velocity by assuming a constant rate of ^{224}Ra production down core, our model computes a residence time required to produce the observed change in dissolved activity as a function of isotopic production and decay. Notably, we find aqueous ^{224}Ra activities at equilibrium to vary by as much as an order of magnitude over a sampling interval of 12 cm vertically (Figure 2.6A and Figure 2.7). Such a result suggests that considering a constant rate of production for all recovered sediments is not suitable for materials analyzed here

Our vertical exchange model, shown in Equation 2.5, estimates contact time between sediments and interstitial fluid by calculating progress toward the equilibrium ^{224}Ra activity expected under a given rate of production. As such, we use the observed difference between Ra_{eq} and Ra_t to solve for porefluid residence time (t) within each sediment section. The initial activity (Ra_i) is equal to that of the porefluid recovered from the source layer situated above ($i+1$) or below

($i-1$) that of the receiving layer (i). Ra_{eq} is equal to the dissolved ^{224}Ra activity measured at equilibrium for the receiving layer such that Ra_i under active transport would equal Ra_{eq} when $t \geq 21$ days. Functionally, we then estimate Ra_t for t from 0 to 21 days (at 6 min resolution) for a given transport direction scenario. Porefluid residence time is then optimized by selecting the value of t for which the calculated Ra_t value most closely matches that of our measured ^{224}Ra activity recovered from the source layer. If model conditions are not solvable or yield contact times in excess of 21 days, it can be determined that the approach is not suitable to determine vertical fluid flow rates at these sites. Notably, the slowest theoretical vertical velocity resolvable by this utilizing this model are 0.2 cm day^{-1} assuming a 20 day residence time associated with a 4 cm thick sediment section from which porewater was recovered and residence time was determined.

Porefluid transport direction is assessed by imposing an initial directional condition and subsequently testing for a possible solution. For example, if the ^{224}Ra equilibrium activity (Ra_{eq}) is greater than the observed activity of the source layer (Ra_i), any appreciable porefluid contact time with host sediments would increase the dissolved ^{224}Ra activity such that $Ra_i < Ra_t < Ra_{eq}$ (Figure 2.9A). If the reverse is true, in which the equilibrium ^{224}Ra activity (Ra_{eq}) is lower than the observed activity of the source layer (Ra_i), the unsupported ^{224}Ra would decay faster than it would be produced (Figure 2.9B), and so the activity would decrease as $Ra_i > Ra_t > Ra_{eq}$. In some cases, a solution to Equation 2.5 is not possible under certain flow direction scenarios. For example, if $Ra_{eq} > Ra_t < Ra_i$, no solution is possible, indicating the imposed ^{224}Ra transport direction is not supported by the data and is therefore eliminated from consideration. Because we test for possible fluid transport into and out of the sediments, numerically eliminating one transport direction often reduces uncertainty associated with our fluid flux estimates.

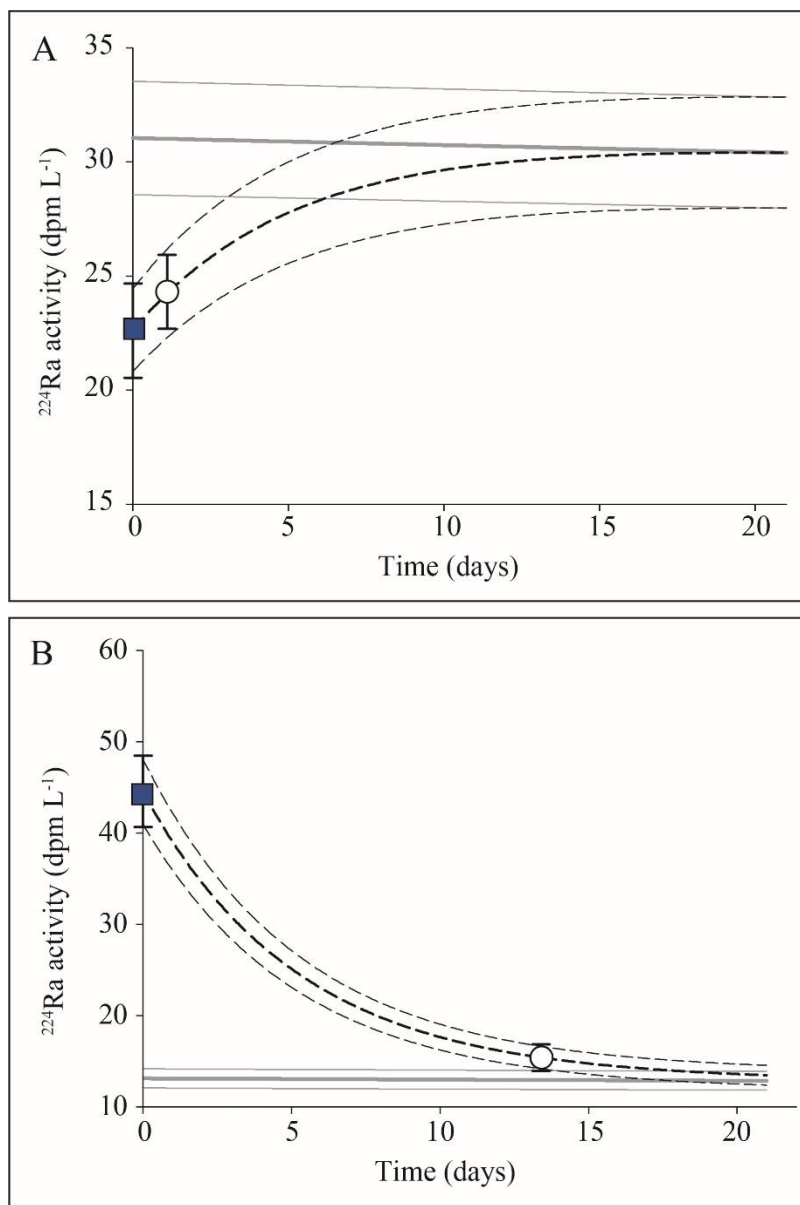


Figure 2.9. Theoretical dissolved ^{224}Ra (A) ingrowth and (B) decay as a function of time. Predicted change in aqueous ^{224}Ra activity (thick dashed line) from an initial condition (square) and a known equilibrium activity (thick gray line). Theoretically, the precise ingrowth/decay time may be determined for any activity measured at time t (circle). Error bars represent $\pm 1\sigma$ standard deviation of all estimates determined using standard propagation of error related to counting statistics of ^{224}Ra analysis.

The time required to support dissolved ^{224}Ra activities observed in porefluid recovered from sediment cores is referred to herein as the porefluid residence time. Notably, this time is determined by the same approach used to estimate the isotopically derived contact time (Section 2.4.3), but distinct in that it represents the amount of time required for porefluid to migrate through a sediment section (i.e., the residence time of porefluid within a particular sediment section). Measured activities (Ra_t , Ra_{eq} , and Ra_i) each have inherent analytical uncertainties. In an effort to fully encompass the error associated with our estimated residence times, we solve for t by considering the analytical uncertainty associated with each Ra_x term individually (Equation 2.5). Error is then equal to the 1σ standard deviation of the range in residence times estimated by applying the maximum uncertainty associated with each term. Briefly, we estimate an error for t by applying the uncertainty associated with each radium term considered in Equation 2.5. For all possible combinations of Ra_t , Ra_{eq} , and Ra_i by adding, subtracting or not applying the uncertainty to each Ra term. This results in 27 different numeric combinations for which t can be estimated. We take the $1-\sigma$ standard deviation of all 27 possible solutions for t as the error associated with our estimates of porefluid residence time. This error estimate is reduced by an average of 30% by taking the standard deviation of all t estimates when also evaluating t by applying 50% and 25% of the uncertainty to each Ra term. This approach to estimating error does not account for a normal distribution of errors and therefore offers a maximum range of potential residence time estimates from which we compute the standard deviation. From our estimates of residence time within any particular sediment layer, we determine an effective volumetric fluid flux by computing the water volume within that layer (as sediment volume times porosity), and dividing that quantity by the surface area of the sediment core and by the residence time ($\text{mL cm}^{-2} \text{ day}^{-1}$).

Applications of the vertical exchange model will be detailed in Chapter 3 for the Gulf of Mexico and Chapter 4 for Guaymas Basin before a discussion concerning fluid fluxes determined for cold seeps and hydrothermal sties is presented in Chapter 5. Because we apply the vertical exchange model to deep-sea sediment cores collected near regions of documented seepage, we describe the interstitial medium as ‘porefluid’ as these fluids may contain appreciable hydrocarbon concentrations and other unique constituents (Suess 2014).

2.5.2. Radiotracer Corrections

Due to the radioactive nature of our chosen chemical proxy, changes in measured activities may manifest purely as a consequence of elapsed time between collection and analysis and so require correction. This discussion is included here as it applies specifically to the application of the vertical exchange model and will be included in the data processing procedures utilized in the forthcoming chapters. One additional correction beyond those discussed in this section was applied only to evaluate porefluid exchange at Guaymas Basin and so will be discussed where appropriate in Chapter 4.

Our initial ^{224}Ra measurement is reflective of not only the ^{224}Ra present due to environmental conditions (e.g., radium partitioning, radium production rate, and fluid flow), but is also influenced by the time elapsed between sample acquisition and analysis. In order to resolve disequilibria in ^{224}Ra between aqueous and particulate phases at the time of sampling, we must account for any changes in our initial measurement due to continued sediment:water contact time after core collection. Conceptually, if no fluid is actively exchanging through the sampled sediments, our initial measurement will be equal to our equilibrium measurement (i.e., porefluid

^{224}Ra will be in equilibrium with exchangeable sediment-supported ^{224}Ra levels) and no correction is required. This condition effectively means the ^{224}Ra produced on the grain surface by ^{228}Th decay and subsequently subject to desorption into porefluid is in steady state with the amount of porefluid ^{224}Ra decay, so therefore the ^{224}Ra activity remains unchanged. However, if vertical fluid transport is occurring at the time of sampling, such transport may remove some ^{224}Ra dissolved in porefluid and a disequilibrium scenario would be observed after collection. This effect can be significant as samples collected using the HOV *Alvin* include supplemental mission/vehicle recovery time as well as time for core description and may be in excess of several hours. Under such a circumstance, the activity of porefluid ^{224}Ra may either be in excess (relative to the amount of ^{224}Ra supported at equilibrium) or deficient (to the equilibrium activity) and therefore would be subject to change simply as a result of prolonged sediment:water contact time. To determine if - and in what way - our initial measurement may have been subject to change by this process, we must first determine the rate of exchangeable ^{224}Ra production supported by particulate ^{228}Th associated with each sample (this correction is detailed below).

Our equilibrium measurement of dissolved ^{224}Ra activity associated with each discrete sediment sample represents the maximum porefluid activity supported by the recovered materials. These measurements must also be corrected for time-dependent change by correcting for ^{228}Th decay that may have occurred over the duration of the equilibrium experiment. This correction assumes that ^{228}Th is in excess of sedimentary ^{228}Ra (due to the soluble nature of radium isotopes; Rama and Moore, 1996) and thus our measured equilibrium activity is lower than the hypothetical activity present before ^{228}Th decay occurs. For this enrichment to occur, a sink of ^{228}Ra must have existed in the environment prior to collection, rendering ^{228}Th in relative excess. Although we cannot know for sure at the time of sampling, active fluid seepage could be the cause of such

excess as dissolved ^{228}Ra would be transported out of the system. While minimal, this correction is necessary because the time to complete the equilibrium experiments commonly exceeded 50 days. In general, this correction resulted in a minimal adjustment of ~3-5 % of the measured activity. We assume a linear relationship between elapsed time and percent decayed to estimate the correction factor (c):

$$c = \left(\frac{0.5}{T_{1/2}} \right) \Delta d \quad (2.6)$$

where 0.5 is decayed fraction of ^{228}Th over its half-life ($T_{1/2} = 697.7$ days) and Δd represents the time elapsed (in days) between the first and second filter measurement. This correction factor is then used to determine the fraction of ^{228}Th activity lost to decay between the two measurements and the measured activity is subsequently adjusted for this loss. A linear approximation is appropriate over short time scales (1-2 months) as a linear relationship adequately describes isotopic ingrowth/decay during very early stages of time-dependent exponential change (~5% change in ^{228}Th over this time period estimated using Equation 2.3; $r^2=0.996$). This correction is applied to the data provided in the Appendix (Table A.5).

Corrected ^{224}Ra equilibrium measurements are thus representative of the maximum possible exchangeable ^{224}Ra supported by the sediments at the time of sampling. This value is equal to the rate of ^{224}Ra production that would influence our initial ^{224}Ra measurement via ^{228}Th decay. Because we know the parent activity (i.e., the corrected equilibrium measurement; A_p^0) and the activity of porefluid ^{224}Ra measured after contact with sediments (i.e., the uncorrected at-sea activity; A_d) determined after the porefluid samples remained in contact with sediments for time (t) after collection and before centrifugation, we can estimate the porefluid ^{224}Ra activity (corrected initial measurement; A_d^0) present during sample collection (Equation 2.3) Here, λ_p and λ_d

represent the decay constants of ^{228}Th ($6.90 \times 10^{-7} \text{ min}^{-1}$) and ^{224}Ra ($1.34 \times 10^{-4} \text{ min}^{-1}$), respectively. A schematic diagram of the corrections applied to model data is included in the Appendix (Figure A1.). Lastly, we applied a 3 point boxcar filter over isotope activities associated with 3 vertically adjoining sediment sections to filter out the effect that small differences between consecutive isotope measurements might have on our estimated fluid fluxes. Because of the exponential relationship between dissolved ^{224}Ra activity and residence time, this effect is most significant at greater residence times (approaching equilibrium).

2.5.3. Model Assumptions

We explored the potential effects of a changing radium distribution coefficient (K_d), removal from the desorbable pool via incorporation into barite, and removal from the dissolved phase via adsorption onto metal (hydr)oxides (Section 2.4) on dissolved ^{224}Ra activities. A variety of materials was used (Table 2.1) to identify which potentially important ^{224}Ra sources and sinks should be considered in a vertical exchange model. A review of mass balance terms and statement of potential ^{224}Ra effect is provided below for each source/sink term (Figure 2.1).

2.5.3.1. Adsorption and Desorption

Spatially or temporally variable K_d values were not observed to control distributions of dissolved ^{224}Ra activities under the conditions tested and have therefore not been included in the vertical exchange model for deep-sea sediments. Vertical ^{224}Ra distributions appeared unrelated to collection depth below the sediment-water interface, suggesting K_d is constant over the depths

sampled (0 to 20 cmbsf; Figure 2.2A and Figure 2.3B). The most compelling evidence warranting inclusion of a K_d parameter in the vertical exchange model was indicated only by a weak relationship between dissolved ^{226}Ra activities and in-situ porosity (Figure 2.3). Although ^{224}Ra distribution may be related to porosity, the change in fluid volume from one layer to the next is often minimal and therefore porosity related change in ^{224}Ra is assumed insignificant. On average, porosity change between layers observed throughout our field sampling (Chapters 3-4) is $\sim 4\%$. Assuming a change in radium of equal proportion, this effect is well within our analytical uncertainty. Further, since at-sea and equilibrium measurements were conducted under the same porosity, K_d effects on Ra_t and Ra_{eq} measurements should be equivalent.

Our experimental results confirm drying sediments $\leq 60^\circ\text{C}$ and subsequently rehydrating the materials to in-situ porosity had no effect on dissolved radium activities beyond error as previously observed (Beck and Cochran, 2013). Furthermore, when isotopic disequilibrium is measured, it cannot be explained solely by a redistribution of ^{224}Ra as dissolved ^{224}Ra would equilibrate with K_d moderated activities supported by host sediments. This finding suggests that when disequilibrium is observed it is either attributable to a ^{224}Ra transport mechanism or some unknown sink.

Although we could not identify evidence for an effect on dissolved ^{224}Ra activities related to redistribution as a function of spatially and temporally variable K_d values, it is worth considering how such a process could influence our residence time (and subsequent fluid flux) estimates. If dissolved ^{224}Ra activities in any layer of porefluids changed as a consequence of a different K_d value, such an impact would lead to an over estimation in residence time (Equation 2.5). Regardless of the relative change in K_d , a difference would always cause a change in dissolved ^{224}Ra faster than would otherwise be attributed to production and decay, so our approach to

estimating residence time without considering any variable K_d would lead to over estimations of residence time and therefore provide conservative fluid flux estimates. For this reason, by assuming uniform K_d values throughout a sediment core (as also assumed by Krest and Harvey (2003), a change in ^{224}Ra due exclusively to isotopic production and decay (excluding changes attributable to sorption/desorption) offers conservative estimates of porefluid residence time and fluid flux.

2.5.3.2. Barite Incorporation

Radium removal via incorporation into barite as $\text{Ba}(\text{Ra})\text{SO}_4$ could act as a sink of ^{224}Ra from not only the dissolved phase, but also the desorbable pool entirely. This effect could be especially problematic as measured values of Ra_{eq} would be reduced relative to in-situ Ra_{eq} activities and ultimately misrepresent true porefluid residence time. Because radium is expected to co-precipitate with any barite matrix formed (Doerner and Hoskins, 1925), time-series monitoring of radiogenic daughter products can facilitate comparison between predicted activities and those measured. Predictions assume the only changes in gaseous ^{222}Rn are related to the initial and equilibrium activities of ^{222}Rn as a function of production and decay (Equation 2.4).

Although measured ^{222}Rn activities did deviate slightly from those predicted, this effect was not significant over typical sediment core processing times of a few hours (Figure 2.5). While the error associated with initial ^{222}Rn measurements was large, we did not find compelling evidence to support including a $\text{Ba}(\text{Ra})\text{SO}_4$ removal term in our vertical exchange model. Even though several sites across the Gulf of Mexico have been the focus of barite formation at cold seeps (e.g., Feng and Roberts, 2011), we did not see evidence of this process affecting ^{224}Ra

associated with sediments recovered from a natural hydrocarbon seep within the Gulf of Mexico.

However, if such a sink were affecting aqueous radium activities, the removal of ^{224}Ra would result in a reduced Ra_{eq} activity at a later time (t) as compared to that present at collection. The potential consequence of this underestimation depends on the relationship between Ra_{eq} and Ra_i . If $Ra_{\text{eq}} > Ra_i$, this scenario would cause an overestimation in the time required to achieve Ra_t via Equation 2.5 yielding conservative fluid flux estimates. However, if $Ra_{\text{eq}} < Ra_i$, this scenario would cause an underestimation in the time required to achieve Ra_t via Equation 2.5. To specifically avoid complications in constraining Ra_B we do not consider samples from sites where barite chimneys or brine lakes have been identified for Guaymas Basin or the Gulf of Mexico (Feng and Roberts, 2011; Núñez-Useche et al., 2018). Importantly, we only evaluated the potential for barite incorporation of Ra from GOM sediments and assume this finding also holds true for Guaymas Basin as equipment was not available for immediate analysis of materials recovered from this site. We did not sample areas within Guaymas Basin where chimneys were present and avoided sites identified by Núñez-Useche et al. (2018) as regions where barite precipitation was confirmed.

2.5.3.3. Sorption onto Metal Hydr(oxides)

As conditions in deep-sea pore spaces may be largely devoid of oxygen over our target depths below the sediment-water interface at seep sites, sample processing under ambient atmospheric conditions could oxidize otherwise reduced metals and potentially scavenge dissolved ^{224}Ra from porefluid (Figure 2.1). To examine the potential consequence of this process on dissolved ^{224}Ra activities, we processed duplicate sediment cores recovered from the Gulf of

Mexico and Guaymas Basin under ‘normal’ and inert atmospheric conditions. For Gulf of Mexico cores, only two of eight particulate filters contained measurable amounts of excess ^{224}Ra (Table 2.2), although excess activity was observed for both air and He treatments suggesting the processing atmosphere alone cannot explain this result. Furthermore, when normalized to Ra_{eq} , slightly more ^{224}Ra was present in solution for ambient air treatments as compared to the inert sampling treatments for both Gulf of Mexico (Figure 2.6) and Guaymas Basin (Figure 2.7) sediments. Because this trend is counter to that which we would expect if metal scavenging of ^{224}Ra onto metal (hydr)oxide precipitates was controlling the distribution of ^{224}Ra , we concluded that the effect of metal scavenging on dissolved ^{224}Ra was negligible for the materials tested.

Strong linear trends between aqueous ^{224}Ra observed at sea and Ra_{eq} from these experiments suggest that although disequilibrium was observed (i.e., $\text{Ra at sea} \neq \text{Ra}_{\text{eq}}$), the relative abundance of dissolved ^{224}Ra at-sea (as compared to as determined at equilibrium) remained constant with depth regardless of processing environment (Figure 2.6A and Figure 2.7). Therefore, scavenging of ^{224}Ra to metal (hydr)oxides formed as a result of our sample handling protocols is assumed to be negligible for both the Gulf of Mexico and Guaymas Basin sites. Such a trend suggests if scavenging was influencing our observations, all layers for both cores recovered from each site were effected equally. In other words, the effects of metal scavenging are either negligible on the aqueous ^{224}Ra inventory or constant with depth meaning any radium measured at-sea and at equilibrium will be a result of a constant sink and does not effect the net inventory of radium we observe for a given sediment core.

If we have underestimated the removal of ^{224}Ra due to redox related scavenging, we expect that Ra_{eq} would remain unaffected as scavenged ^{224}Ra would be unsupported by resident grains. However, Ra_t and Ra_i could be reduced depending on factors including iron and manganese

concentrations and speciation (Mott et al., 1993). Although no experimental evidence in support of Ra scavenging related to processing environment was observed, predicting the impacts of such a process on our fluid flux outcomes is complicated as change could affect Ra_i and Ra_e by different amounts as the concentrations of dissolved metals may vary down-core and as such affect each Ra term differently.

2.5.3.4. Isotopic Production and Decay

When a change in dissolved ^{224}Ra activity is observed through time, and the dissolved equilibrium activity between a saline solution (porefluid or experimental fluid) and host sediments is known, contact time between the materials can be determined (Figure 2.8). Through a series of laboratory incubations, it was demonstrated that discrete isotopic sampling can be used to determine sediment-water contact time when no changes in solid-aqueous partitioning (K_d) are dominating aqueous ^{224}Ra distributions.

To understand fluid exchange through deep-sea sediments, we need to consider changes in space concurrently with changes in time (as isotopic production and decay). The strong linear relationship between dissolved ^{224}Ra activities recovered from porefluid and associated equilibrium activities (Section 2.4.2) is suggestive of three key points: (1) disequilibrium was consistently observed between dissolved ^{224}Ra activities and equilibrium activities supported by host sediments from 0 to 16 cmbsf (Gulf of Mexico) and 0 to 12 cmbsf (Guaymas Basin); (2) the square of the linear correlation coefficient (all ≥ 0.997) suggests residence time between recovered porefluid and host sediments within each sediment section is conserved vertically (Figures 2.6A and 2.7); and (3) the ratio of dissolved ^{224}Ra to equilibrium ^{224}Ra is conserved vertically (e.g.,

vertical continuity of radium mass). These observations serve as the foundation on which our vertical exchange model, modified from Krest and Harvey (2003) for deep-sea sediments and utilized throughout the following chapters is developed. The efficacy of our vertical exchange model will be qualitatively evaluated in Chapter 3.

2.6. References

- Aharon, P., Van Gent, D., Fu, B., Scott, L.M., 2001. Fate and effects of barium and radium-rich fluid emissions from hydrocarbon seeps on the benthic habitats of the Gulf of Mexico offshore Louisiana. OCS Study MMS 2001-004. Prepared by the Louisiana State University, Coastal Marine Institute. U.S. Department of the Interior, Minerals Management Service, Gulf of Mexico OCS Region, New Orleans, LA. 142.
- Bateman, H. 1910. Solution of a system of differential equations occurring in the theory of radioactive transformations. *Mathematical Proceedings of the Cambridge Philosophical Society*. 15, 423
- Beck, A.J., Cochran, M.A., 2013. Controls on solid-solution partitioning of radium in saturated marine sands. *Marine Chemistry, Radium and Radon Tracers in Aquatic Systems* 156, 38–48. <https://doi.org/10.1016/j.marchem.2013.01.008>
- Berner, R.A., 1980. Early diagenesis—a theoretical approach. Princeton Series in Geochemistry, Princeton University Press.
- Bollinger, M.S., Moore, W.S., 1993. Evaluation of salt marsh hydrology using radium as a tracer. *Geochimica et Cosmochimica Acta* 57, 2203–2212. [https://doi.org/10.1016/0016-7037\(93\)90562-B](https://doi.org/10.1016/0016-7037(93)90562-B)
- Brandt, F., Curti, E., Klinkenberg, M., Rozov, K., Bosbach, D., 2015. Replacement of barite by a (Ba,Ra)SO₄ solid solution at close-to-equilibrium conditions: A combined experimental and theoretical study. *Geochimica et Cosmochimica Acta* 155, 1–15.
- Brooks, J.M., Kennicutt, M.C., Fisher, C.R., Macko, S.A., Cole, K., Childress, J.J., Bidigare, R.R., Vetter, R.D., 1987. Deep-sea hydrocarbon seep communities: evidence for energy and nutritional carbon Sources. *Science* 238, 1138–1142. <https://doi.org/10.1126/science.238.4830.1138>
- Cai, P., Shi, X., Moore, W.S., Dai, M., 2012. Measurement of ²²⁴Ra:²²⁸Th disequilibrium in coastal sediments using a delayed coincidence counter. *Marine Chemistry* 138–139, 1–6. <https://doi.org/10.1016/j.marchem.2012.05.004>.
- Chanyotha, S., Kranrod, C., Kritsanuwat, R., Lane-Smith, D., Burnett, W.C., 2016. Optimizing laboratory-based radon flux measurements for sediments. *Journal of Environmental Radioactivity* 158-15947-55.
- Colbert, S.L., Hammond, D.E., 2008. Shoreline and seafloor fluxes of water and short-lived Ra isotopes to surface water of San Pedro Bay, CA. *Marine Chemistry* 108, 1–17. <https://doi.org/10.1016/j.marchem.2007.09.004>
- Corbett, D.R., Crenshaw, J., Null, K., Peterson, R.N., Peterson, L.E., Lyons, W.B., 2017.

- Nearshore mixing and nutrient delivery along the western Antarctic Peninsula. *Antarctic Science* 29, 397–409. <https://doi.org/10.1017/S095410201700013X>
- D'souza, N.A., Subramaniam, A., Juhl, A.R., Hafez, M., Chekalyuk, A., Phan, S., Yan, B., MacDonald, I.R., Weber, S.C., Montoya, J.P., 2016. Elevated surface chlorophyll associated with natural oil seeps in the Gulf of Mexico. *Nature Geoscience* 9, 215–218. <https://doi.org/10.1038/ngeo2631>
- Dekas, A.E., Poretsky, R.S., Orphan, V.J., 2009. Deep-sea archaea fix and share nitrogen in methane-consuming microbial consortia. *Science* 326, 422–426. <https://doi.org/10.1126/science.1178223>
- Doerner, H.A., Hoskins, W.M., 1925. Co-precipitation of radium and barium sulfates. *Journal of the American Chemical Society* 47, 662–675. <https://doi.org/10.1021/ja01680a010>
- Faure, G., Mensing, T.M., 2005. *Isotopes: Principles and applications* 3rd Edition. Wiley
- Feng, D., Roberts, H.H., 2011. Geochemical characteristics of the barite deposits at cold seeps from the northern Gulf of Mexico continental slope. *Earth and Planetary Science Letters* 309, 89–99. <https://doi.org/10.1016/j.epsl.2011.06.017>
- Fisher, A.T., Becker, K., 1991. Heat flow, hydrothermal circulation and basalt intrusions in the Guaymas Basin, Gulf of California. *Earth and Planetary Science Letters* 103, 84–99. [https://doi.org/10.1016/0012-821X\(91\)90152-8](https://doi.org/10.1016/0012-821X(91)90152-8)
- Fisher, A.T., Giambalvo, E., Sclater, J., Kastner, M., Ransom, B., Weinstein, Y., Lonsdale, P., 2001. Heat flow, sediment and pore fluid chemistry, and hydrothermal circulation on the east flank of Alarcon Ridge, Gulf of California. *Earth and Planetary Science Letters* 188, 521–534. [https://doi.org/10.1016/S0012-821X\(01\)00310-7](https://doi.org/10.1016/S0012-821X(01)00310-7)
- Fitzsimmons, J.N., Boyle, E.A., Jenkins, W.J., 2014. Distal transport of dissolved hydrothermal iron in the deep South Pacific Ocean. *PNAS* 111, 16654–16661. <https://doi.org/10.1073/pnas.1418778111>
- Gonneea, M.E., Morris, P.J., Dulaiova, H., Charette, M.A., 2008. New perspectives on radium behavior within a subterranean estuary. *Marine Chemistry, Measurement of Radium and Actinium Isotopes in the marine environment* 109, 250–267. <https://doi.org/10.1016/j.marchem.2007.12.002>
- Heberling, F., Metz, V., Böttle, M., Curti, E., Geckeis, H., 2018. Barite recrystallization in the presence of ²²⁶Ra and ¹³³Ba. *Geochimica et Cosmochimica Acta* 232, 124–139. <https://doi.org/10.1016/j.gca.2018.04.007>
- Hong, Q., Cai, P., Shi, X., Quing, L., Wang, G., 2017. Solute transport into the Jiulong River estuary via pore water exchange and submarine groundwater discharge: New insights

- from $^{224}\text{Ra}/^{228}\text{Th}$ disequilibrium. *Geochimica Acta* 198, 338–359.
<https://dx.doi.org/10.1016/j.gca.2016.11.002>
- Hughes, A.L.H., Wilson, A.M., Moore, W.S., 2015. Groundwater transport and radium variability in coastal porewaters. *Estuarine Coastal and Shelf Science* 164, 94-104.
- Joye, S.B., Boetius, A., Orcutt, B.N., Montoya, J.P., Schulz, H.N., Erickson, M.J., Lugo, S.K., 2004. The anaerobic oxidation of methane and sulfate reduction in sediments from Gulf of Mexico cold seeps. *Chemical Geology, Geomicrobiology and Biogeochemistry of Gas Hydrates and Hydrocarbon Seeps* 205, 219–238.
<https://doi.org/10.1016/j.chemgeo.2003.12.019>
- Joye, S.B., Bowles, M.W., Samarkin, V.A., Hunter, K.S., Niemann, H., 2010. Biogeochemical signatures and microbial activity of different cold-seep habitats along the Gulf of Mexico deep slope. *Deep Sea Research Part II: Topical Studies in Oceanography, Gulf of Mexico Cold Seeps* 57, 1990–2001. <https://doi.org/10.1016/j.dsr2.2010.06.001>
- Kelley, D.S., Karson, J.A., Früh-Green, G.L., Yoerger, D.R., Shank, T.M., Butterfield, D.A., Hayes, J.M., Schrenk, M.O., Olson, E.J., Proskurowski, G., Jakuba, M., Bradley, A., Larson, B., Ludwig, K., Glickson, D., Buckman, K., Bradley, A.S., Brazelton, W.J., Roe, K., Elend, M.J., Delacour, A., Bernasconi, S.M., Lilley, M.D., Baross, J.A., Summons, R.E., Sylva, S.P., 2005. A Serpentinite-Hosted Ecosystem: The Lost City Hydrothermal Field. *Science* 307, 1428–1434. <https://doi.org/10.1126/science.1102556>
- Kennicutt II, M.C., Brooks, J.M., Bidigare, R.R., Fay, R.R., Wade, T.L., McDonald, T.J., 1985. Vent-type taxa in a hydrocarbon seep region on the Louisiana slope. *Nature* 317, 351-353.
- Kraemer, T.F., Reid, D.F., 1984. The occurrence and behavior of radium in saline formation water of the U.S. Gulf Coast region. *Chemical Geology* 46, 153–174.
[https://doi.org/10.1016/0009-2541\(84\)90186-4](https://doi.org/10.1016/0009-2541(84)90186-4)
- Krest, J.M., Harvey, J.W., 2003. Using natural distributions of short-lived radium isotopes to quantify groundwater discharge and recharge. *Limnology and Oceanography* 48:1, 290-298.
- Lambe, T.W., 1951. Soil testing for engineers. Series in Soil Engineering, Wiley.
- Land, L.S., Kupecz, J.A., Mack, L.E., 1988. Louann salt geochemistry (Gulf of Mexico sedimentary basin, U.S.A.): A preliminary synthesis. *Chemical Geology, Fluid-Rock Interactions in the Salt Dome Environment* 74, 25–35. [https://doi.org/10.1016/0009-2541\(88\)90144-1](https://doi.org/10.1016/0009-2541(88)90144-1)
- Lapham, L., Alperin, M., Chanton, J., Martens, C., 2008. Upward advection rates and methane fluxes, oxidation, and sources at two Gulf of Mexico brine seeps. *Marine Chemistry* 112,

65-7. doi: 10.1016/j.marchem.2008.06.001

- Lemaitre, N., Bayon, G., Ondréas, H., Caprais, J.-C., Freslon, N., Bollinger, C., Rouget, M.-L., de Prunelé, A., Ruffine, L., Olu-Le Roy, K., Sarthou, G., 2014. Trace element behaviour at cold seeps and the potential export of dissolved iron to the ocean. *Earth and Planetary Science Letters* 404, 376–388. <https://doi.org/10.1016/j.epsl.2014.08.014>
- MacDonald, I.R., Boland, G.S., Baker, J.S., Brooks, J.M., Kennicutt, M.C., Bidigare, R.R., 1989. Gulf of Mexico hydrocarbon seep communities: II. Spatial distribution of seep organisms and hydrocarbons at Bush Hill. *Marine Biology* 101, 235–247. <https://doi.org/10.1007/BF00391463>
- Miller, N.C., Lizarralde, D., 2013. Thick evaporites and early rifting in the Guaymas Basin, Gulf of California. *Geology* 41, 283–286. <https://doi.org/10.1130/G33747.1>
- Moore, W.S., 1976. Sampling ^{228}Ra in the deep ocean. *Deep-Sea Research* 23, 647–651.
- Moore, W.S., 2000. Ages of continental shelf waters determined from ^{223}Ra and ^{224}Ra . *Journal of Geophysical Research*. 105:C9, 22117–22122.
- Moore, W.S., 2008. Fifteen years experience in measuring ^{224}Ra and ^{223}Ra by delayed-coincidence counting. *Marine Chemistry, Measurement of Radium and Actinium Isotopes in the marine environment* 109, 188–197. <https://doi.org/10.1016/j.marchem.2007.06.015>
- Moore W.S., Arnold R., 1996. Measurement of ^{223}Ra and ^{224}Ra in coastal waters using a delayed coincidence counter. *Journal of Geophysical Research: Oceans* 101, 1321–1329. <https://doi.org/10.1029/95JC03139>
- Mott, H.V., Singh, S., Kondapally, V.R., 1993. Factors affecting radium removal using mixed iron-manganese oxides. *Journal of American Water Works Association* 85, 114–121.
- Núñez-Useche, F., Canet, C., Liebetrau, V., Puig, T.P., Ponciano, A.C., Alfonso, P., Berndt, C., Hensen, C., Mortera-Gutierrez, C., Rodríguez-Díaz, A.A., 2018. Redox conditions and authigenic mineralization related to cold seeps in central Guaymas Basin, Gulf of California. *Marine and Petroleum Geology* 95, 1–15. <https://doi.org/10.1016/j.marpetgeo.2018.04.010>
- Orcutt, B.N., Sylvan, J.B., Knab, N.J., Edwards, K.J., 2011. Microbial ecology of the dark ocean above, at, and below the seafloor. *Microbiology and Molecular Biology Reviews* 75:2, 361–422.
- Paull, C.K., Chanton, J.P., Neumann, A.C., Coston, J.A., Martens, C.S., Showers, W., 1992. Indicators of methane-derived carbonates and chemosynthetic organic carbon deposits: examples from the Florida Escarpment. *PALAIOS* 7, 361–375. <https://doi.org/10.2307/3514822>.

- Paull, C.K., Hecker, B., Commeau, R., Freeman-Lynde, R.P., Neumann, C., Corso, W.P., Golubic, S., Hook, J.E., Sikes, E., Curray, J., 1984. Biological communities at the Florida Escarpment resemble hydrothermal vent taxa. *Science* 226, 965–967. <https://doi.org/10.1126/science.226.4677.965>
- Peterson, R.N., Burnett, W.C., Dimova, N., and Santos, I.R., 2009. Comparison of measurement methods for radium-226 on manganese-fiber. *Limnology and Oceanography: Methods*, 7, 196-205.
- Pohlman, J.W., Bauer, J.E., Waite, W.F., Osburn, C.L., Chapman, N.R., 2011. Methane hydrate-bearing seeps as a source of aged dissolved organic carbon to the oceans. *Nature Geoscience* 4, 37–41. <https://doi.org/10.1038/ngeo1016>
- Porcelli, D., Swarzenski, P.W., 2003. The behavior of U- and Th-series nuclides in groundwater. *Reviews in Mineralogy and Geochemistry* 52, 317–361. <https://doi.org/10.2113/0520317>
- Portail, M., Olu, K., Dubois, S.F., Escobar-Briones, E., Gelinas, Y., Menot, L., Sarrazin, J., 2016. Food-web complexity in Guaymas Basin hydrothermal vents and cold seeps. *PLOS ONE* 11, e0162263. <https://doi.org/10.1371/journal.pone.0162263>
- Rama, Moore, W.S., 1996. Using the radium quartet for evaluating groundwater input and water exchange in salt marshes. *Geochimica et Cosmochimica Acta* 60, 4645–4652. [https://doi.org/10.1016/S0016-7037\(96\)00289-X](https://doi.org/10.1016/S0016-7037(96)00289-X)
- Rosenberg, Y.O., Sade, Z., Ganor, J., 2018. The precipitation of gypsum, celestine, and barite and coprecipitation of radium during seawater evaporation. *Geochimica et Cosmochimica Acta* 233, 50–65. <https://doi.org/10.1016/j.gca.2018.04.019>
- Sadat-Noori, M., Santos, I.R., Tait, D.R., Reading, M.J., Sanders, C.J., 2017. High porewater exchange in a mangrove-dominated estuary revealed from short-lived radium isotopes. *Journal of Hydrology* 553, 188–198. <https://doi.org/10.1016/j.jhydrol.2017.07.058>
- Seyfried, W.E., Bischoff, J.L., 1981. Experimental seawater-basalt interaction at 300°C, 500 bars, chemical exchange, secondary mineral formation and implications for the transport of heavy metals. *Geochimica et Cosmochimica Acta* 45, 135–147. [https://doi.org/10.1016/0016-7037\(81\)90157-5](https://doi.org/10.1016/0016-7037(81)90157-5)
- Suess, E., 2014. Marine cold seeps and their manifestations: geological control, biogeochemical criteria and environmental conditions. *International Journal of Earth Sciences: Geologische Rundschau* 103, 1889-1916. doi: 10.1007/s00531-014-1010-0
- Sun, Y., Torgersen, T., 1998. The effects of water content and Mn-fiber surface conditions on ²²⁴Ra measurement by ²²⁰Rn emanation. *Marine Chemistry* 62, 299–306. [https://doi.org/10.1016/S0304-4203\(98\)00019-X](https://doi.org/10.1016/S0304-4203(98)00019-X)

- Weber, J., Barthel, J., Klinkenberg, M., Bosbach, D., Kruth, M., Brandt, F., 2017. Retention of ^{226}Ra by barite: The role of internal porosity. *Chemical Geology* 466, 722–732. <https://doi.org/10.1016/j.chemgeo.2017.07.021>
- Weber, S.C., Peterson, L., Battles, J.J., Roberts, B.J., Peterson, R.N., Hollander, D.J., Chanton, J.P., Joye, S.B., Montoya, J.P., 2016. Hercules 265 rapid response: Immediate ecosystem impacts of a natural gas blowout incident. *Deep Sea Research Part II: Topical Studies in Oceanography* 129, 66–76. <https://doi.org/10.1016/j.dsr2.2015.11.010>
- Webster, I.T., Hancock, G.J., Murray, A.S., 1995. Modelling the effect of salinity on radium desorption from sediments. *Geochimica et Cosmochimica Acta* 59, 2469–2476. [https://doi.org/10.1016/0016-7037\(95\)00141-7](https://doi.org/10.1016/0016-7037(95)00141-7)
- Wheat, C.G., Mottl, M.J., Fisher, A.T., Kadko, D., Davis, E.E., Baker, E., 2004. Heat flow through a basaltic outcrop on a sedimented young ridge flank. *Geochemistry Geophysics Geosystems* 5:12.

CHAPTER 3

ESTIMATING SUBSURFACE POREFLUID RESIDENCE TIME AND FLUID FLUX AT COLD SEEPS IN THE GULF OF MEXICO

3.1. Introduction

The Gulf of Mexico (GOM) seafloor is arguably one of the most active of all modern passive margins underlying a marine basin. The unique geologic history of the GOM has led to abundant seafloor seepage sites which host diverse seep-dependent ecosystem assemblages (Cordes et al., 2007). Paull et al. (1984) first termed ‘submarine cold seep’ to describe these benthic ecological oases supported by an enriched supply of reduced compounds via subsurface fluid seepage occurring at near-ambient ocean temperatures. Although much remains to be understood about seep biota, submarine seeps are regarded as one of the most physically and chemically diverse biomes on Earth with several new seep species being discovered annually (Bris et al., 2016).

Discharge of seep fluids is most often caused by overpressurization, commonly resulting from rapid deposition of low permeability sediments (Talukder, 2012), which prohibits uniform dewatering and ultimately results in suprahydrostatic levels within interstitial sediment spaces (Osborne and Swarbrick, 1997). Evaporite deposits throughout the subsurface lithology of the GOM have responded to the overburden by flowing upward as diapirs, forcing fissures, faults, and

folds into strata along ascension. Consequently, subsurface fluids can migrate along fault lines from thousands of meters below the seafloor. Conversely, cold seep fluids can originate a few centimeters below the sediment-water interface (e.g., sediment dewatering) and travel along small compensation faults (Roberts and Carney, 1997). Commonly, gas accumulation associated with thermogenic organic matter breakdown as well as microbially moderated biogenic transformations of carbon will migrate towards the seafloor resulting in subsurface fluid transport (Judd et al., 2002). While the physical driver and depth of fluid origination may influence the geochemistry of the seeps, both geochemical concentration and rate of fluid transport are thought to moderate resulting ecosystem dynamics.

The stages of cold seep development are qualitatively related to the distribution of seafloor bio-geological and geochemical processes (Macelloni et al., 2013), however the presence of particular seepage features alone is not sufficient to estimate the rate of fluid transport. Ubiquitous cold seep features including mud volcanoes, carbonate chimneys, asphalt seeps, and methane plumes (Suess, 2014) provide obvious indicators of flow and visual markers to target sampling efforts. Although several indicators of seafloor seepage exist, hydrocarbon sheens at the sea surface are commonly used to identify cold seeps as they can be observed directly and via satellites (Garcia-Pineda et al., 2010). However, persistent and intermittent oil sheens are most commonly associated with vigorous seafloor seepage of oil-rich fluids (Johansen et al., 2017), so relying on methods exclusively effective under only high flow conditions may bias our understanding of cold seeps. While biologic communities are often associated with cold seep discharge sites, it has been hypothesized that some sites of especially active seafloor seepage remain uncolonized because common inhabitants are physically blown from the sediment surface and are therefore unable to exist in dense colonies (Teske et al., 2016).

Across the GOM, natural hydrocarbon seepage is prolific with well over one thousand seafloor seep formations suspected, but most sites remain unexplored by scientists (MacDonald, 2011). Seepage at these sites is not restricted to hydrocarbon discharge and may also include formation fluids and entrained porefluid which have proven more challenging to study (Suess, 2014). Existing efforts to quantify rates of diffuse seafloor seepage in the deep-sea often involve in-situ instrumentation (Solomon et al., 2008) with costly deployment and recovery demands or the use of chemical proxies (e.g., Cl^- gradients) that rely on specific conditions, such as the presence of hypersaline fluids (Lapham et al., 2008).

Although sites of active seepage out of the sediments may be relatively easy to identify by the presence of discrete biological assemblages and physical seafloor manifestations (e.g., chimneys, mounds, and volcanoes), fluid transport must either be occurring at significant rates or for sufficient time to physically change the shape of the seafloor. However, seepage likely occurs in many places at much lower rates than those that influence seafloor topography. For example, cold seep communities appear to exist far beyond the immediate proximity of an obvious subsurface fluid source with bacterial mats extending tens of meters from direct evidence of active seepage (Suess, 2014). In-situ sensors have recorded material concentrations and estimated fluid transport through mat-covered sediments (Solomon et al., 2008) affirming that dense microbial communities are associated with seafloor seepage. Given the wide range of seepage rates in these environments, the development of additional tools to measure such processes represents a strong need among the research community.

Here, we test the suitability of the vertical exchange model developed in Chapter 2 to ultimately determine porefluid fluxes through deep-sea sediments. The objective of this work is to determine if the vertical exchange model yields reasonable fluid flux estimates between seep and

control sites. To accomplish this, we collect sediment cores from two active seepage sites and one control site and determine subsurface porefluid residence time and an effective fluid flux required to support ^{224}Ra porefluid profiles observed. To satisfy our objective, we compare our observations of dissolved ^{224}Ra activities to equilibrium activities in order to determine porefluid residence time. Importantly, sites selected for this research are not areas where seepage was directly observed. Rather, cores were recovered from areas where seepage proxies were identified but flow rates were unknown.

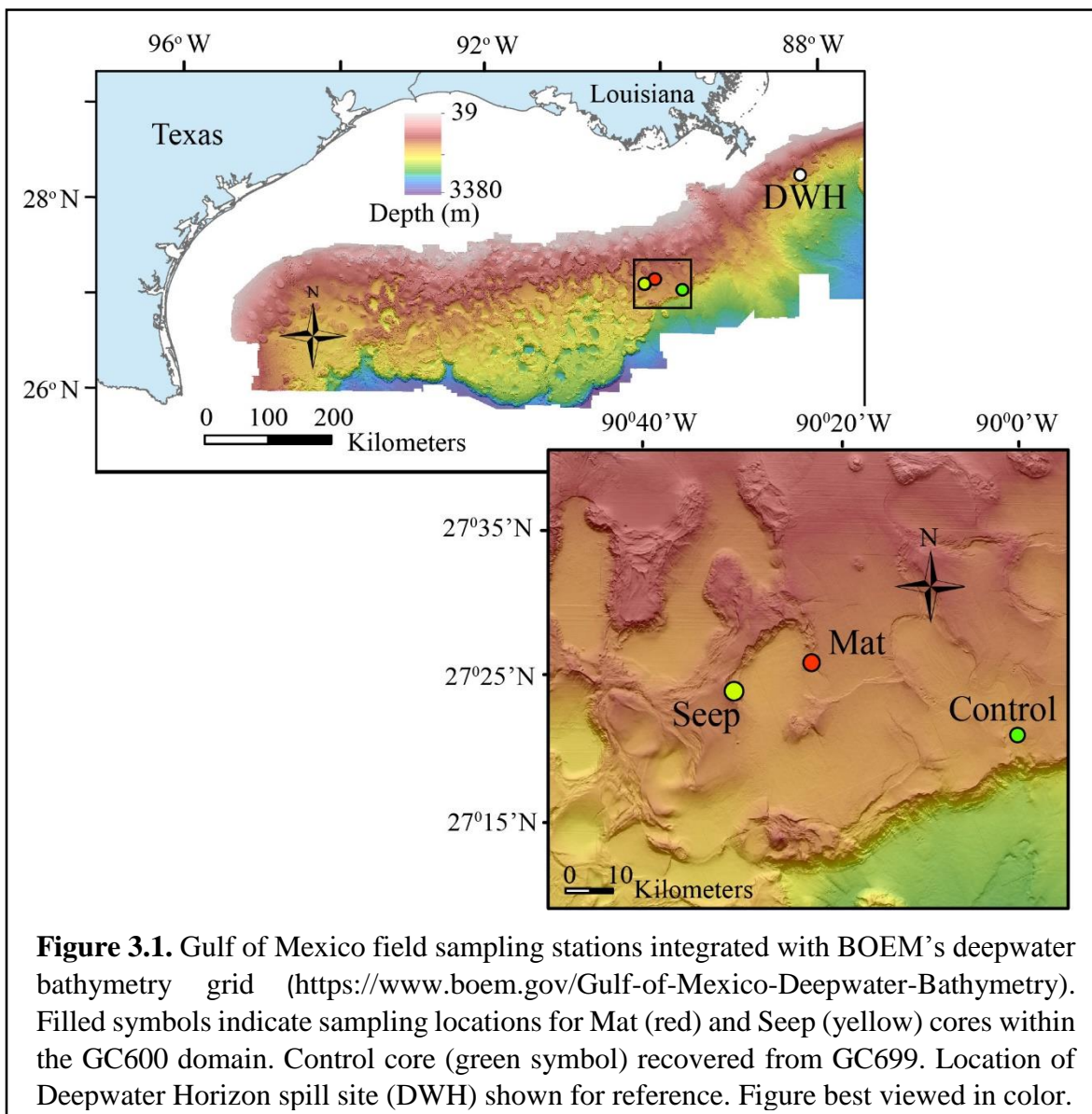
3.2.Methods

3.2.1. Gulf of Mexico Study Site

The Gulf of Mexico contains deep carbonate and salt deposits of Mesozoic age buried under significant sediment reserves which have contributed to salt fluidization resulting in diapirs and domes (Judd and Hovland, 2009). Salt tectonics has created fractures and faults often acting as many fluid migration pathways along which hydrocarbons, brine, and porefluid may be transported (Kennicutt et al., 1998). Migration of subsurface fluids towards the seafloor has resulted in extensive areas of natural hydrocarbon seepage with estimates of more than 19,000 individual seeps located within a region just offshore of Texas alone (Watkins and Worzel, 1978). The northern margin of the Gulf is especially active where free gas is a ubiquitous feature of shallow sediments with gas-charged sediment regions extending up to 500 m in length (Anderson and Bryant, 1990).

Throughout the Gulf of Mexico, deep-sea seeping fluids are ubiquitous in association with vestimentiferan tubeworms (Young et al., 1996), bathymodiolus mussels (Smith et al., 2000), and lucinid and vesicomycid clams (MacDonald et al., 1990). Here, community structure is dependent upon the availability of compounds necessary for chemosynthesis and as such the fluid flux from the subsurface determines the success of deep-water communities within the Gulf of Mexico (Judd and Hovland, 2009).

Because the GOM is characterized by expansive regions of active seafloor seepage, we recovered sediment cores from fluid exchange and near-by control sites as an opportunity to qualitatively test our vertical exchange model (Chapter 2). Sediment cores were recovered from three sites within the Gulf of Mexico (Figure 3.1) to serve as proof of concept for the vertical exchange model. Although submarine seepage throughout the Gulf of Mexico can be broadly classified by seep fluid chemistry (i.e., methane- or sulfide-rich) or discharge conduit (i.e., barite chimney or mud volcano), we consider seep sites to be distinct from our control site. In other words, we do not measure methane or sulfide concentrations, but rather target areas where visual indicators of seepage through soft sediments were present. Here, our control site is defined as lacking visual indications of seepage. Specifically, no water column density anomalies were detected here and no conspicuous microbial mat cover was observed upon visual inspection of the recovered sediment core.



Our seep sites are located within Green Canyon (GC) lease block 600 (GC600), a site of well documented natural hydrocarbon seepage (e.g., D'souza et al., 2016; Wang et al., 2016; Johansen et al., 2017). Regions of the GC600 seafloor have been described as being biologically and geologically complex, with massive cold seep carbonates, bacterial mats, gorgonians, cnidarians, vesicomycid clams, and vestimentiferan tubeworms identified (Roberts et al., 2010).

In contrast, our control site (Green Canyon lease block 699-GC699) is located 42 km and 55 km SE of Seep and Mat core recovery sites, respectively. The region has a similar maximum water depth ~1300 m and was targeted as a nearby control as no seepage indicators including microbial mat and acoustic water column density anomalies were identified during sampling and core recovery.

3.2.2. Core Collection and Sample Processing

Sediment cores were collected during research cruises aboard the *R/V Atlantis* (cruise AT26-13) in 2014 and aboard the *R/V Endeavor* (cruise EN586) in 2016. Two cores were obtained from distinct regions within GC600 where independent evidence of active fluid transport was observed ('Mat' and 'Seep' cores; Table 3.1). Samples were collected as pushcores using the *HOV Alvin* (Mat core) and also as multicores using a shipboard multiple core (Seep core and Control core). Push core tubes had a 6.4 cm inner-diameter and multiple core tubes had a 9.5 cm diameter inner-diameter. Subsamples for porosity and bulk density were placed in pre-weighed glass vials. Porosity was determined by mass loss upon drying and converted to a volumetric parameter using the bulk density determined by volume displacement (Lambe, 1951).

Porefluid was extracted and processed for ^{224}Ra following methods described in Chapter 2. In short, porefluids for ^{224}Ra analysis (Ra_i and Ra_r ; Equation 2.5) were extracted from sediment cores sectioned at 4 cm intervals following centrifugation at 5,000 RPM for 15 minutes and subsequent filtration through 0.45 μm syringe filters. Recovered porefluid was then passed twice over a 25 g aliquot of dry MnO_2 impregnated acrylic fiber to quantitatively adsorb dissolved Ra

(Moore, 1976; Moore, 2008). Fibers were rinsed and partially dried using a compressed air stream (Sun and Torgerson, 1998) and analyzed using a Radium Delayed Coincidence Counter (RaDeCC) as per Moore and Arnold (1996). Initial measurements were later corrected for dissolved ^{228}Th contributions (Moore, 2008). We determined aqueous equilibrium ^{224}Ra activities (R_{aq} ; Equation 2.5) by creating an experimental slurry using the original sediment sections from which porefluid was initially extracted. Slurries were retained in reaction flasks for three weeks with until terminations occurred following similar ^{224}Ra extraction methods to those described above.

Table 3.1. Metadata for sediment cores analyzed in for Chapter 3.

Core	Site	Collection year	Latitude, Longitude	Water depth (m)	*Porosity	[§] Bulk density (g cm ⁻³)
Mat	GC600	2014	27° 22.174' N, 90° 34.289' W	1225	**0.65 - 0.83	1.3 - 1.4
Seep	GC600	2014	27° 25.644' N, 90° 26.092' W	1203	**0.65 - 0.83	2.5 – 2.8
Control	GC699	2016	27° 17.499' N, 90° 02.425' W	1370	0.75 - 0.80	2.2 – 2.5

* Porosity is presented as a range throughout the core

** Taken as averages from sediment cores collected during a 2016 cruise from a similar GC600 location.

[§] Bulk density is presented as a range throughout the core

3.2.2.1. Core Descriptions

Mat core was collected through a white bacterial mat of *Beggiatoa sp.* (Figure 3.2) during *Alvin* dive 4691. The total core was 19 cm in length, with a white, fibrous microbial mat covering the sediment surface. The upper 2 cm appeared marbled black and tan and from 2 to 9 cmbsf, the sediments appeared dark brown with a few oily patches. The remaining sediments appeared tan with oil pockets. Evidence of oil occupying the interstitial pore spaces was confirmed using a UV

light and likely explains the unusually low bulk density of Mat core sediments (Table 3.1). A total of 0.24 L of overlying core-top water was recovered and immediately processed for dissolved ^{224}Ra .

Seep core was collected approximately 15 km west of Mat core (Figure 3.1). This region was of interest because water column acoustic (density) anomalies were detected from the ship-based multibeam sonar system suggesting active seepage (Figure 3.3). Seep core was collected central to the multibeam survey area and totaled 24 cm in length with the upper 4 cm appearing darker in color than the remaining sediments. Although no oily pockets were observed, a slight sheen and hydrocarbon odor was noted following centrifugation of sediments ca. 20 cmbsf. Overlying core-top water was recovered (0.95 L) and was immediately processed for dissolved ^{224}Ra .

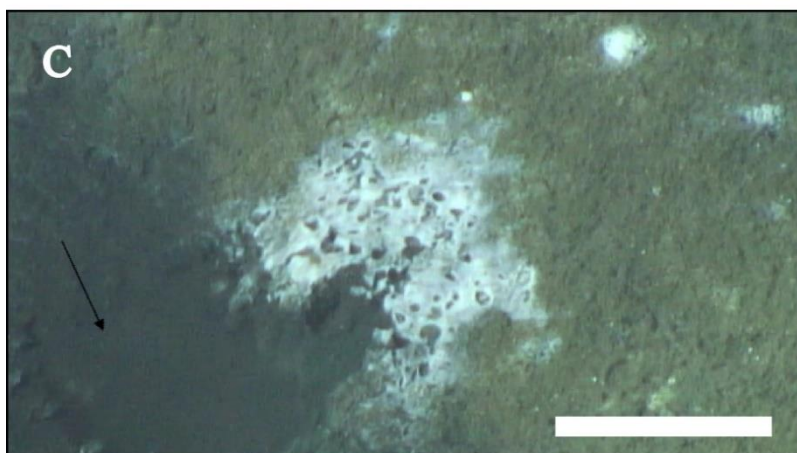
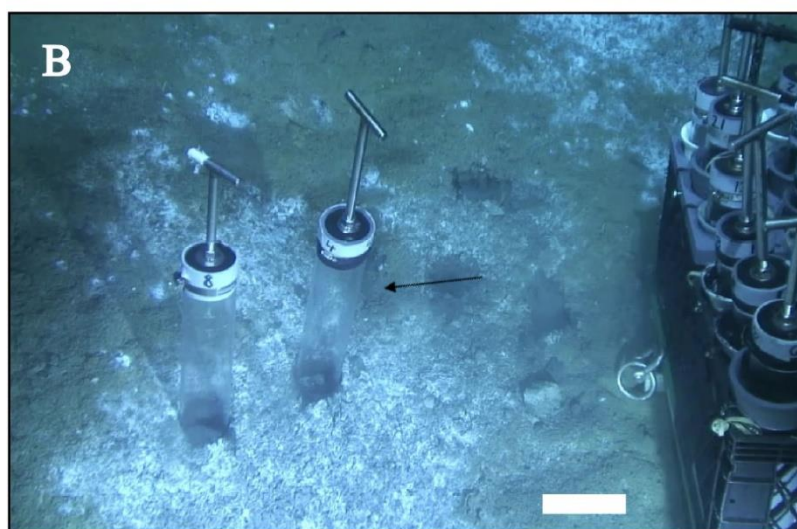
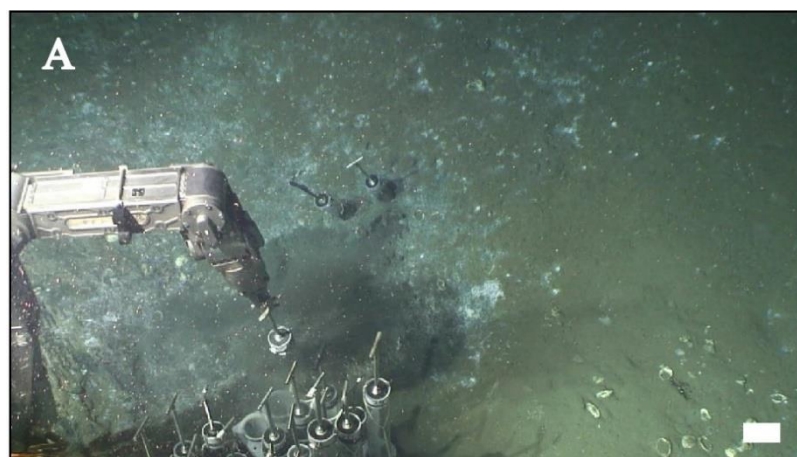
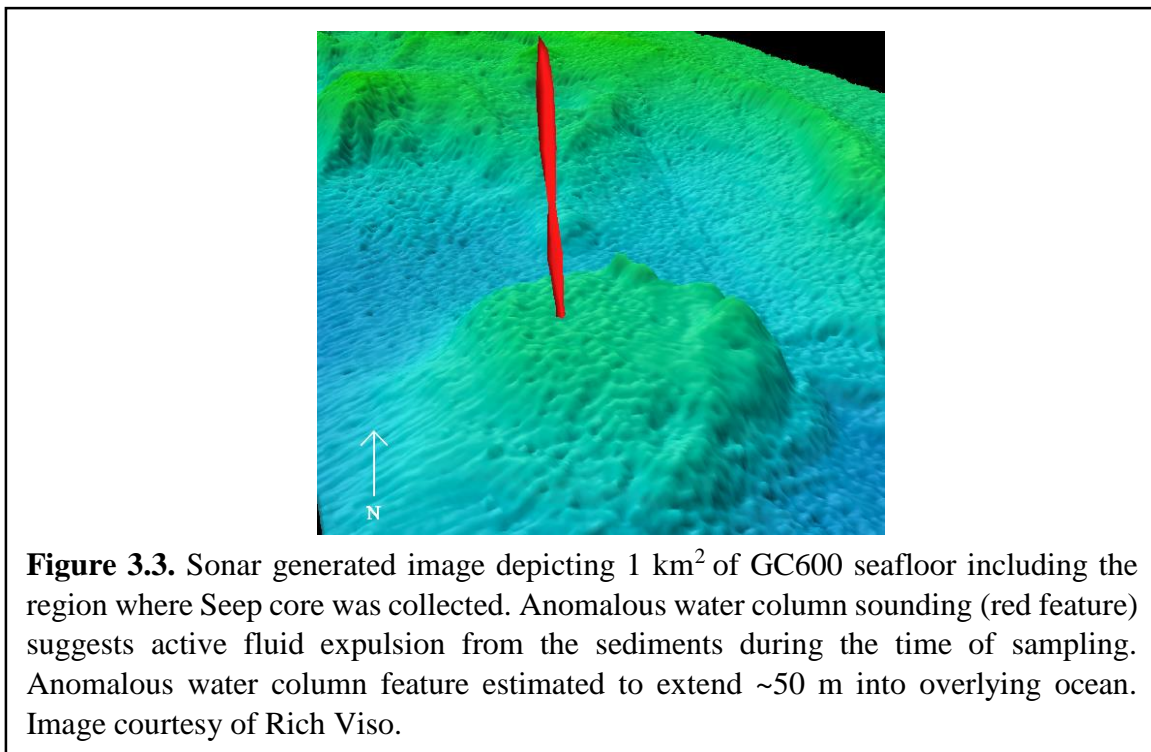


Figure 3.2. Sampling site of Mat core recovered from GC600. (A) Mat situated within a depression surrounded by olive-green sediments and shell hash. Arrows indicate (B) Mat core recovery site and (C) dark, reducing sediment exposed after sampling. Scale bars correspond to (A, B) 10 cm and (C) 5 cm.

We collected Control core where no independent indicators of active fluid seepage were present to understand how the vertical exchange model and advective ^{224}Ra flux estimates may apply to a variety of environmental conditions (Table 3.1). Control core totaled 64 cm in length and was notably distinct in color from Mat and Seep cores. Sediments appeared tan in color in contrast to the gray/black reducing sediments recovered from GC600. No obvious structural or color changes were observed upon recovery or processing of Control core. Sediment texture was also distinct in that material was much coarser than material typically retrieved from water depths >1000 m located hundreds of kilometers from shore. A total of 5.4 L of overlying core-top water was recovered. Notably, porosity increased modestly down core as compared to a more typical profile where fluid volume decreases with depth (e.g., Figure 2.3B; Table 3.1)



3.2.3. Advective Fluid Flux Calculations

We determine the effective fluid flux through sediments using the vertical exchange model developed in Chapter 2 and compare these results to vertical fluid transport rates independently estimated using a 1-dimensional advection-diffusion model. The arrangement of solutes in space can be explained by both a diffusive and advective property of transport. To separate these effects, we use a modified steady-state 1-dimensional advection-diffusion equation (Equation 3.1) based on Craig (1969) to determine the advective vertical velocity of fluid out of the sediments (into the overlying water). Assuming the only factors controlling ^{224}Ra activity in time are the generation and decay of ^{224}Ra , we rearrange the equation and solve for the advective vertical velocity (ω) in a given sediment layer (i) for upward fluid flow through sediments (+z):

$$\omega = \frac{\left[\frac{\left(\Phi_{i+1/2} D_{sed} \frac{C_{i+1} - C_i}{z_{i+1} - z_i} \right) - \left(\Phi_{i-1/2} D_{sed} \frac{C_{i-1} - C_i}{z_{i-1} - z_i} \right) + R_{net}(z)}{(z_{i+1} - z_{i-1})/2} \right]}{\frac{C_{i+1} - C_i}{z_{i+1} - z_i}} \quad (3.1)$$

where the index (i) increases with depth, Φ is porosity, C is the number of dissolved ^{224}Ra atoms in a layer of porefluid, D_{sed} is the effective diffusion coefficient (Equation 3.2), z is depth in cm below seafloor (cmbsf), and R_{net} is the difference between the production of ^{224}Ra into the water via sediment supply and the isotopic decay of ^{224}Ra . R_{net} is applied as an average over the interval $i-1/2$ to $i+1/2$. At radioactive equilibrium, R_{net} would equal 0. This approach can only be used if the sedimentary supply of ^{224}Ra source is constant in time, an assumption often applied when using Ra isotopes to estimate environmental transport times (Moore, 2000; Peterson et al., 2008). That

is, the production rate ^{224}Ra (by way of ^{228}Th decay) is constant. Fluid (and therefore ^{224}Ra) supply from horizontal transport is possible, but assumed minimal and is therefore not included in this calculation. This assumption is also applied in the vertical exchange model and is revisited in section 3.2 of this chapter.

The diffusion coefficient of ^{224}Ra through a semi-porous matrix (D_{sed}) is defined as (Boudreau 1997):

$$D_{sed} = \frac{D_{aq}}{1-2\ln(\Phi)} \quad (3.2)$$

where the molecular diffusion coefficient of Ra in an aqueous solution (D_{aq}) is constant and equal to $4.65 \times 10^{-10} \text{ m}^2 \text{ s}^{-1}$ at 5°C (Schulz 2000).

3.3. Results and Discussion

3.3.1. Porefluid Residence Time and Advective Transport

Porefluid contact time with sediments and ^{224}Ra transport rates were determined for three sediment cores collected from the Northern Gulf of Mexico. The presence of bacterial communities and acoustic water column density anomalies suggested active fluid transport out of the sediments at the Mat and Seep core sampling locations, respectively. Yet, these types of qualitative visual and geophysical evidence are not sufficient to quantify fluxes. As such, we seek to corroborate results from the vertical exchange model with qualitative data types, and also to determine an advective ^{224}Ra transport rate and associated fluid flux required to support estimated porefluid residence time.

3.3.1.1. Mat Core

Lush bacterial mats are relatively common overlying sediments within the GC region in concert with oil stained sediments (Figure 3.2; Sassen et al., 1993). *Beggiatoa* are dependent upon CO₂ generated by bacteria oxidizing seeping hydrocarbons and can even directly oxidize hydrocarbon products to fulfill energy needs (Nikolaus et al., 2003). Abundant mat-covered sediments are suggestive of active hydrocarbon seepage during the time of sampling (Joye et al., 2004). Although it has been suggested that mat color may be useful to categorize flow in a qualitative manner (e.g., diffusive or advective), mat color or size alone cannot be used to estimate fluid flux as porefluid geochemistry greatly controls mat success (Gilhooly et al., 2007).

Mat core was sectioned into four equal sediment sections of 129 cm³ from 0 to 16 cmbsf. An average porefluid volume of 33 ± 19 mL was recovered from each section after centrifugation. Dissolved porefluid ²²⁴Ra activities ranged from 2.0 ± 0.3 dpm L⁻¹ to 19.6 ± 1.3 dpm L⁻¹ with 2.3 ± 0.2 dpm L⁻¹ observed in the core-top water. Ra_{eq} values determined via laboratory incubations were greater than porefluid activities extracted from the sediment core and ranged from 36.2 ± 2.8 dpm L⁻¹ to 63.4 ± 3.2 dpm L⁻¹ (Figure 3.4A).

Model results suggest porefluid residence time within each 4 cm vertical section ranged from 0.4 ± 0.1 days to 2.6 ± 0.3 days with fluid transport possible in both directions for the shallow-most layer ($i = 2$ cm). For example, it is mathematically possible that Ra_i at 2 cmbsf could have been supplied by upward flow (assuming Ra_i at 6 cmbsf represents Ra_i) or downward flow (assuming overlying core-top water represents Ra_i). The vertical exchange model inherently assumes that production and decay of ²²⁴Ra are the only sources and sinks of radium influencing

our measurements. While we think this assumption is reasonable in the subsurface, it is very likely that dilution with ambient ocean water acts as an additional sink of ^{224}Ra in the overlying water. Thus, a solution assuming a downward flow of water into the sediments is almost always possible at the sediment-water interface using the core-top end-member as Ra_i with no way of objectively knowing how representative this result is in representing active fluid exchange. However, to conserve mass with respect to depth, it cannot be that this is actually occurring at Mat core where all other depths suggest radium and fluid transport direction is out of the sediments. For these reasons, residence time estimates assuming ^{224}Ra transport into the sediments for the shallow-most sediment layer are excluded from our analysis here and throughout.

We solve Equation 3.1 to estimate the advective transport rate required to support the vertical distribution of ^{224}Ra activities observed in Mat core porefluid. The average advective transport rate for each 4 cm section is estimated to be $7.2 \pm 2.4 \text{ cm day}^{-1}$ (Figure 3.5). These results suggest an advective term ($36.3 \text{ atoms cm}^{-3} \text{ day}^{-1}$) two orders of magnitude larger than the diffusive term ($0.2 \text{ atoms cm}^{-3} \text{ day}^{-1}$) of ^{224}Ra over the sampling interval. To compare this approach to estimate porefluid transport with results from the vertical exchange model, we divide our sampling interval by the average residence time of 0.6 ± 0.2 days for each 4 cm vertical section (Figure 3.4B).

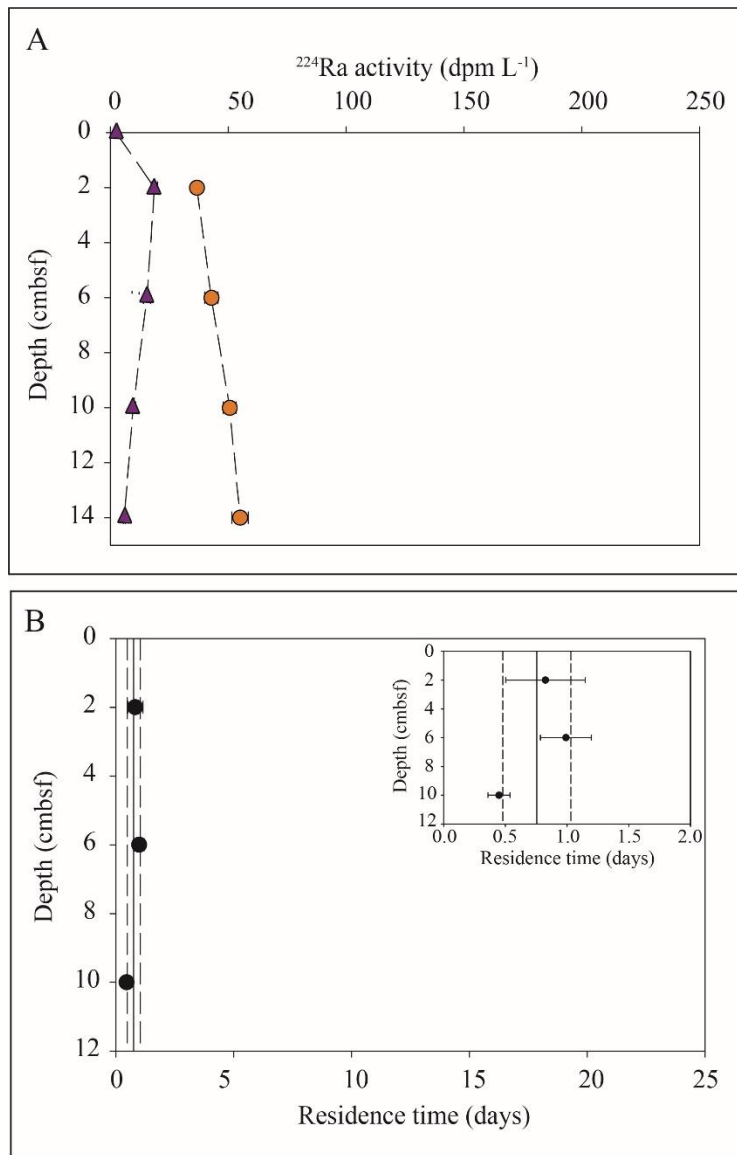


Figure 3.4. (A) Aqueous ^{224}Ra depth profiles measured at sea (R_{a_i} and R_{a_e} ; triangles) and at equilibrium ($R_{a_{eq}}$; circles) for Mat core. Error bars represent $\pm 1\sigma$ standard deviation of all estimates determined using standard propagation of error related to counting statistics of ^{224}Ra analysis. (B) Porefluid residence time where solutions were only possible imposing a +z transport direction. The solid line represent the depth-averaged mean and dashed lines illustrate the mean $\pm 1\sigma$ standard deviation. X-axis scales set to match those in Figures 3.6 and 3.7 to facilitate direct comparison.

This approach yields an identical average advective transport term of $7.2 \pm 2.4 \text{ cm day}^{-1}$ (Figure 3.5). While the depth averaged fluid transport rates are equal, the estimates generated via the vertical exchange model for any particular layer are often slightly greater than those determined via the advection-diffusion equation, although well within error or one another. Because the difference in flux estimates generated using the 1-d advection-diffusion equation and the vertical exchange model is well within our analytical error for each estimate, it would seem model results agree where advective transport dominates. Furthermore, the vertical exchange model is entirely dependent upon using disequilibrium to evaluate porefluid residence time. Similar velocities suggest R_{net} must dominate ω as determined via the 1-D advection-diffusion model. The similarity of these results is not surprising as both approaches consider the similar data, however when using the vertical exchange model, data from only two sediment sections is used at a time as compared to three with Equation 3.1. The similarity in rates as determined by the two approaches supports the assumption of vertical fluid transport (and therefore ^{224}Ra transport) over the sampled domain. Fluid transport rates are likely supported by exchange mechanisms specifically affecting shallow porewater and could be supplemented by a supply of more deeply sourced porewater transported by entirely separate mechanisms (see Figure 1.1). The time-scale associated with the fluid transport that ^{224}Ra and the vertical exchange model is sensitive to has been referred to as the ‘memory effect’ of the isotope (Rama and Moore, 1996). This idea was posited to explain fluid flow estimates which varied by an order of magnitude or more between estimates determined using different isotopes of radium (^{223}Ra , ^{224}Ra , ^{226}Ra , and ^{228}Ra ; Rama and Moore, 1996). Although the exact cause of these discrepancies appears to be unknown, fluid flow rates determined using short-lived radium isotopes (^{223}Ra , $T_{1/2}$

= 11.4 days and ^{224}Ra , $T_{1/2} = 3.6$ days) were observed to yield faster rates as compared to the longer lived isotopes (^{228}Ra $T_{1/2} = 5.8$ days and ^{226}Ra , $T_{1/2} = 1602$ years).

Interestingly, porefluid residence time in this core decreased with depth (Figure 3.4B). We suspect the decreased residence time with depth is due to the decreased porosity down core. Under a constant vertical velocity, a reduction in pore space would then lead to a reduced residence time. Upward ^{224}Ra transport through the sediments is shown consistently both implicitly via the vertical exchange model and explicitly via the 1-D advection-diffusion equation and suggests that a modest subsurface supply of porefluid and dissolved materials may explain the presence of mat covered sediments at this location.

Although porosity was not be measured directly for Mat core, but taken as an average using other GC600 sediment cores recovered from the region, it is likely that differences in porefluid volume recovered were a consequence of changing porosity (i.e., compaction) as the total volume of each mud sample remained constant. Within these porefluid samples, Ra_t values were consistently lower than corresponding Ra_{eq} values measured at similar porosities, suggesting that contact times were never long enough to achieve equilibrium within any particular sediment layer. Our ^{224}Ra -derived advective transport rates are consistent with the presence of mat-covered sediments as both suggest an active flow of materials out of the seafloor was occurring during collection.

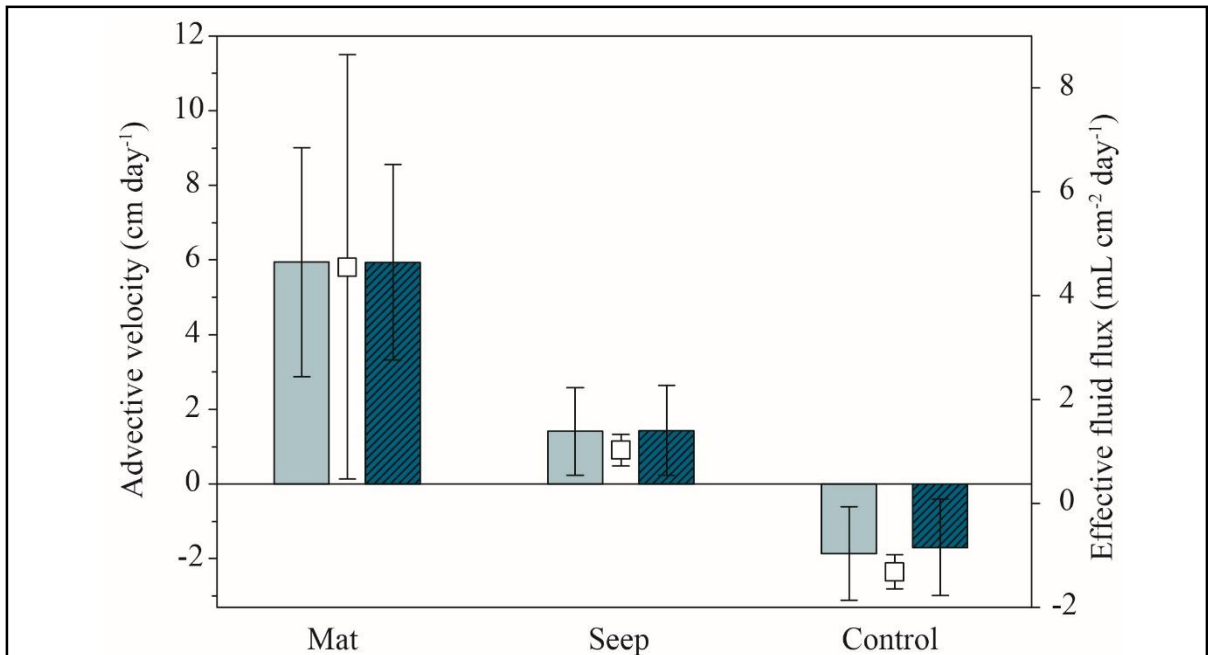


Figure 3.5. Mean advective velocities required to support aqueous interstitial porefluid ^{224}Ra distributions. Velocities are estimated using the 1-D advective transport equation (Equation 3.1; shaded bars) and by dividing our sampling interval by the porefluid residence time determined using the vertical exchange model (Equation 2.5; hatched bars). Effective fluid flux (open squares; right-hand Y-axis) is plotted for each core using contact times generated using the vertical exchange model, sampled area, and porosity (see section 3.2). Error bars represent $\pm 1\sigma$ standard deviation of estimates determined via standard propagation of error related to counting statistics for each ^{224}Ra term. Positive values indicate transport in the $+z$ direction (out of sediments) and negative values indicate transport in the $-z$ direction (into sediments).

3.3.1.2. Seep Core

Seep core was sectioned into six samples, each with a total mud volume of 285 cm^3 representing 4 cm thick sediment sections representing depths of 0 to 24 cmbsf. An average porefluid volume of $59 \pm 16 \text{ mL}$ was recovered from the six sediment samples and contained dissolved ^{224}Ra activities ranging from 14.3 ± 1.4 to $318.2 \pm 19.3 \text{ dpm L}^{-1}$ (Figure 3.6A). Within the core-top waters, dissolved ^{224}Ra activities were $1.1 \pm 0.1 \text{ dpm L}^{-1}$. Interestingly, Ra_{eq} values

ranged from 15.0 ± 0.8 to 73.5 ± 3.1 dpm L⁻¹ and were substantially lower than Ra_t values. This result suggests that, similar to Mat core, some mechanism was acting to maintain disequilibrium of porefluid ²²⁴Ra activities with sediment geochemistry. However, as our at-sea ²²⁴Ra activities were greater than Ra_{eq} , our observations were influenced by a source of ²²⁴Ra beyond parent production from host sediments. Regardless, porefluid residence time can be estimated via the at sea ²²⁴Ra activity returning to equilibrium in a net decay scenario (Figure 2.9B, Chapter 2).

Enrichments in our at sea observations of ²²⁴Ra may be related to hydrocarbons in the deepest section of the core. Peterson et al. (2013) noted the co-occurrence of ²²⁴Ra enrichments and elevated fluorometry values in the water column at GC600 and suggested seepage associated with hydrocarbons may be especially elevated in ²²⁴Ra. While this does not explain ²²⁴Ra activities associated with Mat core that contained abundant oil coated sediments, it is likely that site-specific geochemistry and porefluid source exert significant control on dissolved ²²⁴Ra activities and the presence or absence of hydrocarbons is not a reliable predictor of isotope activity. Nonetheless, the additional supply of ²²⁴Ra beyond the equilibrium activities supported by Seep core sediments can be used to quantify porefluid residence time via Equation 2.5.

Seep core porefluid contact times ranged from 0.9 ± 0.6 to 8.6 ± 1.3 days for each 4 cm sediment section, with an average of 4.2 ± 3.0 days (Figure 3.6B). Again, porefluid residence time decreased with increased depth below seafloor as porefluid volume and porosity decreased.

To evaluate the likelihood of active fluid transport being the mechanism that maintains porefluid residence time below 21 days, we applied Equation 3.1 to estimate a ²²⁴Ra-derived advective transport rate. For all layers, the observed ²²⁴Ra porefluid distribution could be explained by an advective transport out of the sediments at rates ranging from 3.8 to 0.5 cm day⁻¹ for each 4 cm section with an average of 1.7 ± 1.4 cm day⁻¹ (Figure 3.5). As was the case for Mat core, we

divided the sampling interval by our porefluid residence times generated via the vertical exchange model and again received identical results (average transport rate of $1.7 \pm 1.4 \text{ cm day}^{-1}$). Although specific layer solutions varied, again the average transport rate of ^{224}Ra (and porefluid) was equal for both approaches. While these approaches are based on the same observational data, their mathematical treatments are independent of each other, so the similarity in average core conditions provides confidence in the model results.

While the advective ^{224}Ra flux at Seep core is not as significant as that for Mat core, the advective component of transport (Equation 3.1) of $84.6 \text{ atoms cm}^{-3} \text{ day}^{-1}$ is still an order of magnitude larger than the radium diffusion term ($1.5 \text{ atoms cm}^{-3} \text{ day}^{-1}$). Although acoustic water column density anomalies may be used to identify bubble plumes (Pohlman et al., 2017), we did not directly sample the associated feature as no obvious indications of gas or oil enrichments were observed in the sediment column. It is not surprising that our transport estimates are considerably less than one might expect given the ancillary evidence of seepage. Because our approach to sample the seafloor feature (situated in $\sim 1200 \text{ m}$ water depth) utilized a shipboard multiple core deployment and recovery system, it is likely that we sampled across some ‘background sediment’ as opposed to entirely over the discharge area. However, the difference in vertical fluid velocities between Mat and Seep core is not beyond error (Figure 3.5). Either way, ^{224}Ra advective transport estimates independently support the suggestion of effluxing porefluid producing the large scale seepage identified via multibeam imaging and appear distinct from fluid flux estimates determined for Control core.

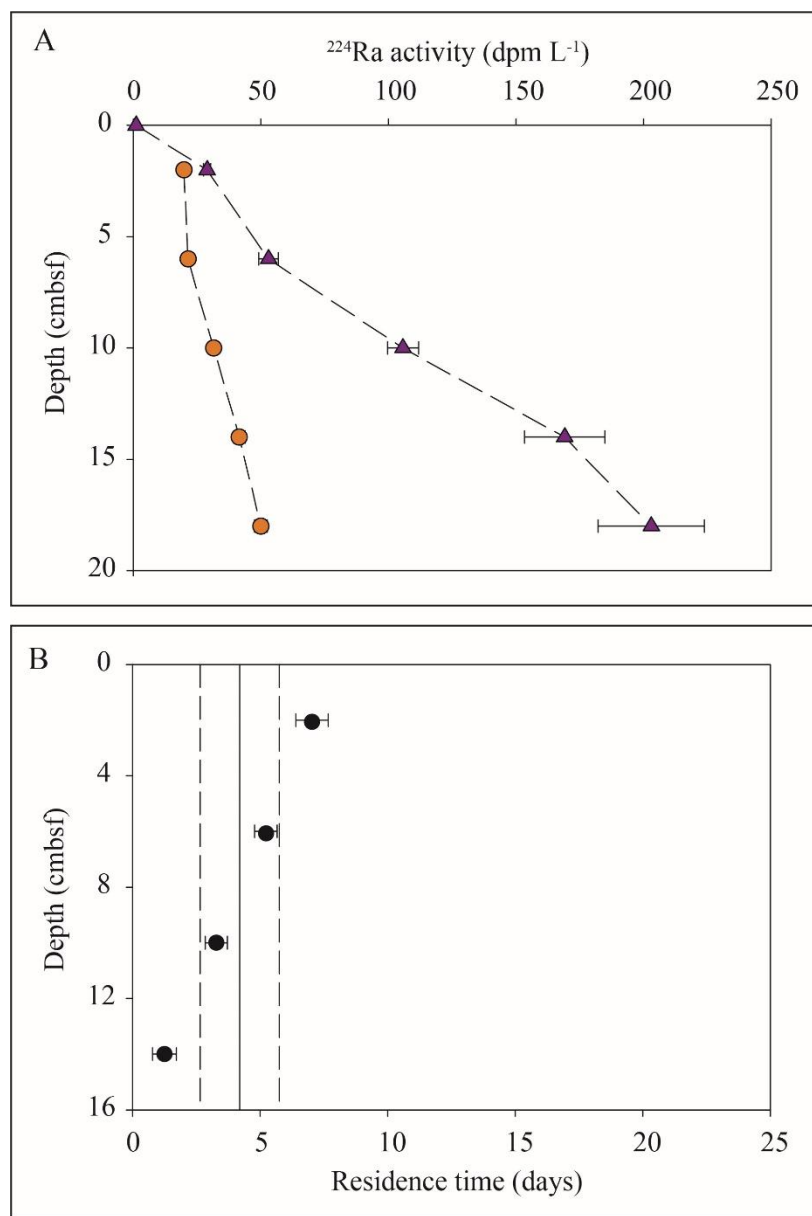


Figure 3.6. (A) Aqueous ^{224}Ra depth profiles measured at sea (Ra_i and Ra_t ; triangles) and at equilibrium (Ra_{eq} ; circles) for Seep core. Error bars represent $\pm 1\sigma$ standard deviation of all estimates determined using standard propagation of error related to counting statistics of ^{224}Ra analysis. (B) Porefluid residence time where solutions were only possible imposing a +z transport direction. The solid line represent the depth-averaged mean and dashed lines illustrate the mean $\pm 1\sigma$ standard deviation. Scales set to match those in Figures 3.4 and 3.7 to facilitate direct comparison.

3.3.1.3. Control Core

Control core was sectioned into nine sediment samples, each with a total volume of 285 cm³ representing 4 cm sections from 0 to 36 cmbsf. The core-top water recovered from Control core contained a dissolved ²²⁴Ra activity of 0.32 ± 0.03 dpm L⁻¹, and was an order of magnitude lower than overlying water at Mat core. An average porefluid volume of 70 ± 12 mL was recovered from nine sediment sections and contained dissolved ²²⁴Ra activities ranging from 4.6 ± 0.5 to 43.0 ± 4.3 dpm L⁻¹ (Figure 3.7A). Ra_{eq} estimates obtained via incubation experiments were, on average, a factor of 2 larger than those observed at-sea and ranged in activity from 9.4 ± 0.5 to 104.1 ± 5.4 dpm L⁻¹ where isotope activities at equilibrium were observed to increase with increased depth below the sediment water interface (0 to 36 cmbsf) and activities measured at-sea increased with increased depth below the SWI (0 to 14 cmbsf) until activities appear unrelated to depth circa 14 cmbsf.

Porefluid residence time estimated by imposing a +z (upward) transport direction resulted in a porefluid residence time of ≥ 21 days for the 0 to 4 cmbsf sediment sample whereas no solution was possible for greater depths below seafloor under this transport condition. This result is supported by the isotope activities recovered from the shallow porewater where the at-sea activity was observed to be nearly equal to the equilibrium activity indicating the residence time equal to or greater than the time required to generate radioactive equilibrium between dissolved ²²⁴Ra and the fraction of the ²²⁸Th parent required to support the radium. However, the at-sea activities decrease closer to the SWI. Because the equilibrium activity is still higher than the activities measured at-sea, production rate > decay rate and so a decrease of ²²⁴Ra must indicate a dilution of ²²⁴Ra in porewater by the transport of low end-member water (assuming all sinks have been

accurately constrained; Figure 3.7A). Assuming ^{224}Ra was transported downward ($-z$), porefluid residence time ranged from 1.6 ± 0.4 to 2.1 ± 0.3 days (Figure 3.7). Importantly, the residence time of interstitial porefluid recovered from Control core is often at or beyond our ability to determine for fluid transport occurring in the $+z$, but an average of 1.8 ± 0.4 days assuming transport of fluid was occurring down core. Due to the half-life and radioactive nature of our chosen proxy, the ^{224}Ra activity will not change after reaching equilibrium. We simply report this as a residence time greater than or equal to 21 days as we have no way of isotopically distinguishing a residence time of 21 days from anything > 21 days.

Layer specific residence times were converted into an advective transport rate required to sustain observed ^{224}Ra distributions. Using the 1-D advection/diffusion equation (Equation 3.1), we find that fluid transport and ^{224}Ra distribution is most influenced by the advective velocity ($1039.9 \text{ atoms cm}^{-3} \text{ day}^{-1}$) as compared to the mean diffusive term ($20.6 \text{ atoms cm}^{-3} \text{ day}^{-1}$) for Control core sediments. We find the average advective velocity as determined by Equation 3.1 to equal $-1.9 \pm 1.3 \text{ cm day}^{-1}$. For comparison, we divided our sampling interval by the residence time estimated for each 4 cm section (Equation 2.5) to yield an average vertical velocity of $-1.7 \pm 1.3 \text{ cm day}^{-1}$ (equivalent to an estimated total transport of $1468.4 \text{ atoms cm}^{-3} \text{ day}^{-1}$). For Control core, we identify fluid transport to be occurring in the $-z$ direction suggesting the dominant transport direction is into the sediments (from 0 to 14 cmbsf) (Figure 3.5).

Despite having observed similar Ra_{eq} for all three cores, differences in the Ra_t values resulted in unique solutions to residence times and advective porefluid transport rate and direction. For Control core, we suspect that having observed ^{224}Ra activities at equilibrium (i.e., $Ra_t = Ra_{eq}$) suggests that no significant advective transport mechanism was adding or removing ^{224}Ra to/from the interstitial inventory in the shallow most layer, however disequilibrium

observed at depth (below 4 cmbsf) could only be explained by a dilution of ^{224}Ra in porefluid. We estimate an average residence time of porefluid within each 4 cm section of 6.6 ± 0.3 days. While the average residence time of Control core porefluid is larger than the average identified for Mat and Seep cores, large error associated with Seep core suggests that the residence times obtained for Control and Seep core cannot be distinguished beyond error. However, it is noteworthy to mention that Control core was the only sediment core recovered where transport in the $-z$ was supported by the isotope data for any layers. While we do not expect that the isotopic disequilibrium supported by an apparent $-z$ transport direction for Control core porewater represents the fluid exchange condition for much of the Gulf of Mexico seafloor. Rather, we think this result can be supported by several proposed mechanisms acting to exchange fluids through shallow sediments, bioirrigation, bubble-driven exchange, topography driven exchange, and/or density driven exchange (Figure 1.1)

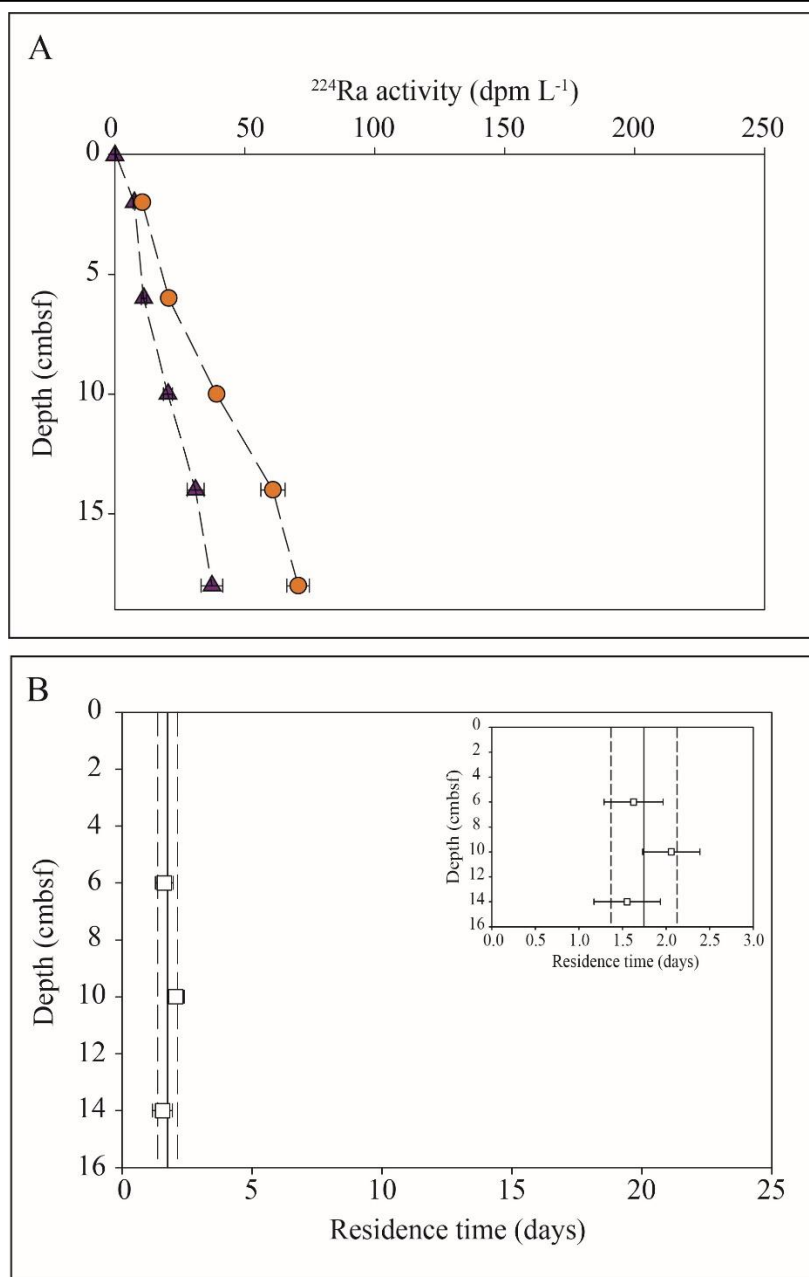


Figure 3.7. (A) Aqueous ^{224}Ra depth profiles measured at sea (Ra_i and Ra_t ; triangles) and at equilibrium (Ra_{eq} ; circles) for Control core. Error bars represent $\pm 1\sigma$ standard deviation of all estimates determined using standard propagation of error related to counting statistics of ^{224}Ra analysis. (B) Porefluid residence time assuming $-z$ transport direction where residence time estimated for 2 cmbsf equals 21 days assuming a $+z$ transport direction. Solid lines represent the depth-averaged mean while dashed lines illustrate the mean $\pm 1\sigma$ standard deviation. Scales set to match those in Figures 3.4 and 3.6 to facilitate direct comparison.

3.3.2. *Effective Fluid Fluxes*

Of the three cores analyzed, interstitial porefluid residence time was identified by applying a vertical exchange model (Equation 2.5) similar to that first described by Krest and Harvey (2003). We identified three regions where porefluid residence times were significantly less than 21 days within each 4 cm interval (0.6 days for Mat core and 4.2 days for Seep core and 6.6 days for Control core). Such short residence times must be maintained by a vertical transport rate of 5.9, 1.4 cm day⁻¹, and 1.7 cm day⁻¹, respectively. To estimate the volumetric rate of transport for our cold seep sites, we divide the porefluid volume in each sediment section by the estimated contact time. We thus estimate a rate of replacement that must be maintained to support the estimated sediment-water contact time over the volume of interstitial water present in each sediment section. The vertical volumetric fluid flux estimated for Mat core is greatest (150 ± 55 mL day⁻¹) compared to Seep core (71 ± 74 mL day⁻¹) and Control core (97 ± 60 mL day⁻¹). Assuming the entire surface area sampled is exchanging fluid evenly, we can normalize to the surface area sampled to estimate the volume of porefluid exchanged per cm² of seafloor for each region. By this approach, we can compare each core directly as the area sampled for Mat core was nearly half that of Seep and Control cores (32 cm² and 71 cm², respectively). Just as the estimated advective transport term was larger for Mat core, the volumetric flux per area of seafloor is greatest outward for Mat core (4.6 mL cm⁻² day⁻¹) and inward for Control core (-1.3 mL cm⁻² day⁻¹; Figure 3.5). This result is supported by the dissolved ²²⁴Ra activity measured in the core-top waters for each sample.

We observed the highest ²²⁴Ra activities in the overlying water of Mat core where the greatest rate of ²²⁴Ra supply was occurring (2.3 dpm L⁻¹; 178 mL day⁻¹), a moderate amount of

^{224}Ra in the core-top waters recovered from Seep core (1.1 dpm L^{-1} ; 84 mL day^{-1}), and the lowest was associated with Control core (0.3 dpm L^{-1} ; 97 mL day^{-1} —fluid influx to sediments) where the effective fluid flux to the overlying water was lowest. Although the amount of ^{224}Ra detected in the overlying water is likely influenced by more than just the ^{224}Ra supply rate (e.g., different amounts of mixing with lower activity ocean water), the measured ^{224}Ra within the core-top water does support the relative magnitude of fluid flux and flow direction estimated for each core.

Because the distribution of ^{224}Ra is redox sensitive, we oxidized all samples to enable comparison between field and laboratory results (see Chapter 2 for a more detail regarding the vertical exchange model and oxidation/reduction conditions). Although we were careful to avoid hypersaline porefluids in this assessment, black, reducing sediments are a common feature of cold seep systems such as those scattered throughout the GOM and often identified in very shallow sediments (Figure 3.2). Comparing dissolved ^{224}Ra activities generated from reducing sediments with those associated with the oxidized form of the same sediments could affect our residence time estimates as oxidized forms of Mn and Fe can be significant radium sinks (Beck and Cochran, 2013). Krest and Harvey (2003) applied a 1-D advection/diffusion model to estimate a single uniform ^{224}Ra production rate (similar to Ra_{eq}) to avoid potential redox complications associated with porefluid extraction.

Tamborski et al. (2017) used a similar approach to that here where sediment incubations were conducted to determine the equilibrium ^{224}Ra activity. However, in that work, K_D moderated production rates (Ra_{eq}) were optimized and treated as a constant following Krest and Harvey (2003). While such an assumption is reasonable, we observed an eleven-fold difference in the maximum exchangeable ^{224}Ra activity throughout Control core (Figure 3.7A). Even if redox controls moderated the absolute activity of exchangeable radium, the relative range remains

independent of this effect as all samples were handled identically. Regardless of how the production rate (Ra_{eq}) is applied, residence time may still be estimated, although site-specific considerations including geochemical heterogeneity may favor one approach over another.

It is important to address the inherent model assumption that radium transport (e.g., mass) is primarily vertical as a consequence of vertical fluid transport and geochemical processes illustrated in Figure 2.1. Although in-situ measurements by Solomon et al. (2008) suggest some horizontal fluid transport may occur at cold seep sites, flow was predominately occurring in the vertical direction. Vertical chemical and pressure gradients if not uniform in space or time, could promote horizontal gradients (which transport would act to remove), however sediment compaction makes the effect minimal and detection extremely unlikely (Lloyd et al., 2010) meaning advective vertical velocities are significantly larger than advective horizontal gradients. Furthermore, we compare our flow estimates to similar values from cold seep sites within the GOM that have an identified range of -161 to 273 cm yr^{-1} (Solomon et al., 2008). Similar to the convention applied here, negative values indicate flow into the sediments and positive values suggest outward, effluxing flow. For comparison, we identified rates of -679 to 2170 cm yr^{-1} . However, because the utility of ^{224}Ra and the vertical exchange model is restricted to processes causing radioactive disequilibrium (1 to 21 days), applying velocities identified here over yearly time-scales hardly seems appropriate. As implied by the conceptual diagram presented in Chapter 1 (Figure 1.1), our fluid flux and velocity estimates likely represent a composite result of multiple mechanisms including bioirrigation and tidal exchange which would not present as constant drivers of exchange over yearly time scales. Solomon et al. (2008) detailed a reversal in fluid flow direction after having observed persistent outward flow over hundreds of days near a gas vent in

the GOM. We believe this tool is useful for short-term flow conditions which may vary over hourly to daily scales but do not result in porefluid residence time in excess of 21 days.

Although seepage sites are known to exhibit temporal variability (Johansen et al., 2017), transport estimates in this study demonstrate the comparability of the geochemical vertical exchange model with in-situ detectors for sites of slow, diffuse flow. Well-studied sites within the GC600 region capable of generating persistent surface sheens exhibit transport rates on the order of hundreds of cubic meters per year (Johansen et al., 2017), roughly three orders of magnitude higher than the maximum rates identified in this work. Although Johansen et al. (2017) did not normalize to seepage area, it is known that the seepage face is no larger than 1 m² (Rick Peterson, personal communication). It is not surprising that subsurface fluid transport rates identified in this study are less than those occurring at sites of vigorous seepage capable of creating persistent oil sheens. Instead our effective fluid flux estimates appear closer to rates reported for other chemical proxy approaches used to estimate vertical transport rates (Torres et al., 2002; Lapham et al., 2008; Solomon et al., 2008).

While fluid transport rates over the sampled sediment surface appear modest, Larkin et al. (1994) noted GOM bacterial mat sizes to range from 0.02 to 100 m². Applying our volumetric porefluid flux estimate for Mat core (4.6 mL cm⁻² day⁻¹) across these areas suggests a range of 0.9 to 4,500 L of porefluid per day is discharged across the entire mat surface. Even more surprisingly, if we apply our volumetric porefluid flux determined for Seep core to the same range in area, we estimate 0.2 to 1,000 L of porefluid are discharged from uncolonized sediments each day. Although such upscaling may not be entirely accurate as our sampled area (from 3.2x10⁻³ to 7.1x10⁻³ m²) was an order of magnitude smaller than the smallest documented microbial mat size, it could provide useful boundary conditions for similar bacterial mats and deep-sea seepage

habitats. Notably, this work documents seepage rates associated with cold seep features and demonstrates that porefluid ^{224}Ra activities may be used in either a 1-D advection-diffusion equation (Equation 3.1) or this vertical exchange model (Equation 2.5) to estimate characteristics of porefluid transport.

The presented approach is effective over a range of fluid transport rates corresponding to porefluid residence times between 0.1 and 21 days over the sampling interval. Application of the vertical exchange model described throughout is related to site-specific parameters including mineral geochemistry, ^{224}Ra partition coefficients, sediment porosity, and sediment-porefluid contact time. Evaluating fluid flow via ^{224}Ra distributions may prove useful where existing methods are not appropriate because transport rates are too slow for detection via alternative methods. Although similar discharge rate estimates are available through chloride analyses (e.g., Lapham et al., 2008), such techniques are only useful in regions where porefluid chloride concentrations are supersaturated and may therefore limit application. Because hypersaline sites are often associated with the formation of barite, which serves as a dissolved radium sink (Aharon et al., 2001), the method described here should be used with caution or modified appropriately under such circumstances as we did not test the efficacy of the detailed approach in hypersaline environments. The vertical exchange model therefore extends the environments to determine fluid flow via geochemical proxy for deep-sea seepage systems.

3.4. Conclusions

Geochemical profiles of dissolved ^{224}Ra activities were examined relative to equilibrium ^{224}Ra activities to determine porefluid residence time for two cold seep sites and a control site. A vertical exchange model was applied to evaluate these residence times relative to a control core collected in the Gulf of Mexico. To explain the range in porefluid residence times throughout the sampling region, we estimate the advective transport rate required to support our observations.

Porefluid residence times suggest significant differences in the rates of subsurface fluid transport for collected sediment cores. The depth averaged residence time of 0.6 ± 0.2 days for each 4 cm section of sediment for a core collected through a bacterial mat (Mat core) was much less than that for Seep core (4.2 ± 3.0 days) where acoustic anomalies detected in the region suggested active seepage near the sample collection site. Both cold seep cores (Mat core and Seep core) recovered from GC600 had much lower porefluid residence times than that of porefluid recovered from Control core at site GC699 (mean = 6.6 ± 9.6 days for each 4 cm section).

An average advective transport term two orders of magnitude larger than that of the average diffusive term is required to explain dissolved ^{224}Ra distributions in Mat core ($36.3 \text{ atoms cm}^{-3} \text{ day}^{-1}$ as compared to $0.2 \text{ atoms cm}^{-3} \text{ day}^{-1}$). This result suggests that $4.6 \pm 4.1 \text{ mL cm}^{-2} \text{ day}^{-1}$ is supplied to the microbial mat each day and ultimately the overlying ocean. Comparatively, $1.0 \pm 0.3 \text{ mL}$ of porefluid per cm^2 of seafloor per day was supplied to the overlying water through Seep core sediments. Notably, no obvious microbial mat cover was present on Seep core sediments. Perhaps the absence of obvious microbial mat could be explained by the lower seepage rate estimated for Seep core as opposed to Mat core. However, because we did not measure any other

solute concentrations this could also be explained by the porefluid geochemistry or perhaps the material flux. It is also possible that the advective velocities associated with Mat and Seep cores are more similar than they appear considering the especially large error associated with Mat core velocities.

We compared porefluid flow estimates for samples recovered from GC600 to our Control core where porefluid residence time estimates and porefluid distributions of ^{224}Ra are best explained via vertical advective velocities acting in the $-z$ direction, ultimately transporting water into the sediments presumably from the overlying ocean. We estimate an average effective fluid flux of $-1.3 \pm 0.3 \text{ mL cm}^{-2} \text{ day}^{-1}$. Mechanisms to support fluid flow into the sediments over surficial sediment scales (decimeters) are shown in Figure 2.1 and can include bioirrigation as well as bubble, tidal, density, and topography driven exchange (Santos et al., 2012).

Results for our GC600 cores agree well with prior fluid flow estimates for similar diffuse seepage sites. Of the regions studied, porefluid transport rates are modest, but significant either in magnitude or composition relative to non-seep sediments such that seep sediments support significantly higher cell numbers as compared to non-seep sediments (Pop Ristova et al., 2015). Diverse seep communities often exist in a proximal region to outward fluid transport as defined by the seepage footprint. As such, lower transport rates of unique solutes may be of great significance to the dense ecological communities associated with cold seeps. Our vertical exchange model offers volumetric fluid flux estimates supported by visual evidence of seepage and control conditions with rates similar to those in the literature. As such, the work here qualitatively demonstrates the applicability of the vertical exchange model to determine an effective fluid flux.

3.5. References

- Aharon P., Van Gent D., Fu B., Scott L. M., 2001. Fate and effects of barium and radium-rich fluid emissions from hydrocarbon seeps on the benthic habitats of the Gulf of Mexico offshore Louisiana. OCS Study MMS 2001-004. Prepared by the Louisiana State University, Coastal Marine Institute. U.S. Department of the Interior, Minerals Management Service, Gulf of Mexico OCS Region, New Orleans, LA. 142.
- Anderson, A.L., Bryant, W.R., 1990. Gassy sediment occurrence and properties: Northern Gulf of Mexico. *Geo-Marine Letters* 10, 209–220. <https://doi.org/10.1007/BF02431067>
- Beck, A.J., Cochran, M.A., 2013. Controls on solid-solution partitioning of radium in saturated marine sands. *Marine Chemistry, Radium and Radon Tracers in Aquatic Systems* 156, 38–48. <https://doi.org/10.1016/j.marchem.2013.01.008>
- Boudreau, B.P., 1997. Diagenetic models and their implementation. Springer. 414.
- Bris, N.L., Arnaud-Haond S., Beaulieu S., Cordes E., Hilario A., Rogers A., van de Gaever S., Wantanabe H., 2016. Chapter 45. Hydrothermal vents and cold seeps. *The First Global Integrated Marine Assessment – World Oceans Assessment*.
- Cordes, E.E., Carney, S.L., Hourdez, S., Carney, R.S., Brooks, J.M., Fisher, C.R., 2007. Cold seeps of the deep Gulf of Mexico: Community structure and biogeographic comparisons to Atlantic equatorial belt seep communities. *Deep Sea Research Part I: Oceanographic Research Papers* 54, 637–653. <https://doi.org/10.1016/j.dsr.2007.01.001>
- Craig, H., 1969. Abyssal carbon and radiocarbon in the Pacific. *Journal of Geophysical Research*, 74 (23), 5491-5506.
- D'souza, N.A., Subramaniam, A., Juhl, A.R., Hafez, M., Chekalyuk, A., Phan, S., Yan, B., MacDonald, I.R., Weber, S.C., Montoya, J.P., 2016. Elevated surface chlorophyll associated with natural oil seeps in the Gulf of Mexico. *Nature Geoscience* 9, 215–218. <https://doi.org/10.1038/ngeo2631>
- Garcia-Pineda, O., MacDonald, I., Zimmer, B., Shedd, B., Roberts, H., 2010. Remote-sensing evaluation of geophysical anomaly sites in the outer continental slope, northern Gulf of Mexico. *Deep Sea Research Part II: Topical Studies in Oceanography* 57, 1859–1869. <https://doi.org/10.1016/j.dsr2.2010.05.005>
- Gilhooly, W.P., Carney, R.S., Macko, S.A., 2007. Relationships between sulfide-oxidizing bacterial mats and their carbon sources in northern Gulf of Mexico cold seeps. *Organic Geochemistry, on the forefront of terrestrial and marine organic geochemistry: A tribute to John I. Hedges* 38, 380–393. <https://doi.org/10.1016/j.orggeochem.2006.06.005>
- Johansen, C., Todd, A.C., MacDonald, I.R., 2017. Time series video analysis of bubble release

- processes at natural hydrocarbon seeps in the Northern Gulf of Mexico. *Marine and Petroleum Geology* 82, 21–34. <https://doi.org/10.1016/j.marpetgeo.2017.01.014>
- Joye, S.B., Boetius, A., Orcutt, B.N., Montoya, J.P., Schulz, H.N., Erickson, M.J., Lugo, S.K., 2004. The anaerobic oxidation of methane and sulfate reduction in sediments from Gulf of Mexico cold seeps. *Chemical Geology* 205, 219–238. <https://doi.org/10.1016/j.chemgeo.2003.12.019>
- Judd, A., Hovland, M., 2009. *Seabed fluid flow: the impact on geology, biology and the marine environment*. Cambridge University Press.
- Judd, A.G., Hovland, M., Dimitrov, L.I., Gil, S.G., Jukes, V., 2002. The geological methane budget at Continental Margins and its influence on climate change. *Geofluids* 2, 109–126. <https://doi.org/10.1046/j.1468-8123.2002.00027.x>
- Kennicutt, M., Brooks, J., Bidigare, R., Denoux, G.J., 1988. Gulf of Mexico hydrocarbon seep communities—I. Regional distribution of hydrocarbon seepage and associated fauna. *Deep Sea Research Part A. Oceanographic Research Papers*. 35. 1639-1651. 10.1016/0198-0149(88)90107-0.
- Krest, J.M., Harvey, J.W., 2003. Using natural distributions of short-lived radium isotopes to quantify groundwater discharge and recharge. *Limnology and Oceanography* 48, 290–298. <https://doi.org/10.4319/lo.2003.48.1.0290>
- Lambe, T.W., 1951. *Soil testing for engineers*. Series in Soil Engineering, Wiley.
- Lapham, L.L., Alperin, M., Chanton, J., Martens, C., 2008. Upward advection rates and methane fluxes, oxidation, and sources at two Gulf of Mexico brine seeps. *Marine Chemistry* 112, 65–71. <https://doi.org/10.1016/j.marchem.2008.06.001>
- Larkin, J., Henk, M.C., Aharon, P., 1994. *Beggiatoa* in microbial mats at hydrocarbon vents in the Gulf of Mexico and warm mineral springs, Florida. *Geo-Marine Letters* 14:2-3, 97-103. <https://doi.org/10.1007/BF01203720>
- Lloyd, K.G., Albert, D.B., Biddle, J.F., Chanton, J.P., Pizarro, O., Teske, A., 2010. Spatial structure and activity of sedimentary microbial communities underlying a *Beggiatoa* spp. mat in a Gulf of Mexico hydrocarbon seep. *PLoS ONE* 5, e8738. <https://doi.org/10.1371/journal.pone.0008738>
- MacDonald, I. 2011. Remote sensing and sea-truth measurements of methane flux to the atmosphere (HYFLUX project) National Energy Technology Laboratory, Department of Energy, United States, Final Report, 85 pages, 85 appendices. <https://doi.org/10.2172/1041004>
- MacDonald, I.R., Guinasso, N.L. Jr., Reilly, J.F., Brooks, J.M., Callender, W.R., Gabrielle, S.G.,

1990. Gulf of Mexico hydrocarbon seep communities: VI. Patterns in community structure and habitat. *Geo-Marine Letters* 10, 244-252.
- Macelloni, L., Brunner, C.A., Caruso, S., Lutken, C.B., D'Emidio, M., Lapham, L.L., 2013. Spatial distribution of seafloor bio-geological and geochemical processes as proxies of fluid flux regime and evolution of a carbonate/hydrates mound, northern Gulf of Mexico. *Deep Sea Research Part I: Oceanographic Research Papers* 74, 25–38. <https://doi.org/10.1016/j.dsr.2012.12.006>
- Moore, W.S., 1976. Sampling ^{228}Ra in the deep ocean. *Deep-Sea Research* 23, 647-651.
- Moore, W.S., 2000. Ages of continental shelf waters determined from ^{223}Ra and ^{224}Ra . *Journal of Geophysical Research*. 105:C9, 22117-22122.
- Moore, W.S., 2008. Fifteen years experience in measuring ^{224}Ra and ^{223}Ra by delayed-coincidence counting. *Marine Chemistry, Measurement of Radium and Actinium Isotopes in the marine environment* 109, 188–197. <https://doi.org/10.1016/j.marchem.2007.06.015>
- Moore W.S., Arnold R., 1996. Measurement of ^{223}Ra and ^{224}Ra in coastal waters using a delayed coincidence counter. *Journal of Geophysical Research: Oceans* 101, 1321–1329. <https://doi.org/10.1029/95JC03139>
- Nikolaus, R., Ammerman, J., MacDonald, I., 2003. Distinct pigmentation and trophic modes in *Beggiatoa* from hydrocarbon seeps in the Gulf of Mexico. *Aquatic Microbial Ecology* 32, 85–93. <https://doi.org/10.3354/ame032085>
- Osborne, M., Swarbrick, R., 1997. Mechanisms for generating overpressure in sedimentary basins: A reevaluation. *Aapg Bulletin* 81, 1023–1041.
- Paull C., Hecker B., Commeau R., Freeman-Lynde R., Neumann C., Corso W., Golubic S., Hook J., Sikes E., Curray J., 1984. Biological communities at the Florida Escarpment resemble hydrothermal vent taxa. *Science* 226, 965-967.
- Pohlman, J.W., Greinert, J., Ruppel, C., Silyakova, A., Vielstädte, L., Casso, M., Mienert, J., Bünz, S., 2017. Enhanced CO_2 uptake at a shallow Arctic Ocean seep field overwhelms the positive warming potential of emitted methane. *PNAS* 201618926. <https://doi.org/10.1073/pnas.1618926114>
- Pop Ristova, P., Wenzhöfer, F., Ramette, A., Felden, J., Boetius, A., 2015. Spatial scales of bacterial community diversity at cold seeps (Eastern Mediterranean Sea). *The ISME Journal* 9, 1306–1318. <https://doi.org/10.1038/ismej.2014.217>
- Peterson, R.N., Burnett, W.C., Taniguchi, M., Chen, J., Santos, I.R., Ishitobi, T., 2008. Radon and radium isotope assessment of submarine groundwater discharge in the Yellow River

- delta, China. *Journal of Geophysical Research* 113.
<https://doi.org/10.1029/2008JC004776>
- Peterson, R.N., Viso, R.F., MacDonald, I.R., Joye, S.B., 2013. On the utility of radium isotopes as tracers of hydrocarbon discharge. *Marine Chemistry, Radium and Radon Tracers in Aquatic Systems* 156, 98–107. <https://doi.org/10.1016/j.marchem.2013.02.008>
- Roberts, H., Carney, R., 1997. Evidence of episodic fluid, gas, and sediment venting on the northern Gulf of Mexico continental slope. *Economic Geology* 92, 863–879.
<https://doi.org/10.2113/gsecongeo.92.7-8.863>
- Roberts, H.H., Shedd, W., Hunt, J., 2010. Dive site geology: DSV ALVIN (2006) and ROV JASON II (2007) dives to the middle-lower continental slope, northern Gulf of Mexico. *Deep Sea Research Part II: Topical Studies in Oceanography* 57, 1837–1858.
<https://doi.org/10.1016/j.dsr2.2010.09.001>
- Sassen, R., Roberts, H.H., Aharon, P., Larkin, J., Chinn, E.W., Carney, R., 1993. Chemosynthetic bacterial mats at cold hydrocarbon seeps, Gulf of Mexico continental slope. *Organic Geochemistry* 20, 77–89. [https://doi.org/10.1016/0146-6380\(93\)90083-N](https://doi.org/10.1016/0146-6380(93)90083-N)
- Schulz, H.D., 2000. Quantification of early diagenesis: dissolved constituents in marine pore water. In: Schulz and Zabel (Eds). *Marine Geochemistry*
- Smith, E.B., Scott, K.M., Nix, E.R., Korte, C., Fisher, C.R., 2000. Growth and condition of seep mussels (*bathymodiolus Childressi*) at a Gulf of Mexico brine pool. *Ecology* 81, 2392–2403. [https://doi.org/10.1890/0012-9658\(2000\)081\[2392:GACOSM\]2.0.CO;2](https://doi.org/10.1890/0012-9658(2000)081[2392:GACOSM]2.0.CO;2)
- Solomon, E.A., Kastner, M., Jannasch, H., Robertson, G., Weinstein, Y., 2008. Dynamic fluid flow and chemical fluxes associated with a seafloor gas hydrate deposit on the northern Gulf of Mexico slope. *Earth and Planetary Science Letters* 270, 95–105.
<https://doi.org/10.1016/j.epsl.2008.03.024>
- Suess, E., 2014. Marine cold seeps and their manifestations: geological control, biogeochemical criteria and environmental conditions. *International Journal of Earth Sciences* 103, 1889–1916. <https://doi.org/10.1007/s00531-014-1010-0>
- Sun, Y., Torgersen, T., 1998. The effects of water content and Mn-fiber surface conditions on ^{224}Ra measurement by ^{220}Rn emanation. *Marine Chemistry* 62, 299–306.
[https://doi.org/10.1016/S0304-4203\(98\)00019-X](https://doi.org/10.1016/S0304-4203(98)00019-X)
- Talukder, A.R., 2012. Review of submarine cold seep plumbing systems: leakage to seepage and venting: Seeps plumbing system. *Terra Nova* 24, 255–272.
<https://doi.org/10.1111/j.1365-3121.2012.01066.x>
- Tamborski, J.J., Cochran, J.K., Bokuniewicz, H.J., 2017. Application of ^{224}Ra and ^{222}Rn for

- evaluating seawater residence times in a tidal subterranean estuary. *Marine Chemistry* 189, 32–45. <https://doi.org/10.1016/j.marchem.2016.12.006>
- Torres, M.E., McManus, J., Hammond, D.E., de Angelis, M.A., Heeschen, K.U., Colbert, S.L., Tryon, M.D., Brown, K.M., Suess, E., 2002. Fluid and chemical fluxes in and out of sediments hosting methane hydrate deposits on Hydrate Ridge, OR, I: Hydrological provinces. *Earth and Planetary Science Letters* 201, 525–540. [https://doi.org/10.1016/S0012-821X\(02\)00733-1](https://doi.org/10.1016/S0012-821X(02)00733-1)
- Teske, A., de Beer, D., McKay, L.J., Tivey, M.K., Biddle, J.F., Hoer, D., Lloyd, K.G., Lever, M.A., Røy, H., Albert, D.B., Mendlovitz, H.P., MacGregor, B.J., 2016. The Guaymas Basin hiking guide to hydrothermal mounds, chimneys, and microbial mats: complex seafloor expressions of subsurface hydrothermal circulation. *Frontiers in Microbiology* 7. <https://doi.org/10.3389/fmicb.2016.00075>
- Wang, B., Socolofsky, S.A., Breier, J.A., Seewald, J.S., 2016. Observations of bubbles in natural seep flares at MC 118 and GC 600 using in situ quantitative imaging: Quantitative Imaging of Natural Seeps. *Journal of Geophysical Research: Oceans* 121, 2203–2230. <https://doi.org/10.1002/2015JC011452>
- Watkins, J.S., Worzel, J.L., 1978. Serendipity gas seep area, south Texas offshore. *American Association of Petroleum Geologists (Bulletin)* 62, 1067-1074.
- Young, C.M., Vázquez, E., Metaxas, A., Tyler, P.A., 1996. Embryology of vestimentiferan tube worms from deep-sea methane/sulphide seeps. *Nature* 381, 514–516. <https://doi.org/10.1038/381514a0>

CHAPTER 4

SPATIAL ASSOCIATIONS BETWEEN FLUID FLUX, TEMPERATURE, AND MICROBIAL MAT IN GUAYMAS BASIN

4.1. Introduction

Submarine seeps represent a unique network of ecological oases that are sustained by a supply of highly concentrated reduced compounds which support chemosynthesis (Orcutt et al., 2011). Seep communities are almost exclusively dependent upon the conversion of inorganic compounds into organic carbon (Nelson et al., 1989). While much remains to be understood about seep biota, submarine seeps are regarded as one of the most diverse biomes on Earth (Takai and Nakamura, 2010) with an average of 25 new species having been discovered annually from 2002 to 2010 (Bris et al., 2016). Seeps support functionally distinct chemosynthetic communities and generate higher levels of biomass than any other bathypelagic environment (Schuster, 2008). To date, scientists largely agree the biological oases associated with submarine seeps are highly endemic with common heritage at the family, genus, and species level (Kiel, 2009). Such relatedness suggests a feature common to cold and hydrothermal seepage environments is present (e.g. flow rate, seepage geochemistry). Despite the known dependency of endemic seep communities on the supply of reduced compounds via seeping fluids, the magnitude of fluid fluxes across a variety of geobiologic environments remains one of the least understood components of these systems (Suess, 2014).

Microbial life associated with submarine seeps not only supports an entire higher order ecosystem, but also acts to moderate the quantity and speciation of solutes transported into the overlying ocean. Bacterial communities often exploit unique seepage products to fix carbon dioxide and to oxidize methane and other hydrocarbons (Nelson et al., 1989; Teske et al., 2014). For seeps driven by high temperature convection associated with plate rifting and hydrothermal circulation, microbial community structure is influenced both by thermal tolerance as well as carbon and energy supply (Holler et al., 2011; Dowell et al., 2016; McKay et al., 2016). In fact, species richness has been shown to decline with increasing temperatures with an upper limit on life reported at 122°C (Clark, 2014) suggesting these hydrothermal communities are dependent upon a precarious balance between thermal driven flow, geochemistry, temperature, and survival.

Guaymas Basin is one of only a few modern rift systems that contain significant sediment deposits above magmatic intrusions, the heat from which drives fluid circulation through the subsurface and supports seep communities (Garfunkel et al., 1981; Gieskes et al., 1982). Here, conspicuous microbial mat forming colonies dominated by giant *Beggiatoa spp.* are found in areas of seepage emanation (Guendersen et al., 1992). Bacterial mats may thus provide a qualitative seepage indicator, as spatial distributions of *Beggiatoa spp.* have been linked to elevated sediment surface temperatures averaging 8 to 12°C as compared to bare sediment (3 to 4°C) (McKay et al., 2012).

Few attempts have been made to convert qualitative seepage indications like the observed presence of microbial mat into quantitative flow estimates in Guaymas Basin. In the nearly 40 year history of Guaymas Basin research, hydrothermal fluid transport investigations have involved heat flow surveys, distributions of helium-3 and manganese, and transfer estimates of water and carbon resulting from the initial doleritic sill intrusion (Teske et al., 2016). Deep-tow heat flow surveys

conducted in the area estimated basin-wide (~4 by 8 km survey area including 128 survey lines across the southern trough) low-temperature seepage velocities may range from $1 \times 10^{-8} \text{ m s}^{-1}$ to $15 \times 10^{-8} \text{ m s}^{-1}$ (Fisher and Becker, 1991). While the resolution of these efforts is much too coarse to identify spatial relationships between fluid flux and specific microbial mats, they provide important constraints on expected seepage rates for regions within the southern trough of the Guaymas Basin seafloor depression (Figure 4.1). Given that *Beggiatoa spp.* are dependent upon active seepage and are spatially linked to high subsurface temperatures (McKay et al., 2016), it would seem then that fluid flux may be a critical component to support these chemosynthetic colonies. While it is accepted that an advective flow of sulfide is needed to sustain dense (several cm thick) mat dominated by *Beggiatoa* (Gundersen, et al., 1992), such spatial associations identified by McKay et al. (2016) would suggest fluid flux could be at least equally as important in predicting mat presence as porefluid geochemistry could be.

Beggiatoa appear as the visually dominant species forming microbial mats around deep-sea submarine seepage habitats (Bernhard et al., 2000). *Beggiatoa* color has been observed to vary from orange to yellow to white filaments with orange filaments often occupying the central mat space (Teske et al., 2016). Microbial mats within Guaymas Basin often contain both orange and white filaments within a single conspicuous sediment cover feature. Evidence suggests orange *Beggiatoa* (*Candidatus* Maribeggiatoa) are distinct from white filaments by the abundance of an orange cytochrome and proteomic evidence of possible sulfide oxidation with nitrate as the electron receptor (MacGregor et al., 2013b). Although curious spatial distinctions between mat and non-mat covered sediments as well as white and orange mat zonation have been observed, a pure culture has yet to be obtained and so the physiological role of the distinction remains speculative but possibly related to carbon dioxide, oxygen, sulfide, and hydrocarbon content

(MacGregor et al., 2013a). Although mat color has been spatially associated with subsurface temperature gradients (McKay et al., 2012), it remains undocumented as to how vertical volumetric fluid flux, mat presence, and subsurface temperature characteristics are spatially associated in Guaymas Basin sediments.

In this chapter, we seek to constrain rates of fluid flux associated with specific microbial mats dominated by orange and white *Beggiatoa* to determine whether fluid flux and mat presence in Guaymas Basin are spatially associated as was first suspected by Guendersen et al. (1992). The quantification of fluid fluxes over spatial scale similar to discrete microbial mat colonies of ~1m (estimated by personal observation) in this region represents a novel contribution of this work. We expand on observations first made by McKay et al. (2012) who evaluated spatial relationships between microbial mat color and elevated subsurface temperature. By comparing effective fluid flow direction and magnitude across categories of sediment cover and subsurface thermal gradient, we seek to identify relationships between mat color and quantitative fluid flux estimates as determined by our geochemical exchange model (Equation 2.5). To date, it is known that orange *Beggiatoa* are spatially related to larger subsurface temperature gradients than white filaments; yet, it remains unknown whether thermal gradients are the associated with the dominant flow mechanism and therefore may be used to qualitatively estimate fluid flux magnitude.

Conceptual models have suggested that food-web complexity and species richness decreases with increasing hydrothermal discharge velocities in Guaymas Basin (Portail et al., 2016). The basis of this assertion is derived from porefluid methane concentrations used as a proxy for seepage intensity (Portail et al., 2016). In a broader sense, highest biomass concentrations associations with low-temperature, diffuse flow is a common observation among hydrothermal systems (German et al., 2011). These sites are not only biologically unique, but cooler temperature

seepage, presumably at off-axial sites, is thought to support 90% of the total mass flux from hydrothermal systems globally (Orcutt et al., 2011). Therefore, the development of a tool to evaluate diffuse, low-temperature seepage rates would be broadly applicable beyond Guaymas Basin.

4.2. Methods

Our sampling approach focuses on shallow sections of deep-sea sediments to quantify rates of fluid flow through a variety of sites associated with hydrothermal activity and microbial mats. We utilize geochemical characteristics to quantify fluid flow across shallow sediments and consider how these rates may relate to regional biogeography. For this assessment, we focus primarily on three factors: (1) presence of visual bacterial colonization; (2) porefluid and related sedimentary geochemistry; and (3) subsurface temperature. The following sections describe our approach to quantifying essential factors for understanding linkages between fluid flux magnitude and bacterial mat characteristics.

4.2.1. Site and Core Descriptions

Guaymas Basin is the largest submarine depression located along the boundary between the Pacific and North American plates and is thought to have formed during the late Miocene (~10 million years before present; Miller and Lizarralde, 2013). Guaymas Basin has two distinct sub-basins (Figure 4.1). The northern trough is characterized by a relatively shallow doleritic intrusion with associated hydrothermal fluids having temperatures $<200^{\circ}\text{C}$, whereas the southern trough is

marked by a much larger igneous intrusion at greater subsurface depths into terrigenous sediments causing hydrothermal temperatures in excess of 300°C (Gieskes et al., 1982). In both regions, borehole studies reveal that porefluid chemistry at depths greater than ~180 m is similar to hydrothermal vent water emanating from mid-ocean ridge environments (Gieskes et al., 1982). Above the subsurface sill, a significantly decreased porosity, the presence of pyrite and k-feldspar minerals, and porefluid geochemical constituents all suggest that contact metamorphism drives upward flow of interstitial water (Gieskes et al., 1982).

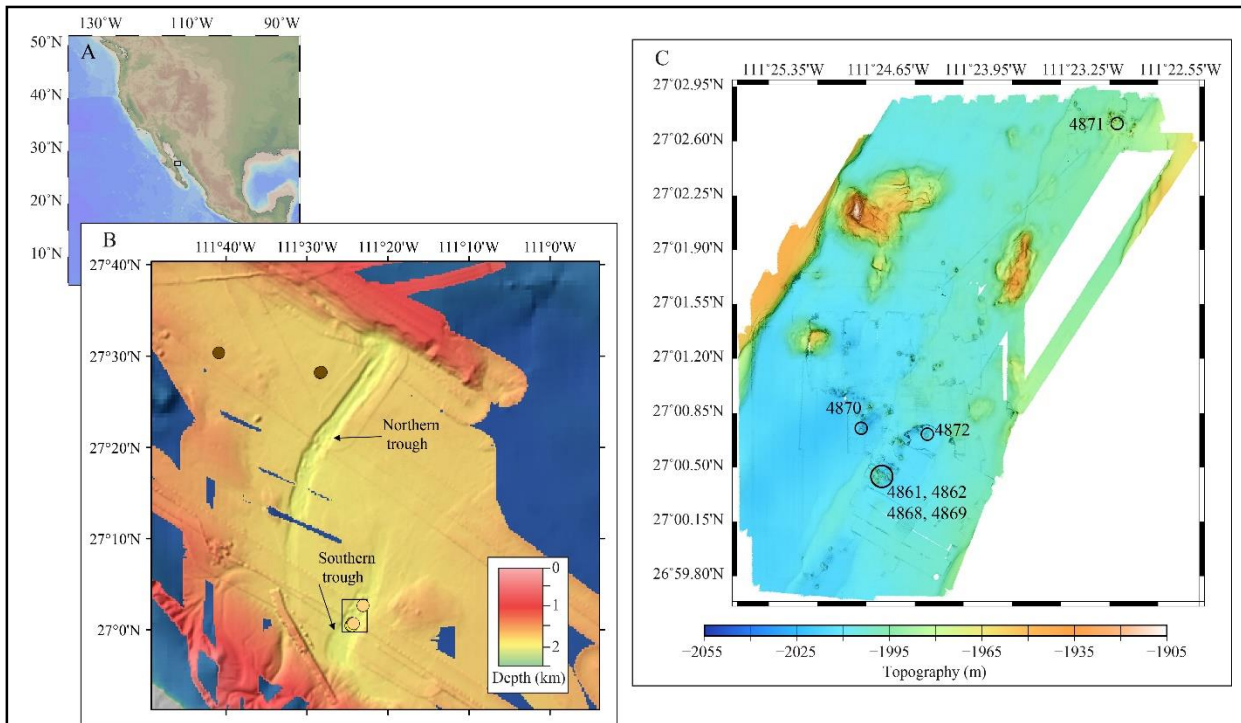


Figure 4.1. (A, B) Northern and Southern troughs within Guaymas Basin, Gulf of California. Collection sites integrated with bathymetric and DEM models provided by NOAA’s NCEI (<https://maps.ngdc.noaa.gov>). Symbol color indicates sediment cover characteristic (brown: inconspicuous; white: white mat; orange: orange mat) (C) Core recovery sites within the Southern trough indicated by dive radius integrated with multibeam data obtained using the ROV *Sentry*. Numbers shown in C indicate HOV *Alvin* dive number.

We analyzed a total of 19 sediment cores and 32 subsurface temperature profiles during a 2016 *R/V Atlantis* cruise in the Gulf of California (AT37-06) to evaluate the rate of fluid flow through surficial sediments throughout Guaymas Basin. Samples obtained during the AT37-06 cruise are briefly compared to those acquired in 2018 (cruise AT45-02) in Section 3. All AT42-05 sediment cores were recovered from the Southern trough in similar sampling areas. Sediment push cores were collected by the HOV *Alvin* from a variety of regions within Guaymas Basin. Sediment cores were collected from 27° 00.42' N to 27° 30.39' N and 111° 23.10' W to 111° 40.87' W (Figure 4.1) during *Alvin* dives 4861 through 4872. In total, 10 sediment cores were recovered from microbial mat (4 white and 6 orange), 8 cores were collected through non-colonized sediments (Table 4.1), and 1 core was collected through a mineral crust. Sediment core lengths ranged from 16 to 55 cm, although sampling artifacts including gaps in layered sediment and melted core tubes often affected sediments circa 20 cm below the seafloor (cmbsf) and below. For this reason, we only consider samples recovered from 0 to 12 cmbsf in this analysis. As we use vertical geochemical gradients to evaluate fluid transport between layers, we do not consider sediment layers which directly adjoin those that may have been compromised during recovery.

Subsurface temperature profiles were measured at the coring locations using a 0.6 m Heatflow probe that includes a linear heater and five thermistors spaced 10 cm apart and is housed in a heat-resistant titanium shield. The thermistor array measures vertical subsurface temperature gradients when inserted into soft sediment.

Porosity was determined by mass loss for most sites and converted from mass to volume using measured sediment bulk density and seawater density (Lamb, 1951). Due to restrictions on supplies at sea, we categorized porosity by sample type to determine representative values for sites

where no direct measurements were possible. Porosity was measured directly for 40% of the samples collected with the supplies available at sea and we use a linear interpolation to estimate porosity changes with depth where porosity measurement were not feasible. Some sediment cores were collected from previously sampled and named sites including Megamat and Cathedral Hill which have porosities reported in a variety of scientific papers (e.g., Biddle et al., 2012; McKay et al., 2012; Ruff et al., 2015; Teske et al., 2016).

4.2.2. Geochemical Methods

From Fisher and Becker (1991), it is estimated that seepage velocities throughout Guaymas Basin may range from $1 \times 10^{-8} \text{ m s}^{-1}$ to $15 \times 10^{-8} \text{ m s}^{-1}$. Over a 2 cm sediment sampling interval, porefluid residence time is thus estimated to range between 1.5 and 23 days per 2 cm section. Considering this expected range, we utilize ^{224}Ra as its radioactive half-life (3.6 days) corresponds to processes occurring over 1 to 21 day time scales and sample sediment cores at 2 cm intervals unless otherwise noted. Our approach to evaluate fluid flow through soft sediments utilizes a vertically-exchanging ^{224}Ra mass-balance approach (as detailed in Chapter 2). After considering potential vertical porefluid flow direction, we account for changes due to radioactive production and decay to estimate the time required to account for any remaining isotopic disequilibrium in ^{224}Ra between sediment surfaces and interstitial porefluid.

After recovery of each sediment core, samples were visually described (sediment structure and cover) and then processed following methods described by Cai et al. (2012). In short, sediment cores were sectioned into 2 to 4 cm intervals and a slurry was prepared using 150 mL of Ra-free tap water and a subsample of sediments (about $\frac{1}{4}$ of total volume from each 2-4 cm thick sediment

slab). The slurry was pH adjusted by adding 5-10 drops of $\text{NH}_3\text{-OH}$ after which 1 mL of 19 mM KMnO_4 and 1 mL of 40 mM MnCl_2 solutions were added to precipitate any ^{224}Ra that may have entered the dissolved phase following the addition of Ra-free tap water (Cai et al., 2012). Solids were vacuum filtered onto preweighed 47 mm GFF cellulose filters and the filtration was terminated when filtrate drops were no longer observed entering the filtrate reservoir. Sediment-covered filters were then dried completely and analyzed for ^{224}Ra via a Radium Delayed Coincidence Counter (RaDeCC; Moore and Arnold, 1996). To determine the total surface-sorbed ^{224}Ra activity associated with the sediments, filters were analyzed several weeks later after ^{224}Ra had equilibrated with surface-bound ^{228}Th . Any discernable difference in ^{224}Ra activity between the two measurements thus represents a disequilibrium between surface-sorbed ^{224}Ra and ^{228}Th .

Aqueous phase analyses of ^{224}Ra reported herein were made by passing a water sample (core-top water and porefluid recovered by centrifugation) slowly through 25 g aliquots of dry acrylic fibers impregnated with MnO_2 (Moore, 1976; Moore, 2008). These fibers were then rinsed with Ra-free tap water, dried to an optimal moisture content (as per Sun and Torgersen, 1998), and similarly counted on the RaDeCC which has been calibrated with a fiber containing a known activity of a NIST-traceable ^{232}Th standard (containing all daughters in equilibrium) and has been verified through routine QA/QC checks.

4.2.2.1. Calibrations

We followed the approach detailed by Cai et al. (2012) as ‘the method of standard addition’ to calibrate our RaDeCC systems for the sediment-coated filters. Five slurries were prepared, with each containing 20 g dry, aged deep-sea sediment, 80 mL of Ra-free tap water, 1 mL of 19 mM

KMnO₄ solution, and 1 mL of 30 mM MnCl₂ solution. The pH was adjusted to 6-7 using a 1% NH₄OH solution. A NIST-traceable ²³²Th standard solution with all daughters in equilibrium (6.4296 dpm mL⁻¹) was added in aliquots of 0, 1, 2, 3, and 4 mL for each of the five standards. Slurries were then filtered onto pre-weighed 47 mm cellulose filters (0.45 μm) and filters were dried completely to allow determination of recovered sediment mass. Filters were then subsequently analyzed on the RaDeCC. System efficiency is determined by regressing dry standard filter ²²⁴Ra measurements (cpm) against known ²³²Th addition (dpm). Filtrate from each replicate was recovered, combined, and analyzed to monitor breakthrough levels. Calibration results are provided in the Appendix (Figure A.2 and Figure A.3)

According to Cai et al. (2012), optimal emanation of radon daughters on sediment-coated filters occurs at a water:sediment mass ratio of 0.5. However, precisely determining the mass of moist filters is not feasible at sea where measurements are unreliable due to the motion of the ship. Furthermore, the moisture content associated with a filter is likely to change as a function of measurement time, which would potentially influence detection and calibration. While this effect can be managed by controlling analysis time, we often see dramatic differences in the time required to achieve < 10 % analytical uncertainty (> 100 counts) via RaDeCC analysis of Mn-impregnated fibers containing dissolved ²²⁴Ra from deep-sea porefluid (with count times ranging from 2 to >12 hours). In light of these conflicting issues, we concluded that evaluating ²²⁴Ra activities emanating from dry sediment-coated filters would yield the most reproducible calibration and analytical results, albeit at a slightly lower efficiency than could be attained using moist filters.

4.2.2.2. Radiotracer Corrections

In addition to correcting the data according to the procedure detailed in Chapter 2 (section 2.5.1.1), we convert measured ^{224}Ra activities adsorbed onto the sediment-coated filters into corresponding aqueous activities using an average partition coefficient identified for Guaymas Basin. By dividing the ^{224}Ra activity measured on the sediment-coated filters by 1 plus the partition coefficient ($1+K_d$), we convert each corrected sediment-sorbed ^{224}Ra activity into a corresponding dissolved ^{224}Ra activity. We then used the dissolved activity of ^{224}Ra to estimate volumetric fluid flux (Equation 2.5). The effect of this correction is included in Table A2 (Appendix) and is unique to the sample acquisition and ^{224}Ra extraction procedure applied at Guaymas Basin.

4.2.2.3. Radium Partitioning

Because a significant portion of ^{224}Ra associated with marine sediments may enter the dissolved phase and therefore become subject to transport, we also measure the dissolved ^{224}Ra activity contained within the core-top supernatant waters. These aqueous samples were concentrated onto Mn-fibers and analyzed according to techniques described in Chapter 2 Section 3. To use these data in concert with results of sediment-coated filters, we convert from sedimentary ^{224}Ra activity to that expected in the dissolved phase based on a series of experiments which evaluated ^{224}Ra partitioning between the solid and dissolved phases. We evaluated the distribution of ^{224}Ra between the particle sorbed and dissolved phases via a series of consecutive fluid replacement experiments similar to those described by Colbert and Hammond (2008) and also described in Chapter 2 Section 4.1. Briefly, a known mass of sufficiently aged sediment was

combined with a defined volume of Ra-free seawater. The slurry was briefly agitated and then held for 10 minutes to achieve sorption equilibrium before the dissolved ^{224}Ra activity was measured by removing an aliquot of water. Following removal, an equivalent volume of Ra-free seawater was added to maintain V_T and this process was repeated several times.

Vertical distributions of corrected, dissolved ^{224}Ra activities were then used in the vertical exchange model (Equation 2.5) to determine the effective residence time of porefluid within discrete layers of Guaymas Basin sediments. Volumetric fluid transport was estimated by dividing the volume of water contained within each sediment section by the isotopically-derived residence time. Fluid volume is defined as total volume of each sediment segment multiplied by its porosity. Dividing each volumetric fluid transport rate by the sampled area then yields an effective fluid flux (reported here as $\text{mL cm}^{-2} \text{ day}^{-1}$).

4.3. Results and Discussion

This work seeks to identify the rate of fluid transport occurring across a variety of sediment cover types in Guaymas Basin. We first discuss the observed ^{224}Ra patterns across all sediment cores, followed by residence time results and resulting fluid fluxes. We then examine these parameters within subgroups categorized by sediment cover characteristics (e.g., microbial mat presence/absence and color) and temperature regime. These groupings allow us to explore any relationships between flow condition and microbial mat characteristics.

4.3.1. Radium Distribution

K_d values are required to convert ^{224}Ra activities from the solid phase to aqueous phase. Radium partitioning was evaluated using a series of serial extraction experiments on separate sediment samples recovered during different cruises (Table 4.1). As discussed in Chapter 2, we have not observed a significant depth dependence of ^{224}Ra partitioning and thus homogenized material to obtain a sample most representative to the depths over which we are estimating porefluid residence time to complete these experiments. Partitioning experiments were conducted following sediment:water proportions similar to those described by Colbert and Hammond (2008). A dry mass (M_s) of 1120 g was used for the AT37-06 experiment with 150 mL recovered for each analysis step (ΔV) and subsequently returned to maintain a constant volume of 647 mL (V_T). For the AT45-02 experiment, 45 g of dry sediment was incubated with a total volume of 325 mL and 76 mL was recovered for each ^{224}Ra analysis step.

Table 4.1. Compilation of metadata concerning material used in the ^{224}Ra solid:aqueous phase partitioning (K_d) experiments.

Cruise	Site name	Alvin dive; core number	Collection date/time (EST)	Sediment depth (cmbsf)	Latitude and longitude
AT37-06	Megamat II	4861; 28	12/12/2016 15:40	1-4, 7-10, 13-16, 19-22	27° 00.4427' N 111° 24.5243' W
AT45-02	Aceto balsamico	4998; 45	11/23/2018 16:46	28 - 32	27° 00.4435' N 111° 24.4394' W

Dissolved ^{224}Ra activities during these serial extraction experiments ranged from 2.0 ± 0.2 to 4.5 ± 0.2 dpm L^{-1} for AT37-06 sediments with an estimated surface-sorbed activity ranging from 25.8 ± 1.3 to 71.9 ± 2.6 dpm kg^{-1} (Figure 4.2A). Uncertainties associated with

dissolved ^{224}Ra activities represent an analytical uncertainty dependent upon total counts logged (a function of counting time and sample activity). AT45-02 samples were counted for an average of 23.2 hours during which an average of 392 counts were logged in the 220 window of the RaDeCC and AT37-06 samples were counted for an average of 17.3 hours logging an average of 264 counts per sample. We estimate a partition coefficient of $18.7 \pm 4.7 \text{ L kg}^{-1}$ for the AT37-06 sediments (see the slope of the regression line between dissolved and particulate radium activities; Figure 4.2A; $r^2 = 0.888$). The ^{224}Ra partition coefficient for AT45-02 material was estimated to be $154.3 \pm 22.6 \text{ L kg}^{-1}$ (Figure 4.2A; $r^2 = 0.959$). The two solid:aqueous partition coefficients determined for ^{224}Ra (slopes shown in Figure 4.2A) were averaged to yield a single K_d value of $86.5 \pm 23.1 \text{ L kg}^{-1}$. This value is used throughout this chapter to estimate the dissolved ^{224}Ra activity associated with measured grain-sorbed activities of ^{224}Ra .

While the depth of sediment recovery was different between K_d experiments (Table 4.1), so too was the subsurface temperature regime (Figure 4.2B). Although average temperatures were most similar at 10 cmbsf (15.7°C and 7.1°C), the range was much larger at the AT37-06 sampling site (15.6°C to 54.1°C) than for the AT45-02 site (4.8°C to 22.7°C). Because we cannot know if the higher grain affinity of the AT45-02 sediments is a consequence of temperature, geochemistry, or grain surface charge/texture, we used both to identify a best representative K_d value for Guaymas Basin.

Chapter 2 presents results of an experiment which revealed no apparent depth related trends in radium partitioning, but K_d results suggest ^{224}Ra distribution may vary by nearly an order of magnitude across sites. It is likely that grain surface area, charge potential, and/or metal content (via hydrothermal alteration) could explain these observations although such effects were not the focus of this work. Rather, we acknowledge this uncertainty in K_d as a potential limitation of the

approach and discuss the consequence of this limitation on errors associated with our effective fluid flux estimates in Chapter 2.

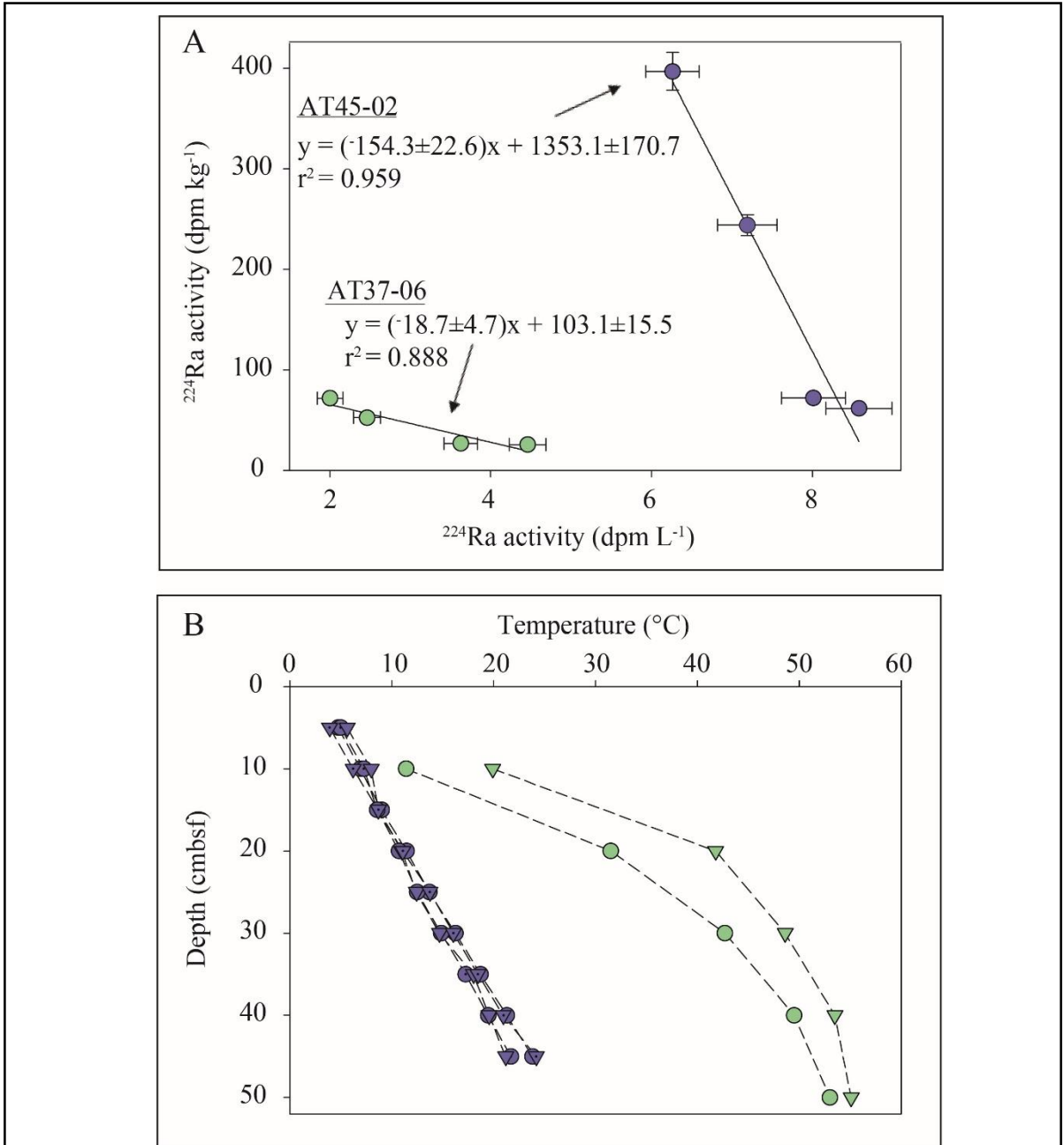
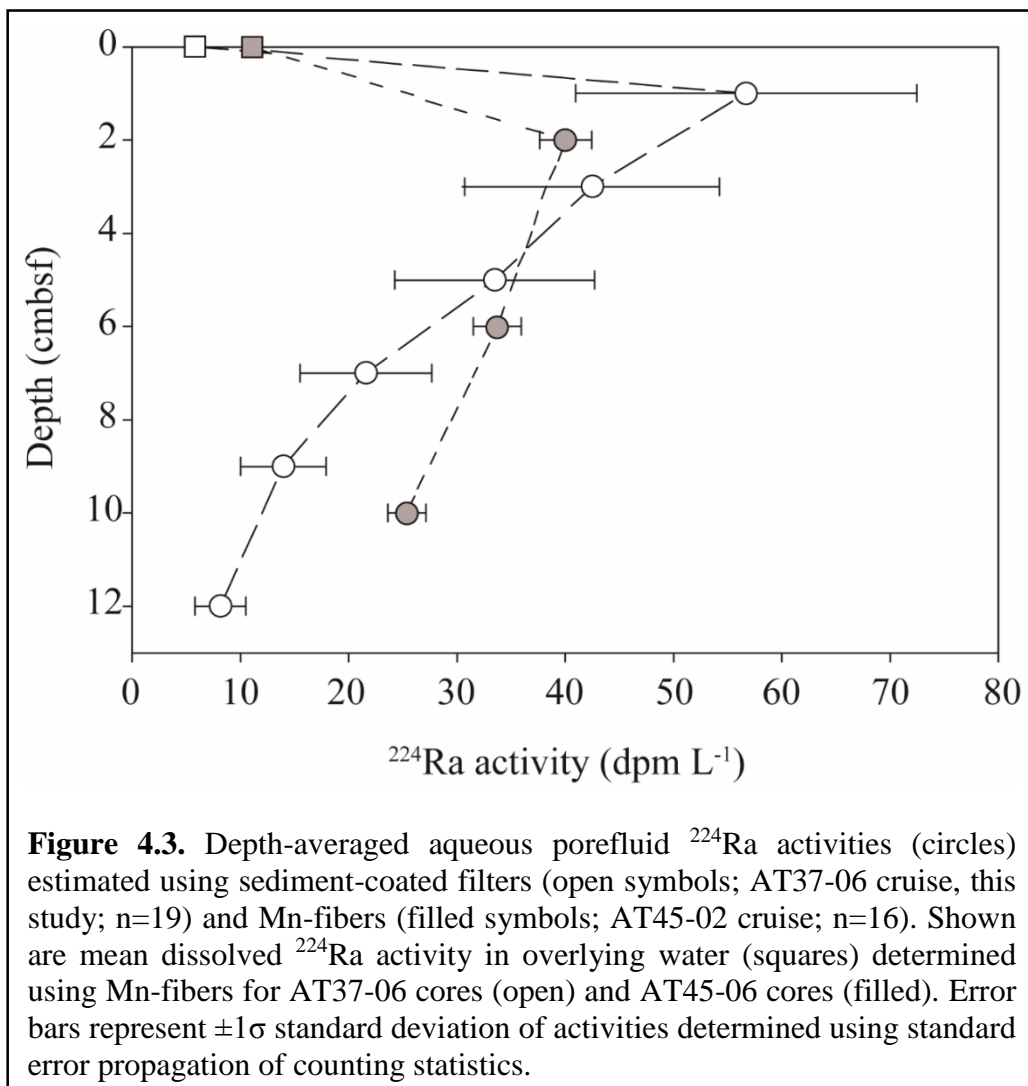


Figure 4.2. (A) Results from serial volume extraction experiments used to determine ^{224}Ra distribution coefficient (K_d) for samples collected during AT37-06 (green) and AT45-02 (blue). Standard error propagation using $\pm 1\sigma$ analytical uncertainties was used to determine uncertainties associated with each estimated term (B) Subsurface temperature profiles measured in-situ for each sample.

In an effort to determine the accuracy of our K_d estimate, we compare porefluid activities of dissolved ^{224}Ra derived from sediment-covered filter analysis divided by $(K_d + 1)$ from the AT37-06 cruise (data presented in this chapter) to dissolved activities measured directly using Mn-coated fibers during the AT45-02 cruise. By averaging all dissolved ^{224}Ra activities estimated using sediment-coated filters and comparing them to dissolved activities determined using Mn-coated fibers for each depth to 10 cmbsf, we observe no difference beyond error for each depth with the exception of samples below 9 cmbsf (Figure 4.3). Although it is unlikely that two data sets representing distinct and unique sampling locations would yield identical depth dependent trends, this comparison indicates close agreement between average profile shape and ^{224}Ra activity range determined via two distinct methods. Moreover, since the vertical exchange model considers the relative change in ^{224}Ra with depth, and since all data used through this chapter are treated identically with respect to K_d , this potential artifact should have no consequence on the resulting fluid transport estimates.



4.3.2. General Overview

A total of 19 sediment cores were collected during 10 Alvin dives and subsequently processed to measure vertical distributions of surface-sorbed ^{224}Ra (Table 4.2). Sediment cover and environmental characteristics (including large bacterial mats, towering chimneys, Riftia gardens, and bare sediment) varied substantially across the sampling regions. A full list of measured values for all discussed cores is presented in the Appendix (Table A.5).

Table 4.2. Site metadata for sediment cores collected during the AT37-06 cruise from which fluid flow rate and direction are evaluated.

Site	Alvin dive; core number	Latitude, longitude	Sediment cover
Megamat II / Twin Peaks	4861; 21	27° 0.4440 'N, 111° 24.5231 'W	Bare sediment
Megamat II / Twin Peaks	4861; 12	27° 0.4444 'N, 111° 24.5243 'W	Bare sediment
Smoker "x"/Marker 22	4862; 29	27° 0.4424 'N, 111° 24.5921 'W	Bare sediment
Smoker "x"/Marker 22	4862;27	27° 0.4635 'N, 111° 24.5565 'W	Orange mat
Smoker "x"/Marker 22	4862; 6	27° 0.4543 'N,111° 24.5698 'W	White mat
Ring Vent/ Mound 1	4864; 16	27° 30.3733 'N, 111° 40.8938 'W	Bare sediment
Ring Vent/9a	4866; 12	27° 28.1766 'N, 111° 28.4014 'W	Bare sediment
Octopus Mound	4867; 31	27° 28.2339 'N, 111° 28.3875 'W	Bare sediment
Ultra Mound	4868; 9	27° 0.4377 'N, 111° 24.5217 'W	White mat
Ultra Mound	4868; 18	27° 0.4377 'N, 111° 24.5217 'W	Orange mat
Ultra Mound	4869; 19	27° 0.4504 'N, 111° 24.5399 'W	Orange mat
Ultra Mound	4869; 1	27° 0.4504 'N, 111° 24.5399 'W	White mat
Aceto balsamico	4870; 22	27° 0.4699 'N, 111° 24.4361 'W	Yellow crust
Survey Site 1	4871; 25	27° 2.6641 'N, 111° 23.0814 'W	Orange mat
Survey Site 1	4871; 11	27° 2.6642 'N, 111° 23.0817 'W	Orange mat
Survey Site 1	4871; 9	27° 2.6633 'N, 111° 23.0817 'W	Bare sediment
Cathedral Hill	4872; 15	27° 0.6836 'N, 111° 24.2659 'W	Orange mat
Cathedral Hill	4872; 3	27° 0.6836 'N, 111° 24.2659 'W	White mat
Cathedral Hill	4872; 2	27° 0.6836 'N, 111° 24.2659 'W	Bare sediment

We first compare our sediment-sorbed ^{224}Ra activities with those previously reported for the region. The average surface-sorbed ^{224}Ra activity for all 19 sediment cores was 3.0 ± 0.2 dpm g^{-1} with an average equilibrium activity of 4.2 ± 0.2 dpm g^{-1} . For comparison, we determine the average ^{228}Th activity (dpm g^{-1}) on Guaymas Basin particles using data reported by Smoak et al. (1999) who examined sinking particles within the Gulf of California intercepted by a series of sediment trap deployments. The average ^{228}Th activity of sinking particles should be higher than that which we measure in shallow sediments for two reasons. First, our study only measures the exchangeable fraction of ^{224}Ra available for dissolution which is substantially less than the total grain activity (total surface-sorbed + imbedded in the mineral matrix). Second, we expect that ^{228}Th will initially be in excess of ^{228}Ra supported by the particle surfaces as ^{228}Th is scavenged by sinking particles (Clegg and Whitfield, 1991). Therefore, equilibrium surface-sorbed ^{224}Ra activities are expected to be less than even the fraction of ^{228}Th sorbed to grain surfaces. Because an average activity of 12.5 dpm g^{-1} can be estimated from the work by Smoak et al. (1999), our data are reasonable relative to the literature.

In general, dissolved ^{224}Ra activities associated with interstitial porefluid exhibited a minimum activity of 1.6 ± 0.4 dpm L^{-1} and a maximum of 403.8 ± 108.1 dpm L^{-1} and were generally found to decrease with depth below the sediment-water interface (Figure 4.4A). Despite considerable differences in dissolved ^{224}Ra activities associated with the upper sediment sections, ^{224}Ra activities were much more similar at depth. This behavior could be related to excess ^{228}Th scavenged by sinking particles which initially supports a higher dissolved ^{224}Ra activity in the shallow sediment column. With a sedimentation rate of 1 cm per decade (Curry et al., 1979), however, if such deposition alone explained the high surficial activities, we would expect no differences in activity at or below 1 cmbsf as ^{228}Ra would also be growing toward equilibrium

with surface-sorbed ^{232}Th and so would not be able to support such high ^{228}Th activities. It is not surprising that differences in dissolved ^{224}Ra activities remain at depth across sites as changes in exchangeable ^{224}Ra production may also explain some of the inter-site variability (Figure 4.4B).

Subsurface residence time was determined using dissolved ^{224}Ra activities via the vertical exchange model as described in Chapter 2. Transport is evaluated in both the $+z$ and $-z$ directions using time dependent isotopic change. For flow estimates out of the sediments ($+z$), subsurface fluid residence time in each 2 cm section ranged from 0.06 to ≥ 21 days, whereas interstitial fluid residence time assuming transport into the sediments ($-z$) covered identical time scales (Figure 4.4C). However, mean residence time was significantly less for all samples under a dominant upward ($+z$) transport direction as compared to $-z$ (4.4 and 16.1 days, respectively). Although a wide range in interstitial fluid residence times was observed for both transport directions, the majority of possible residence time estimates require active transport from depth and appear consistent with depth and across site with over 70% of subsurface residence times being < 4 days and only 3% of observations reaching ≥ 21 days for all 19 cores (Figure 4.4C). In comparison, $\sim 18\%$ of residence times under a $-z$ transport direction were < 4 days and $\sim 65\%$ were ≥ 21 days. For all sampled sediment cores, a transport direction out of the sediments, toward the overlying ocean ($+z$ direction) more than twice as commonly explained vertical dissolved ^{224}Ra gradients as compared to transport into the sediments ($-z$ direction). Because **transport direction** is not necessarily related to thermal gradient, but instead appears as a general characteristic of the data set, this could be related to largescale hydrothermalism affecting the basin scale (kilometers) as compared to highly localized flow features.

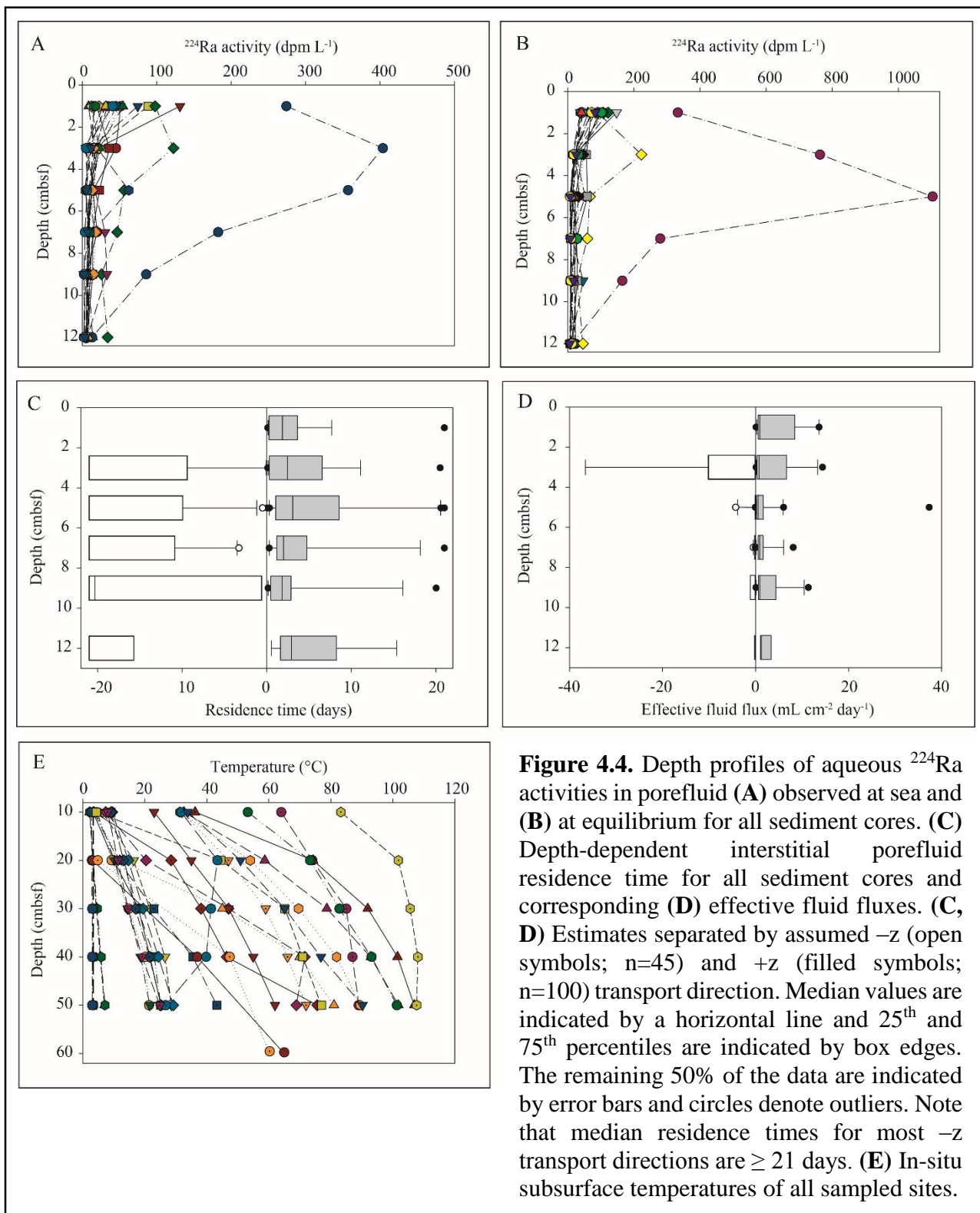


Figure 4.4. Depth profiles of aqueous ^{224}Ra activities in porefluid (**A**) observed at sea and (**B**) at equilibrium for all sediment cores. (**C**) Depth-dependent interstitial porefluid residence time for all sediment cores and corresponding (**D**) effective fluid fluxes. (**C**, **D**) Estimates separated by assumed $-z$ (open symbols; $n=45$) and $+z$ (filled symbols; $n=100$) transport direction. Median values are indicated by a horizontal line and 25th and 75th percentiles are indicated by box edges. The remaining 50% of the data are indicated by error bars and circles denote outliers. Note that median residence times for most $-z$ transport directions are ≥ 21 days. (**E**) In-situ subsurface temperatures of all sampled sites.

Similar ranges in fluid flux were observed irrespective of transport direction (± 0.7 to ± 37 mL cm⁻² day⁻¹) (Figure 4.4D). Mean fluid fluxes were comparable for all sites across subsurface depth and effective transport direction (+z: 2.9 mL cm⁻² day⁻¹; -z: -1.7 mL cm⁻² day⁻¹), although mean fluid flux out of the sediments (+z) was nearly a factor of 2 larger. Because >90% of subsurface temperature profiles showed differences in temperature with depth, this result could suggest thermal gradients are driving fluid discharge from sediments in the areas sampled. Positive fluid flux estimates suggest a greater fluid flux magnitude is required to explain observed ²²⁴Ra distributions as compared to a negative flux (+z: 73% greater than 1 mL cm⁻² day⁻¹; -z: 13% greater than 1 mL cm⁻² day⁻¹). Minimum discernable flow rates correspond to a porefluid residence time of 21 days or longer. Here, we cannot resolve isotopic disequilibria at or beyond 21 days of continued production so our detection limits are ~ 1 L m⁻² day⁻¹. Maximum fluid flux estimates are related mostly to the sorption equilibrium requiring ~ 10 min of porefluid contact with sediments. In theory, our maximum detectable fluid flux is thus ~ 350 L m⁻² day⁻¹.

4.3.3. Temperature and Fluid Transport

Subsurface temperature ranges between sites and with depth showed considerable variability (Figure 4.4E). Because we observed near ambient ocean temperature (~ 3 °C) in the overlying seawater, a few decimeters above the sediment-water interface an elevated subsurface temperature is indicative of a thermal gradient across the sediment-water interface. Minimum recorded subsurface temperature was 2.2°C measured 10 cmbsf and our maximum recorded was 108.1°C at 50 cmbsf. Vertical temperature gradients also varied across sites from non-existent to linear to non-linear. Although some subsurface profiles retained ambient temperatures throughout,

other cores were collected where temperatures at depth approached the known limits of life (Clarke, 2014).

To test for a potential relationship between thermal gradient across the sediment-water interface and effective fluid flux, sediment cores were grouped based on the maximum temperature recorded during sampling ($<10^{\circ}\text{C}$, $10<40^{\circ}\text{C}$, $40<80^{\circ}\text{C}$, and $>80^{\circ}\text{C}$). Often, maximum temperature was observed at the greatest subsurface depth where both observed and equilibrium ^{224}Ra activities are similar across group type suggesting the largest thermal gradient was associated with these sites (Figures 4.5A and 4.5B). Mean ^{224}Ra activities in uppermost sediment layers were distinct across temperature groups whereas equilibrium activities were much more similar (Figures 4.5A and 4.5B). These observations suggest in-situ temperature does not greatly affect ^{224}Ra production although correlations have been observed elsewhere (e.g., Rama and Moore, 1996). However, lower maximum temperatures were associated with lower mean ^{224}Ra activities while higher temperatures were associated with higher mean dissolved ^{224}Ra activities for all subsurface samples, except for temperatures $> 80^{\circ}\text{C}$ which were often associated with lower average initial ^{224}Ra activities. Because the equilibrated activities associated with this temperature group do not follow a similar pattern, it would seem as though maximum subsurface temperature is related to the ^{224}Ra inventory when the temperature is between 10°C and 80°C .

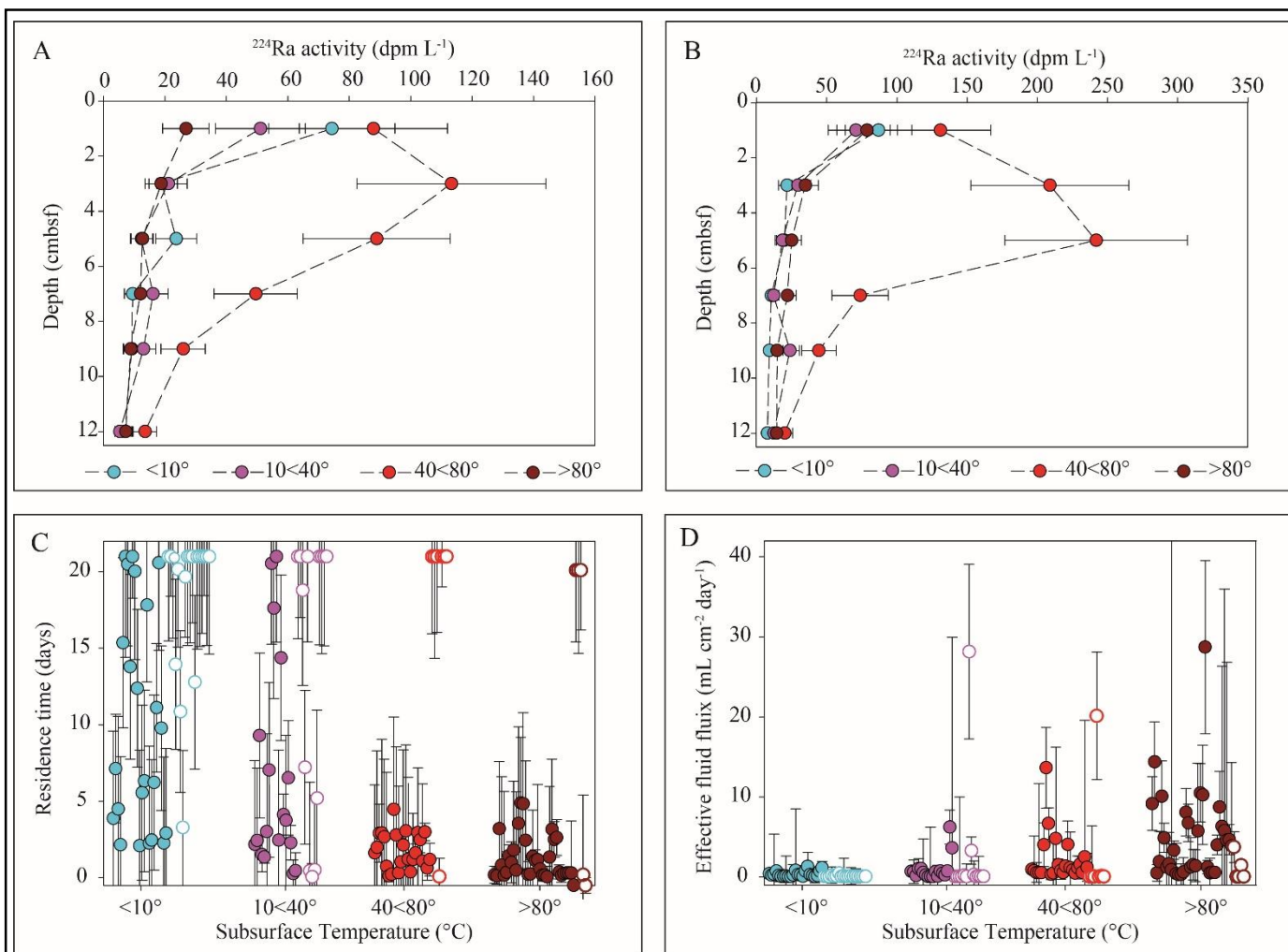


Figure 4.5. (A) Average aqueous porefluid ^{224}Ra activity depth profile measured at sea and (B) at equilibrium grouped by maximum subsurface temperature category. Error bars depict the average analytical uncertainty. (C) Interstitial porefluid residence time and (D) effective fluid flux for -z (open symbols) and +z (filled symbols) transport directions grouped by maximum observed temperature. Error bars represent $\pm 1\sigma$ standard deviation.

Interstitial porefluid residence time for each sediment section determined using the vertical exchange model for +z and -z transport directions are similarly grouped by temperature (Figure 4.5C). In general, -z effective transport directions yield longer effective residence time for all temperature groups. For all depths, lower temperatures were associated with longer and more variable porefluid residence times whereas warmer temperatures were associated with shorter and

less variable residence times (Figure 4.5C). Although we find more instances where the effective transport of ^{224}Ra is occurring in +z for all thermal groups, the proportion of solutions possible assuming a -z to those assuming a +z direction decreases with higher temperature. This finding suggests that the likelihood of fluid transport into the sediments at temperatures $\geq 40^\circ\text{C}$ is significantly less than for regions of lower temperatures. Because thermal driven convection is the likely mechanism controlling fluid transport through sediments in regions of elevated subsurface temperature, this result seems intuitive. However, in areas of no/low thermal anomaly ($<4^\circ\text{C}$), ^{224}Ra distributions may be explained almost equally by +z and -z effective transport directions. Because the natural abundance of ^{224}Ra is relatively low in marine waters compared to porefluid, ^{224}Ra would naturally diffuse into the overlying ocean from the subsurface regardless of transport direction. Although it is not expected that this process alone would result in sustained disequilibrium, we do not distinguish between diffusive and advective transport modes in the model output and so a vertical gradient with lower dissolved ^{224}Ra activities in the shallow subsurface could be explained by the competing effects of diffusion (+z) and advection (-z).

In general, effective fluid flux was found to increase with increased maximum subsurface temperature, regardless of transport direction (Figure 4.5D). However, a +z effective fluid flux direction was nearly 6 times more likely to explain observed trends in dissolved ^{224}Ra activities for cores where subsurface temperature was $> 80^\circ\text{C}$ as compared to a -z direction for subsurface depths between 3 and 12 cmbsf. This further suggests that vertical thermal gradients over ~ 1 m across the sediment-water interface may either be a predominant factor controlling fluid flux or presenting as a consequence of fluid flux magnitude. As we did not seek to discern specific mechanisms, it is unclear at this time as to whether observed thermal gradients are the driver or the consequence of fluid flow. Although greater maximum subsurface temperatures appear related

to both more common instances of fluid flux out of the sediments and larger flux magnitudes, such high temperatures often limit species richness (Clarke, 2014). Since submarine seeps represent an oasis type of environment in the deep-sea, the combined effects of fluid flux magnitude and temperature may exert control on microbial success.

4.3.4. Fluid Flux and Microbial Colonies

We further categorize cores according to sediment cover characteristics (no mat, white mat, and orange mat) to evaluate any potential relationship between fluid flux and microbial mat presence (see Table 4.2). For this analysis, we do not include the core recovered from Aceto balsamico as it was covered in a mineral deposit and was neither bare nor covered in filaments. Sediment cores with no visible mat presence were further divided by temperature into two groups ($<10^{\circ}\text{C}$ maximum temperature and $\geq 10^{\circ}\text{C}$ maximum temperature). Coincidentally, this grouping also distinguished cores recovered just outside a mat from those collected ≥ 1 m from microbial mat. This grouping resulted in four environmental conditions represented by a similar number of cores (cold and bare: 4 cores; warm and bare: 4 cores; white mat: 4 cores; orange mat: 6 cores). Here, we considered effective transport direction, porefluid residence time, and fluid flux over surficial sediment depths ranging from 0 to up to 16 cmbsf to evaluate an average condition for entire cores as compared to specific depths below SWI. Error is presented as the absolute value of the mean uncertainty of all parameter estimates.

Effective fluid flux magnitude and microbial mat presence appear to be related with greater effective fluid fluxes more commonly associated with mat covered sediments than bare sediments

(Figure 4.6A). Furthermore, fluid flux through orange mat was found to be higher than that for white mat, though much more variable with depth. Mat presence and color appear unrelated with subsurface temperature at 10 cmbsf (Figure 4.6B) although orange mats were associated with the highest temperatures measured at this depth. However, not all orange mats were associated with high surficial temperature (Figure 4.6B), suggesting that high temperatures may not be a requirement for orange *Beggiatoa* but rather that these bacteria exploit an opportunistic niche. Our data appear to support the hypothesis suggested by McKay et al. (2012) that orange *Beggiatoa* may be more thermotolerant than white filaments by comparing temperature measured at 10 and 50 cmbsf to mat presence/absence. We find a spatial association between orange and white filaments and subsurface temperature at 50 cmbsf (Figure 4.6C) with all mat covered sediments recovered from regions where temperature were $\geq 50^{\circ}\text{C}$ at depth. In fact, with the exception of one bare sediment core, Figure 4.6C indicates a clear threshold where no microbial mats are found with temperatures at 50 cmbsf below 50°C and no bare sediments are found above that temperature. The temperature profile associated with the one bare sediment exception to this distinction was collected within a white mat ~ 1 m away, so this temperature may not be representative of the sediments collected by the core. However, we only considered material to be 'mat covered' if a visible mat occupied the surface of recovered sediments rather than considering proximity to nearest microbial mat. Data presented in Figure 4.6 represent several cores from distinct regions and conspicuous bacterial mat suggesting a subsurface temperature of $\geq 50^{\circ}\text{C}$ at depth is a common feature below *Beggiatoa* mats in Guaymas Basin.

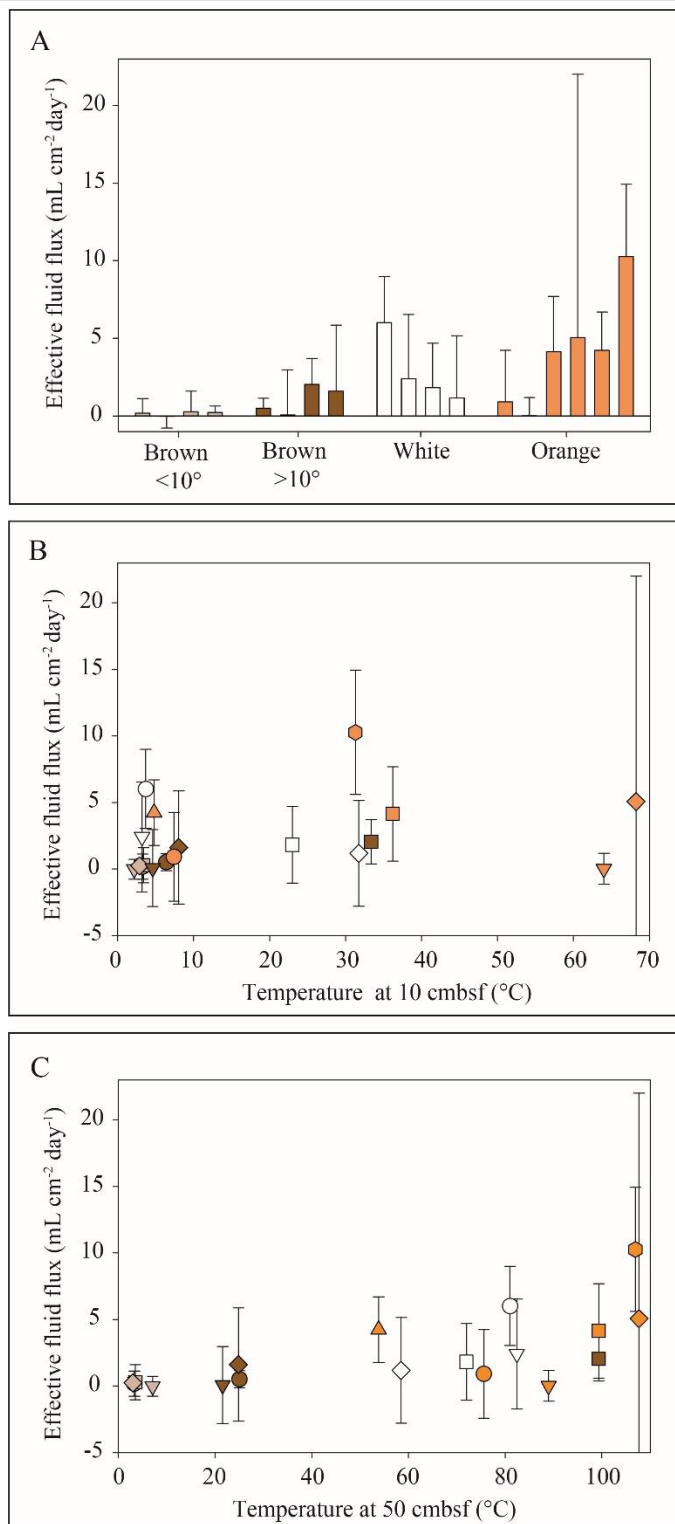
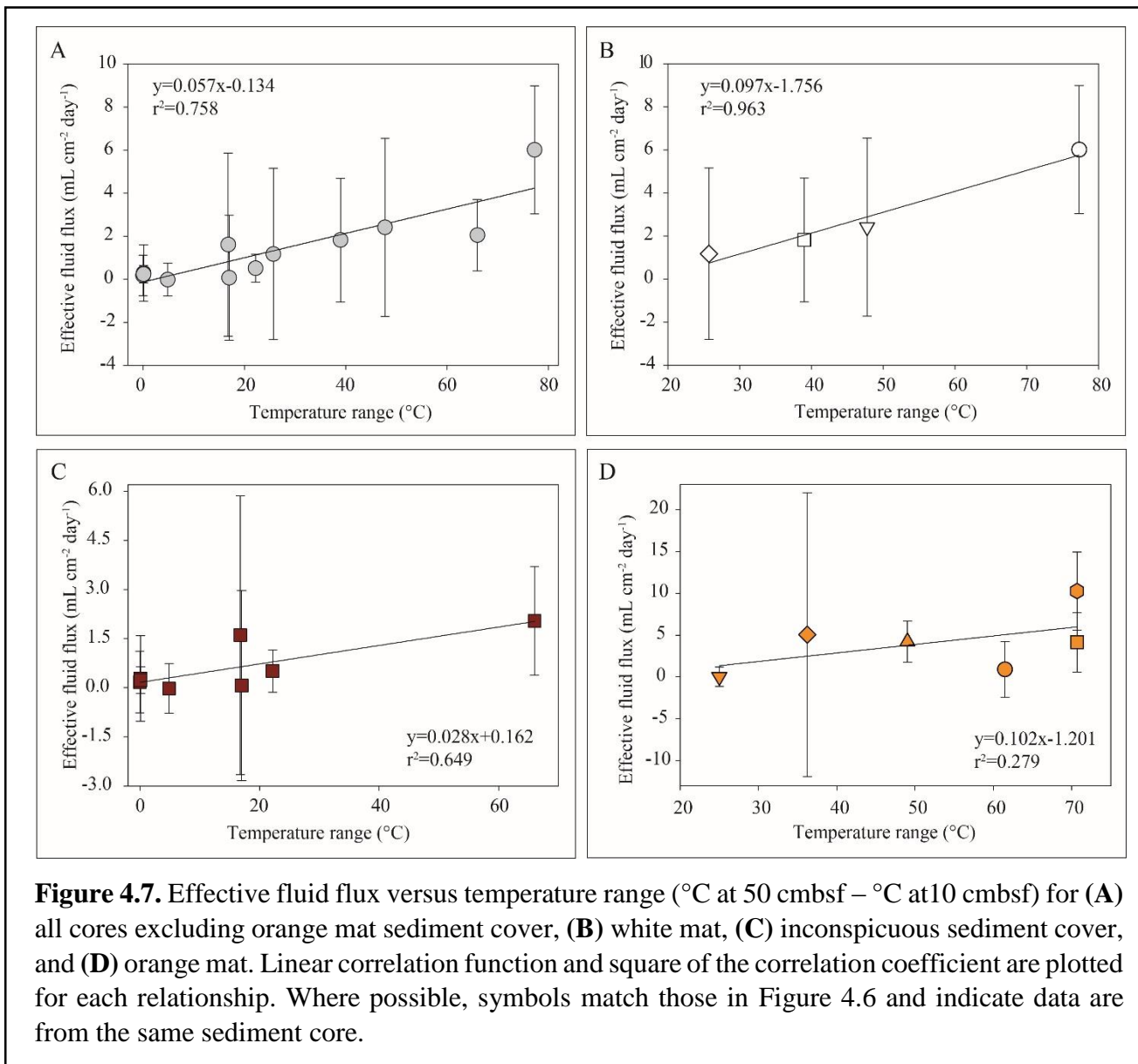


Figure 4.6. (A) Mean effective fluid flux grouped by sediment cover. Mean effective net fluid flux versus in-situ subsurface temperature at (B) 10 cmbsf and (C) 50 cmbsf. Color indicates sediment cover variable as established in A.

We suspect this lack of thermal relationship is a consequence of temporally variable flow and even flow direction reversals through sediments covered by microbial mat. Such reversals were speculated by Gundersen et al. (1992) exclusively for sediments colonized by orange *Beggiatoa* where permeability was increased by precipitation of materials at the SWI and overlying water temperatures were recorded at ambient temperature over the mat whereas subsurface temperatures were elevated. This hypothesis is further supported by McKay et al. (2016) with significant temperature fluctuations of $\sim 20^{\circ}\text{C}$ at 10 cmbsf (ranging from 40 to 60°C) recorded over the scale of hours beneath orange *Beggiatoa*. Such temperature fluctuations were not observed beneath white mat (situated around the periphery of the orange mat) and outside of the mat ('bare' sediment). Because McKay et al. (2016) observed relatively constant subsurface temperature 20cmbsf and below, the change in temperature appears to be a consequence of the periodic inflowing of seawater and not supported by a change in the subsurface thermal end-member. From this, we conclude that forces other than thermally-driven pressure gradients are more significant in controlling rates of porefluid flux through sediments colonized with orange filaments.



Our fluid flux estimates represent a single instance in time in an environment where seepage is expected to be variable on ~ decadal scales, although research in Guaymas Basin is fairly nascent (Teske et al., 2016). While we suspect the geochemical constituents evaluated here would respond rapidly to a change in subsurface transport, bacterial abundance may either lag changes in flow condition or perhaps even require variable flow as has been suggested specifically for orange *Beggiatoa* in Guaymas Basin (Gundersen et al., 1992). Although these

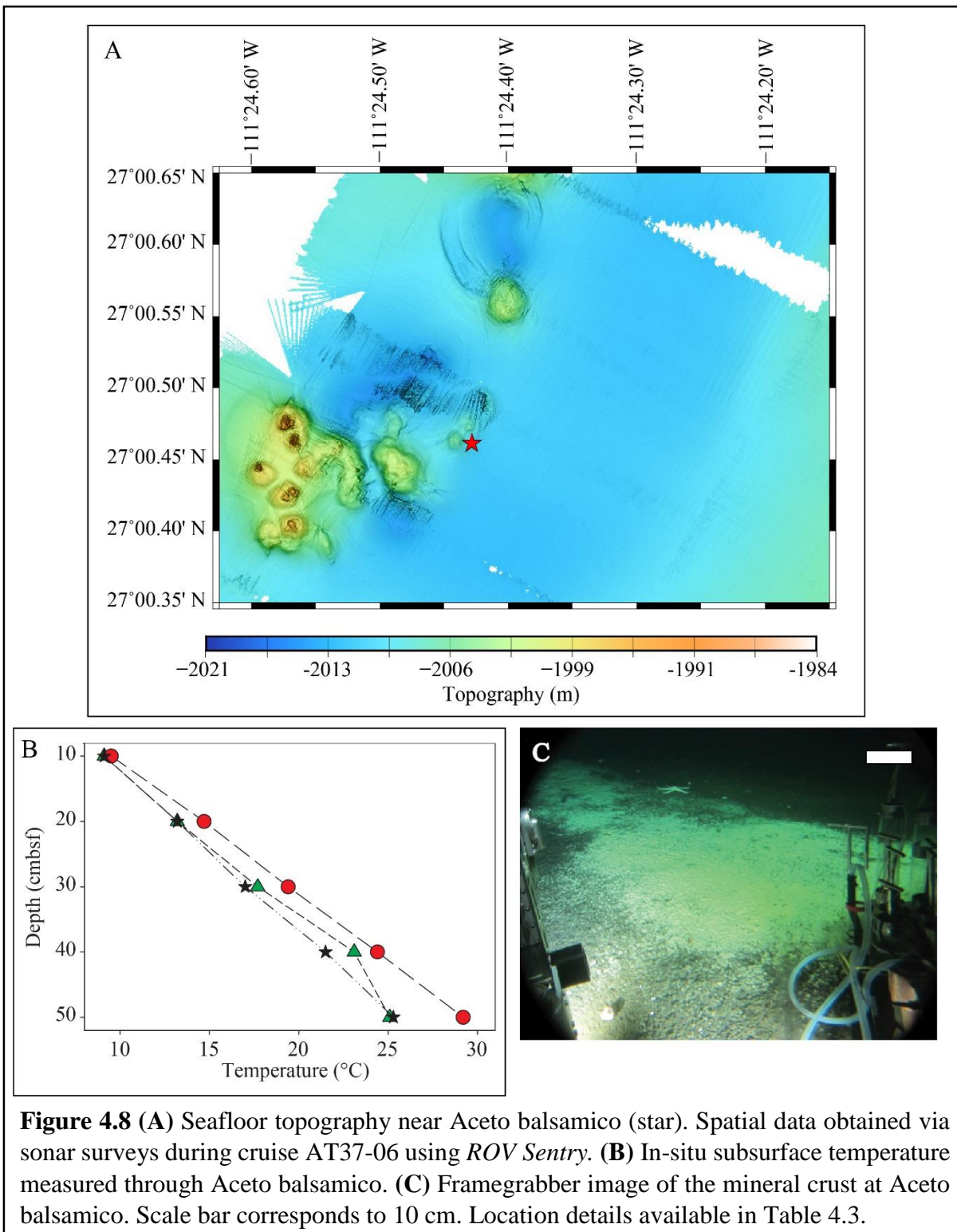
data only represent an instance in time, it is possible that we sampled over a variety of flow conditions and can consider our results as indicators of a temporally variable process. However, to truly identify a relationship between orange *Beggiatoa* and temporally variable fluid flux as compared to white *Beggiatoa*, time-series flow measurements would be a necessary observational approach. For now, the strong correlation between white mat and bare sediment with subsurface temperature range and lack thereof for orange mat remains intriguing as the sample size is relatively small and therefore limits the conclusions we are able to draw about general characteristics across mat color.

4.3.5. Potential for Fluid Recharge

Our data largely reflect either stagnant (no flow) or outward porefluid flux conditions, though such observations are likely a product of sampling bias having used the submersible to target interesting seafloor features for coring. As is generally the case with hydrothermal circulation, seawater inflow conditions must occur to supply the continued hydrothermal discharge across the region. Here, we consider a few hypothetical scenarios of Guaymas Basin recharge required to balance the range of discharge rates we report here. The following scenarios are intended to discuss the conditions that would be required if the discharged fluid is not replenished to ultimately argue that some amount of fluid recharge must be occurring to sustain the observed discharge rates in time.

As discussed throughout this work, it is estimated that anywhere from 1 to 10 mL cm⁻² day⁻¹ of porefluid are discharged from the subsurface. Given that the depth of the axial magma chamber is located between 0.7 to 1 km (Lonsdale and Becker, 1985) below the sediment-water interface

and considering a series of oversimplified assumptions, we estimate the length of time required to expel the entire volume of water within the 1 km thick sediment column and estimate the degree of subsidence that would result if that void volume is not replenished by infiltrating seawater. We consider the following assumptions: (1) no resupply of water either laterally or from depth, (2) that porosity is constant with depth (at 0.4), and (3) that fluid flux is constant in time and space (considering a 1 m² area of seafloor). Considering a fluid flux range of 3.65 to 36.5 m³ m⁻² yr⁻¹ (based on converting flux estimates in this study), we estimate that the entire volume of interstitial porefluid would be expelled in 11 to 110 years. This estimate is in line with observations by Campbell et al. (1988) suggesting several localized hydrothermal sites have been active for at least the past 10 years. However, such a phenomenon would result in a sediment compaction rate (and subsequent subsidence) of 3 to 36 m yr⁻¹ assuming the effects of thermal expansion are ignored. Although several slump and crater features have been associated with hydrothermal chimneys (Ondréas et al., 2018), the occurrence of such features has not been documented in Guaymas Basin. Instead, relative seafloor position would have to be balanced by sedimentation under active discharge conditions. Although substantial, the rate of sedimentation to the region (1 – 1.2x10⁻³ m yr⁻¹; Curray et al., 1979) is far too low to maintain position over 11 to 110 years. Therefore, it seems reasonable that some amount of fluid recharge is necessary to sustain our observations of outflow. Furthermore, because entire hydrothermal sites are hypothesized to persist for 10⁴ years (Campbell et al., 1988), a mechanism to sustain such extensive lifetimes must include fluid recharge as the rates identified in this work represent ‘slow’ flow features and do not even consider chimney type ‘fast’ flow features.



The concept of fluid recharge is certainly not unique to this work and has been previously suggested for Guaymas Basin (e.g., Fisher and Becker, 1991) and for other hydrothermal environments (Mottl and Wheat, 1994; Walker et al., 2008; Lauer et al., 2018). It has been proposed that recharge can occur locally through high permeability outcrops (Lauer et al., 2018) and through subsurface faults associated with low profile abyssal hills (Fisher et al., 2001). While we did estimate a modest net fluid flux into the sediments of $-0.2 \pm 0.75 \text{ mL cm}^{-2} \text{ day}^{-1}$ for a core with bare sediment cover, we also sampled a mat at Aceto balsamico targeted for having peculiar subsurface geochemical profiles including sulfur data that suggest either a sulfur-depleted subsurface fluid source or incomplete sulfur cycling (Teske et al., 2016). This region is characterized by an unusual yellow crust/mat presumed to have obtained color from extensive sulfur deposits staining the sediments (Figure 4.8). This sediment core deserves separate consideration from those described above as the effective fluid flux estimate indicates a hydrothermal recharge rate of $-3.4 \pm 1.7 \text{ mL cm}^{-2} \text{ day}^{-1}$ (Table 4.3).

Table 4.3. Core metadata for the Aceto balsamico core. Collection date/time is in EST, ^{224}Ra activities are given in dpm L^{-1} and residence time is presented in days.

Alvin dive; core number	Collection date/time	Latitude, longitude	Observed ^{224}Ra activity	Equilibrium ^{224}Ra activity	Residence time
4870; 22	12/22/2016 11:35	27° 0.4699' N, 111° 24.4361' W	19.8 ± 5.6	28.1 ± 7.9	9.97 ± 2.19

Although we have no independent evidence to corroborate these estimates, our observed ^{224}Ra profile at this site may be explained by either an additional sink of ^{224}Ra or a dilution of the subsurface ^{224}Ra pool via recharge of seawater. The yellow crust could be indicative of radium removal via solid precipitation and incorporation into barium sulfate as ^{224}Ra is co-precipitated with barium (Aharon et al., 2001). Alternatively, the yellow crust may remain after removal by

seawater recharge into the sediments. Although we do not have sufficient ancillary data to support either conclusion, the unusual yellow crust does appear along the base of a modest abyssal hill (Figure 4.8) where shimmering water has been observed emanating from the top of the seafloor protrusion ~5 m from our core collection site. The presence of shimmering water is often suggestive of active hydrothermal discharge occurring at high temperatures and could support the hypothesis of recharge occurring at the base of abyssal hills near areas of active discharge through a thermal convection like circulation pattern (a phenomenon described by Fisher et al., 2001). To date, however, this observation remains unverified and would require a more intensive sampling effort to characterize the flow condition.

4.4. Summary and Conclusions

We evaluated ^{224}Ra profiles recovered from 19 sediment cores to identify spatial relationships between subsurface fluid flux and microbial mat presence. We targeted orange and white bacteria mats dominated by *Beggiatoa* to determine if fluid flux magnitude was spatially related to mat color. To do so, we measured surface-sorbed ^{224}Ra activities of sediment sections and determined the equilibrium activities for these same sediments. Measurements were converted into dissolved activities such that conditions of disequilibrium from the sediments could be assessed.

A vertical exchange model where radioactive production and decay represent the only sources and sinks of ^{224}Ra to the porefluid inventory was used to determine an effective flux through mat covered sediments. Fluid flux estimates were then determined as the rate of fluid transport that would be required to replace the porefluid volume over the estimated residence time.

Net transport is taken as the average flux from 0 to 12 cmbsf. Effective fluid flux estimates ranged from 0.02 ± 1.16 to 10.26 ± 4.66 mL cm⁻² day⁻¹ for mat covered sediments as compared to seepage rates estimated for non-mat covered sediments (0.07 ± 2.90 to 2.04 ± 1.66 mL cm⁻² day⁻¹). In many instances, the error associated with a given flux estimate is large suggesting the change in ²²⁴Ra as a consequence of environmental residence time is close to the analytical error associated with each isotope activity. This similarity is primarily due to the uncertainty associated with our ²²⁴Ra partition coefficient and the associated consequence on dissolved ²²⁴Ra activities. Unfortunately, results were limited by complications related to at-sea sampling. This approach will be modified in the future and error can be reduced by ~30% if dissolved ²²⁴Ra is measured directly via pre-concentration onto Mn-fibers or perhaps by evaluating K_d using the method of standard addition (Rama and Moore, 1996).

Highest fluid flux estimates were spatially associated with orange mat, however this result was inconsistent as some of the lowest fluid flux estimates were determined for orange mat covered sediment cores. The association between orange mat and high subsurface temperature has been previously observed (McKay et al., 2012) and is supported by data presented here. It is suspected that the stronger compression of isotherms and metabolic zones associated with greater subsurface temperatures can explain the distribution of orange/white mat in this region and we demonstrate that the mechanism to support vertical compression could be fluid fluxes ≥ 4 mL cm⁻² day⁻¹ for orange mat (as compared to ≤ 2 mL cm⁻² day⁻¹ for white mat) although exceptions to this simplification were observed. With a few exceptions, orange and white mat were only observed in regions where the subsurface temperature at 50 cmbsf exceeded 40°C. To our knowledge there is no evidence to support a particular temperature condition as a requirement for the *Beggiatoa* of

Guaymas Basin, although irrespective of mat color and sampling site, we only observed significant mat colonies where subsurface temperature at 50 cmbsf was less than 40°C.

In general, maximum subsurface temperature and net effective fluid flux were related where greater subsurface temperature maxima were associated with higher fluid fluxes regardless of sediment cover. Subsurface temperature gradients were found to have a strong linear relationship to fluid fluxes associated with white mat and appear unrelated to fluid flux associated with orange mat. This lack of association may be related to a variable flux suspected for localized hydrothermal seeps. For example, distributions of dissolved compounds would respond quickly to an instantaneous change in flow whereas mat and subsurface temperature may require additional time to adjust. This idea is supported by additional evidence specifically for orange *Beggiatoa* and high subsurface temperatures (> 80°C) (Gundersen et al., 1992; McKay et al., 2016). Estimates presented here represent single instances in time and are not adequate to determine temporal variability

To support the estimated range in subsurface fluid flux presented here, it is likely that seawater recharge is occurring as sedimentation alone cannot maintain relative seafloor position. Such a process would have to be supported by an underpressured basement relative to local hydrostatic conditions (Fisher et al., 2001). Although we did not measure, nor can we verify the presence of an underpressured basement, we did find fluid recharge conditions for two sediment cores, one with a significant fluid flux of $-3.4 \pm 1.7 \text{ mL cm}^{-2} \text{ day}^{-1}$. While intriguing, we cannot disregard the potential that these results could be attributed to the presence of an additional ^{224}Ra sink. This site has been identified as unique relative to other mat-covered Guaymas Basin sediments observed as of 2017 (Teske et al., 2016) and happens to be situated at the base of an abyssal hill where fluid recharge is more likely (Fisher et al., 2001). It is unclear from this work

which explanation is appropriate until additional chemical profiling during a later cruise (AT 42-05) can be evaluated.

4.5. References

- Aharon, P., Van Gent, D., Fu, B., and Scott, L.M., 2001. Fate and effects of barium and radium-rich fluid emissions from hydrocarbon seeps on the benthic habitats of the Gulf of Mexico offshore Louisiana. OCS Study MMS 2001-004. Prepared by the Louisiana State University, Coastal Marine Institute. U.S. Department of the Interior, Minerals Management Service, Gulf of Mexico OCS Region, New Orleans, LA. 142 pp.
- Bernhard, J.M., Buck, K.R., Farmer, M.A., Bowser, S.S., 2000. The Santa Barbara Basin is a symbiosis oasis. *Nature* 403, 77–80. <https://doi.org/10.1038/47476>
- Biddle, J.F., Cardman, Z., Mendlovitz, H., Albert, D.B., Lloyd, K.G., Boetius, A., Teske, A., 2012. Anaerobic oxidation of methane at different temperature regimes in Guaymas Basin hydrothermal sediments. *The ISME Journal* 6, 1018–1031. <https://doi.org/10.1038/ismej.2011.164>
- Bris, N.L., Arnaud-Haond, S., Beaulieu, S., Cordes, E., Hilario, A., Rogers, A., van de Gaever, S., Wantanabe, H., 2016. Chapter 45. Hydrothermal vents and cold seeps. *The First Global Integrated Marine Assessment – World Oceans Assessment*.
- Cai, P., Shi, X., Moore, W.S., Dai, M., 2012. Measurement of ^{224}Ra : ^{228}Th disequilibrium in coastal sediments using a delayed coincidence counter. *Marine Chemistry* 138–139, 1–6. <https://doi.org/10.1016/j.marchem.2012.05.004>.
- Campbell, A.C., Bowers, T.S., Measures, C.I., Falknew, K.K., Khadem, M., Edmond, J.M., 1988. A time series of vent fluid compositions from 21°N, East Pacific Rise (1979, 1981, 1985), and the Guaymas Basin, Gulf of California (1982, 1985). *Journal of Geophysical Research* 93:B5, 4537–4549. <https://doi.org/10.1029/JB093iB05p04537>
- Clarke, A., 2014. The thermal limits to life on Earth. *International Journal of Astrobiology* 13:2, 141–154. doi:10.1017/S1473550413000438
- Clegg, S.L., Whitfield, M., 1991. A generalized model for the scavenging of trace metals in the open ocean—II. Thorium scavenging. *Deep Sea Research Part A. Oceanographic Research Papers* 38, 91–120. [https://doi.org/10.1016/0198-0149\(91\)90056-L](https://doi.org/10.1016/0198-0149(91)90056-L)
- Colbert, S.L., Hammond, D.E., 2008. Shoreline and seafloor fluxes of water and short-lived Ra isotopes to surface water of San Pedro Bay, CA. *Marine Chemistry* 108, 1–17. <https://doi.org/10.1016/j.marchem.2007.09.004>
- Curry, J.R., Moore, D.G., Aguayo, E.J., 1979. Leg 64 seeks evidence on development of basin. *Geotimes* 24:7, 18–20.
- Dowell, F., Cardman, Z., Dasarathy, S., Kellermann, M.Y., Lipp, J.S., Ruff, S.E., Biddle, J.F., McKay, L.J., MacGregor, B.J., Lloyd, K.G., Albert, D.B., Mendlovitz, H., Hinrichs, K.-U., Teske, A., 2016. Microbial communities in methane- and short chain alkane-rich

- hydrothermal sediments of Guaymas Basin. *Frontiers in Microbiology* 7, 17.
<https://doi.org/10.3389/fmicb.2016.00017>
- Fisher, A.T., Becker, K., 1991. Heat flow, hydrothermal circulation and basalt intrusions in the Guaymas Basin, Gulf of California. *Earth and Planetary Science Letters* 103, 84–99.
[https://doi.org/10.1016/0012-821X\(91\)90152-8](https://doi.org/10.1016/0012-821X(91)90152-8)
- Fisher, A.T., Giambalvo, E., Sclater, J., Kastner, M., Ransom, B., Weinstein, Y., Lonsdale, P., 2001. Heat flow, sediment and pore fluid chemistry, and hydrothermal circulation on the east flank of Alarcon Ridge, Gulf of California. *Earth and Planetary Science Letters* 188, 521–534. [https://doi.org/10.1016/S0012-821X\(01\)00310-7](https://doi.org/10.1016/S0012-821X(01)00310-7)
- Garfunkel, Z., Zak, I., Freund, R., 1981. Active faulting in the Dead Sea Rift. *Tectonophysics* 80:1-4, 1-26.
- German, C.R., Ramirez-Llodra, E., Baker, M.C., Tyler, P.A., ChEss Scientific Steering Committee, 2011. Deep-water chemosynthesis ecosystem research during the census of marine life decade and beyond: A proposed deep-ocean road map. *PLOS ONE* 6:8 e23529
- Gieskes, J.M., Kastner, M., Einsele, G., Kelts, K., Niemitz, J., 1982. 55. Hydrothermal activity in the Guaymas Basin, Gulf of California: A synthesis. 1159-1167.
- Gundersen, J.K., Jorgensen, B.B., Larsen, E., Jannasch, H.W., 1992. Mats of giant sulphur bacteria on deep-sea sediments due to fluctuating hydrothermal flow. *Nature* 360, 454.
<https://doi.org/10.1038/360454a0>
- Holler, T., Widdel, F., Knittel, K., Amann, R., Kellermann, M.Y., Hinrichs, K.-U., Teske, A., Boetius, A., Wegener, G., 2011. Thermophilic anaerobic oxidation of methane by marine microbial consortia. *International Society of Microbial Ecology Journal* 5, 1946–1956.
<https://doi.org/10.1038/ismej.2011.77>
- Kiel, S., 2009. The vent and seep biota – Aspects from microbes to ecosystems. Eds: Landman NH, Harries P. Springer Dordrecht Heidelberg London New York.
- Lauer, R.M., Fisher, A.T., Winslow, D.M., 2018. Three-dimensional models of hydrothermal circulation through a seamount network on fast-spreading crust. *Earth and Planetary Science Letters* 501, 138–151. <https://doi.org/10.1016/j.epsl.2018.08.025>
- Lonsdale, P., Becker, K., 1985. Hydrothermal plumes, hot springs, and conductive heat flow in the Southern Trough of Guaymas Basin. *Earth and Planetary Science Letters* 73, 211–225. [https://doi.org/10.1016/0012-821X\(85\)90070-6z](https://doi.org/10.1016/0012-821X(85)90070-6z)
- MacGregor, B.J., Biddle, J.F., Harbort, C., Matthyse, A.G., Teske, A., 2013a. Sulfide oxidation, nitrate respiration, carbon acquisition, and electron transport pathways suggested by the

- draft genome of a single orange Guaymas Basin *Beggiatoa* (*Cand. Maribeggiatoa*) sp. filament. *Marine Genomics* 11, 53–65. <https://doi.org/10.1016/j.margen.2013.08.001>
- MacGregor, B.J., Biddle, J.F., Siebert, J.R., Staunton, E., Hegg, E.L., Matthyse, A.G., Teske, A., 2013b. Why orange Guaymas Basin *Beggiatoa* spp. are orange: single-filament-genome-enabled identification of an abundant octaheme cytochrome with hydroxylamine oxidase, hydrazine oxidase, and nitrite reductase activities. *Applied and Environmental Microbiology* 79, 1183–1190. <https://doi.org/10.1128/AEM.02538-12>
- McKay, L., Klokman, V.W., Mendlovitz, H.P., LaRowe, D.E., Hoer, D.R., Albert, D., Amend, J.P., Teske, A., 2016. Thermal and geochemical influences on microbial biogeography in the hydrothermal sediments of Guaymas Basin, Gulf of California. *Environmental Microbiology Reports* 8, 150–161. <https://doi.org/10.1111/1758-2229.12365>
- McKay, L.J., MacGregor, B.J., Biddle, J.F., Albert, D.B., Mendlovitz, H.P., Hoer, D.R., Lipp, J.S., Lloyd, K.G., Teske, A.P., 2012. Spatial heterogeneity and underlying geochemistry of phylogenetically diverse orange and white *Beggiatoa* mats in Guaymas Basin hydrothermal sediments. *Deep Sea Research Part I: Oceanographic Research Papers*, 67, 21-31. doi.org/10.1016/j.dsr.2012.04.011.
- Moore, W.S., 1976. Sampling ^{228}Ra in the deep ocean. *Deep-Sea Research* 23, 647-651.
- Moore, W.S., 2008. Fifteen years experience in measuring ^{224}Ra and ^{223}Ra by delayed-coincidence counting. *Marine Chemistry, Measurement of Radium and Actinium Isotopes in the marine environment* 109, 188–197. <https://doi.org/10.1016/j.marchem.2007.06.015>
- Moore, W., Arnold, R., 1996. Measurement of ^{223}Ra and ^{224}Ra in coastal waters using a delayed coincidence counter. *Journal of Geophysical Research* 101, 1321–1329.
- Mottl, M.J., Wheat, C.G., 1994. Hydrothermal circulation through mid-ocean ridge flanks: Fluxes of heat and magnesium. *Geochimica et Cosmochimica Acta* 58, 2225–2237. [https://doi.org/10.1016/0016-7037\(94\)90007-8](https://doi.org/10.1016/0016-7037(94)90007-8)
- Nelson, D.C., Wirsén, C.O., Jannasch, H.W., 1989. Characterization of large, autotrophic *Beggiatoa* spp. abundant at hydrothermal vents of the Guaymas Basin. *Applied and Environmental Microbiology* 55:11, 2909-2917.
- Ondréas, H., Scalabrin, C., Fouquet, Y., Godfroy, A., 2018. Recent high-resolution mapping of Guaymas hydrothermal fields (Southern Trough). *Bulletin de la Société Géologique de France* 189. <https://doi.org/10.1051/bsgf/2018005>
- Orcutt, B.N., Sylvan, J.B., Knab, N.J., Edwards, K.J., 2011. Microbial ecology of the dark ocean above, at, and below the seafloor. *Microbiology and Molecular Biology Reviews* 75:2 361-422.

- Portail, M., Olu, K., Dubois, S.F., Escobar-Briones, E., Gelinas, Y., Menot, L., Sarrazin, J., 2016. Food-Web Complexity in Guaymas Basin Hydrothermal Vents and Cold Seeps. PLOS ONE 11, e0162263. <https://doi.org/10.1371/journal.pone.0162263>
- Rama, Moore, W.S., 1996. Using the radium quartet for evaluating groundwater input and water exchange in salt marshes. *Geochimica et Cosmochimica Acta* 60:23, 4645-4652.
- Ruff, S.E., Biddle, J.F., Teske, A.P., Knittel, K., Boetius, A., Ramette, A., 2015. Global dispersion and local diversification of the methane seep microbiome. *PNAS* 112, 4015–4020. <https://doi.org/10.1073/pnas.1421865112>
- Schuster, S.C., 2008. Next-generation sequencing transforms today's biology. *Nature Methods* 5:1, 16-18.
- Smoak, J.M., Moore, W.S., Thunell, R.C., Shaw, T.J., 1999. Comparison of ²³⁴Th, ²²⁸Th, and ²¹⁰Pb fluxes with fluxes of major sediment components in the Guaymas Basin, Gulf of California. *Marine Chemistry* 65, 177–194. [https://doi.org/10.1016/S0304-4203\(98\)00095-4](https://doi.org/10.1016/S0304-4203(98)00095-4)
- Suess, E., 2014. Marine cold seeps and their manifestations: geological control, biogeochemical criteria and environmental conditions. *International Journal of Earth Sciences: Geologische Rundschau* 103 1889-1916. doi: 10.1007/s00531-014-1010-0
- Takai, K., Nakamura, K., 2010. Archaeal diversity and community development in deep-sea hydrothermal vents. *Current Opinion in Microbiology* 14:3, 282-291.
- Teske, A., Callaghan, A.V., LaRowe, D.E., 2014. Biosphere frontiers of subsurface life in the sedimented hydrothermal system of Guaymas Basin. *Frontiers in Microbiology* 5. <https://doi.org/10.3389/fmicb.2014.00362>
- Teske, A., de Beer, D., McKay, L., Tivey, M., Biddle, J., Hoer, D., Lloyd, K., Lever, M., Røy, H., Albert, D., Mendlovitz, H., Macgregor, B., 2016. The Guaymas Basin hiking guide to hydrothermal mounds, chimneys, and microbial mats: complex seafloor expressions of subsurface hydrothermal circulation. *Frontiers in Microbiology* 7:75, 1-23. doi:10.389/fmicb.2016.00075
- Walker, B. D., McCarthy, M. D., Fisher, A. T. and Guilderson, T. P., 2008. Dissolved inorganic carbon isotopic composition of low-temperature axial and ridge-flank hydrothermal fluids of the Juan de Fuca Ridge. *Marine Chemistry* 108:1, 123–136. doi:10.1016/j.marchem.2007.11.002

CHAPTER 5

GULF OF MEXICO AND GUAYMAS BASIN FLUID FLUXES

5.1. Gulf of Mexico and Guaymas Basin Revisited

The deep-sea is used here to describe water depths greater than 200 m, and is considered to be our planet's largest potential living space (Orcutt et al., 2011). In this region, life is either linked to the surface ocean by utilizing organic carbon generated by photosynthesis or decoupled from the surface, thriving on deep ocean chemosynthesis (Jannasch and Wirsen, 1979). Chemosynthetic communities utilize methane and sulfate to generate 'new' organic carbon. In the deep-sea, the reduced compounds are of lithogenic origin and only made available to these communities by upward fluid migration through sediments (Ramirez-Llodra et al., 2010). Such fluid transport may arrive at the seafloor with subsequent discharge occurring vigorously (venting) or diffusely (seepage) with greater macrofaunal density and diversity associated with seepage rather than venting (Portail et al., 2015).

Submarine seepage, regardless of driving force, has been found to support communities with similar classifications at genera and family levels, including bacterial mats and symbiont-hosting invertebrates like siboglinid tubeworms, vesicomycid clams, and mytilid mussels (Tunnicliffe et al., 1998; Duperron et al., 2013). Enrichments of inorganic carbon and sulfide support chemosynthetic communities associated with fluid discharge similarly between ambient ocean (cold seep) and elevated (hydrothermal seep) temperature waters, although the fluid flux

supplying those chemicals may differ in space and time (Levin et al., 2016). It is generally understood that community distribution can be dependent upon fluid flux (Gundersen et al., 1992; Sibuet and Olu 1998; Levin, 2005) with greater methane and sulfide concentrations often characteristic of seep compared to non-seep sediments. However, gradients distinguishing seep-affected areas (i.e., the seepage footprint) are poorly constrained and thus warrant further exploration (Suess, 2014; Levin et al., 2016).

Despite the suspected dependency of these communities on materials supplied via seeping fluid, seepage rates remain poorly constrained (Armstrong et al., 2012; Suess, 2014; Levin et al., 2016; Teske et al., 2016). To address the need for fluid flux studies across seepage habitat types, we have presented a conceptual model designed to study deep-sea fluid transport through surficial sediments recovered from regions characteristic of cold and hydrothermal seeps. This vertical exchange model was subsequently tested using three sediment cores recovered from cold seep and control sites within deep-sea regions of Gulf of Mexico. Effective fluid flux estimates were then evaluated and spatial associations between microbial mat, subsurface temperature were identified for Guaymas Basin, a site impacted by hydrothermal activity.

Our vertical exchange model, modified from Krest and Harvey (2003), evaluates fluid flux through deep-sea sediments by utilizing a soluble radioisotope, ^{224}Ra , which is distributed throughout interstitial porefluid of vertically adjoining sediment layers as fluid migration occurs. The activity of aqueous ^{224}Ra in any layer relative to that in a neighboring layer may be used to determine porefluid residence time if the equilibrium activity of porefluid ^{224}Ra in contact with those sediments is known. Accuracy of the model is qualitatively evaluated using sediments recovered from both the Gulf of Mexico and the Gulf of California where cold and hydrothermal

seepage, respectively, has been observed regionally but fluid exchange rates through sediments have traditionally been inferred (e.g., Joye et al., 2004; Teske et al., 2016, McKay et al., 2012).

Our vertical exchange model is first tested in areas of suspected seepage within the Gulf of Mexico. Seepage indicators included a water column feature detected via multibeam sonar imaging and a bacterial mat observed using the HOV *Alvin*. We identify a range in porefluid residence times of 0.6 to 4 days for sites for suspected seepage sites. Such short residence times are explained by 1 dimensional advective transport velocities of 5.9 and 1.4 cm day⁻¹ and 1-dimensional vertical volumetric fluid fluxes of 4.6 and 1.0 mL cm⁻² day⁻¹, respectively. We demonstrate that results from the vertical exchange model are equal to those determined via a 1-D advection/diffusion equation (e.g., Krest and Harvey, 2003). In comparison, average porefluid residence time from 0 to 16 cmbsf per 4 cm sediment layer in our control core was 6.6 days, with an average advective vertical velocity of -1.7 cm day⁻¹ and a fluid flux estimate of -1.3 mL cm⁻² day⁻¹. From this effort, we have drawn the following conclusions: (1) model results of effective fluid flux out of the sediments are reasonable and supported by ancillary observational data; and (2) the effective fluid flux magnitudes determined using the vertical exchange model are within the range reported in the literature and are reasonable with what is to be expected, especially between control and seepage sites.

We supplement our qualitative model evaluation by applying the vertical exchange model to ²²⁴Ra profiles recovered from Guaymas Basin, a hydrothermal discharge site within the Gulf of California. Although logistical constraints required modification of the approach utilized in the Gulf of Mexico, fluid flux estimates using the vertical exchange model were successfully derived. The total exchangeable pool of ²²⁴Ra was evaluated and subsequently converted into aqueous fractions after a regional assessment of radium partitioning was complete and K_d was determined.

One advantage of such approach was the removal of any potential uncertainty in ^{224}Ra partitioning with a changing porosity. Spatial relationships between fluid flux and microbial mat cover were found for Guaymas Basin sediments with higher average fluid fluxes associated with mat-covered sediments than fluid fluxes through inconspicuous sediment cover. This result, again, provides qualitative verification for the model as these communities are known to be associated with greater supply rates of reduced compounds relative to surrounding sediment (Gundersen et al., 1992). We identify both a higher maximum fluid flux through orange microbial mat as well as a larger variability across different orange mats compared to white mat. Although subsurface temperature range was greater associated with orange mat, a significant direct relationship between white mat fluid flux and temperature was observed (Pearson's correlation; $r=0.98$). Temporally variable flow under orange *Beggiatoa* mats as has previously been suggested for especially high subsurface temperatures ($>40^\circ\text{C}$) (McKay et al., 2016) may have led to the lack of such a relationship between orange mat fluid flux and temperature. Results from this work suggest: (1) fluid flux estimates for sediment cores recovered from a hydrothermal setting are consistent with expectations that higher fluid fluxes are associated with bacterial mat compared to inconspicuous sediment cover; (2) spatial associations between subsurface temperature range and fluid flux through white mat suggest fluid flux may be moderated most greatly by the subsurface thermal gradients. (3) Fluid flux through orange mat appears unrelated to subsurface thermal gradients although orange filaments and subsurface temperature appear related. This may be explained by a mechanism other than thermal convection predominantly controlling fluid flux through some of the sediment cores recovered from ocean mat areas.

We attempt to draw comparisons between deep-sea seepage habitats as a summary of this work. To do so, we have synthesized porefluid isotope data from three cruises in the Gulf of

Mexico to determine the effective fluid flux across 14 sites. Sample collection efforts supporting this comparison did not control for a variety of factors including number of sediment cores and, perhaps more importantly, the number of cores where seepage is expected relative to the number of non-seep cores. Such a comparison is not intended to broadly characterize conditions across an entire seep habitat as sample collection from Guaymas Basin was not random and instead focused on microbial mat covered sediments. In contrast, most sediment cores recovered from the Gulf of Mexico were collected using a shipboard deployment and recovery system and represent a less precise core sampling method. Nonetheless, there is value in discussion on effective fluid flux estimated for deep-sea sediments recovered from the Gulf of Mexico and Guaymas Basin. As a precursor to this effort, we first introduce all fluid flux observations for the Gulf of Mexico.

5.2. Gulf of Mexico Fluid Flux Observations

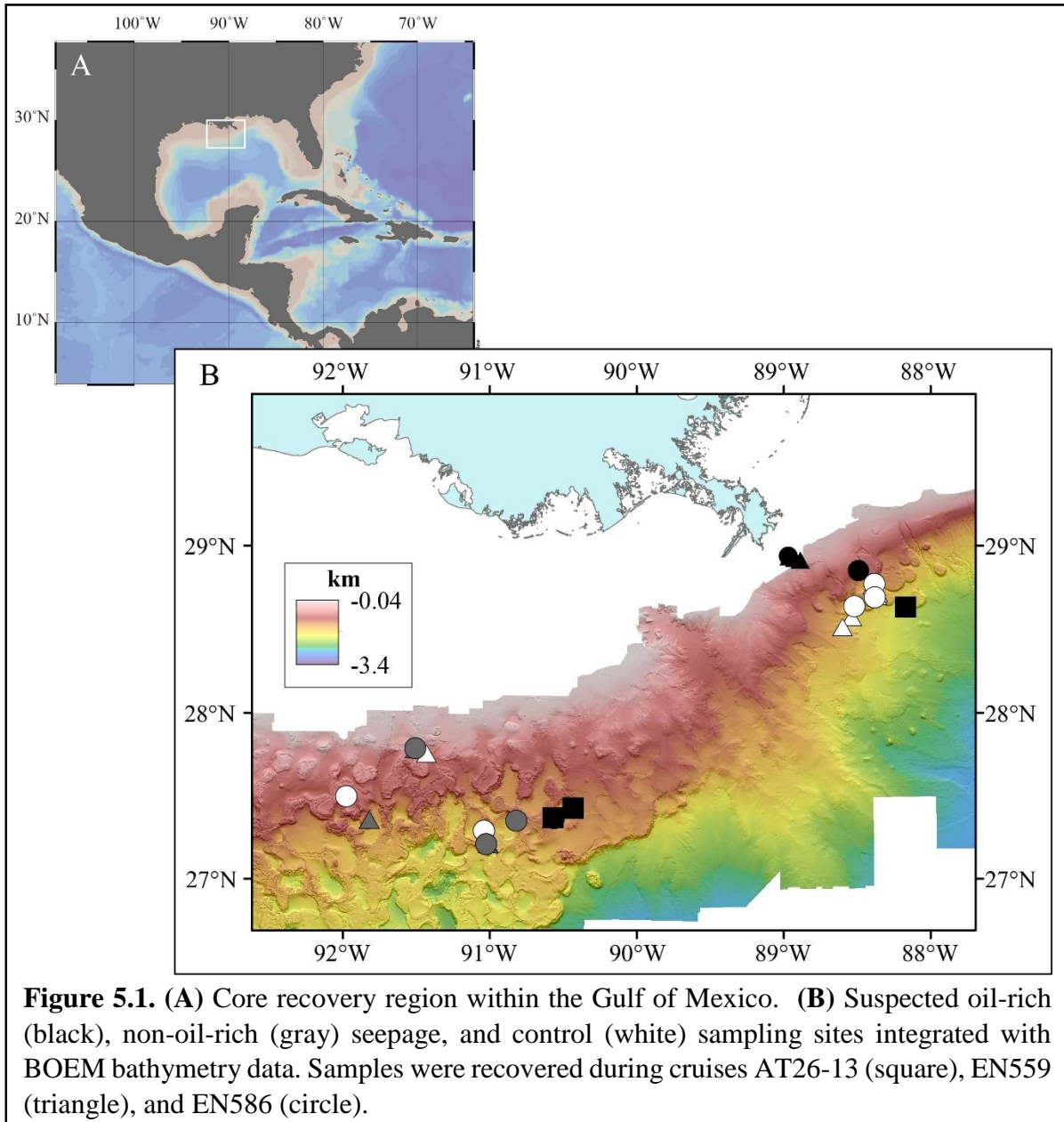
In total, 35 sediment cores were collected from the Gulf of Mexico during three cruises from 2014 through 2016 (Figure 5.1; Table A.1), including the 3 cores previously described in Chapter 3. Recovered cores were no more than 50 cm in length and represent areas ranging from Deepwater Horizon oil spill impact sites, to natural oil and gas seeps, to deep-water control sites. Fluid flux was determined by applying our vertical exchange model to aqueous porefluid ^{224}Ra distributions (0 to 20 cmbsf) in interstitial water recovered via centrifugation and concentrated onto Mn-fiber (Chapter 2 and Chapter 3; Table A.2).

We first consider local-scale variability in effective fluid flux from one seepage site where sampling was most frequent across GOM cruises. Green Canyon lease block 600 (GC600) is a well-studied natural hydrocarbon seep site (e.g., Krajewski et al., 2018; Rogener et al., 2018).

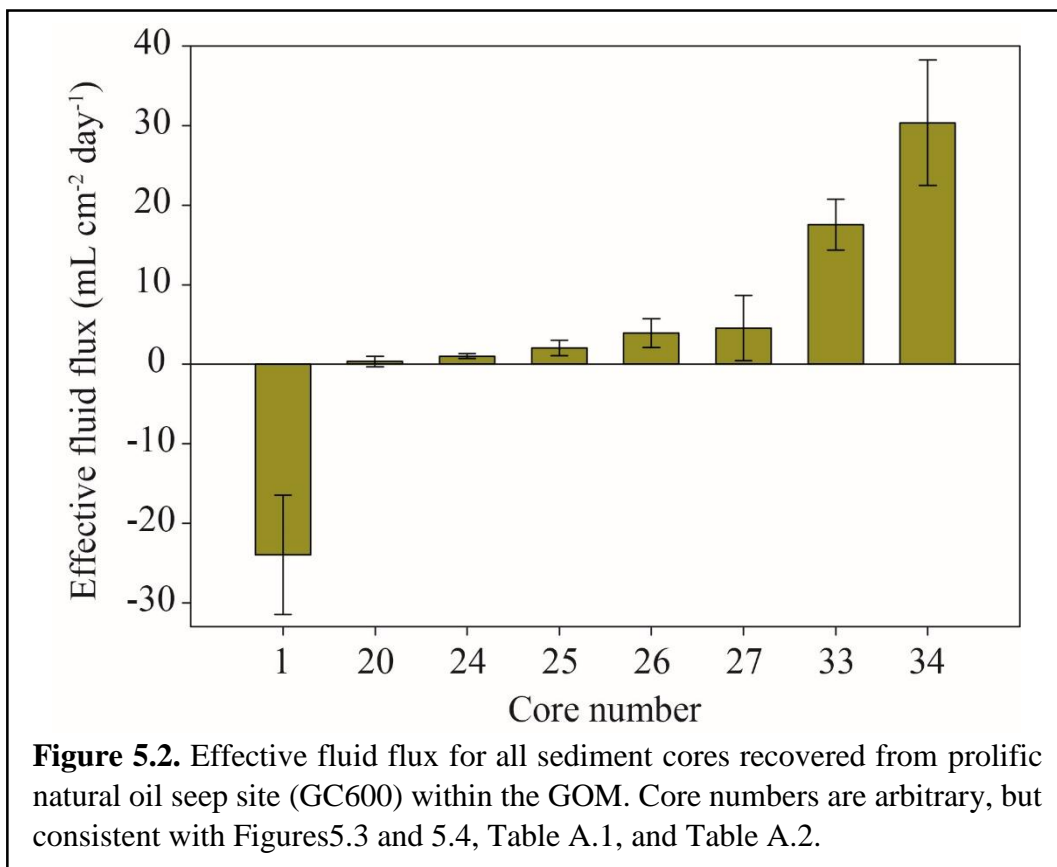
Sediment cores recovered from this site were consistently oil-rich with dark oil patches found before and after centrifugation for most sampled depths. For this site, effective fluid flux ranged from -24.0 ± 7.5 to 30.4 ± 7.9 mL cm⁻² day⁻¹ (Figure 5.2). Although fluid flux through cold seep sediment may exhibit tidal periodicity (e.g., Torres et al., 2002; Solomon et al., 2008; Johansen et al., 2017), fluid flux and tidal stage for all cores recovered from GC600 (Figure 5.2) were not significantly related (Pierson's correlation; $r=-0.179$, $n=8$; $p>0.05$). Instead, the variability in fluid flux may be indicative of heterogeneity across the region with differences in effective fluid flux that are consistent with highly localized seafloor seepage communities. Although the magnitude of effective fluid flux was not found to be related to tidal stage alone, it has been shown that deep-sea seepage can be irregular so our estimated rates may not apply longer time scales (e.g., years) as is a common for seepage studies (Torres et al., 2002).

While downward flow into the sediments has been suggested for a variety of cold seeps across the globe, we do not believe that mechanism can necessarily be invoked to explain our large negative value for Core number 1. This core was unique in that active fizzing, bubbling, and apparent discharge was observed to be occurring even after recovering the core onto the ship's deck. The overlying core-top water was oily, leaving all sampling material coated in a film of sticky, tar-like oil. While this phenomenon may not be unique to Core number 1, it has not been observed to that degree for any other core described here. The effective fluid flux suggests a strong fluid transport into the sediments, but we do not believe this finding was characteristic of the conditions occurring at the seafloor and instead attribute this result to an artifact of recovery. We speculate that these particularly gas-charged sediments substantially out-gassed during core ascent and recovery. Gas ebullition through sediments can result in porefluid transport, but the magnitude

and directionality may be more related to gas bubble migration than that of the porefluids themselves (Klein, 2006).



If this explanation is appropriate for Core number 1, it would seem that the vertical exchange model may significantly underestimate any sedimentary gas flux if the size of each mixing cell is smaller than the sampling resolution. In this situation, over a sampled area, the flow condition could be both into (-z) and out of (+z) the sediments. Because we are evaluating the net circumstance of ^{224}Ra transport, we would not detect the true volumetric flux from such localized exchange areas. However, limiting integrating over time and/or space is in this application, it is an unfortunate circumstance of evaluating flow using chemical proxies, including chloride, methane, and calcium. However, in-situ bubble driven circulation may be distinguished from significant gas ebullition as a consequence of ascent by evaluating the sediment interface and the clarity of the overlying water. Gas discharge occurring post-collection may cause resuspension of bottom sediments, resulting in cloudy overlying water. This occurrence has been observed throughout these cruises, so cores with these characteristics were not used here. Excluding Core number 1, we estimate an average effective fluid flux through GC600 sediments of $8.6 \pm 2.7 \text{ mL cm}^{-2} \text{ day}^{-1}$ (Figure 5.2). We will not further consider Core number 1 in our discussion.



The Gulf of Mexico is known to contain seepage sites that discharge not only oil-rich fluid, but also fluids enriched in methane and sulfide (Joye et al., 2004). To examine any potential differences between effective fluid flux and porefluid characteristics, we categorize our suspected seepage sites into two groups: oil-rich and non-oil-rich. These are only qualitative groupings of the samples as hydrocarbon concentrations were not measured for these specific cores; for some cores, we did confirm hydrocarbon presence via optical fluorescence under a UV light, but this approach still only provides a qualitative assessment. We define oil-rich cores as those in which oil was observed either before or after centrifuging, whereas non-oil-rich cores are those from seepage sites where sediments cores did not exhibit UV fluorescence and no oil was observed before or after centrifuging.

Overall, 21 sediment cores were recovered from suspected seepage sites, including 13 from oil-rich sites (Taylor Energy, GC600, MC118, MC253; Figure 5.3A) and 8 from non-oil-rich sites (GC574, GC185, and GC767; Figure 5.3B). We estimate an average effective fluid flux of $8.4 \pm 4.2 \text{ mL cm}^{-2} \text{ day}^{-1}$ for oil-rich sites compared to an average of $1.1 \pm 2.0 \text{ mL cm}^{-2} \text{ day}^{-1}$ for non-oil cores. Although no obvious discharge indicators (e.g., cloudy overlying water) were noted for non-oil-rich cores, the lower effective fluid flux determined for these cores could indicate complicated circulation patterns. For example, water driven out of the sediments by rising gas bubbles may be replaced by down-flowing overlying water as suggested by recharge occurring up to 10 cmbsf (O'hara et al., 1995; Zimmerman et al., 1997). However, this explanation is purely speculative as ancillary data to support this process for these specific sediment cores does not exist. Unlike Core number 1, this process would not be indicative of a sampling artifact and rather could indicate complicated fluid circulation surrounding highly localized gas seeps.

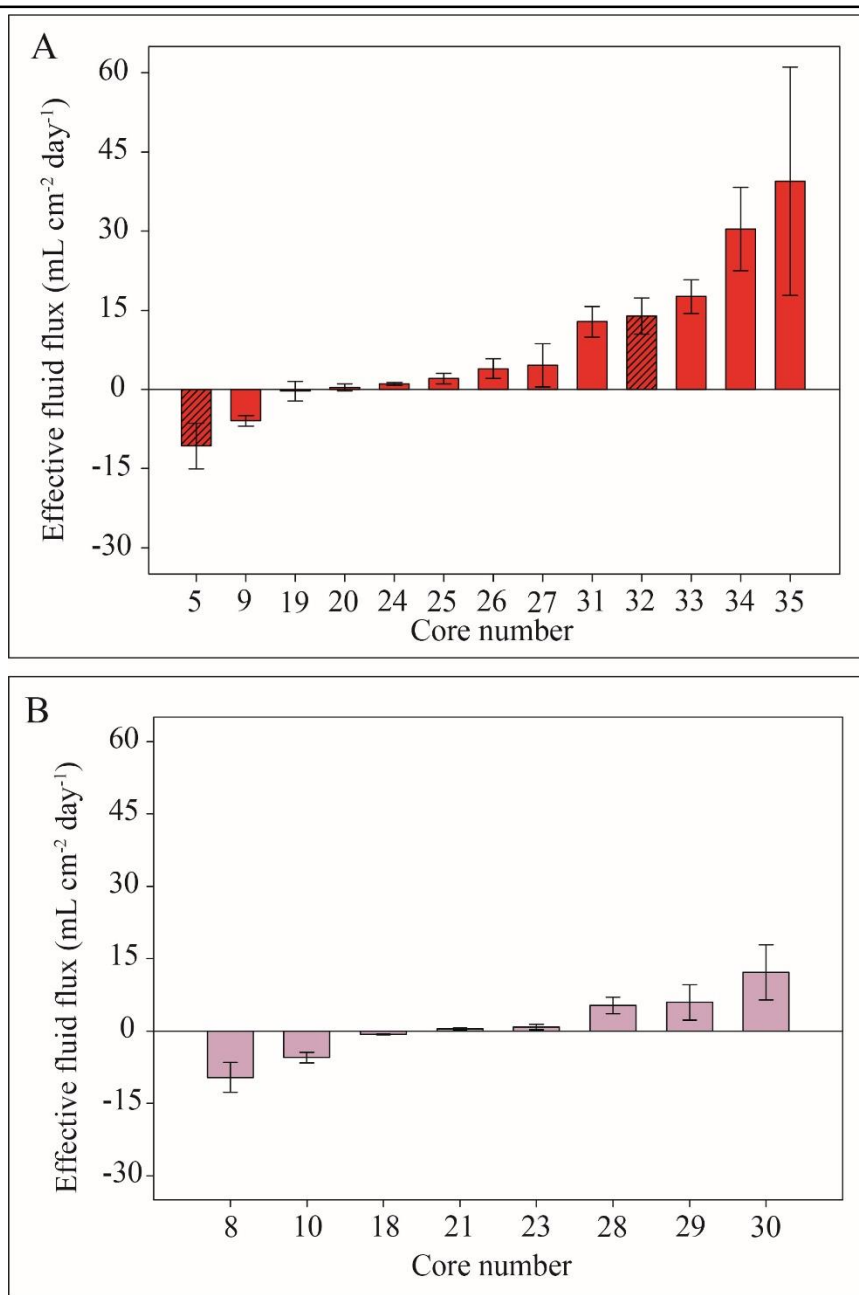


Figure 5.3. Effective fluid flux for suspected seepage sites distinguished by (A) oil-rich and (B) non-oil-rich porefluid characteristics for sediment cores recovered from the Gulf of Mexico. (A) Hatched bars designate data associated with Taylor Energy (MC20), a shallow water site situated in water depths of ~120m. All other sampling sites are located at depths >200 m.

We collected 3 sediment cores from the Taylor Energy site where 21 hydrocarbon extraction wells were broken off and buried under a mud flow during Hurricane Ivan (Kaiser, 2015). These wells continue to leak oil through overlying sediments and into the water column. Fluid fluxes estimated for sediment cores recovered from the Taylor Energy site (core numbers 5, 17, and 32; Figure 5.3A) show a full range of fluid transport conditions, from recharge at $-0.3 \pm 1.8 \text{ mL cm}^{-2} \text{ day}^{-1}$ to discharge at $13.9 \pm 3.4 \text{ mL cm}^{-2} \text{ day}^{-1}$. These data are especially intriguing as recent reporting has reinvigorated discussion regarding remediation strategies for the failed structure as chronic discharge persisting for more than a decade has been ongoing (Asl et al., 2016). Here, we have some indication that vertical fluid transport was occurring in one of three cores recovered from this site.

5.3. Gulf of Mexico and Guaymas Basin Comparison

A similar range in fluid flux was identified for both the Gulf of Mexico and Guaymas Basin (Figure 5.4). Notably, relative uncertainties are much lower for Gulf of Mexico estimates due to the additional error associated with the K_d value needed to convert to aqueous ^{224}Ra activities from solid phase activity measurements from Guaymas Basin. Error could be reduced by evaluation of aqueous ^{224}Ra directly as was done for Gulf of Mexico samples, but this approach was not possible for Guaymas Basin samples due to logistical issues with equipment. Yet, an advantage to solid phase extraction is a higher sampling resolution because less sediment volume is required to achieve desired counting statistics ($\leq 10\%$ uncertainty). In fact, if distribution coefficients can be better constrained, solid phase extractions may allow sampling intervals of 1 cm (Cai et al., 2012) as compared to 4 cm necessary for aqueous ^{224}Ra evaluation (Chapter 3). This modification could

support studies to better test the assumption of no lateral flow by increasing vertical resolution without necessarily increasing the error. Furthermore, because we take the advective velocity to equal the sampling interval divided by the residence time, sampling over smaller intervals allows detection of slower flow rates by as much as a four-fold decrease (assuming a 21 day residence time and a change in sampling interval from 1 to 4 cm).

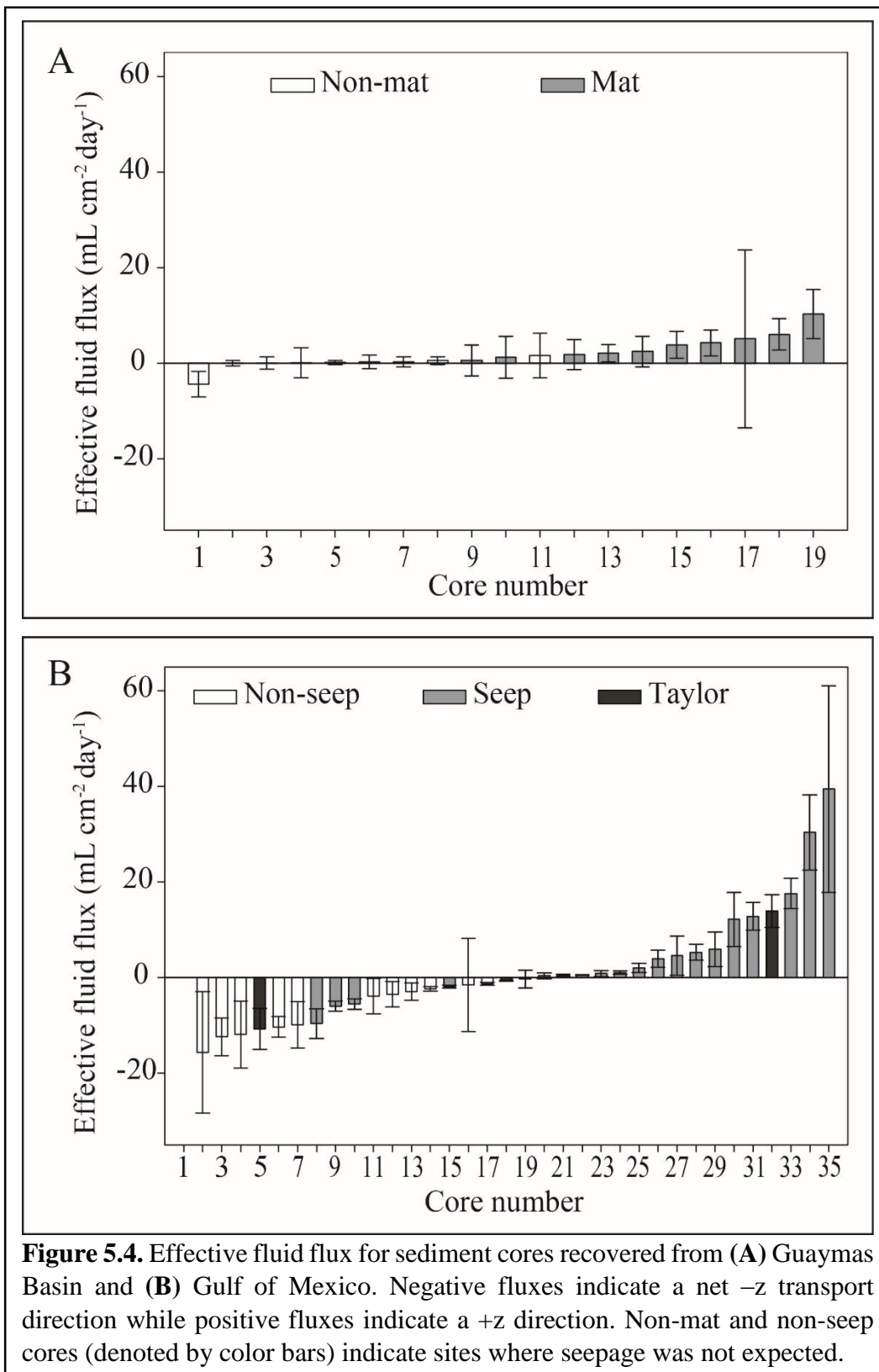
For both the GOM and Guaymas Basin, fluid flux out of the sediments was identified at higher rates for sediment cores recovered from areas where seepage was suspected. This qualitative verification supports our approach to studying deep-sea fluid fluxes through surficial sediments despite the fact that seepage indicators varied between habitat types, primarily because of the different core recovery methods. For example, all sediment cores from Guaymas Basin were collected using the HOV *Alvin*, so we could target specific microbial mats to retrieve sediment cores where seepage was suspected. These cores are compared to cores recovered from inconspicuous sediment cover regions. The seepage footprint affecting surficial sediments may vary (Suess, 2014) as microbial mats range in size from $<1 \text{ m}^2$ to 20 m^2 (Torres et al., 2002; Teske et al., 2016). Sampling at this precision using a ship-based platform was not possible for most GOM cruises.

Fluid flux determined for these cores is compared to the effective fluid flux determined for control cores where seepage is not expected. Despite the expected heterogeneity of seafloor seepage expressions, we observed greater fluid flux estimates for sites where seepage was suspected compared to control/non-seep sites for the GOM (Figure 5.4A) and for Guaymas Basin (Figure 5.3B). We find an average fluid flux for sampled areas within the Gulf of Mexico of $5.6 \pm 3.3 \text{ mL cm}^{-2} \text{ day}^{-1}$ for all sites where seepage was suspected and an average of $-5.9 \pm 3.8 \text{ mL cm}^{-2} \text{ day}^{-1}$ for 13 non-seep sites. Similarly, in Guaymas Basin, mat covered sediments where seepage is

suspected show an average fluid flux of $3.5 \pm 4.8 \text{ mL cm}^{-2} \text{ day}^{-1}$ compared to non-mat covered cores with fluxes averaging $0.0 \pm 1.8 \text{ mL cm}^{-2} \text{ day}^{-1}$.

Our highest estimated fluid flux among all sediment cores was recovered from a cold seep in the Gulf of Mexico. While this result may be surprising, it likely does not indicate a fundamental difference between the two sites. Broad comparisons between the Gulf of Mexico and Guaymas Basin cannot be made as different sampling styles and seepage indicators were used for each basin. Yet, an identical species of bacteria has been identified at both sites (Jannasch et al., 1989; Zhang et al., 2005). We did recover two sediment cores from the GOM where bacterial filaments were similar to the white *Beggiatoa* within Guaymas Basin. Although the sample size is far too small for meaningful statistical assessment, fluid flux ranged from $0.4 \pm 0.7 \text{ mL cm}^{-2} \text{ day}^{-1}$ to $4.6 \pm 4.1 \text{ mL cm}^{-2} \text{ day}^{-1}$ for GOM mat-covered sediments and $1.2 \pm 4.4 \text{ mL cm}^{-2} \text{ day}^{-1}$ to $6.0 \pm 3.3 \text{ mL cm}^{-2} \text{ day}^{-1}$ for Guaymas Basin mat sediments. The lower fluid flux through GOM mat is interesting as fluid flux through white mat in Guaymas Basin was strongly related to subsurface temperature range. While fluid flux out of the sediments was observed in the both seepage habitats, control sites also exhibited similarities between sites. Here, 'control' is used to describe areas where no bacterial mat was observed and/or no indication of seepage is known for the region. While we did identify a few sediment cores where fluid flux was near zero, especially in the Gulf of Mexico, we occasionally estimate fairly significant downward fluid flux into the upper sediments. Although not all estimates are beyond the associated analytical error, we identified 16 of 35 sediment cores with a downward (negative) effective fluid flux (Figure 5.4). While this frequency appears significant, flow reversal mechanisms for muddy sediments have been proposed and additional indications of such phenomena have been observed at deep-sea seepage sites where inflow into the sediments can last hours to months (Henry et al., 1992; Linke et al, 1994; Zimmerman et al.,

1997; Torres et al., 2002; Levin, 2005). It has even been suspected that the average rate of flow driven by compaction is less than subsidence and balanced by the incorporation of seawater in the uppermost sediments (Bjørlykke, 1993). Another reasonable mechanism to explain these results may be a decreased localized sub-pressure where gas venting occurs which effectively decreases porefluid pressure below hydrostatic leading to the downward flow of interstitial water near discharge zones (Solomon et al., 2008). We suspect this process was not observed for Guaymas Basin because of sampling bias targeting mat sediments. Also, hydrothermal recharge may be more restricted because of elevated subsurface temperatures and may occur primarily through abyssal hills and other porous outcrops (Fisher et al., 2001; Lauer et al., 2018).



We have identified spatially variable fluid flux conditions where traditional indicators of seepage (oil/bubble plumes and bacterial mats) were associated with higher fluid fluxes for both the Gulf of Mexico and Guaymas Basin. However, in some instances, fluid flux out of the sediments was required to explain aqueous porefluid ^{224}Ra distributions for sediment cores where no supporting evidence of active seepage was identified – such results may suggest recent activation of porefluid flow at these sites. Control sites, especially where subsurface temperature was not elevated in Guaymas Basin, did not appear to exhibit a significant fluid flux. Fluid recharge may be occurring through sediments of both the Gulf of Mexico and Guaymas Basin, although exact mechanisms are unknown. Targeted sampling of bacterial mats (*Beggiatoa* spp.) between Gulf of Mexico and Guaymas Basin may allow a more quantitative comparison between the seepage habitats in future studies as comparing fluid flux across a common sediment cover characteristic could elucidate potential flow thresholds required for significant colonization.

5.4. References

- Armstrong, C.W., Foley, N.S., Tinch, R., van den Hove, S., 2012. Services from the deep: Steps towards valuation of deep sea goods and services. *Ecosystem Services* 2, 2–13. <https://doi.org/10.1016/j.ecoser.2012.07.001>
- Asl, S.D., Amos, J., Woods, P., Garcia-Pineda, O., MacDonald, I.R., 2016. Chronic, anthropogenic hydrocarbon discharges in the Gulf of Mexico. *Deep Sea Research Part II: Topical Studies in Oceanography, The Gulf of Mexico Ecosystem - before, during and after the Macondo Blowout* 129, 187–195. <https://doi.org/10.1016/j.dsr2.2014.12.006>
- Bjørlykke, K., 1993. Fluid flow in sedimentary basins. *Sedimentary Geology, Basin Analysis and Dynamics of Sedimentary Basin Evolution* 86, 137–158. [https://doi.org/10.1016/0037-0738\(93\)90137-T](https://doi.org/10.1016/0037-0738(93)90137-T)
- Bris, N.L., Arnaud-Haond, S., Beaulieu, S., Cordes, E., Hilario, A., Rogers, A., van de Gaever, S., Watanabe, H., 2016. Chapter 46 – Hydrothermal vents and cold seeps 18.
- Cai, P., Shi, X., Moore, W.S., Dai, M., 2012. Measurement of ^{224}Ra : ^{228}Th disequilibrium in coastal sediments using a delayed coincidence counter. *Marine Chemistry* 138–139, 1–6. <https://doi.org/10.1016/j.marchem.2012.05.004>
- Duperron, S., Gaudron, S.M., Rodrigues, C.F., Cunha, M.R., Decker, C., Olu, K., 2013. An overview of chemosynthetic symbioses in bivalves from the North Atlantic and Mediterranean Sea. *Biogeosciences* 10, 3241–3267.
- Fisher, A.T., Giambalvo, E., Sclater, J., Kastner, M., Ransom, B., Weinstein, Y., Lonsdale, P., 2001. Heat flow, sediment and pore fluid chemistry, and hydrothermal circulation on the east flank of Alarcon Ridge, Gulf of California. *Earth and Planetary Science Letters* 188, 521–534. [https://doi.org/10.1016/S0012-821X\(01\)00310-7](https://doi.org/10.1016/S0012-821X(01)00310-7)
- Gundersen, J.K., Jorgensen, B.B., Larsen, E., Jannasch, H.W., 1992. Mats of giant sulphur bacteria on deep-sea sediments due to fluctuating hydrothermal flow. *Nature* 360, 454. <https://doi.org/10.1038/360454a0>
- Henry, P., Foucher, J., Le Pichon, X., Sibuet, M., Kobayashi, K., Tarits, P., Chamot-Rooke, N., Furuta, T., Schultheiss, P., 1992. Interpretation of temperature measurements from the Kaiko-Nankai cruise: Modeling of fluid flow in clam colonies. *Earth and Planetary Science Letters* 109, 355–371. [https://doi.org/10.1016/0012-821X\(92\)90098-G](https://doi.org/10.1016/0012-821X(92)90098-G)
- Jannasch, H.W., Wirsén, C.O., 1979. Chemosynthetic primary production at East Pacific sea floor spreading centers. *BioScience* 29, 592–598. <https://doi.org/10.2307/1307765>
- Jannasch, H.W., Nelson, D.C., Wirsén, C.O., 1989. Massive natural occurrence of unusually large bacteria (*Beggiatoa* sp.) at hydrothermal deep-sea vent site. *Nature* 342, 834–836.

- Johansen, C., Todd, A.C., MacDonald, I.R., 2017. Time series video analysis of bubble release processes at natural hydrocarbon seeps in the Northern Gulf of Mexico. *Marine and Petroleum Geology* 82, 21–34. <https://doi.org/10.1016/j.marpetgeo.2017.01.014>
- Joye, S.B., Boetius, A., Orcutt, B.N., Montoya, J.P., Schulz, H.N., Erickson, M.J., Lugo, S.K., 2004. The anaerobic oxidation of methane and sulfate reduction in sediments from Gulf of Mexico cold seeps. *Chemical Geology* 205, 219–238. <https://doi.org/10.1016/j.chemgeo.2003.12.019>
- Kaiser, M.J., 2015. Hurricane clean-up activity in the Gulf of Mexico, 2004–2013. *Marine Policy* 51, 512–526. <https://doi.org/10.1016/j.marpol.2014.09.001>
- Krajewski, L.C., Lobodin, V.V., Johansen, C., Bartges, T.E., Maksimova, E.V., MacDonald, I.R., Marshall, A.G., 2018. Linking natural oil seeps from the Gulf of Mexico to their origin by use of Fourier transform ion cyclotron resonance mass spectrometry. *Environmental Science and Technology*. 52, 1365–1374. <https://doi.org/10.1021/acs.est.7b04445>
- Klein, S., 2006. Sediment porewater exchange and solute release during ebullition. *Marine Chemistry*, 8th International Estuarine Biogeochemistry Symposium - Introduction 102, 60–71. <https://doi.org/10.1016/j.marchem.2005.09.014>
- Krest, J.M., Harvey, J.W., 2003. Using natural distributions of short-lived radium isotopes to quantify groundwater discharge and recharge. *Limnology and Oceanography* 48, 290–298. <https://doi.org/10.4319/lo.2003.48.1.0290>
- Lauer, R.M., Fisher, A.T., Winslow, D.M., 2018. Three-dimensional models of hydrothermal circulation through a seamount network on fast-spreading crust. *Earth and Planetary Science Letters* 501, 138–151. <https://doi.org/10.1016/j.epsl.2018.08.025>
- Levin, L., 2005. Ecology of Cold Seep Sediments: Interactions of fauna with flow, chemistry, and microbes, in: Gibson, R., Gordon, J., Atkinson, R. (Eds.), *Oceanography and Marine Biology*. CRC Press, pp. 1–46. <https://doi.org/10.1201/9781420037449.ch1>
- Levin, L.A., Baco, A.R., Bowden, D.A., Colaco, A., Cordes, E.E., Cunha, M.R., Demopoulos, A.W.J., Gobin, J., Grupe, B.M., Le, J., Metaxas, A., Netburn, A.N., Rouse, G.W., Thurber, A.R., Tunnicliffe, V., Van Dover, C.L., Vanreusel, A., Watling, L., 2016. Hydrothermal vents and methane seeps: Rethinking the sphere of influence. *Frontiers in Marine Science* 3. <https://doi.org/10.3389/fmars.2016.00072>
- Linke, P., Suess, E., Torres, M., Martens, V., Rugh, W.D., Ziebis, W., Kulm, L.D., 1994. In situ measurement of fluid flow from cold seeps at active continental margins. *Deep Sea Research Part I: Oceanographic Research Papers* 41, 721–739. [https://doi.org/10.1016/0967-0637\(94\)90051-5](https://doi.org/10.1016/0967-0637(94)90051-5)

- McKay, L., Klokman, V.W., Mendlovitz, H.P., LaRowe, D.E., Hoer, D.R., Albert, D., Amend, J.P., Teske, A., 2016. Thermal and geochemical influences on microbial biogeography in the hydrothermal sediments of Guaymas Basin, Gulf of California. *Environmental Microbial Reports* 8, 150–161. <https://doi.org/10.1111/1758-2229.12365>
- McKay, L.J., MacGregor, B.J., Biddle, J.F., Albert, D.B., Mendlovitz, H.P., Hoer, D.R., Lipp, J.S., Lloyd, K.G., Teske, A.P., 2012. Spatial heterogeneity and underlying geochemistry of phylogenetically diverse orange and white *Beggiatoa* mats in Guaymas Basin hydrothermal sediments. *Deep Sea Research Part I: Oceanographic Research Papers* 67, 21–31. <https://doi.org/10.1016/j.dsr.2012.04.011>
- O’Hara, S.C., Dando, P.R., Schuster, U., Bennis, A., Boyle, J.D., Chui, F.T.W., Hatherell, T.V.J., Niven, S.J., Taylor, L.J., 1995. Gas seep induced interstitial water circulation: observations and environmental implications. *Continental Shelf Research* 15:8, 931-948.
- Orcutt, B.N., Sylvan, J.B., Knab, N.J., Edwards, K.J., 2011. Microbial Ecology of the Dark Ocean above, at, and below the Seafloor. *Microbiology and Molecular Biology Reviews* 75, 361–422. <https://doi.org/10.1128/MMBR.00039-10>
- Portail, M., Olu, K., Dubois, S.F., Escobar-Briones, E., Gelinas, Y., Menot, L., Sarrazin, J., 2016. Food-Web Complexity in Guaymas Basin Hydrothermal Vents and Cold Seeps. *PLOS ONE* 11, e0162263. <https://doi.org/10.1371/journal.pone.0162263>
- Ramirez-Llodra, E., Brandt, A., Danovaro, R., Escobar, E., German, C.R., Levin, L.A., Arbizu, P.M., Menot, L., Buhl-Mortensen, P., Narayanaswamy, B.E., Smith, C.R., Tittensor, D.P., Tyler, P.A., Vanreusel, A., Vecchione, M., 2010. Deep, diverse and definitely different: unique attributes of the world’s largest ecosystem. *Biogeosciences Discussions* 7, 2361–2485. <https://doi.org/10.5194/bgd-7-2361-2010>
- Rogener, M.K., Bracco, A., Hunter, K.S., Saxton, M.A., Joye, S.B., 2018. Long-term impact of the Deepwater Horizon oil well blowout on methane oxidation dynamics in the northern Gulf of Mexico. *Elementa: Science of the Anthropocene* 6, 73. <https://doi.org/10.1525/elementa.332>
- Sibuet, M., Olu, K., 1998. Biogeography, biodiversity and fluid dependence of deep-sea cold-seep communities at active and passive margins. *Deep-Sea Research II* 45, 517-567.
- Solomon, E.A., Kastner, M., Jannasch, H., Robertson, G., Weinstein, Y., 2008. Dynamic fluid flow and chemical fluxes associated with a seafloor gas hydrate deposit on the northern Gulf of Mexico slope. *Earth and Planetary Science Letters* 270, 95–105. <https://doi.org/10.1016/j.epsl.2008.03.024>
- Suess, E., 2014. Marine cold seeps and their manifestations: geological control, biogeochemical criteria and environmental conditions. *International Journal of Earth Sciences : Geologische Rundschau*; Berlin 103, 1889–1916. <http://dx.doi.org/10.1007/s00531-014-1010-0>

- Teske, A., de Beer, D., McKay, L.J., Tivey, M.K., Biddle, J.F., Hoer, D., Lloyd, K.G., Lever, M.A., Røy, H., Albert, D.B., Mendlovitz, H.P., MacGregor, B.J., 2016. The Guaymas Basin hiking guide to hydrothermal mounds, chimneys, and microbial mats: complex seafloor expressions of subsurface hydrothermal circulation. *Frontiers in Microbiology* 7. <https://doi.org/10.3389/fmicb.2016.00075>
- Torres, M.E., McManus, J., Hammond, D.E., de Angelis, M.A., Heeschen, K.U., Colbert, S.L., Tryon, M.D., Brown, K.M., Suess, E., 2002. Fluid and chemical fluxes in and out of sediments hosting methane hydrate deposits on Hydrate Ridge, OR, I: Hydrological provinces. *Earth and Planetary Science Letters* 201, 525–540. [https://doi.org/10.1016/S0012-821X\(02\)00733-1](https://doi.org/10.1016/S0012-821X(02)00733-1)
- Tunnicliffe, V., McArthur, A.G., McHugh, D., 1998. A Biogeographical Perspective of the Deep-Sea Hydrothermal Vent Fauna, in: Blaxter, J.H.S., Southward, A.J., Tyler, P.A. (Eds.), *Advances in Marine Biology*. Academic Press, pp. 353–442. [https://doi.org/10.1016/S0065-2881\(08\)60213-8](https://doi.org/10.1016/S0065-2881(08)60213-8)
- Zimmermann, S., Hughes, R.G., Flügel, H.J., 1997. The effect of methane seepage on the spatial distribution of oxygen and dissolved sulphide within a muddy sediment. *Marine Geology, Gas in Marine Sediments, Geology/Geochemistry/Microbiology* 137, 149–157. [https://doi.org/10.1016/S0025-3227\(96\)00085-0](https://doi.org/10.1016/S0025-3227(96)00085-0)
- Zhang, C.L., Huang, Z., Cantu, J., Pancoast, R.D., Brigmon, R.L., Lyons, T.W., Sassen, R., 2005. Lipid biomarkers and carbon isotope signatures of a microbial (*Beggiatoa*) mat associated with gas hydrates in the Gulf of Mexico. *Applied and Environmental Microbiology* 71:4, 2106-2112. <http://dx.doi.org/10.1128/AEM.71.4.2106-2112.2005>

CHAPTER 6

CLOSING REMARKS

6.1. Synthesis and Significance

This work presents a novel approach toward evaluating deep-sea fluid fluxes through shallow sediment sections. This dissertation outlines the motivation toward evaluating fluid flow through sites where seepage may be especially active including cold and hydrothermal fluid discharge sites. While chemical and thermal distributions measured in the subsurface and overlying water (e.g., Lapham et al., 2008; Fisher and Becker, 1991), as well as flux chambers (e.g., Solomon et al., 2008) have been used to estimate fluid transport rates through sediments, studies concerning fluid seepage remain one of the least understood components of global seepage studies (Suess, 2014).

The conceptual framework for the vertical exchange model developed as a part of this work was modified slightly from Krest and Harvey (2003) and adapted for deep-sea sedimentary systems. While deep-sea sediments are the subject of this work, this approach may likewise be modified for use in shallow water and coastal systems provided all source and sinks of ^{224}Ra to porefluid was be accurately constrained. Importantly, Chapter 2 details several potential factors affecting aqueous ^{224}Ra distributions in deep-sea seepage sediments and the approach to identify factors of significance toward development of the vertical exchange model presented as the foremost contribution of this work. This model is specifically advantageous over that proposed by

Krest and Harvey (2003) as we eliminate the assumption that ^{224}Ra production is constant with depth by experimental determination for the aqueous ^{224}Ra equilibrium activity for all recovered materials. Significant differences in the maximum exchangeable ^{224}Ra activity associated with sediments recovered in vertical sequence were found to exhibit an 11-fold increase from 0 to 16 cmbsf and are related to the ^{224}Ra production rate.

A few assumptions are considered in applying the vertical exchange model. Perhaps most importantly, it is assumed that lateral flow is insignificant in controlling porefluid distributions of ^{224}Ra and instead assume any identified transport is occurring in the vertical direction (either positive or negative z). It is also assumed that all sources and sinks (Figure 2.1) have been accurately accounted for as it concerns samples used in this work. The vertical exchange model was not utilized in areas where removal mechanisms including Ra-Ba co-precipitation into barite were believed to occur so as to present as a sink of ^{224}Ra , although process is known to act as a radium sink where chimney formation is active (Moore and Stakes, 1990). Brine seeps are also not recommended as changes in salinity may influence grain adsorption and desorption (Webster et al., 1995). This approach then compliments existing geochemical methods which model flow rates using chloride gradients measured in brine-filled porespace (e.g., Lapham et al., 2008).

Although the applicability of this method to evaluate brine transport and regions where active barite precipitation is occurring was not tested, this approach is not dependent on thermal alteration or dye release and recovery techniques and so is available to evaluate fluid flow in regions previously inaccessible to such research. Minimum and maximum vertical advective velocity resolution limits are related to the residence time of the porefluid within each sediment section and the sediment sampling interval. We recovered porewater from 4 cm thick sediment sections to acquire ~30 to 100 mL per section and found this reasonable for processing. We consider 1 day to

be our minimum detectable residence time and 21 days to be our maximum residence time (~ 0.3 to 6 half-lives of ^{224}Ra ; $T_{1/2}=3.6$ days). This results in a range of discernable vertical velocities from ~ 0.19 to 4 cm day^{-1} although changing the sampling interval could influence the minimum and maximum detectable vertical velocities.

The vertical exchange model was first qualitatively tested in a cold seep environment where volumetric fluid flux was previously unreported. In the Gulf of Mexico, fluid flux from seepage sites ranged from 1 to $4 \text{ mL cm}^{-2} \text{ day}^{-1}$ as compared to a control site ($-1 \text{ mL cm}^{-2} \text{ day}^{-1}$) where no seepage indicators were identified (Chapter 3). The second environmental evaluation of the vertical exchange model considered fluid flux across sediment cover data using cores recovered from Guaymas Basin. Here, statistically significant relationships between subsurface temperature range and volumetric fluid flux were identified for sediment cores recovered through conspicuous white bacterial mat cover as well as for apparently uncolonized sediments. The correlation between fluid flux and temperature gradient is considered as the second environmental confirmation that the vertical exchange model may be used to evaluate deep-sea fluid transport through sediments (Chapter 4).

This work posits a novel approach to evaluate fluid flux through deep-sea systems described throughout as the vertical exchange model. This method facilitated direct comparison of fluid flux magnitude between a cold seep and hydrothermal seepage system where average fluid flux for cold seep sediments sampled ($5.6 \text{ mL cm}^{-2} \text{ day}^{-1}$) was similar to the average fluid flux identified for hydrothermal sediments sampled ($3.5 \text{ mL cm}^{-2} \text{ day}^{-1}$; Chapter 5).

6.2 References

- Fisher, A.T., Becker, K., 1991. Heat flow, hydrothermal circulation and basalt intrusions in the Guaymas Basin, Gulf of California. *Earth and Planetary Science Letters* 103, 84–99. [https://doi.org/10.1016/0012-821X\(91\)90152-8](https://doi.org/10.1016/0012-821X(91)90152-8)
- Krest, J.M., Harvey, J.W., 2003. Using natural distributions of short-lived radium isotopes to quantify groundwater discharge and recharge. *Limnology and Oceanography* 48, 290–298. <https://doi.org/10.4319/lo.2003.48.1.0290>
- Lapham, L., Alperin, M., Chanton, J., Martens, C., 2008. Upward advection rates and methane fluxes, oxidation, and sources at two Gulf of Mexico brine seeps. *Marine Chemistry* 112, 65–7. doi: 10.1016/j.marchem.2008.06.001
- Moore, W.S., Stakes, D., 1990. Ages of barite-sulfide chimneys from the Mariana Trough. *Earth and Planetary Science Letters* 100, 265–274. [https://doi.org/10.1016/0012-821X\(90\)90189-5](https://doi.org/10.1016/0012-821X(90)90189-5)
- Solomon, E.A., Kastner, M., Jannasch, H., Robertson, G., Weinstein, Y., 2008. Dynamic fluid flow and chemical fluxes associated with a seafloor gas hydrate deposit on the northern Gulf of Mexico slope. *Earth and Planetary Science Letters* 270, 95–105. <https://doi.org/10.1016/j.epsl.2008.03.024>
- Suess, E., 2014. Marine cold seeps and their manifestations: geological control, biogeochemical criteria and environmental conditions. *International Journal of Earth Sciences* 103, 1889–1916. <https://doi.org/10.1007/s00531-014-1010-0>
- Webster, I.T., Hancock, G.J., Murray, A.S., 1995. Modelling the effect of salinity on radium desorption from sediments. *Geochimica et Cosmochimica Acta* 59, 2469–2476. [https://doi.org/10.1016/0016-7037\(95\)00141-7](https://doi.org/10.1016/0016-7037(95)00141-7)

APPENDICIES

Appendix I.

This section contains data relevant to samples discussed throughout the Dissertation. Contents include five data tables and three figures. Contents are organized by the order in which they may supplement material presented in the Dissertation. Figure A.1 presents a conceptual diagram concerning correcting isotope activities for use in the vertical exchange model. Table A.1 contains collection details for the 35 sediment cores recovered from the Gulf of Mexico used for this work. These data supplement the content presented in Chapter 3 and Chapter 5. Table A.2 offers a list of measured and corrected porefluid ^{224}Ra activities and empirically derived from the 35 sediment cores recovered from the Gulf of Mexico. These data supplement the work presented in Chapter 3 and Chapter 5. Table A.3 details residence time and Table A.4 lists volumetric flux results for each sediment section discussed in the dissertation obtained from the Gulf of Mexico. These data are especially relevant for Chapter 5. Figure A.2 and Figure A.3 depict calibration curves for sediment-coated filters first discussed in Chapter 4 and Chapter 5. Table A.5 includes a list of measured and corrected isotope activities measured and empirically derived for all 19 sediment cores recovered from Guaymas Basin during cruise AT37-06 concerning data presented in Chapters 4 and 5. Tables A.6 and A.7 include porefluid residence time and volumetric flux estimates for sediment sections recovered from Guaymas Basin and supplement concepts discussed in Chapter 4 and Chapter 5.

Appendix II.

Leigha Peterson's curriculum vitae.

Appendix III.

Derivation of standard radioactive ingrowth equation (Equation 2.3).

APPENDIX I.

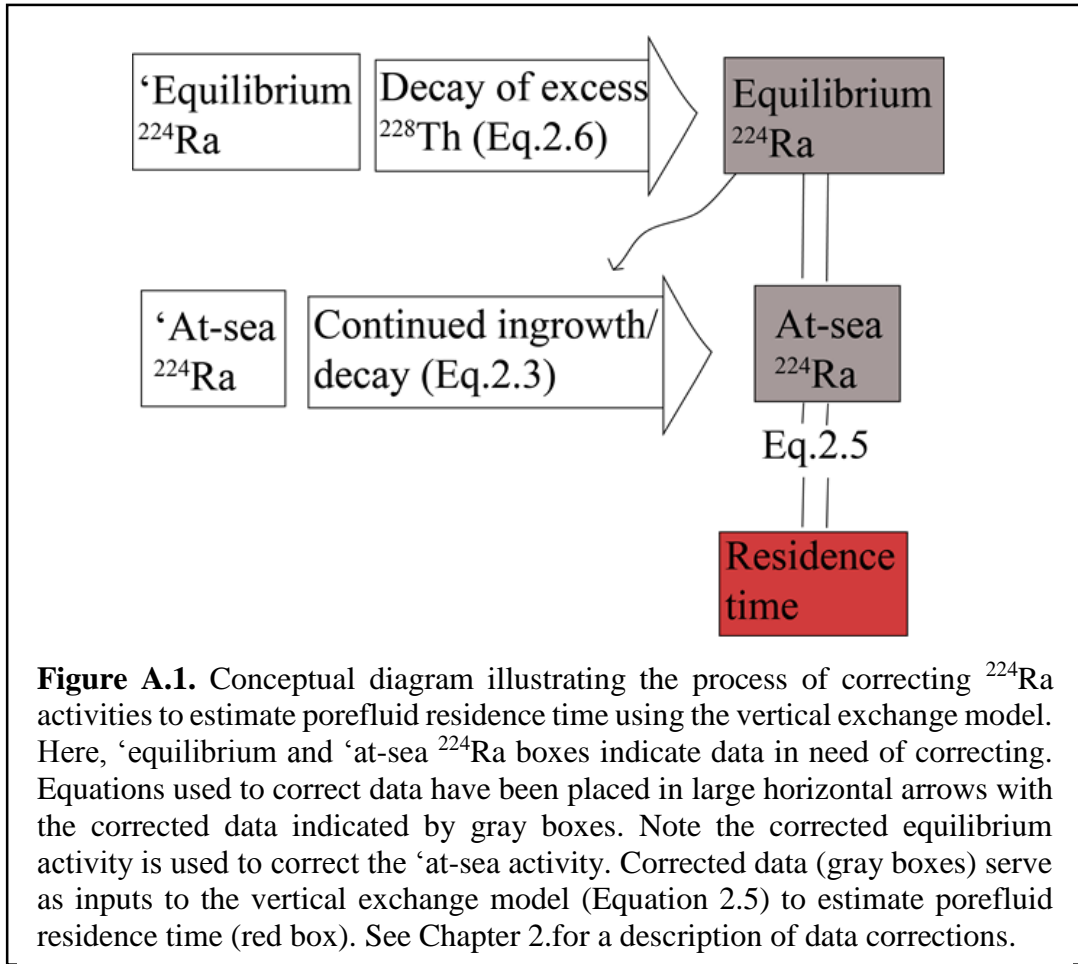


Figure A.1. Conceptual diagram illustrating the process of correcting ^{224}Ra activities to estimate porefluid residence time using the vertical exchange model. Here, 'equilibrium and 'at-sea ^{224}Ra boxes indicate data in need of correcting. Equations used to correct data have been placed in large horizontal arrows with the corrected data indicated by gray boxes. Note the corrected equilibrium activity is used to correct the 'at-sea activity. Corrected data (gray boxes) serve as inputs to the vertical exchange model (Equation 2.5) to estimate porefluid residence time (red box). See Chapter 2.for a description of data corrections.

Table A.1 Metadata for sediment cores recovered from the Gulf of Mexico. Site name refers to that designated by the Bureau of Ocean Energy Management (BOEM) and core number refers to the fluid flux rank variable used in Chapter 5 (Fig. 5.2, Fig. 5.3, and 5.4). Collection date and time are given in Eastern Standard Time (EST) and seep condition indicates characteristics of the sampling region.

Site name; core number	Cruise	Latitude and Longitude	Collection date & time	Seep condition
GC600; 1	EN586	27° 21.940 'N, 90° 33.807 'W	7/28/16 11:48	Oil seep
OC26; 2	EN559	28° 41.87 'N, 88° 21.92 'W	6/20/15 21:07	Impact
OC26; 3	EN559	28° 45.870 'N, 88° 23.650 'W	5/29/15 22:30	Impact
BP463; 4	EN559	28° 30.84 'N, 88° 36.03 'W	6/19/15 17:25	Impact
^Taylor; 5	EN559	28° 54.75 'N, 88° 53.33 'W	6/9/15 21:05	^Oil seep
OC26; 6	EN559	28° 42.90 'N, 88° 21.54 'W	6/20/15 18:33	Impact
BP444; 7	EN559	28° 34.50 'N, 88° 32.26 'W	6/19/15 19:30	Impact
GC574; 8	EN586	27° 21.090 'N, 90° 49.202 'W	8/8/16 21:00	Gas seep
MC253; 9	AT26-13	28° 38.040 'N, 88° 10.200 'W	4/2/14 8:25	Oil seep
GC574; 10	EN559	27° 21.44 'N, 91° 49.25 'W	6/14/15 10:00	Gas seep
OC26; 11	EN586	28° 41.503 'N, 88° 22.770 'W	8/6/16 8:31	§Impact
OC26; 12	EN586	28° 41.503 'N, 88° 22.770 'W	8/6/16 8:31	Impact
BIP17; 13	EN586	28° 38.287 'N, 88° 31.183 'W	8/1/16 9:35	Impact
GC186; 14	EN559	27° 45.43 'N, 91° 26.02 'W	6/5/15 13:20	Control
GB480; 15	EN586	27° 29.966 'N, 91° 58.721 'W	7/26/16 19:45	Control
§GC699; 16	EN586	27° 17.498 'N, 90° 02.422 'W	8/13/16 21:47	Control
GC699; 17	EN586	27° 17.499 'N, 90° 02.425 'W	7/31/16 19:45	Control
GC185; 18	EN586	27° 47.28 'N, 91° 30.44 'W	7/26/16 3:39	Gas seep
^Taylor; 19	EN586	28° 56.251 'N, 88° 58.175 'W	8/2/16 3:23	^Oil seep
GC600; 20	EN559	27° 21.922 'N, 90° 33.819 'W	6/1/15 17:00	Oil seep
GC767; 21	EN559	27° 12.54 'N, 91° 00.86 'W	6/18/15 16:50	Gas seep
BIP24; 22	EN586	28° 46.219 'N, 88° 22.989 'W	8/1/16 20:50	Impact
GC767; 23	EN586	27° 12.619 'N, 91° 01.556 'W	8/10/16 19:13	Gas seep

§Control core, !Seep Core, *Mat core (Chapter 3)

^Sediment cores recovered from a shallow water site (~120 m) near 21 buried well pipes actively conveying oil into shallow sediments from a deep geologic reservoir. This is distinguished from other seeps by water depths < 200 m and by known buried infrastructure.

Table A.1 Continued

Site name; core number	Cruise	Latitude and Longitude	Collection date & time	Seep condition
¹ GC600; 24	AT26-13	27° 25.644 'N, 90° 26.092 'W	4/8/14 12:45	¹ Oil seep
GC600; 25	EN559	27° 21.903 'N, 90° 33.802 'W	5/30/15 21:00	Oil seep
GC600; 26	AT26-13	27° 22.174 'N, 90° 34.289 'W	4/5/14 12:31	Oil seep
*GC600; 27	AT26-13	27° 22.174 'N, 90° 34.289 'W	4/5/14 12:00	*Oil seep
GC767; 28	EN586	27° 12.599 'N, 91° 01.548 'W	7/30/16 20:47	Gas seep
GC767; 29	EN559	27° 12.59 'N, 91° 00.59 'W	6/16/15 17:20	Gas seep
GC185; 30	EN559	27° 46.984 'N, 91° 30.446 'W	6/3/15 18:00	Oil seep
MC118; 31	EN586	28° 51.112 'N, 88° 29.463 'W	8/14/16 14:07	Oil seep
[^] Taylor; 32	EN559	28° 55.40 'N, 88° 55.64 'W	6/9/15 22:30	[^] Oil seep
GC600; 33	EN586	27° 22.202 'N, 90° 34.191 'W	7/27/16 21:09	Oil seep
GC600; 34	EN586	27° 21.952 'N, 90° 33.787 'W	8/12/16 21:42	Oil seep
MC118; 35	EN586	28° 51.112 'N, 88° 29.463 'W	8/14/16 14:07	Oil seep

^{\$}Control core, ¹Seep Core, *Mat core (Chapter 3)

[^]Sediment cores recovered from a shallow water site (~120 m) near 21 buried well pipes actively conveying oil into shallow sediments from a deep geologic reservoir. This is distinguished from other seeps by water depths < 200 m and by known buried infrastructure.

Table A.2. Aqueous porefluid ^{224}Ra activities recovered from cores collected within the Gulf of Mexico. Site name refers to that designated by BOEM and core number refers to the fluid flux rank variable used in Chapter 5 (Fig. 5.2, Fig. 5.3, and 5.4) and Table A.1. Initial activities are those measured at-sea and equilibrium activities are those measured in solution following a 21 day incubation.

Site core;	Depth (cmbsf)	[?] Initial (dpm L ⁻¹)	^{**} Initial (dpm L ⁻¹)	[?] Equilibrium (dpm L ⁻¹)	^{**} Equilibrium (dpm L ⁻¹)
GC600;					
1					
	2	16.7 ± 1.4	18.8 ± 1.4	21.5 ± 1.7	33.4 ± 1.8
	6	21.7 ± 1.9	19.1 ± 1.8	42.8 ± 2.7	36.7 ± 2.8
	10	20.3 ± 2.0	21.6 ± 1.9	41.4 ± 2.5	47.2 ± 2.6
	14	24.9 ± 2.5	22.1 ± 2.4	51.9 ± 3.6	46.6 ± 3.7
	18	23.3 ± 2.3	23.3 ± 2.2	41.0 ± 2.1	48.3 ± 2.2
OC26; 2					
	2	1.5 ± 0.2	6.0 ± 0.1	5.3 ± 0.4	39.1 ± 0.5
	6	13.5 ± 1.2	7.2 ± 0.9	61.0 ± 6.0	47.2 ± 7.0
	10	12.3 ± 0.7	10.9 ± 0.6	53.6 ± 5.3	62.7 ± 6.3
	14	14.2 ± 0.8	12.3 ± 0.7	44.8 ± 4.5	51.2 ± 5.3
	18	15.8 ± 1.0	13.5 ± 0.9	31.8 ± 3.2	45.2 ± 3.7
OC26; 3					
	2	1.2 ± 0.2	2.8 ± 0.2	34.5 ± 2.7	55.4 ± 3.3
	6	7.5 ± 1.0	5.6 ± 0.6	58.0 ± 2.9	62.9 ± 3.4
	10	14.5 ± 2.0	10.3 ± 1.5	65.1 ± 6.3	73.3 ± 7.5
	14	17.7 ± 1.6	12.8 ± 1.4	60.5 ± 6.0	76.3 ± 7.2
BP463,					
4					
	2	0.4 ± 0.1	3.6 ± 0.0	2.5 ± 0.2	18.7 ± 0.3
	6	8.3 ± 0.8	8.1 ± 0.7	29.4 ± 2.6	53.2 ± 3.1
	10	22.0 ± 2.2	14.8 ± 1.7	103.7 ± 7.3	95.8 ± 8.6
	14	25.6 ± 2.5	17.5 ± 2.0	111.0 ± 7.3	109.6 ± 8.6
^Taylor;					
5					
	2	8.5 ± 0.8	8.0 ± 0.7	28.2 ± 2.5	43.1 ± 2.9
	6	10.7 ± 1.1	10.7 ± 0.9	46.7 ± 3.9	47.3 ± 4.4
	10	17.9 ± 1.8	12.4 ± 1.6	48.6 ± 4.6	53.0 ± 5.3
	14	14.3 ± 1.0	14.3 ± 0.8	43.1 ± 4.2	52.7 ± 4.9
OC26; 6					
	2	0.8 ± 0.2	3.1 ± 0.1	4.1 ± 0.3	13.6 ± 0.4
	6	6.4 ± 0.4	4.2 ± 0.4	19.0 ± 0.8	25.6 ± 0.9

[?]Measured ^{224}Ra activities; ^{**}Corrected ^{224}Ra activities. Corrections described in Chapter 2.

^{\$}Control core, [!]Seep Core, ^{*}Mat core (Chapter 3)

[^]Sediment cores recovered from a shallow water site (~120 m) See Table 1.A for more details concerning this site.

Table A.2. Continued

Site core;	Depth (cmbsf)	[?] Initial (dpm L ⁻¹)	^{**} Initial (dpm L ⁻¹)	[?] Equilibrium (dpm L ⁻¹)	^{**} Equilibrium (dpm L ⁻¹)
BP444; 7	10	8.4 ± 0.7	6.9 ± 0.5	42.0 ± 3.9	43.7 ± 4.7
	14	11.0 ± 0.6	9.7 ± 0.5	50.1 ± 3.7	52.4 ± 4.4
	18	15.6 ± 0.8	11.3 ± 0.7	41.1 ± 3.0	53.8 ± 3.6
	2	0.0 ± 0.0	4.1 ± 0.0	2.1 ± 0.2	23.8 ± 0.2
	6	9.9 ± 1.0	6.7 ± 0.8	38.2 ± 3.8	33.8 ± 4.5
GC574; 8	10	13.8 ± 1.4	10.7 ± 1.2	45.7 ± 4.5	54.6 ± 5.3
	14	14.7 ± 1.5	12.5 ± 1.2	54.9 ± 5.5	57.9 ± 6.4
	18	15.5 ± 1.5	12.9 ± 1.3	46.8 ± 4.5	59.9 ± 5.3
	2	1.4 ± 0.2	1.1 ± 0.2	0.5 ± 0.1	0.4 ± 0.1
	6	0.9 ± 0.1	1.1 ± 0.1	0.3 ± 0.1	0.5 ± 0.1
MC253; 9	10	1.1 ± 0.2	1.4 ± 0.2	0.7 ± 0.1	0.7 ± 0.1
	14	2.2 ± 0.3	2.4 ± 0.3	0.9 ± 0.1	1.8 ± 0.1
	18	3.9 ± 0.5	3.1 ± 0.5	3.7 ± 0.3	2.4 ± 0.3
	2	15.5 ± 1.0	9.8 ± 0.6	39.9 ± 2.8	67.0 ± 2.9
	6	26.8 ± 1.5	14.3 ± 0.6	91.7 ± 4.1	73.5 ± 4.2
GC574; 10	10	36.0 ± 2.6	20.4 ± 1.7	85.0 ± 4.1	86.2 ± 4.2
	14	38.2 ± 2.7	28.4 ± 1.9	77.5 ± 4.3	72.2 ± 4.3
	18	37.7 ± 2.3	31.0 ± 2.1	50.3 ± 3.1	65.0 ± 3.1
	2	0.8 ± 0.1	0.2 ± 0.1	9.0 ± 0.5	8.9 ± 0.5
	6	0.3 ± 0.1	1.0 ± 0.0	6.2 ± 0.4	7.3 ± 0.5
OC26; 11	10	2.7 ± 0.3	1.7 ± 0.3	3.6 ± 0.3	9.9 ± 0.4
	14	3.2 ± 0.4	4.9 ± 0.3	15.6 ± 0.7	28.2 ± 0.8
	2	0.7 ± 0.1	1.3 ± 0.1	0.5 ± 0.1	1.2 ± 0.1
	6	1.9 ± 0.2	4.6 ± 0.2	1.8 ± 0.1	7.9 ± 0.2
	10	11.5 ± 1.1	7.7 ± 1.1	20.7 ± 0.6	22.3 ± 0.6
	14	10.8 ± 1.1	14.0 ± 1.0	42.0 ± 2.8	35.8 ± 2.9

[?]Measured ²²⁴Ra activities; ^{**}Corrected ²²⁴Ra activities. Corrections described in Chapter 2.

[§]Control core, [!]Seep Core, ^{*}Mat core (Chapter 3)

[^]Sediment cores recovered from a shallow water site (~120 m) See Table 1.A for more details concerning this site.

Table A.2. Continued

Site core;	Depth (cmbsf)	[?] Initial (dpm L ⁻¹)	^{**} Initial (dpm L ⁻¹)	[?] Equilibrium (dpm L ⁻¹)	^{**} Equilibrium (dpm L ⁻¹)
	18	22.1 ± 2.2	15.4 ± 2.1	40.8 ± 2.6	42.9 ± 2.7
OC26; 12	2	2.1 ± 0.2	4.4 ± 0.2	0.3 ± 0.0	6.7 ± 0.0
	6	6.9 ± 0.5	6.3 ± 0.5	12.6 ± 0.8	11.8 ± 0.8
	10	10.8 ± 1.1	9.5 ± 1.0	21.2 ± 1.4	20.8 ± 1.4
	14	12.5 ± 1.2	11.0 ± 1.2	26.5 ± 1.7	24.7 ± 1.8
BIP17; 13	2	0.9 ± 0.1	4.2 ± 0.1	0.7 ± 0.1	6.3 ± 0.1
	6	7.8 ± 0.9	5.9 ± 0.8	11.4 ± 1.0	13.5 ± 1.0
	10	10.9 ± 0.9	10.0 ± 0.8	26.7 ± 1.9	27.8 ± 2.0
	14	15.9 ± 1.3	11.3 ± 1.1	41.9 ± 2.8	35.7 ± 2.9
GC186; 14	2	0.2 ± 0.0	4.1 ± 0.0	2.3 ± 0.2	7.0 ± 0.2
	6	8.2 ± 0.8	8.4 ± 0.8	9.6 ± 1.0	26.7 ± 1.1
	10	19.4 ± 1.9	14.3 ± 1.7	56.3 ± 5.2	52.0 ± 6.1
GB480; 15	2	2.8 ± 0.3	2.3 ± 0.3	3.1 ± 0.2	3.9 ± 0.2
	6	1.9 ± 0.2	4.2 ± 0.2	4.4 ± 0.3	12.5 ± 0.3
	10	8.4 ± 0.9	9.2 ± 0.8	29.0 ± 0.8	26.6 ± 0.8
	14	18.8 ± 1.9	15.6 ± 1.8	44.1 ± 2.5	42.0 ± 2.6
[§] GC699; 16	2	2.5 ± 0.2	3.0 ± 0.2	4.9 ± 0.3	5.7 ± 0.3
	6	3.6 ± 0.3	3.2 ± 0.3	6.2 ± 0.4	6.5 ± 0.4
	10	3.5 ± 0.5	3.4 ± 0.5	7.8 ± 0.4	6.4 ± 0.5
	14	3.3 ± 0.5	3.3 ± 0.5	4.4 ± 0.3	6.3 ± 0.3
GC699; 17	2	4.6 ± 0.5	7.4 ± 0.5	9.4 ± 0.5	10.5 ± 0.5
	6	10.3 ± 1.0	11.1 ± 1.0	10.8 ± 0.8	20.7 ± 0.8
	10	18.8 ± 1.9	20.4 ± 1.8	39.9 ± 1.9	39.1 ± 2.0
	14	33.2 ± 3.3	31.0 ± 3.3	62.7 ± 4.5	60.8 ± 4.7
	18	43.0 ± 4.3	37.4 ± 4.2	73.7 ± 4.2	70.5 ± 4.4

[?]Measured ²²⁴Ra activities; ^{**}Corrected ²²⁴Ra activities. Corrections described in Chapter 2.

[§]Control core, [!]Seep Core, ^{*}Mat core (Chapter 3)

[^]Sediment cores recovered from a shallow water site (~120 m) See Table 1.A for more details concerning this site.

Table A.2. Continued

Site core;	Depth (cmbsf)	[?] Initial (dpm L ⁻¹)		^{**} Initial (dpm L ⁻¹)		[?] Equilibrium (dpm L ⁻¹)		^{**} Equilibrium (dpm L ⁻¹)		
GC185;										
18										
	2	0.0	± 0.0	0.2	± 0.0	3.1	± 0.2	2.6	± 0.2	
	6	0.4	± 0.1	0.8	± 0.1	1.9	± 0.1	2.7	± 0.1	
	10	2.0	± 0.3	3.2	± 0.3	2.7	± 0.2	4.5	± 0.2	
	14	7.3	± 0.7	8.2	± 0.7	8.7	± 0.7	12.5	± 0.8	
	18	15.9	± 1.4	11.4	± 1.4	25.0	± 1.7	17.3	± 1.8	
[^] Taylor;										
19										
	2	12.1	± 0.8	17.5	± 0.7	31.2	± 0.8	39.7	± 0.8	
	6	23.2	± 1.2	20.6	± 1.2	45.2	± 0.9	37.4	± 1.0	
	10	27.0	± 2.6	23.5	± 2.5	31.6	± 1.6	38.9	± 1.6	
	14	20.7	± 1.7	21.2	± 1.6	35.5	± 1.8	27.3	± 1.8	
	18	16.0	± 1.1	18.3	± 1.1	11.6	± 0.8	24.5	± 0.8	
GC600;										
20										
	2	6.4	± 0.6	5.6	± 0.6	5.5	± 0.5	6.2	± 0.6	
	6	4.9	± 0.5	5.7	± 0.5	5.3	± 0.4	5.6	± 0.5	
	10	5.7	± 0.5	6.8	± 0.5	3.7	± 0.3	5.2	± 0.4	
	14	9.6	± 0.8	11.1	± 0.8	4.6	± 0.4	5.7	± 0.4	
	18	17.2	± 1.2	13.7	± 1.2	6.6	± 0.5	6.5	± 0.6	
GC767;										
21										
	2	3.0	± 0.3	2.8	± 0.3	3.0	± 0.2	2.9	± 0.3	
	6	2.7	± 0.4	2.7	± 0.4	2.0	± 0.2	4.2	± 0.2	
	10	2.5	± 0.3	5.3	± 0.3	5.6	± 0.4	19.8	± 0.5	
	14	12.8	± 1.3	6.4	± 1.1	43.0	± 3.9	40.3	± 4.6	
	18	8.8	± 0.9	8.5	± 0.6	54.4	± 3.2	57.2	± 3.7	
BIP24;										
22										
	2	44.2	± 3.0	41.0	± 3.0	0.7	± 0.1	15.1	± 0.1	
	6	37.6	± 2.4	27.5	± 2.4	28.3	± 1.9	25.4	± 2.0	
	10	0.7	± 0.1	16.4	± 0.1	44.2	± 3.0	38.2	± 3.1	
	14	11.4	± 1.0	5.7	± 0.9	37.6	± 2.4	42.6	± 2.5	
GC767;										
23										

[?]Measured ²²⁴Ra activities; ^{**}Corrected ²²⁴Ra activities. Corrections described in Chapter 2.

[§]Control core, [!]Seep Core, ^{*}Mat core (Chapter 3)

[^]Sediment cores recovered from a shallow water site (~120 m) See Table 1.A for more details concerning this site.

Table A.2. Continued

Site core;	Depth (cmbfsf)	[?] Initial (dpm L ⁻¹)		^{**} Initial (dpm L ⁻¹)		[?] Equilibrium (dpm L ⁻¹)		^{**} Equilibrium (dpm L ⁻¹)	
	2	2.0	± 0.2	2.1	± 0.2	2.7	± 0.2	2.7	± 0.2
	6	2.2	± 0.2	2.6	± 0.2	2.5	± 0.2	2.8	± 0.2
	10	3.6	± 0.5	2.4	± 0.5	2.7	± 0.2	2.7	± 0.2
	14	1.6	± 0.3	2.3	± 0.3	2.7	± 0.2	2.9	± 0.2
	18	1.8	± 0.2	1.6	± 0.2	3.1	± 0.2	3.0	± 0.2
[!] GC600; 24	2	14.4	± 1.4	28.9	± 1.4	13.1	± 0.7	19.9	± 0.7
	6	41.7	± 3.7	53.0	± 3.8	26.1	± 1.1	21.4	± 1.1
	10	93.8	± 5.6	105.7	± 6.0	24.1	± 1.5	31.5	± 1.5
	14	159.8	± 14.5	169.1	± 15.7	42.9	± 2.2	41.6	± 2.2
	18	215.6	± 19.2	203.0	± 20.8	55.8	± 2.5	50.1	± 2.5
GC600; 25	2	36.4	± 2.7	25.8	± 2.7	33.3	± 3.2	37.7	± 3.7
	6	16.4	± 1.6	19.5	± 1.5	31.8	± 3.1	46.7	± 3.6
	10	9.5	± 0.9	12.2	± 0.6	55.9	± 5.5	62.8	± 6.3
	14	17.9	± 1.8	13.0	± 1.5	74.7	± 6.0	75.5	± 7.0
	18	20.4	± 1.5	16.1	± 1.3	64.9	± 5.4	80.9	± 6.3
GC600; 26	2	23.3	± 2.2	15.6	± 2.3	18.3	± 0.5	31.6	± 0.5
	6	12.7	± 1.4	13.2	± 0.8	43.9	± 0.9	42.1	± 0.9
	10	8.6	± 1.3	6.8	± 1.3	62.1	± 1.3	54.2	± 1.3
	14	12.6	± 2.1	8.9	± 0.8	53.8	± 4.2	54.7	± 4.2
	18	18.5	± 1.7	9.0	± 1.2	45.6	± 3.3	50.5	± 3.3
[*] GC600 ; 27	2	21.5	± 1.4	18.7	± 1.3	31.0	± 2.4	36.7	± 2.4
	6	19.9	± 1.8	15.5	± 1.6	41.2	± 2.8	42.8	± 2.8
	10	14.5	± 1.8	9.6	± 1.1	54.4	± 2.7	50.6	± 2.8
	14	8.9	± 1.5	5.9	± 0.5	54.0	± 3.4	55.0	± 3.5
GC767; 28	2	2.8	± 0.3	2.5	± 0.3	3.2	± 0.2	3.6	± 0.2

[?]Measured ²²⁴Ra activities; ^{**}Corrected ²²⁴Ra activities. Corrections described in Chapter 2.

^{\$}Control core, [!]Seep Core, ^{*}Mat core (Chapter 3)

[^]Sediment cores recovered from a shallow water site (~120 m) See Table 1.A for more details concerning this site.

Table A.2. Continued

Site core;	Depth (cmbfsf)	[?] Initial (dpm L ⁻¹)		**Initial (dpm L ⁻¹)		[?] Equilibrium (dpm L ⁻¹)		**Equilibrium (dpm L ⁻¹)	
GC767; 29	6	2.2	± 0.2	2.0	± 0.2	3.7	± 0.2	3.5	± 0.2
	10	1.1	± 0.1	1.4	± 0.1	3.2	± 0.2	3.2	± 0.2
	14	1.1	± 0.1	1.4	± 0.1	2.3	± 0.2	2.9	± 0.2
	18	1.9	± 0.3	1.5	± 0.3	3.0	± 0.2	2.7	± 0.2
	2	2.3	± 0.2	1.9	± 0.2	6.7	± 0.4	6.3	± 0.5
GC185; 30	6	1.9	± 0.2	1.3	± 0.2	4.1	± 0.3	6.6	± 0.4
	10	0.6	± 0.1	5.8	± 0.0	6.2	± 0.5	16.6	± 0.5
	14	16.5	± 1.6	9.1	± 1.5	32.2	± 3.2	41.5	± 3.8
	18	14.7	± 1.5	13.5	± 1.1	67.5	± 6.6	58.6	± 7.8
	2	6.7	± 0.7	6.0	± 0.6	8.2	± 0.7	8.5	± 0.8
MC118; 31	6	5.6	± 0.6	5.8	± 0.6	6.4	± 0.6	8.2	± 0.7
	10	5.4	± 0.7	5.7	± 0.7	6.4	± 0.4	6.7	± 0.5
	14	6.2	± 0.7	5.8	± 0.7	4.6	± 0.3	6.7	± 0.4
	18	5.8	± 0.7	6.0	± 0.7	6.1	± 0.5	6.3	± 0.6
	2	10.8	± 1.1	11.5	± 1.1	18.1	± 1.6	18.6	± 1.6
Taylor; 32	6	12.5	± 0.8	11.1	± 0.8	18.9	± 0.5	24.0	± 0.5
	10	10.9	± 1.0	11.6	± 1.0	34.5	± 3.1	33.6	± 3.1
	14	13.1	± 1.2	12.3	± 1.1	46.9	± 1.0	42.7	± 1.0
	18	15.3	± 1.5	13.2	± 1.4	46.1	± 1.0	46.7	± 1.0
	2	8.4	± 0.8	12.5	± 0.8	10.7	± 0.4	32.2	± 0.5
GC600; 33	6	18.4	± 1.8	12.9	± 1.7	45.3	± 4.5	40.8	± 5.2
	10	15.7	± 1.5	14.0	± 1.3	50.3	± 4.8	51.0	± 5.6
	14	13.2	± 1.3	12.7	± 1.2	37.5	± 3.7	50.5	± 4.3
	2	9.4	± 0.6	11.3	± 0.6	19.3	± 1.8	31.2	± 1.9
	6	14.0	± 1.4	10.5	± 1.4	40.6	± 2.8	34.4	± 2.9
	10	9.8	± 0.9	10.9	± 0.8	39.3	± 2.6	39.2	± 2.7

[?]Measured ²²⁴Ra activities; **Corrected ²²⁴Ra activities. Corrections described in Chapter 2.

[§]Control core, [!]Seep Core, ^{*}Mat core (Chapter 3)

[^]Sediment cores recovered from a shallow water site (~120 m) See Table 1.A for more details concerning this site.

Table A.2. Continued

Site core;	Depth (cmbsf)	[?] Initial (dpm L ⁻¹)	^{**} Initial (dpm L ⁻¹)	[?] Equilibrium (dpm L ⁻¹)	^{**} Equilibrium (dpm L ⁻¹)
GC600; 34	14	11.2 ± 1.0	10.4 ± 1.0	33.2 ± 2.3	46.2 ± 2.4
	18	13.3 ± 1.2	11.0 ± 1.0	60.9 ± 3.1	48.9 ± 3.2
	2	7.1 ± 0.7	10.5 ± 0.7	11.4 ± 0.4	15.4 ± 0.4
	6	14.0 ± 1.4	10.4 ± 1.4	18.4 ± 4.9	19.3 ± 5.1
	10	10.5 ± 1.0	10.5 ± 1.0	25.9 ± 2.6	24.2 ± 2.7
	14	7.8 ± 0.8	10.7 ± 0.8	25.6 ± 2.2	26.3 ± 2.3
MC118; 35	18	15.0 ± 1.7	11.0 ± 1.6	24.6 ± 2.4	26.0 ± 2.5
	2	18.1 ± 1.8	14.8 ± 1.8	25.1 ± 1.8	38.3 ± 1.8
	6	13.5 ± 1.3	14.7 ± 1.2	51.1 ± 3.3	42.7 ± 3.4
	10	16.0 ± 1.5	13.4 ± 1.4	51.3 ± 2.8	52.3 ± 2.9
	14	16.0 ± 1.5	12.6 ± 1.4	53.6 ± 1.2	58.2 ± 1.2
	18	12.8 ± 1.3	11.8 ± 1.0	68.8 ± 3.7	61.6 ± 3.7

[?]Measured ²²⁴Ra activities; ^{**}Corrected ²²⁴Ra activities. Corrections described in Chapter 2.

[§]Control core, [!]Seep Core, ^{*}Mat core (Chapter 3)

[^]Sediment cores recovered from a shallow water site (~120 m) See Table 1.A for more details concerning this site.

Table A.3. Porefluid residence time and porosity for sediment samples associated with sediment cores recovered from the Gulf of Mexico. Residence time is estimated by assuming transport toward the overlying ocean (+z) and also into the sediments (-z). Site name refers to that designated by BOEM and core number refers to the fluid flux rank variable used in Chapter 5 (Fig. 5.2, Fig. 5.3, and 5.4) and Table A.1 and Table A.2 and Table A.4.

Site core;	Depth (cmbsf)	Porosity	Residence time +z (days)			Residence time -z (days)		
GC600;								
1								
	2	0.82	-	±	-	n/a	±	n/a
	6	0.74	-	±	-	0.1	±	0.2
	10	0.72	-	±	-	0.5	±	0.3
	14	0.67	-	±	-	0.1	±	0.2
	18	0.73	n/a	±	n/a	0.2	±	0.2
OC26;								
2								
	2	0.86	-	±	-	n/a	±	n/a
	6	0.82	-	±	-	0.2	±	0.1
	10	0.80	-	±	-	0.4	±	0.1
	14	0.78	-	±	-	0.2	±	0.1
	18	0.80	n/a	±	n/a	0.2	±	0.1
OC26;								
3								
	2	0.86	-	±	-	n/a	±	n/a
	6	0.82	-	±	-	0.2	±	0.0
	10	0.80	-	±	-	0.4	±	0.1
	14	0.78	n/a	±	n/a	0.2	±	0.1
BP463;								
4								
	2	0.86	-	±	-	n/a	±	n/a
	6	0.82	-	±	-	0.5	±	0.1
	10	0.80	-	±	-	0.4	±	0.1
	14	0.78	n/a	±	n/a	0.1	±	0.1
Taylor;								
5								
	2	0.87	-	±	-	n/a	±	n/a
	6	0.81	-	±	-	0.4	±	0.1
	10	0.78	-	±	-	0.4	±	0.1
	14	0.80	n/a	±	n/a	0.2	±	0.1
OC26;								
6								
	2	0.86	-	±	-	n/a	±	n/a

Residence time is not determined for the bottom-most sediment section (+z transport direction) and for the top-most sediment section (-z transport direction) where initial ^{224}Ra activities are potentially sourced outside of the sampled domain. Such instances are indicated by 'n/a'. Where empirical estimates were not solvable results are indicated by a '-' symbol.

Table A.3. Continued

Site core;	Depth (cmbsf)	Porosity	Residence time +z (days)			Residence time -z (days)		
BP444; 7	6	0.82	-	±	-	0.3	±	0.1
	10	0.80	-	±	-	0.4	±	0.1
	14	0.78	n/a	±	n/a	0.3	±	0.1
	2	0.86	-	±	-	n/a	±	n/a
	6	0.82	-	±	-	0.5	±	0.1
	10	0.80	-	±	-	0.5	±	0.1
	14	0.78	-	±	-	0.2	±	0.1
GC574; 8	18	0.80	n/a	±	n/a	0.0	±	0.1
	2	0.83	-	±	-	n/a	±	n/a
	6	0.80	2.0	±	0.8	0.1	±	0.7
	10	0.77	4.5	±	0.9	-	±	-
	14	0.71	4.1	±	1.9	20.3	±	1.4
MC253; 9	18	0.70	n/a	±	n/a	6.6	±	4.7
	2	0.84	-	±	-	n/a	±	n/a
	6	0.76	-	±	-	0.4	±	0.0
	10	0.75	-	±	-	0.5	±	0.1
	14	0.71	-	±	-	0.9	±	0.2
GC574; 10	18	0.70	n/a	±	n/a	0.4	±	0.2
	2	0.83	-	±	-	n/a	±	n/a
	6	0.80	-	±	-	0.6	±	0.0
	10	0.77	-	±	-	0.4	±	0.1
OC26; 11	14	0.71	n/a	±	n/a	0.7	±	0.1
	2	0.84	16.7	±	2.0	n/a	±	n/a
	6	0.82	-	±	-	3.5	±	0.2
	10	0.78	-	±	-	1.0	±	0.2
	14	0.77	-	±	-	1.3	±	0.2
18	0.80	n/a	±	n/a	0.2	±	0.2	
OC26;								

Residence time is not determined for the bottom-most sediment section (+z transport direction) and for the top-most sediment section (-z transport direction) where initial ^{224}Ra activities are potentially sourced outside of the sampled domain. Such instances are indicated by 'n/a'. Where empirical estimates were not solvable results are indicated by a '-' symbol.

Table A.3. Continued

Site core;	Depth (cmbsf)	Porosity	Residence time +z (days)			Residence time -z (days)		
12								
	2	0.84	-	±	-	n/a	±	n/a
	6	0.82	-	±	-	1.5	±	0.3
	10	0.78	-	±	-	1.3	±	0.3
	14	0.77	n/a	±	n/a	0.5	±	0.3
BP17;								
13								
	2	0.88	18.9	±	1.4	n/a	±	n/a
	6	0.82	-	±	-	4.6	±	0.7
	10	0.78	-	±	-	0.5	±	0.2
	14	0.79	n/a	±	n/a	0.6	±	0.1
GC186;								
14								
	2	0.84	21.0	±	0.0	n/a	±	n/a
	6	0.82	-	±	-	1.1	±	0.1
	10	0.80	n/a	±	n/a	0.7	±	0.2
GB480;								
15								
	2	0.81	21.0	±	0.0	n/a	±	n/a
	6	0.75	-	±	-	1.0	±	0.1
	10	0.71	-	±	-	1.3	±	0.1
	14	0.72	n/a	±	n/a	1.1	±	0.2
GC699;								
16								
	2	0.78	21.0	±	0.0	n/a	±	n/a
	6	0.78	-	±	-	1.6	±	0.3
	10	0.75	-	±	-	2.1	±	0.3
	14	0.80	n/a	±	n/a	1.6	±	0.4
GC699;								
17								
	2	0.72	-	±	-	n/a	±	n/a
	6	0.71	-	±	-	0.2	±	0.3
	10	0.67	0.2	±	0.5	0.4	±	0.5
	14	0.65	-	±	-	-	±	-
	18	0.72	n/a	±	n/a	-	±	-
GC185;								
18								
	2	0.84	-	±	-	n/a	±	n/a

Residence time is not determined for the bottom-most sediment section (+z transport direction) and for the top-most sediment section (-z transport direction) where initial ^{224}Ra activities are potentially sourced outside of the sampled domain. Such instances are indicated by 'n/a'. Where empirical estimates were not solvable results are indicated by a '-' symbol.

Table A.3. Continued

Site core;	Depth (cmbsf)	Porosity	Residence time +z (days)			Residence time -z (days)		
Taylor; 19	6	0.82	21.0	±	0.0	1.4	±	0.1
	10	0.80	21.0	±	0.0	5.2	±	0.7
	14	0.83	-	±	-	4.0	±	0.6
	18	0.80	n/a	±	n/a	2.1	±	0.9
	2	0.87	-	±	-	n/a	±	n/a
GC600; 20	6	0.81	-	±	-	0.9	±	0.2
	10	0.78	0.7	±	0.4	0.8	±	0.4
	14	0.80	1.9	±	0.9	-	±	-
	18	0.79	n/a	±	n/a	-	±	-
	2	0.84	-	±	-	n/a	±	n/a
GC767; 21	6	0.76	18.4	±	5.3	7.7	±	5.2
	10	0.73	7.2	±	1.5	-	±	-
	14	0.68	2.2	±	0.7	-	±	-
	18	0.66	n/a	±	n/a	-	±	-
	2	0.85	4.5	±	5.1	n/a	±	n/a
BP24; 22	6	0.81	21.0	±	0.0	-	±	-
	10	0.77	-	±	-	-	±	-
	14	0.79	-	±	-	0.2	±	0.1
	18	0.78	n/a	±	n/a	0.2	±	0.1
	2	0.87	-	±	-	n/a	±	n/a
GC767; 23	6	0.79	21.0	±	3.2	11.4	±	4.3
	10	0.80	2.0	±	0.2	-	±	-
	14	0.74	n/a	±	n/a	-	±	-
	2	0.84	-	±	-	n/a	±	n/a
	6	0.81	2.7	±	5.5	6.1	±	5.1
10	0.77	1.8	±	5.2	-	±	-	
14	0.78	3.4	±	1.6	-	±	-	
18	0.78	n/a	±	n/a	-	±	-	

Residence time is not determined for the bottom-most sediment section (+z transport direction) and for the top-most sediment section (-z transport direction) where initial ^{224}Ra activities are potentially sourced outside of the sampled domain. Such instances are indicated by 'n/a'. Where empirical estimates were not solvable results are indicated by a '-' symbol.

Table A.3. Continued

Site core;	Depth (cmbsf)	Porosity	Residence time +z (days)			Residence time -z (days)		
GC600; 24								
	2	0.84	7.0	±	0.6	n/a	±	n/a
	6	0.76	5.2	±	0.4	-	±	-
	10	0.73	3.3	±	0.4	-	±	-
	14	0.68	1.3	±	0.5	-	±	-
	18	0.66	n/a	±	n/a	-	±	-
GC600; 25								
	2	0.84	2.1	±	0.9	n/a	±	n/a
	6	0.76	0.2	±	0.2	-	±	-
	10	0.73	-	±	-	-	±	-
	14	0.68	-	±	-	0.1	±	0.1
	18	0.66	n/a	±	n/a	0.2	±	0.1
GC600; 26								
	2	0.84	0.7	±	0.4	n/a	±	n/a
	6	0.76	1.0	±	0.1	-	±	-
	10	0.73	-	±	-	-	±	-
	14	0.68	-	±	-	0.2	±	0.1
	18	0.66	n/a	±	n/a	0.0	±	0.1
GC600; 27								
	2	0.84	0.8	±	0.3	n/a	±	n/a
	6	0.76	1.0	±	0.2	-	±	-
	10	0.73	0.4	±	0.1	-	±	-
	14	0.68	-	±	-	-	±	-
GC767; 28								
	2	0.86	1.8	±	0.8	n/a	±	n/a
	6	0.80	1.6	±	0.5	-	±	-
	10	0.76	0.3	±	0.2	-	±	-
	14	0.79	-	±	-	-	±	-
	18	0.78	n/a	±	n/a	0.6	±	0.6
GC767; 29								
	2	0.85	0.6	±	0.2	n/a	±	n/a
	6	0.81	-	±	-	-	±	-

Residence time is not determined for the bottom-most sediment section (+z transport direction) and for the top-most sediment section (-z transport direction) where initial ^{224}Ra activities are potentially sourced outside of the sampled domain. Such instances are indicated by 'n/a'. Where empirical estimates were not solvable results are indicated by a '-'. symbol.

Table A.3. Continued

Site core;	Depth (cmbsf)	Porosity	Residence time +z (days)			Residence time -z (days)		
GC185; 30	10	0.77	-	±	-	1.8	±	0.1
	14	0.79	-	±	-	0.5	±	0.1
	18	0.78	n/a	±	n/a	0.5	±	0.1
	2	0.84	0.5	±	0.8	n/a	±	n/a
	6	0.82	0.2	±	0.8	-	±	-
	10	0.80	-	±	-	-	±	-
MC118; 31	14	0.83	-	±	-	0.4	±	5.2
	18	0.80	n/a	±	n/a	2.5	±	5.6
	2	0.87	0.3	±	0.4	n/a	±	n/a
	6	0.78	-	±	-	-	±	-
	10	0.74	-	±	-	0.1	±	0.1
	14	0.70	-	±	-	0.1	±	0.1
Taylor; 32	18	0.69	n/a	±	n/a	0.1	±	0.1
	2	0.87	0.2	±	0.4	n/a	±	n/a
	6	0.81	0.5	±	0.3	-	±	-
	10	0.78	-	±	-	-	±	-
	14	0.80	n/a	±	n/a	0.6	±	0.4
	GC600; 33	2	0.84	0.2	±	0.1	n/a	±
6		0.75	-	±	-	-	±	-
10		0.73	0.1	±	0.1	0.1	±	0.1
14		0.64	-	±	-	-	±	-
18		0.68	n/a	±	n/a	0.1	±	0.1
GC600; 34		2	0.87	0.1	±	0.5	n/a	±
	6	0.78	-	±	-	-	±	-
	10	0.74	-	±	-	0.0	±	0.2
	14	0.72	-	±	-	0.1	±	0.2
	18	0.58	n/a	±	n/a	0.1	±	0.2
	MC118;							

Residence time is not determined for the bottom-most sediment section (+z transport direction) and for the top-most sediment section (-z transport direction) where initial ^{224}Ra activities are potentially sourced outside of the sampled domain. Such instances are indicated by 'n/a'. Where empirical estimates were not solvable results are indicated by a '±' symbol.

Table A.3. Continued

Site core;	Depth (cmbsf)	Porosity	Residence time +z (days)			Residence time -z (days)		
35								
	2	0.81	0.2	±	0.2	n/a	±	n/a
	6	0.73	0.1	±	0.1	-	±	-
	10	0.76	0.1	±	0.1	-	±	-
	14	0.72	0.1	±	0.1	-	±	-
	18	0.72	n/a	±	n/a	-	±	-

Residence time is not determined for the bottom-most sediment section (+z transport direction) and for the top-most sediment section (-z transport direction) where initial ^{224}Ra activities are potentially sourced outside of the sampled domain. Such instances are indicated by 'n/a'. Where empirical estimates were not solvable results are indicated by a '-'. '±' symbol.

Table A.4. Vertical volumetric porefluid flux determined for sediment samples associated with sediment cores recovered from the Gulf of Mexico. Fluid flux is estimated by assuming transport toward the overlying ocean (+z) and also into the sediments (-z). Site name refers to that designated by BOEM and core number refers to the fluid flux rank variable used in Chapter 5 (Fig. 5.2, Fig. 5.3, and 5.4) and Table A.1 and Table A.2 and Table A.3.

Site core;	Depth (cmbsf)	Fluid flux +z (mL cm ⁻² day ⁻¹)			Fluid flux -z (mL cm ⁻² day ⁻¹)		
GC600;							
1							
	2	-	±	-	n/a	±	n/a
	6	-	±	-	-38.4	±	9.6
	10	-	±	-	-6.2	±	6.8
	14	-	±	-	-27.3	±	6.7
	18	n/a	±	n/a	-12.3	±	3.2
OC26;							
2							
	2	-	±	-	n/a	±	n/a
	6	-	±	-	-20.5	±	29.8
	10	-	±	-	-9.1	±	2.0
	14	-	±	-	-17.5	±	6.4
	18	n/a	±	n/a	-16.0	±	12.3
OC26;							
3							
	2	-	±	-	n/a	±	n/a
	6	-	±	-	-13.1	±	1.9
	10	-	±	-	-8.8	±	2.4
	14	n/a	±	n/a	-15.3	±	7.6
BP463;							
4							
	2	-	±	-	n/a	±	n/a
	6	-	±	-	-6.7	±	0.7
	10	-	±	-	-7.8	±	1.5
	14	n/a	±	n/a	-21.3	±	18.8
Taylor;							
5							
	2	-	±	-	n/a	±	n/a
	6	-	±	-	-8.9	±	3.4
	10	-	±	-	-8.5	±	3.3
	14	n/a	±	n/a	-14.8	±	6.2
OC26;							
6							
	2	-	±	-	n/a	±	n/a

Fluid flux is not determined for the bottom-most sediment (+z transport direction) and for the top-most sediment section (-z transport direction) where initial ²²⁴Ra activities are potentially sourced outside of the sampled domain. Such instances are indicated by 'n/a'. Where empirical estimates were not solvable results are indicated by a '-' symbol.

Table A.4. Continued

Site core;	Depth (cmbsf)	Fluid flux +z (mL cm ⁻² day ⁻¹)			Fluid flux -z (mL cm ⁻² day ⁻¹)		
BP444; 7	6	-	±	-	-12.6	±	3.2
	10	-	±	-	-8.8	±	1.5
	14	n/a	±	n/a	-9.6	±	1.7
	2	-	±	-	n/a	±	n/a
	6	-	±	-	-7.1	±	1.7
	10	-	±	-	-7.0	±	2.0
GC574; 8	14	-	±	-	-15.5	±	11.0
	18	n/a	±	n/a	-78.7	±	24.6
	2	-	±	-	n/a	±	n/a
	6	1.6	±	0.7	-60.3	±	16.7
	10	0.7	±	0.2	-	±	-
MC253; 9	14	0.7	±	0.4	-0.1	±	0.0
	18	n/a	±	n/a	-0.4	±	0.4
	2	-	±	-	n/a	±	n/a
	6	-	±	-	-8.0	±	1.0
	10	-	±	-	-6.5	±	1.3
GC574; 10	14	-	±	-	-3.3	±	0.8
	18	n/a	±	n/a	-7.6	±	6.2
	2	-	±	-	n/a	±	n/a
	6	-	±	-	-5.1	±	0.3
	10	-	±	-	-7.1	±	2.6
OC26; 11	14	n/a	±	n/a	-4.3	±	0.4
	2	0.2	±	0.0	n/a	±	n/a
	6	-	±	-	-0.9	±	0.0
	10	-	±	-	-3.2	±	0.9
	14	-	±	-	-2.4	±	0.4
18	n/a	±	n/a	-12.9	±	17.1	

OC26;

Fluid flux is not determined for the bottom-most sediment (+z transport direction) and for the top-most sediment section (-z transport direction) where initial ²²⁴Ra activities are potentially sourced outside of the sampled domain. Such instances are indicated by 'n/a'. Where empirical estimates were not solvable results are indicated by a '-'. ' symbol.

Table A.4. Continued

Site core;	Depth (cmbsf)	Fluid flux +z (mL cm ⁻² day ⁻¹)			Fluid flux -z (mL cm ⁻² day ⁻¹)		
12	2	-	±	-	n/a	±	n/a
	6	-	±	-	-2.1	±	0.5
	10	-	±	-	-2.5	±	0.7
	14	n/a	±	n/a	-6.0	±	6.9
BP17; 13	2	0.2	±	0.0	n/a	±	n/a
	6	-	±	-	-0.7	±	0.1
	10	-	±	-	-6.0	±	5.8
	14	n/a	±	n/a	-5.2	±	1.4
GC186; 14	2	0.2	±	0.0	n/a	±	n/a
	6	-	±	-	-3.0	±	0.4
	10	n/a	±	n/a	-4.3	±	1.1
GB480; 15	2	0.2	±	0.0	n/a	±	n/a
	6	-	±	-	-3.0	±	0.4
	10	-	±	-	-2.2	±	0.3
	14	n/a	±	n/a	-2.6	±	0.6
GC699; 16	2	0.1	±	0.0	n/a	±	n/a
	6	-	±	-	-1.9	±	0.5
	10	-	±	-	-1.5	±	0.2
	14	n/a	±	n/a	-2.1	±	0.6
GC699; 17	2	-	±	-	n/a	±	n/a
	6	-	±	-	-16.0	±	16.9
	10	17.5	±	5.7	-6.1	±	6.7
	14	-	±	-	-	±	-
	18	n/a	±	n/a	-	±	-
GC185; 18	2	-	±	-	n/a	±	n/a

Fluid flux is not determined for the bottom-most sediment (+z transport direction) and for the top-most sediment section (-z transport direction) where initial ²²⁴Ra activities are potentially sourced outside of the sampled domain. Such instances are indicated by 'n/a'. Where empirical estimates were not solvable results are indicated by a '-'. symbol.

Table A.4. Continued

Site core;	Depth (cmbsf)	Fluid flux +z (mL cm ⁻² day ⁻¹)			Fluid flux -z (mL cm ⁻² day ⁻¹)		
Taylor; 19	6	0.2	±	0.0	-2.3	±	0.2
	10	0.2	±	0.0	-0.6	±	0.1
	14	-	±	-	-0.8	±	0.1
	18	n/a	±	n/a	-1.5	±	0.8
	2	-	±	-	n/a	±	n/a
GC600; 20	6	-	±	-	-3.7	±	1.7
	10	4.5	±	3.3	-3.7	±	1.6
	14	1.7	±	0.8	-	±	-
	18	n/a	±	n/a	-	±	-
	2	-	±	-	n/a	±	n/a
GC767; 21	6	0.2	±	0.6	-0.4	±	1.1
	10	0.4	±	0.1	-	±	-
	14	1.2	±	0.8	-	±	-
	18	n/a	±	n/a	-	±	-
	2	0.8	±	0.4	n/a	±	n/a
BP24; 22	6	0.2	±	0.0	-	±	-
	10	-	±	-	-	±	-
	14	-	±	-	-18.8	±	9.2
	18	n/a	±	n/a	-14.5	±	14.4
	2	-	±	-	n/a	±	n/a
GC767; 23	6	0.2	±	0.1	-0.3	±	0.1
	10	1.6	±	0.1	-	±	-
	14	n/a	±	n/a	-	±	-
	2	-	±	-	n/a	±	n/a
	6	1.2	±	0.3	-0.5	±	0.7
GC767; 23	10	1.8	±	0.5	-	±	-
	14	0.9	±	0.8	-	±	-
	18	n/a	±	n/a	-	±	-

Fluid flux is not determined for the bottom-most sediment (+z transport direction) and for the top-most sediment section (-z transport direction) where initial ²²⁴Ra activities are potentially sourced outside of the sampled domain. Such instances are indicated by 'n/a'. Where empirical estimates were not solvable results are indicated by a '-' symbol.

Table A.4. Continued

Site core;	Depth (cmbsf)	Fluid flux +z (mL cm ⁻² day ⁻¹)			Fluid flux -z (mL cm ⁻² day ⁻¹)		
GC600; 24	2	0.5	±	0.0	n/a	±	n/a
	6	0.6	±	0.1	-	±	-
	10	0.9	±	0.1	-	±	-
	14	2.2	±	1.0	-	±	-
	18	n/a	±	n/a	-	±	-
GC600; 25	2	1.6	±	1.3	n/a	±	n/a
	6	2.5	±	0.6	-	±	-
	10	-	±	-	-	±	-
	14	-	±	-	-42.4	±	46.9
	18	n/a	±	n/a	-11.0	±	22.8
GC600; 26	2	4.9	±	3.2	n/a	±	n/a
	6	2.9	±	0.4	-	±	-
	10	-	±	-	-	±	-
	14	-	±	-	-11.8	±	5.8
	18	n/a	±	n/a	-164.4	±	42.1
GC600; 27	2	4.1	±	9.9	n/a	±	n/a
	6	3.1	±	0.8	-	±	-
	10	6.5	±	1.5	-	±	-
	14	-	±	-	-	±	-
GC767; 28	2	1.9	±	1.1	n/a	±	n/a
	6	2.0	±	1.1	-	±	-
	10	11.9	±	2.9	-	±	-
	14	-	±	-	-	±	-
	18	n/a	±	n/a	-5.2	±	8.9
GC767; 29	2	5.9	±	3.6	n/a	±	n/a
	6	-	±	-	-	±	-

Fluid flux is not determined for the bottom-most sediment (+z transport direction) and for the top-most sediment section (-z transport direction) where initial ²²⁴Ra activities are potentially sourced outside of the sampled domain. Such instances are indicated by 'n/a'. Where empirical estimates were not solvable results are indicated by a '-'. symbol.

Table A.4. Continued

Site core;	Depth (cmbsf)	Fluid flux +z (mL cm ⁻² day ⁻¹)			Fluid flux -z (mL cm ⁻² day ⁻¹)		
GC185; 30	10	-	±	-	-1.7	±	0.1
	14	-	±	-	-6.4	±	2.5
	18	n/a	±	n/a	-6.5	±	2.7
	2	7.2	±	4.7	n/a	±	n/a
	6	17.1	±	6.8	-	±	-
	10	-	±	-	-	±	-
MC118; 31	14	-	±	-	-8.8	±	35.2
	18	n/a	±	n/a	-1.3	±	1.3
	2	12.8	±	2.9	n/a	±	n/a
	6	-	±	-	-	±	-
	10	-	±	-	-27.1	±	5.8
	14	-	±	-	-26.0	±	7.0
Taylor; 32	18	n/a	±	n/a	19.2	±	6.0
	2	20.9	±	4.7	n/a	±	n/a
	6	6.9	±	2.2	-	±	-
	10	-	±	-	-	±	-
	14	n/a	±	n/a	-5.8	±	70.0
GC600; 33	2	17.6	±	3.2	n/a	±	n/a
	6	-	±	-	-	±	-
	10	27.8	±	7.5	-38.6	±	8.4
	14	-	±	-	-	±	-
	18	n/a	±	n/a	-30.1	±	7.4
GC600; 34	2	30.4	±	7.9	n/a	±	n/a
	6	-	±	-	-	±	-
	10	-	±	-	-84.7	±	22.8
	14	-	±	-	-38.4	±	43.5
	18	n/a	±	n/a	-24.7	±	6.0
MC118;							

Fluid flux is not determined for the bottom-most sediment (+z transport direction) and for the top-most sediment section (-z transport direction) where initial ²²⁴Ra activities are potentially sourced outside of the sampled domain. Such instances are indicated by 'n/a'. Where empirical estimates were not solvable results are indicated by a '-' symbol.

Table A.4. Continued

Site core;	Depth (cmbsf)	Fluid flux +z (mL cm ⁻² day ⁻¹)			Fluid flux -z (mL cm ⁻² day ⁻¹)		
35	2	83.8	±	21.6	n/a	±	n/a
	6	12.8	±	44.3	-	±	-
	10	30.3	±	7.7	-	±	-
	14	30.8	±	12.8	-	±	-
	18	n/a	±	n/a	-	±	-

Fluid flux is not determined for the bottom-most sediment (+z transport direction) and for the top-most sediment section (-z transport direction) where initial ²²⁴Ra activities are potentially sourced outside of the sampled domain. Such instances are indicated by 'n/a'. Where empirical estimates were not solvable results are indicated by a '-' symbol.

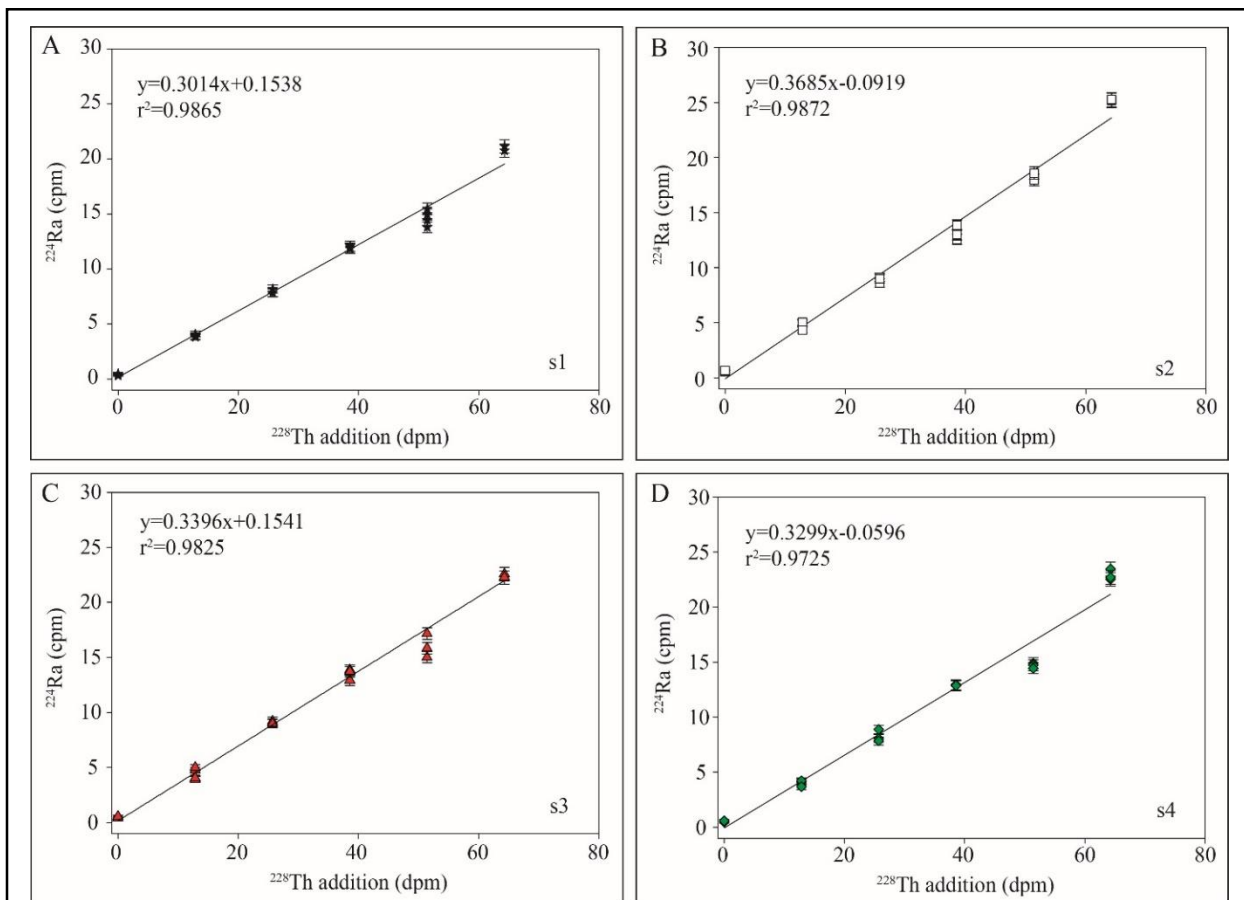


Figure A.2. Calibration curves and counting efficiency (slope) for RaDeCC analysis of sediment-coated filters. Standards were prepared using the method of standard addition for systems (A) 1, (B) 2, (C) 3, (D) 4. Note that calibrations were applied only for sediment-coated filter analysis relevant to analysis discussed in Chapter 4 and Chapter 5. Separate calibrations were performed for analysis of Mn-fibers.

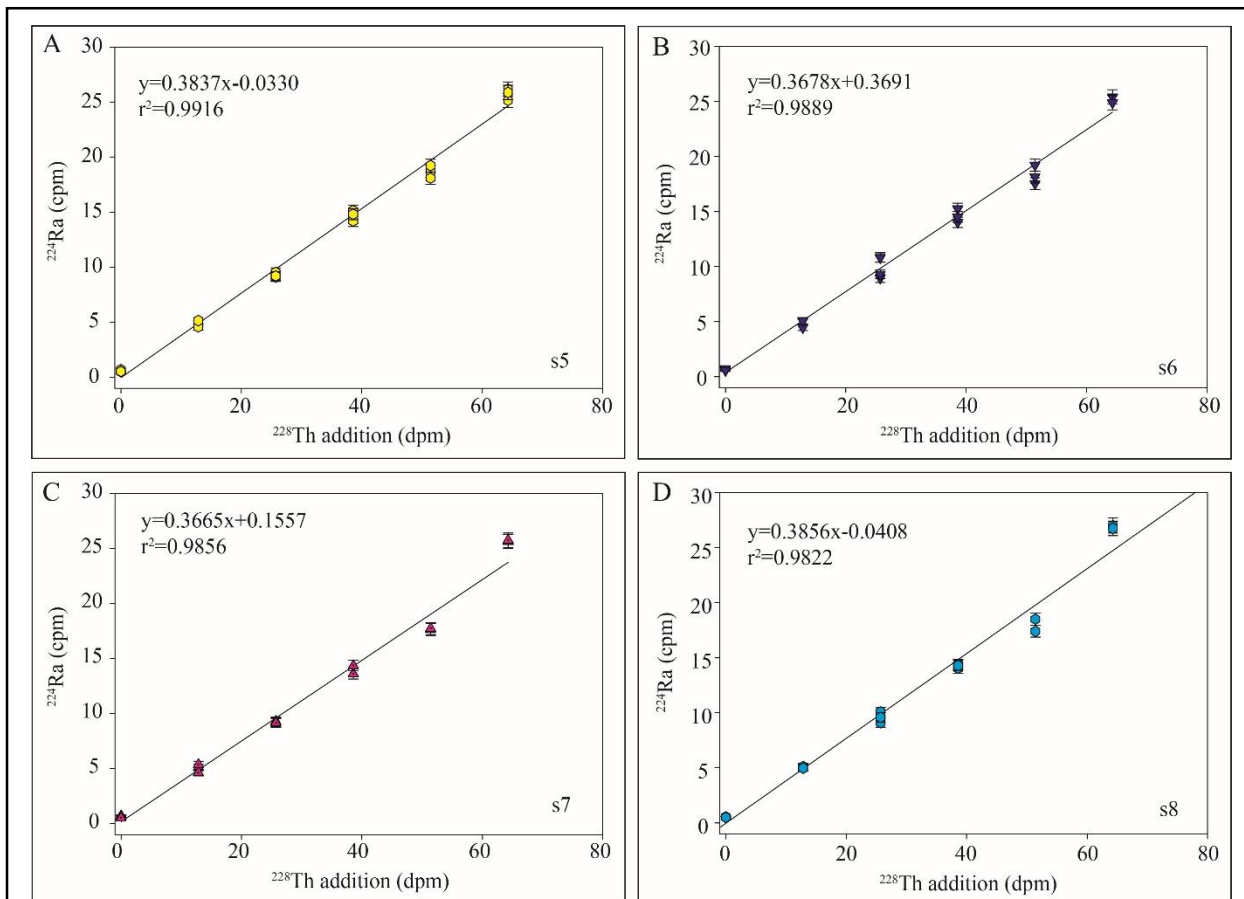


Figure A.3. Calibration curves and counting efficiency (slope) for RaDeCC analysis of sediment-coated filters. Standards were prepared using the method of standard addition for systems (A) 5, (B) 6, (C) 7, (D) 8. Note that calibrations were applied only for sediment-coated filter analysis relevant to analysis discussed in Chapter 4 and Chapter 5. Separate calibrations were performed for analysis of Mn-fibers.

Table A.5. Surface-sorbed ^{224}Ra and aqueous activities measured at sea and at equilibrium for samples recovered from Guaymas Basin. Dive number refers to the HOV *Alvin* dive number during cruise AT37-06 and core number refers to the fluid flux rank variable used in Chapter 5 (Figure 5.4).

Site; Depth core (cmbsf)	$^{\text{?}}$ Initial (dpm g $^{-1}$)			** Initial (dpm g $^{-1}$)			$^{\text{?}}$ Equilibrium (dpm L $^{-1}$)			** Equilibrium (dpm L $^{-1}$)		
4870;												
1												
1	2.6	±	0.3	16.0	±	7.7	3.2	±	0.3	31.5	±	10.5
3	0.8	±	0.1	16.2	±	1.2	2.2	±	0.2	32.3	±	7.1
5	1.8	±	0.2	17.0	±	4.7	2.8	±	0.2	24.5	±	9.3
7	2.3	±	0.2	26.3	±	8.4	1.2	±	0.1	31.3	±	4.0
9	3.1	±	0.3	23.0	±	9.1	3.9	±	0.4	23.3	±	12.9
12	0.6	±	0.1	14.4	±	1.9	0.8	±	0.1	21.1	±	2.7
4864;												
2												
1	3.9	±	0.2	32.3	±	12.1	3.9	±	0.2	35.6	±	12.3
3	1.8	±	0.2	42.0	±	5.6	2.1	±	0.2	41.1	±	7.1
5	5.3	±	0.5	31.7	±	17.2	4.4	±	0.4	29.7	±	14.6
7	1.2	±	0.1	28.3	±	3.8	1.0	±	0.1	24.0	±	3.3
9	0.9	±	0.1	10.4	±	2.8	0.7	±	0.0	9.9	±	2.3
12	0.7	±	0.1	7.8	±	2.2	0.8	±	0.1	7.9	±	2.7
16	0.5	±	0.1	6.8	±	1.6	0.5	±	0.0	7.8	±	1.6
4869;												
3												
1	5.0	±	0.2	38.1	±	14.4	6.1	±	0.1	46.7	±	19.2
3	1.9	±	0.1	28.9	±	6.1	1.8	±	0.1	36.5	±	5.8
5	1.0	±	0.1	16.1	±	2.9	1.4	±	0.1	18.9	±	4.3
7	1.4	±	0.1	11.3	±	4.4	1.7	±	0.2	16.4	±	5.6
9	0.8	±	0.1	12.4	±	2.3	1.1	±	0.1	16.6	±	3.7
12	1.2	±	0.1	9.7	±	3.8	1.4	±	0.1	12.8	±	4.7
16	0.7	±	0.1	10.5	±	2.1	0.7	±	0.0	12.5	±	2.3
4861;												
4												
1	4.8	±	0.7	36.5	±	14.9	5.7	±	0.5	45.5	±	18.5
3	2.0	±	0.3	28.8	±	7.1	2.0	±	0.2	33.2	±	6.7
5	1.1	±	0.2	14.6	±	4.0	0.7	±	0.1	14.1	±	2.4
7	0.7	±	0.2	10.8	±	2.5	0.8	±	0.1	9.3	±	2.7
9	1.0	±	0.2	8.2	±	3.8	0.8	±	0.1	9.7	±	2.7
12	0.6	±	0.1	8.4	±	1.7	0.8	±	0.1	10.2	±	2.6
16	0.8	±	0.1	6.7	±	2.3	0.9	±	0.1	10.4	±	3.0

$^{\text{?}}$ Activities of ^{224}Ra measured using sediment-coated filters; ** Corrected aqueous ^{224}Ra activities. Corrections described in Chapter 2.

Table A.5. Continued

Site; Depth core (cmbsf)	²²⁴ Initial (dpm g ⁻¹)			**Initial (dpm g ⁻¹)			²²⁴ Equilibrium (dpm L ⁻¹)			**Equilibrium (dpm L ⁻¹)		
4867; 5												
1	11.6	±	0.6	74.9	±	34.8	12.3	±	0.5	83.0	±	38.8
3	1.8	±	0.1	53.1	±	5.6	1.7	±	0.2	57.9	±	5.6
5	0.8	±	0.1	12.8	±	2.7	0.6	±	0.1	12.6	±	2.1
7	0.8	±	0.1	9.6	±	2.4	0.9	±	0.1	9.7	±	2.9
9	0.9	±	0.1	8.2	±	2.9	1.0	±	0.1	9.5	±	3.2
12	0.5	±	0.0	7.4	±	1.5	0.6	±	0.0	8.5	±	1.9
16	0.5	±	0.1	5.7	±	1.7	0.6	±	0.0	7.0	±	1.9
4866; 6												
1	3.0	±	0.2	25.4	±	8.9	3.7	±	0.1	33.5	±	11.5
3	1.7	±	0.2	21.2	±	5.0	2.0	±	0.1	25.0	±	6.4
5	1.0	±	0.1	13.1	±	3.6	0.7	±	0.0	14.3	±	2.2
7	0.8	±	0.1	9.7	±	2.4	1.0	±	0.1	9.2	±	3.1
9	0.7	±	0.1	8.1	±	2.1	0.7	±	0.1	9.2	±	2.3
12	0.7	±	0.1	7.3	±	2.2	0.7	±	0.0	7.5	±	2.1
16	0.6	±	0.1	7.1	±	1.8	0.5	±	0.0	7.2	±	1.7
4862; 7												
1	8.0	±	0.8	52.1	±	24.6	9.3	±	0.8	63.7	±	30.4
3	1.5	±	0.2	38.0	±	5.1	1.5	±	0.1	46.5	±	5.0
5	0.9	±	0.1	11.3	±	2.8	1.0	±	0.1	13.2	±	3.4
7	0.7	±	0.1	8.4	±	2.1	0.8	±	0.1	10.2	±	2.6
9	0.7	±	0.1	7.3	±	2.3	0.8	±	0.1	8.5	±	2.5
12	0.6	±	0.1	7.7	±	2.1	0.6	±	0.1	7.6	±	2.0
16	0.7	±	0.1	7.6	±	2.4	0.6	±	0.0	6.9	±	1.8
4861; 8												
1	5.2	±	0.5	47.8	±	14.4	8.0	±	0.5	68.3	±	25.3
3	3.9	±	0.4	36.5	±	12.8	3.6	±	0.3	53.5	±	11.7
5	1.4	±	0.2	25.9	±	4.3	2.0	±	0.2	28.1	±	6.6
7	1.7	±	0.4	12.9	±	6.6	1.5	±	0.2	21.2	±	5.2
9	0.8	±	0.2	10.0	±	2.1	1.9	±	0.2	21.1	±	6.1
12	0.8	±	0.2	6.6	±	1.7	2.0	±	0.2	22.6	±	6.5
16	1.0	±	0.2	7.2	±	2.8	1.9	±	0.1	22.8	±	5.9
4862; 9												

²²⁴Activities of ²²⁴Ra measured using sediment-coated filters; **Corrected aqueous ²²⁴Ra activities. Corrections described in Chapter 2.

Table A.5. Continued

Site; core	Depth (cmbsf)	[?] Initial (dpm g ⁻¹)			^{**} Initial (dpm g ⁻¹)			[?] Equilibrium (dpm L ⁻¹)			^{**} Equilibrium (dpm L ⁻¹)		
	1	8.3	±	0.6	108.8	±	26.3	7.5	±	0.4	154.7	±	23.8
	3	12.8	±	1.2	91.1	±	33.8	18.7	±	1.3	125.3	±	60.1
	5	5.1	±	0.3	74.3	±	15.0	5.6	±	0.5	115.3	±	18.5
	7	4.3	±	0.2	42.5	±	12.4	5.0	±	0.5	51.3	±	16.6
	9	2.3	±	0.2	35.1	±	7.1	2.4	±	0.2	44.4	±	7.9
	12	3.3	±	0.3	28.3	±	9.4	3.9	±	0.3	33.6	±	12.5
	16	2.3	±	0.2	29.7	±	7.1	2.2	±	0.2	36.0	±	7.4
4872; 10													
	1	4.3	±	0.4	22.4	±	11.3	6.0	±	0.6	44.9	±	20.1
	3	0.8	±	0.1	17.1	±	1.4	1.5	±	0.0	32.3	±	4.8
	5	0.6	±	0.1	4.9	±	1.8	0.6	±	0.0	11.8	±	2.0
	7	0.5	±	0.0	4.0	±	1.0	0.8	±	0.0	8.8	±	2.6
	9	0.4	±	0.0	2.7	±	0.6	0.8	±	0.0	10.6	±	2.5
	12	0.5	±	0.0	4.1	±	0.7	1.1	±	0.1	9.9	±	3.4
	16	0.7	±	0.1	5.0	±	2.1	0.6	±	0.0	10.1	±	2.1
4872; 11													
	1	6.7	±	0.5	42.5	±	20.0	6.9	±	0.4	53.5	±	22.1
	3	1.4	±	0.1	30.0	±	3.2	2.1	±	0.2	38.3	±	6.9
	5	0.5	±	0.0	7.9	±	1.3	0.7	±	0.0	13.5	±	2.2
	7	0.6	±	0.0	4.7	±	1.9	0.6	±	0.0	10.9	±	2.1
	9	0.7	±	0.0	4.4	±	0.5	1.4	±	0.1	10.4	±	4.6
	12	0.4	±	0.0	3.8	±	1.1	0.5	±	0.0	11.5	±	1.8
	16	0.7	±	0.0	4.7	±	1.5	0.9	±	0.0	8.7	±	2.9
4869; 12													
	1	1.8	±	0.2	14.0	±	4.2	3.2	±	0.3	26.1	±	10.5
	3	1.2	±	0.1	13.2	±	3.6	1.3	±	0.1	22.9	±	4.1
	5	1.1	±	0.1	11.0	±	3.2	1.4	±	0.1	13.9	±	4.6
	7	0.8	±	0.1	9.4	±	2.4	0.9	±	0.1	12.1	±	2.9
	9	0.7	±	0.1	7.1	±	2.3	0.8	±	0.1	9.6	±	2.7
	12	0.5	±	0.0	6.4	±	1.3	0.7	±	0.1	9.0	±	2.4
4871; 13													
	1	3.0	±	0.3	20.6	±	8.8	3.5	±	0.1	28.9	±	10.9
	3	1.1	±	0.1	15.2	±	2.8	1.4	±	0.1	26.2	±	4.4
	5	0.9	±	0.1	7.7	±	1.2	1.7	±	0.1	21.2	±	5.6

[?]Activities of ²²⁴Ra measured using sediment-coated filters; ^{**}Corrected aqueous ²²⁴Ra activities. Corrections described in Chapter 2.

Table A.5. Continued

Site; core	Depth (cmbsf)	⁷ Initial (dpm g ⁻¹)			^{**} Initial (dpm g ⁻¹)			[?] Equilibrium (dpm L ⁻¹)			^{**} Equilibrium (dpm L ⁻¹)		
4868; 14	7	1.3	±	0.1	6.7	±	2.5	2.2	±	0.2	22.0	±	7.2
	9	1.0	±	0.1	7.9	±	2.0	1.6	±	0.1	22.4	±	5.2
	12	1.1	±	0.1	7.4	±	2.1	1.8	±	0.1	20.4	±	5.9
	1	4.3	±	0.4	26.8	±	10.8	8.0	±	0.7	71.1	±	26.1
	3	2.0	±	0.2	23.6	±	4.2	4.0	±	0.1	55.3	±	12.6
	5	1.6	±	0.2	13.3	±	4.8	2.0	±	0.1	28.0	±	6.3
	7	0.8	±	0.1	10.1	±	2.1	1.1	±	0.1	15.0	±	3.4
	9	0.6	±	0.0	7.9	±	1.5	0.7	±	0.1	12.7	±	2.4
4871; 15	12	1.1	±	0.1	7.4	±	2.9	1.4	±	0.1	11.4	±	4.6
	16	0.6	±	0.1	8.4	±	1.7	0.7	±	0.0	12.7	±	2.4
	1	2.8	±	0.3	27.3	±	5.3	6.0	±	0.5	63.3	±	19.5
	3	3.6	±	0.3	25.7	±	10.0	4.7	±	0.3	61.9	±	15.1
	5	2.8	±	0.3	23.9	±	6.3	5.0	±	0.4	47.2	±	16.1
	7	1.5	±	0.1	16.5	±	3.8	2.2	±	0.2	38.3	±	7.5
	9	1.5	±	0.2	11.2	±	3.8	2.5	±	0.2	22.4	±	8.0
	12	0.7	±	0.1	8.3	±	1.9	1.0	±	0.1	22.0	±	3.2
4868; 16	16	0.9	±	0.1	5.6	±	1.3	2.1	±	0.2	18.3	±	7.0
	1	3.6	±	0.4	17.0	±	3.4	10.2	±	0.4	73.4	±	32.3
	3	2.0	±	0.1	15.7	±	6.0	2.2	±	0.1	54.3	±	6.9
	5	1.2	±	0.1	14.0	±	3.5	1.4	±	0.1	17.1	±	4.4
	7	0.7	±	0.1	9.3	±	1.8	0.8	±	0.0	11.8	±	2.6
	9	0.8	±	0.1	7.3	±	2.2	0.8	±	0.1	9.7	±	2.7
4872; 17	1	3.3	±	0.3	12.8	±	4.9	8.6	±	0.4	67.2	±	27.1
	3	1.2	±	0.1	9.8	±	2.2	2.8	±	0.1	49.1	±	8.7
	5	0.5	±	0.1	7.4	±	1.0	1.1	±	0.1	24.8	±	3.4
	7	1.3	±	0.1	6.2	±	2.9	2.4	±	0.2	17.2	±	7.8
	9	0.6	±	0.1	5.5	±	1.4	0.9	±	0.1	18.9	±	2.8
	12	0.5	±	0.1	4.5	±	0.4	1.5	±	0.1	14.6	±	4.8
	16	0.8	±	0.1	4.3	±	2.0	1.3	±	0.0	16.8	±	4.2
	4862;												

[?]Activities of ²²⁴Ra measured using sediment-coated filters; ^{**}Corrected aqueous ²²⁴Ra activities. Corrections described in Chapter 2.

Table A.5. Continued

Site; core	Depth (cmbsf)	[?] Initial (dpm g ⁻¹)		^{**} Initial (dpm g ⁻¹)		[?] Equilibrium (dpm L ⁻¹)		^{**} Equilibrium (dpm L ⁻¹)	
18									
	1	2.3	± 0.2	11.8	± 2.4	5.1	± 0.5	40.5	± 16.9
	3	1.5	± 0.1	10.7	± 4.3	1.8	± 0.1	30.5	± 5.5
	5	0.8	± 0.1	10.2	± 2.4	0.9	± 0.1	13.6	± 2.8
	7	0.7	± 0.1	7.2	± 2.0	0.8	± 0.1	9.3	± 2.7
	9	0.6	± 0.1	6.8	± 1.7	0.7	± 0.0	9.0	± 2.1
	12	0.7	± 0.1	6.7	± 2.1	0.8	± 0.1	8.7	± 2.6
4871; 19									
	1	4.0	± 0.4	18.8	± 6.2	8.9	± 0.2	76.5	± 27.9
	3	2.1	± 0.2	16.9	± 4.3	4.0	± 0.2	61.7	± 12.7
	5	1.6	± 0.2	15.4	± 3.7	2.7	± 0.1	36.5	± 8.5
	7	1.9	± 0.2	15.1	± 5.0	2.5	± 0.2	25.6	± 8.4
	9	1.3	± 0.1	11.9	± 4.1	1.2	± 0.1	17.3	± 3.9
	12	0.4	± 0.0	7.2	± 1.0	0.6	± 0.0	10.7	± 2.0
	16	0.5	± 0.1	3.5	± 1.0	0.9	± 0.1	8.7	± 2.8

[?]Activities of ²²⁴Ra measured using sediment-coated filters; ^{**}Corrected aqueous ²²⁴Ra activities. Corrections described in Chapter 2.

Table A.6. Porefluid residence time and porosity for sediment samples associated with sediment cores recovered from Guaymas Basin. Residence time is estimated by assuming transport toward the overlying ocean (+z) and also into the sediments (-z). Dive number refers to the HOV *Alvin* dive number during cruise AT37-06 and core number refers to the fluid flux rank variable used in Chapter 5 (Figure 5.4).

Site core;	Depth (cmbf)	Porosity	Residence time +z (days)		Residence time -z (days)		
4870;							
1							
	1	0.87	-	± -	n/a	±	n/a
	3	0.87	-	± -	0.1	±	10.9
	5	0.83	21.0	± 0.3	0.5	±	1.7
	7	0.83	2.5	± 0.4	5.2	±	1.7
	9	0.81	14.4	± 1.4	21.0	±	0.6
	12	0.80	4.1	± 0.3	21.0	±	2.4
4864;							
2							
	1	0.86	21.0	± 0.6	n/a	±	n/a
	3	0.86	20.5	± 0.6	20.2	±	0.3
	5	0.83	13.8	± 2.5	10.9	±	0.3
	7	0.81	21.0	± 0.0	3.3	±	0.2
	9	0.79	20.0	± 0.4	19.7	±	0.1
	12	0.83	12.4	± 1.3	21.0	±	2.2
	16	0.82	n/a	± n/a	21.0	±	0.0
4869;							
3							
	1	0.79	3.6	± 3.8	n/a	±	n/a
	3	0.79	4.9	± 0.4	21.0	±	0.2
	5	0.80	4.8	± 1.3	21.0	±	0.1
	7	0.80	-	± -	-	±	-
	9	0.80	2.4	± 1.8	1.1	±	0.6
	12	0.80	-	± -	-	±	-
	16	0.80	n/a	± n/a	0.4	±	6.1
4861;							
4							
	1	0.86	3.0	± 4.2	n/a	±	n/a
	3	0.86	7.0	± 0.5	18.8	±	9.9
	5	0.83	20.5	± 0.2	7.2	±	0.2
	7	0.81	17.6	± 6.2	21.0	±	0.5
	9	0.79	-	± -	0.5	±	1.6

Residence time is not determined for the bottom-most sediment section (+z transport direction) and for the top-most sediment section (-z transport direction) where initial ^{224}Ra activities are potentially sourced outside of the sampled domain. Such instances are indicated by 'n/a'. Where empirical estimates were not solvable results are indicated by a '±' symbol.

Table A.6. Continued

Site core;	Depth (cmbsf)	Porosity	Residence time +z (days)			Residence time -z (days)		
4867; 5	12	0.83	3.2	±	5.3	0.5	±	6.0
	16	0.82	n/a	±	n/a	-	±	-
	1	0.94	6.2	±	0.3	n/a	±	n/a
	3	0.94	11.1	±	0.1	21.0	±	0.2
	5	0.90	20.6	±	0.8	21.0	±	0.0
	7	0.86	9.8	±	0.3	21.0	±	0.6
	9	0.86	2.3	±	0.5	21.0	±	0.5
	12	0.85	2.9	±	0.8	-	±	-
4866; 6	16	0.84	n/a	±	n/a	-	±	-
	1	0.88	2.1	±	7.7	n/a	±	n/a
	3	0.88	5.6	±	0.4	21.0	±	0.5
	5	0.90	6.3	±	0.4	21.0	±	0.1
	7	0.90	17.8	±	0.5	12.78	±	1.1
	9	0.86	2.3	±	0.7	21.0	±	0.4
	12	0.82	2.5	±	1.7	21.0	±	0.9
	16	0.82	n/a	±	n/a	21.0	±	6.4
4862; 7	1	0.86	3.9	±	0.4	n/a	±	n/a
	3	0.86	7.1	±	0.1	21.0	±	0.5
	5	0.83	4.5	±	5.0	21.0	±	0.1
	7	0.81	2.2	±	0.5	21.0	±	1.1
	9	0.83	-	±	-	-	±	-
	12	0.83	15.4	±	0.8	14.0	±	1.0
	16	0.82	n/a	±	n/a	5.6	±	5.6
	4861; 8	1	0.79	2.2	±	0.5	n/a	±
3		0.80	2.4	±	1.5	-	±	-
5		0.82	9.3	±	0.4	21.0	±	0.3
7		0.82	1.5	±	1.2	21.0	±	0.1
9		0.73	1.4	±	0.4	-	±	-

Residence time is not determined for the bottom-most sediment section (+z transport direction) and for the top-most sediment section (-z transport direction) where initial ^{224}Ra activities are potentially sourced outside of the sampled domain. Such instances are indicated by 'n/a'. Where empirical estimates were not solvable results are indicated by a '-' symbol.

Table A.6. Continued

Site core;	Depth (cmbsf)	Porosity	Residence time +z (days)			Residence time -z (days)		
4862; 9	12	0.76	-	±	-	-	±	-
	16	0.80	n/a	±	n/a	0.2	±	0.5
	1	0.79	1.6	±	0.4	n/a	±	n/a
	3	0.80	2.0	±	4.3	-	±	-
	5	0.82	2.9	±	1.2	-	±	-
	7	0.82	2.9	±	11.1	21.0	±	0.3
	9	0.73	2.7	±	0.3	-	±	-
	12	0.76	0.8	±	2.7	21.0	±	6.2
4872; 10	16	0.80	n/a	±	n/a	21.0	±	5.6
	1	0.86	1.1	±	1.0	n/a	±	n/a
	3	0.86	3.0	±	0.1	-	±	-
	5	0.80	0.6	±	17.0	21.0	±	0.0
	7	0.73	1.2	±	1.7	-	±	-
	9	0.73	-	±	-	-	±	-
	12	0.72	-	±	-	2.8	±	0.9
	16	0.72	n/a	±	n/a	18.4	±	4.7
4872; 11	1	0.88	3.8	±	0.4	n/a	±	n/a
	3	0.88	6.5	±	0.1	21.0	±	0.4
	5	0.86	2.3	±	17.0	21.0	±	0.0
	7	0.86	0.3	±	2.1	-	±	-
	9	0.84	0.5	±	26.3	-	±	-
	12	0.82	-	±	-	-	±	-
	16	0.80	n/a	±	n/a	0.3	±	0.9
	4869; 12	1	0.78	0.3	±	11.4	n/a	±
3		0.78	1.0	±	0.8	-	±	-
5		0.85	2.1	±	1.1	-	±	-
7		0.85	3.1	±	0.5	-	±	-
9		0.84	1.2	±	0.6	-	±	-

Residence time is not determined for the bottom-most sediment section (+z transport direction) and for the top-most sediment section (-z transport direction) where initial ^{224}Ra activities are potentially sourced outside of the sampled domain. Such instances are indicated by 'n/a'. Where empirical estimates were not solvable results are indicated by a '±' symbol.

Table A.6. Continued

Site core;	Depth (cmbsf)	Porosity	Residence time +z (days)			Residence time -z (days)		
4871; 13	12	0.84	n/a	±	n/a	-	±	-
	1	0.76	2.5	±	0.3	n/a	±	n/a
	3	0.76	2.6	±	0.3	-	±	-
	5	0.76	0.4	±	1.2	-	±	-
	7	0.74	-	±	-	-	±	-
	9	0.73	0.2	±	4.4	0.4	±	1.9
	12	0.73	n/a	±	n/a	-	±	-
4868; 14	1	0.89	0.4	±	1.8	n/a	±	n/a
	3	0.89	1.4	±	2.9	-	±	-
	5	0.82	1.0	±	3.9	-	±	-
	7	0.82	1.8	±	108.4	-	±	-
	9	0.82	0.5	±	1.2	-	±	-
	12	0.82	n/a	±	n/a	0.6	±	5.4
	16	0.82	n/a	±	n/a	-	±	-
4871; 15	1	0.87	0.2	±	3.0	n/a	±	n/a
	3	0.87	0.3	±	2.4	-	±	-
	5	0.87	1.4	±	3.6	-	±	-
	7	0.87	1.1	±	1.9	-	±	-
	9	0.84	1.2	±	2.0	-	±	-
	12	0.82	0.6	±	8.5	-	±	-
	16	0.79	n/a	±	n/a	-	±	-
4868; 16	1	0.79	0.1	±	5.0	n/a	±	n/a
	3	0.78	0.2	±	2.0	-	±	-
	5	0.76	4.5	±	0.7	-	±	-
	7	0.75	2.8	±	4.4	21.0	±	0.3
	9	0.73	n/a	±	n/a	-	±	-
	16	0.73	n/a	±	n/a	-	±	-
4872; 17	1	0.88	0.3	±	20.0	n/a	±	n/a
	3	0.88	0.3	±	30.2	-	±	-
	16	0.88	n/a	±	n/a	-	±	-

Residence time is not determined for the bottom-most sediment section (+z transport direction) and for the top-most sediment section (-z transport direction) where initial ^{224}Ra activities are potentially sourced outside of the sampled domain. Such instances are indicated by 'n/a'. Where empirical estimates were not solvable results are indicated by a '±' symbol.

Table A.6. Continued

Site core;	Depth (cmbsf)	Porosity	Residence time +z (days)			Residence time -z (days)		
4862; 18	5	0.74	0.3	±	22.2	-	±	-
	7	0.74	0.3	±	1.9	-	±	-
	9	0.76	0.4	±	10.4	-	±	-
	12	0.77	-	±	-	-	±	-
	16	0.78	n/a	±	n/a	0.4	±	0.5
	18	0.78	n/a	±	n/a	-	±	-
4871; 19	1	0.86	0.2	±	3.4	n/a	±	n/a
	3	0.86	0.1	±	5.0	-	±	-
	5	0.83	3.2	±	1.0	-	±	-
	7	0.79	0.8	±	3.8	21.0	±	0.2
	9	0.79	0.2	±	4.4	-	±	-
	12	0.83	n/a	±	n/a	-	±	-
4871; 19	1	0.86	0.2	±	3.7	n/a	±	n/a
	3	0.86	0.2	±	6.2	-	±	-
	5	0.86	0.1	±	10.8	-	±	-
	7	0.85	1.3	±	0.8	-	±	-
	9	0.84	3.2	±	1.8	-	±	-
	12	0.82	3.4	±	2.0	21	±	5.3
16	0.80	n/a	±	n/a	-	±	-	

Residence time is not determined for the bottom-most sediment section (+z transport direction) and for the top-most sediment section (-z transport direction) where initial ^{224}Ra activities are potentially sourced outside of the sampled domain. Such instances are indicated by 'n/a'. Where empirical estimates were not solvable results are indicated by a '-' symbol.

Table A.7. Vertical volumetric porefluid flux determined for sediment samples associated with sediment cores recovered from the Gulf of Mexico. Fluid flux is estimated by assuming transport toward the overlying ocean (+z) and also into the sediments (-z). Dive number refers to the HOV *Alvin* dive number during cruise AT37-06 and core number refers to the fluid flux rank variable used in Chapter 5 (Figure 5.4).

Site core;	Depth (cmbsf)	Fluid flux +z (mL cm ⁻² day ⁻¹)			Fluid flux -z (mL cm ⁻² day ⁻¹)		
4870; 1	1	-	±	-	n/a	±	n/a
	3	-	±	-	-28.2	±	5.9
	5	0.1	±	0.1	-3.3	±	0.9
	7	0.7	±	0.2	-0.3	±	0.9
	9	0.1	±	0.7	-0.1	±	0.3
	12	0.8	±	0.2	-0.2	±	1.3
4864; 2	1	0.1	±	0.6	n/a	±	n/a
	3	0.1	±	0.7	-0.1	±	0.3
	5	0.1	±	2.8	-0.2	±	0.3
	7	0.1	±	0.0	-0.5	±	0.2
	9	0.1	±	0.4	-0.1	±	0.1
	12	0.3	±	1.4	-0.2	±	2.4
4869; 3	16	n/a	±	n/a	-0.2	±	2.0
	1	0.4	±	4.1	n/a	±	n/a
	3	0.3	±	0.4	-0.1	±	0.2
	5	0.3	±	1.4	-0.1	±	0.1
	7	-	±	-	-	±	-
	9	0.7	±	1.9	-1.5	±	0.6
4861; 4	12	-	±	-	-	±	-
	16	n/a	±	n/a	-8.9	±	4.0
	1	0.6	±	4.6	n/a	±	n/a
	3	0.2	±	0.5	-0.1	±	10.9
	5	0.1	±	0.3	-0.1	±	0.2
	7	0.1	±	6.8	-0.2	±	0.5
9	-	±	-	-0.1	±	1.7	

Fluid flux is not determined for the bottom-most sediment section (+z transport direction) and for the top-most sediment section (-z transport direction) where initial ²²⁴Ra activities are potentially sourced outside of the sampled domain. Such instances are indicated by 'n/a'. Where empirical estimates were not solvable results are indicated by a '-'-symbol.

Table A.7. Continued

Site core;	Depth (cmbsf)	Fluid flux +z (mL cm ⁻² day ⁻¹)		Fluid flux -z (mL cm ⁻² day ⁻¹)		
4867; 5	12	1.0	± 0.7	-7.3	± 3.9	
	16	n/a	± n/a	-	± -	
	1	0.3	± 0.4	n/a	± n/a	
	3	0.2	± 0.1	-0.1	± 0.2	
	5	0.1	± 0.9	-0.1	± 0.0	
	7	0.2	± 0.3	-0.1	± 0.6	
	9	0.8	± 0.5	-0.1	± 0.6	
	12	1.2	± 0.8	-	± -	
4866; 6	16	n/a	± n/a	-	± -	
	1	0.8	± 8.4	n/a	± n/a	
	3	0.3	± 0.5	-0.1	± 0.6	
	5	0.3	± 0.4	-0.1	± 0.1	
	7	0.1	± 0.6	-0.1	± 1.2	
	9	0.8	± 0.8	-0.1	± 0.4	
	12	1.3	± 1.9	-0.2	± 1.0	
	16	n/a	± n/a	-0.1	± 3.6	
4862; 7	1	0.4	± 0.5	n/a	± n/a	
	3	0.2	± 0.1	-0.1	± 0.3	
	5	0.4	± 5.5	-0.1	± 0.0	
	7	0.8	± 0.5	-0.1	± 0.4	
	9	-	± -	-	± -	
	12	0.2	± 0.8	-0.2	± 1.1	
	16	n/a	± n/a	-0.6	± 2.8	
	4861; 8	1	0.7	± 0.6	n/a	± n/a
3		0.7	± 1.6	-	± -	
5		0.2	± 0.5	-0.1	± 0.3	
7		1.1	± 1.4	-0.1	± 0.1	
9		1.1	± 1.0	-	± -	

Fluid flux is not determined for the bottom-most sediment section (+z transport direction) and for the top-most sediment section (-z transport direction) where initial ²²⁴Ra activities are potentially sourced outside of the sampled domain. Such instances are indicated by 'n/a'. Where empirical estimates were not solvable results are indicated by a '-'.^c

Table A.7. Continued

Site core;	Depth (cmbsf)	Fluid flux +z (mL cm ⁻² day ⁻¹)			Fluid flux -z (mL cm ⁻² day ⁻¹)		
4862; 9	12	-	±	-	-	±	-
	16	n/a	±	n/a	-18.1	±	6.7
	1	1.0	±	0.5	n/a	±	n/a
	3	0.8	±	4.7	-	±	-
	5	0.6	±	1.4	-	±	-
	7	0.6	±	12.2	-0.1	±	0.3
	9	0.5	±	0.3	-	±	-
	12	4.0	±	3.0	-0.1	±	6.9
4872; 10	16	n/a	±	n/a	-0.1	±	0.6
	1	1.6	±	1.1	n/a	±	n/a
	3	0.6	±	0.2	-	±	-
	5	2.5	±	18.7	-0.1	±	0.0
	7	1.2	±	1.9	-	±	-
	9	-	±	-	-	±	-
	12	-	±	-	-2.7	±	33.5
	16	n/a	±	n/a	-1.0	±	1.8
4872; 11	1	0.5	±	0.4	n/a	±	n/a
	3	0.3	±	0.1	-0.1	±	0.4
	5	0.8	±	0.5	-0.1	±	0.0
	7	6.2	±	2.4	-	±	-
	9	3.6	±	28.9	-	±	-
	12	-	±	-	-	±	-
	16	n/a	±	n/a	-11.0	±	12.6
	4869; 12	1	4.8	±	12.6	n/a	±
3		1.5	±	0.8	-	±	-
5		0.8	±	1.2	-	±	-
7		0.6	±	0.5	-	±	-
9		1.4	±	0.7	-	±	-

Fluid flux is not determined for the bottom-most sediment section (+z transport direction) and for the top-most sediment section (-z transport direction) where initial ²²⁴Ra activities are potentially sourced outside of the sampled domain. Such instances are indicated by 'n/a'. Where empirical estimates were not solvable results are indicated by a '±' symbol.

Table A.7. Continued

Site core;	Depth (cmbsf)	Fluid flux +z (mL cm ⁻² day ⁻¹)			Fluid flux -z (mL cm ⁻² day ⁻¹)		
4871; 13	12	n/a	±	n/a	-	±	-
	1	0.6	±	0.4	n/a	±	n/a
	3	0.6	±	0.4	-	±	-
	5	4.0	±	1.4	-	±	-
	7	-	±	-	-	±	-
	9	8.7	±	4.9	-3.7	±	2.1
	12	n/a	±	n/a	-	±	-
4868; 14	1	4.9	±	2.0	n/a	±	n/a
	3	1.2	±	3.2	-	±	-
	5	1.6	±	4.3	-	±	-
	7	0.9	±	5.0	-	±	-
	9	3.3	±	1.3	-	±	-
	12	n/a	±	n/a	-5.9	±	2.4
	16	n/a	±	n/a	-	±	-
4871; 15	1	8.1	±	3.3	n/a	±	n/a
	3	6.8	±	2.6	-	±	-
	5	1.3	±	4.0	-	±	-
	7	1.5	±	2.1	-	±	-
	9	1.4	±	2.2	-	±	-
	12	5.8	±	9.3	-	±	-
	16	n/a	±	n/a	-	±	-
4868; 16	1	13.7	±	5.5	n/a	±	n/a
	3	6.7	±	2.2	-	±	-
	5	0.3	±	0.7	-	±	-
	7	0.5	±	4.8	-0.1	±	0.3
	9	n/a	±	n/a	-	±	-
	16	n/a	±	n/a	-	±	-
4872; 17	1	6.3	±	22.0	n/a	±	n/a
	3	5.8	±	33.2	-	±	-

Fluid flux is not determined for the bottom-most sediment section (+z transport direction) and for the top-most sediment section (-z transport direction) where initial ²²⁴Ra activities are potentially sourced outside of the sampled domain. Such instances are indicated by 'n/a'. Where empirical estimates were not solvable results are indicated by a '-' symbol.

Table A.7. Continued

Site core;	Depth (cmbsf)	Fluid flux +z (mL cm ⁻² day ⁻¹)			Fluid flux -z (mL cm ⁻² day ⁻¹)		
4862; 18	5	4.6	±	24.4	-	±	-
	7	4.7	±	2.1	-	±	-
	9	3.9	±	11.5	-	±	-
	12	-	±	-	-	±	-
	16	n/a	±	n/a	-7.8	±	4.9
	1	9.2	±	3.7	n/a	±	n/a
4871; 19	3	14.4	±	5.5	-	±	-
	5	0.5	±	1.1	-	±	-
	7	1.9	±	4.2	-0.1	±	0.2
	9	10.1	±	4.9	-	±	-
	12	n/a	±	n/a	-	±	-
	1	10.5	±	4.0	n/a	±	n/a
3	10.3	±	6.8	-	±	-	
5	28.7	±	11.9	-	±	-	
7	1.3	±	0.9	-	±	-	
9	0.5	±	2.0	-	±	-	
12	1.0	±	0.7	-0.2	±	1.8	
16	n/a	±	n/a	-	±	-	

Fluid flux is not determined for the bottom-most sediment section (+z transport direction) and for the top-most sediment section (-z transport direction) where initial ²²⁴Ra activities are potentially sourced outside of the sampled domain. Such instances are indicated by 'n/a'. Where empirical estimates were not solvable results are indicated by a '±' symbol.

APPENDIX II.

Leigha E. Peterson

301 Allied Drive
School of the Coastal Environment
Coastal Carolina University
Conway, SC 29526

Office: (843) 349-6571

lepeters@coastal.edu

EDUCATION

Doctor of Philosophy (Ph.D.) (anticipated 2019) **Aug. 2014 – present**
Coastal and Marine Systems Science, Coastal Carolina University
Major Professor: Dr. Paul Gayes (843) 349-4015

Master of Science (M.S.) **Jan. 2012 – Aug. 2014**
Coastal Marine and Wetland Studies, Coastal Carolina University
Major Professor: Dr. Richard Peterson (843) 349-4057

Bachelors of Science (B.S.) **Aug. 2008 – Dec. 2011**
Marine Science, Minor: Coastal Geology
Coastal Carolina University

EMPLOYMENT HISTORY

Lecturer **Dec. 2017 – present**
Physical Oceanography
Department of Marine Science, Coastal Carolina University
Diane Fribance (843) 349-5072

Lecturer **Aug. 2017 – Dec. 2017**
Marine Science
Department of Marine Science, Coastal Carolina University
George Boneillo (843) 349-5068

Teaching Assistant **Jan. 2017 – Aug. 2017**
Physical Oceanography, Primary Instructor
Department of Marine Science, Coastal Carolina University
Diane Fribance (843) 349-5072

Research Assistant **May 2012 – Dec. 2016**
Groundwater Discharge Measurement Facility
Center for Marine and Wetland Studies, Coastal Carolina University
Richard Peterson (843) 349-4057

Visiting Scholar **May 2015 – Aug. 2015**
Joye Research Labs, Dr. Mandy Joye
Department of Marine Sciences, University of Georgia
Mandy Joye (706) 542-3636

Graduate Assistant**Jan. 2012 – May 2012**

Center for Marine and Wetland Studies, Coastal Carolina University
Richard Viso (843) 349-4022

Laboratory Assistant**Jun. 2011 – Dec. 2011**

Groundwater Discharge Measurement Facility
Center for Marine and Wetland Studies, Coastal Carolina University
Richard Peterson (843) 349-4057

PROFESSIONAL EXPERIENCE

Research Cruises

- **Guaymas Basin Hydrothermal Impacts** **Dec. 2016**
R/V Atlantis, Chief Scientist: Andreas Teske (UNC), 19 days
 - Evaluated fluid flux from hydrothermal sediments with special interest in ecological impacts.
- **Gulf Of Mexico Cold Seeps** **Apr. 2014, June 2015, June 2016**
R/V Atlantis, Chief Scientist: Joseph Montoya (GT), 28 day; 32 day; 20 day
 - Investigated transport rates of subsurface water and oil through sediments and estimated brine age in the environment.
- **Gulf of Mexico Hydrocarbon Discharge** **Jun. - Jul. 2013** *R/V Endeavor*,
Chief Scientist: Mandy Joye (UGA), 32 days
 - Development of Ra isotopes as tracers of hydrocarbon discharge and degradation rates.
- **Antarctic Meltwater** **Dec. 2012, Mar. 2014**
R/V Laurence M. Gould, Chief Scientist: Reide Corbett (ECU), 20 days
 - Determined interaction of glacial meltwater and nutrients with ocean water along Antarctic continent.

Field and Laboratory Experience

- **Seasonal fluxes into Discovery Bay, Jamaica** **Nov. 2015, Apr. 2016**
 - Estimated groundwater flux to Jamaican embayment over rainy and dry seasons with emphasis on material delivery.
- **Groundwater derived nutrients to Laguna Madre, Texas** **Jun. 2015**
 - Surveyed shorelines for groundwater discharge zones and associated nutrient loads investigating the role of subsurface flow in eutrophication.
- **Groundwater fluxes to Lake Huron** **Jun. 2014**

-
- Used ^{222}Rn to identify groundwater ‘hot-spots’ along the lake shores to assist a large effort investigating potential sources of E. coli to the lake.

 - **Urban tidal creek water budgets** **Jun. 2011- Oct. 2013**
 - Used Rn and Ra isotopes to delineate water sources to coastal creeks in Myrtle Beach and Surfside, SC.

 - **Groundwater dynamics along a Georgia marsh** **Jun. 2013**
 - Assisted graduate thesis research investigating groundwater inputs to the Duplin River using Rn and electrical resistivity.

 - **Groundwater inputs to a tidal creek** **Apr. 2013**
 - Organized electrical resistivity survey to observe surface and sub-surface interactions in Withers Swash, SC.

 - **Antarctic meltwater** **Dec. ‘12 – Feb. ‘13, Dec. ‘13 - Mar. ‘14**
 - Assisted NSF funded project investigating surface vs. subsurface transport of glacial melt water using resistivity, stable, and radio-tracers.

 - **Long Bay hypoxia** **Jun. 2011 – Aug. 2011**
 - Compiled vertical profiles and collected Rn and Ra data from Apache Pier, SC to assess the role of groundwater in Long Bay hypoxia.
-

PUBLICATIONS

- **L. Peterson**, Peterson, R., 2019. Spatial associations between fluid flux, temperature, and microbial mat in Guaymas Basin, Gulf of California. Deep-sea Research. In-prep.

- R. Peterson, Meile, C., **Peterson, L.E.**, Carter, M., Miklesh, D., 2019. Groundwater discharge dynamics into a salt marsh tidal river. Estuarine, Coastal and Shelf Science. 218 324-333

- J. Tao, Peterson R., Befus, K., **Peterson L.**, Robinson C. 2017. Characterization of groundwater discharge to Nottawasaga Bay, Lake Huron with hydraulic and ^{222}Rn measurements. Journal of Great Lakes Research, 43,920-929.

- D.R. Corbett, Crenshaw J, Null K, Peterson R, **Peterson L**, Lyons B. 2017. Nearshore mixing and nutrient delivery along the Western Antarctic Peninsula. Antarctic Science, 29(5), 397-409.

- **L.E. Peterson**, Peterson R., Smith E., Libes S. 2016. Advances in Water Security: Emerging Issues in Groundwater Resources. In: Ali Fares. (Ed.) Prairie View, TX: Springer International Publishing. Chapter 9, Quantifying groundwater export from an urban reservoir: A case study from coastal South Carolina. 223-262 doi: 10.1007/978-3-319-32008-3_9 2016.

- R.N. Peterson, Moore W.S., Chappel S., Viso R., Libes S., **Peterson L.** 2016. A new perspective on coastal hypoxia: The role of saline groundwater. Marine Chemistry, 179, 1-11.

- S.C. Weber, **Peterson L.**, Battles J., Roberts B., Peterson R., Hollander D., Chanton J., Joye, S.B., Montoya J. 2016. Hercules 265 rapid response: Immediate ecosystem impacts of a natural gas blowout incident. Deep Sea Research II, 129, 66-76.

-
- J.C. Hill, Phillips, J.A., Marshall, J.A., O'Brien-Gayes, P.T., **Peterson L.E.** 2011. High-resolution Geophysical Survey and Interpretation for the Morehead City ODMDS and Borrow Area "Y" near Bogue Banks, North Carolina. Technical Report submitted to Geodynamics, LLC.
-

PRESENTATIONS

- **L. Peterson**, R. Peterson, S. Harrison, S.M. Joye, 2016. Toward the development of an oil aging technique using radio-isotopic analytes to evaluate environmental exposure time. 3rd Annual Southeastern Biogeochemistry Symposium, March 11- 13. Knoxville, TN.
- **L. Peterson**, R. Peterson, M. Joye, C. Meile, J. Montoya, S. Weber. 2015. Using fluid advection rate estimates from natural hydrocarbon seeps to constrain bottom boundary water turnover times in deep ocean systems. Gordon Research Conference –Chemical Oceanography, July 26-31. Holderness, NH.
- **L. Peterson**, R. Peterson, S. Joye, C. Meile, J. Montoya, S. Weber, 2015. Comparing fluid advection rates between natural oil and bubble seeps in deep ocean systems using radium isotopes. 10th International Conference on Methods and Applications of Radioanalytical Chemistry, April 12-17. Kailua-Kona, HI
- **L. Peterson**, R. Peterson, S. Joye, C. Meile, J. Montoya, S. Weber, 2015. High-resolution fluid advection rate estimates from natural oil and bubble seeps in deep ocean systems: An examination of heterogeneity. 2nd Annual Southeastern Biogeochemistry Symposium, March 28-29. Atlanta, GA
- **L. Peterson**, R. Peterson, S. Joye, C. Meile, J. Montoya, S. Weber, 2015. Assessing hydrocarbon flow through sediments using radium isotopes. Gulf of Mexico Oil Spill and Ecosystem Science Conference, February 16-19. Houston, TX
- R. Peterson, **L. Peterson**, J. Montoya, S. Weber, C. Meile, S. Joye, 2015. Radium isotopes as conservative tracers of hydrocarbon transport through the water column. Gulf of Mexico Oil Spill and Ecosystem Science Conference, February 16-19. Houston, TX
- T. Ji, R. Peterson, **L. Peterson**, C. Robinson, S. Malott, 2014. Multiple methods to quantify nearshore groundwater discharge to the Great Lakes. 14th Annual Great Lakes Beach Association Conference, November 12-14. Toronto, Canada
- **L. Peterson**, R. Peterson, D.R. Corbett, K. Null, R. Viso, J. Crenshaw, 2014. Spatial partitioning of Ra and ²²²Rn isotopes indicative of fluid origin: Observations using novel high-resolution survey techniques. 5th International Workshop on Radium and Radon, July 21-24. Rio de Janeiro, Brazil
- R. Peterson, **L. Peterson**, S. Joye, J. Montoya, S. Weber, R. Viso, 2014. Radium isotopes as tracers of hydrocarbon discharge and transport through the water column. 5th International Workshop on Radium and Radon, July 21-24. Rio de Janeiro, Brazil

- **L. Peterson**, R. Peterson, E. Smith, A. Defore, R. Viso, 2013. Using Time-series Water Budgets to Assess Tidal Influence on Fluid Composition (Surface and Subsurface Inputs) in Urbanized Tidal Creeks. Southeast Tidal Creek Summit, December 16-18. Wilmington, NC
- D.R. Corbett, **L. Peterson**, J. Crenshaw, D. Hawkins, K. Null, R. Peterson, R. Viso, 2013. Time-series Measurements of Geochemical Tracers and Electrical Resistivity to Evaluate Groundwater-Surface Water Interactions on Anvers Island, Antarctica. American Geophysical Union Conference, December 9-13. San Francisco, CA
- J. Crenshaw, D.R. Corbett, J. Walsh, K. Null, **L. Peterson**, D. Hawkins, R. Peterson, R. Viso, D. Sybert, B. Lyons, 2013. Transport of Terrestrially-derived Nutrients across the Continental Shelf of the Western Antarctic Peninsula, Anvers Island. American Geophysical Union Conference, December 9-13. San Francisco, CA
- K. Null, J. Crenshaw, **L. Peterson**, D. Hawkins, R. Peterson, W.B. Lyons, D.R. Corbett, 2013. Submarine Groundwater Discharge along the Western Antarctic Peninsula: Relative Contributions of Recirculated Seawater and Subsurface Glacial Freshwater. American Geophysical Union Conference, December 9-13. San Francisco, CA
- **L.E. Peterson**, R. Peterson, R. Viso, K. Gregorcyk, E. Smith, 2012. Geochemical Characterization of Groundwater Discharge into Tidal Creeks using Radon-222. 4th International Workshop on Radium and Radon, June 3-8. Narragansett, RI
- S. Chappel, R. Peterson, R. Viso, S. Libes, P. Hutchins, **L. Peterson**, K. Gregorcyk, 2012. Developing the use of Geochemical Tracers in linking Submarine Groundwater Discharge to Hypoxia Formation in Long Bay, S.C., USA. 4th International Workshop on Radium and Radon, June 3-8. Narragansett, RI
- R.N. Peterson, R. Viso, S.Chappel, K. Gregorcyk, S.M. Libes, **L.E. Peterson**, 2012. Continuous Radon Time-Series Measurements Link Submarine Groundwater Discharge to Ocean Hypoxia. 4th International Workshop on Radium and Radon, June 3-8. Narragansett, RI

RESEARCH GRANTS AND AWARDS

Nelson Fellowship	2014-2015
Outstanding graduate studies in marine geology at CCU (\$500)	
Savannah Presbytery M.K. Pentecost Ecology Fund	2012-2013
“An Integrated Approach to Characterize Temporal Variability of Porewater Chemistry and Sediment Porosity Within a Coastal Aquifer” (\$2,000)	
The Slocum-Lunz Foundation	2012-2013
“An Integrated Geophysical and Geochemical Approach to	

Characterize Groundwater Discharge” (\$500)

Graduate Student Incentive Grants, CCU

2012-2013

“Characterizing Groundwater Inputs to Coastal Environments Using
Geochemical and Geophysical Techniques” (\$500)

APPENDIX III.

When a radionuclide (P) decays to a radioactive daughter (D), the rate of decay of D is the difference between the rate at which D is produced by decay of P and its own rate of decay. The rate of decay of P ($-\frac{dP}{dt}$) is given by:

$$-\frac{dP}{dt} = \lambda_p * N_p \quad (\text{A.1})$$

where λ_p is the decay constant of the parent isotope and N_p is the number of atoms of the parent remaining at any time (t).

Similarly, the rate of decay of D ($-\frac{dD}{dt}$) is given by:

$$-\frac{dD}{dt} = \lambda_d * N_d \quad (\text{A.2})$$

where λ_d is the decay constant of the daughter isotope and N_d is the number of atoms of the daughter remaining at any time (t).

Since the amount of D is cumulatively determined by its own radioactive decay as well as ingrowth from decay of P,

$$\frac{dD}{dt} = (\lambda_p * N_p) - (\lambda_d * N_d) \quad (\text{A.3})$$

The number of atoms of parent (N_p) remaining at any time is given by:

$$N_p = N_p^0 e^{-\lambda_p t} \quad (\text{A.4})$$

where N_p^0 is the number of parent atoms present at t=0. Equation A.4 is substituted into Equation A.3 and, by rearranging terms, yields:

$$\frac{dD}{dt} + (\lambda_d * N_d) - (\lambda_p * N_p^0 e^{-\lambda_p t}) = 0 \quad (\text{A.5})$$

Equation A.5 is a first-order linear differential equation first solved by Bateman (1910)¹.

The solution to Equation A.5 is:

$$N_d = \frac{\lambda_p}{\lambda_d - \lambda_p} N_p^0 (e^{-\lambda_p t} - e^{-\lambda_d t}) + N_d^0 e^{-\lambda_d t} \quad (\text{A.6})$$

The first term of Eq. A.6 gives the number of daughter atoms that have formed by parent decay, but have not yet decayed themselves. The second term represents the number of daughter atoms that remain from an initial number (N_d^0).

Since, generally, the activity (A) of an isotope is given by:

$$A = \lambda N \quad (\text{A.7})$$

we multiply each N term in Equation A.6 by its respective decay constant (λ), to convert Equation A.6 into activity units for calculations described throughout the dissertation:

$$A_d = \frac{\lambda_p \lambda_d}{(\lambda_d - \lambda_p)} \frac{A_p^0}{\lambda_p} (e^{-\lambda_p t} - e^{-\lambda_d t}) + A_d^0 e^{-\lambda_d t} \quad (\text{Eq. 2.3})$$

¹ Bateman, H. 1910. Solution of a system of differential equations occurring in the theory of radioactive transformations. *Mathematical Proceedings of the Cambridge Philosophical Society*. 15, 423.